DISS. ETH NO. 22330

Terrestrial mercury cycling investigated with stable mercury isotopes

A thesis submitted to attain the degree of

DOCTOR OF SCIENCES of ETH ZURICH

(Dr. sc. ETH Zurich)

presented by

MARTIN JISKRA

MSc ETH Environ. Sc

born on 17.06.1984

citizen of
Herisau AR, Switzerland

accepted on the recommendation of

Prof. Dr. Ruben Kretzschmar, examiner
Prof. Dr. Bernard Bourdon, co-examiner
Dr. Jan G. Wiederhold, co-examiner
Dr. Jeroen E. Sonke, co-examiner

2014

Table of contents

Summary v

Zusammenfassung ix

Résumé xiii

1 Introduction 1

1.1 Mercury - a global pollutant 2
1.2 Terrestrial mercury cycling 3
1.3 Stable mercury isotopes 5
1.4 Research approach and objectives 9
References 11

2 Mercury isotopes reveal organic matter-driven reductive Hg loss from boreal forest soils 17

2.1 Introduction 19
2.2 Methods 21
  2.2.1 Soil samples 21
  2.2.2 Analytical methods 21
  2.2.3 Radiocarbon dating 22
  2.2.4 Hg isotope model 23
  2.2.5 Hg re-emission flux calculation 23
2.3 Hg isotope signatures of boreal forest soils 24
2.4 Implications for global Hg cycling 28
References 31

3 Sources of mercury in boreal forest catchment runoff: Insights from Hg stable isotope signatures, radiocarbon signatures and Hg:C ratios 35

3.1 Introduction 37

3.2 Experimental section 38

3.2.1 Materials and reagents 38

3.2.2 Study area 39

3.2.3 Soil sample preparation 39

3.2.4 Water sample preparation 40

3.2.5 Analytical methods 43

3.2.6 Mixing models 44

3.3 Results 45

3.4 Discussion 48

3.4.1 Hg isotope signatures 48

3.4.2 Radiocarbon signatures 49

3.4.3 Hg:C ratios 50

3.4.4 Controls on Hg in boreal forest runoff 52

3.4.5 Effects of forest harvest 53

3.4.6 Implications for the transport of terrestrial Hg to aquatic ecosystems 53

References 57

4 Solution speciation controls mercury isotope fractionation of Hg(II) sorption to goethite 63

4.1 Introduction 65

4.2 Experimental section 66

4.2.1 Materials and reagents 66

4.2.2 Batch experiments 68

4.2.3 Analytical methods 68

4.3 Results and discussion 70

4.3.1 Sorption of Hg to goethite 70

4.3.2 Stable Hg isotope fractionation 71

4.3.3 Possible Hg isotope fractionation mechanisms 73

4.3.4 Isotope fractionation during species equilibration in solution ($\mathrm{IE_{SE}}$) 74

4.3.5 Calculated predictions of MDF and NVF 75

4.3.6 Isotope fractionation during surface complex formation ($\mathrm{IE_{OS}}$, $\mathrm{IE_{IS}}$) 77

4.3.7 Control of Hg isotope fractionation 77

4.3.8 Implications for other metal isotope and surface complexation studies. 79
4.3.9 Implications for stable Hg isotopes as environmental tracer 80
References 83

5 Kinetics of Hg(II) exchange between organic ligands, goethite, and natural organic matter studied with an enriched stable isotope approach 89
5.1 Introduction 91
5.2 Experimental section 92
5.2.1 Materials and reagents 92
5.2.2 Batch experiments 93
5.2.3 Analytical methods 98
5.2.4 Data reporting 98
5.2.5 Kinetic modeling 99
5.3 Results and discussion 102
5.3.1 Hg(II)-exchange between dissolved inorganic complexes and resins 102
5.3.2 Hg(II)-exchange between dissolved organic ligands and carboxyl-resin 105
5.3.3 Hg(II)-exchange between dissolved NOM and resins 105
5.3.4 Hg(II)-exchange between dissolved inorganic complexes and goethite 107
5.3.5 Implications of exchange kinetics for laboratory experiments . . . 108
5.3.6 Implications for isotope fractionation experiments 108
5.3.7 Environmental implications 110
References 111

6 Conclusions and outlook 119
6.1 Mechanistic studies of stable isotope fractionation during sorption 120
6.1.1 Outlook on future studies on metal isotope fractionation during sorption 122
6.2 Assessing terrestrial mercury cycling with stable Hg isotopes 123
6.2.1 Outlook for terrestrial Hg cycling 126
References 129

Supporting Information to Chapter 2 133
Materials and methods 134
References 153

Supporting Information to Chapter 3 157
Radiocarbon dating 161
Mixing model 165
References 169

Supporting Information to Chapter 4 171
Materials and reagents 172
Comparison of model approaches 177
References 185

Supporting Information to Chapter 5 187
Materials and reagents 188
Kinetic models - differential equations 189
References 203

Danksagung 205

Curriculum Vitae 209

Summary

Mercury (Hg) is a pollutant of great concern for human and ecosystem health. Emitted to the atmosphere from anthropogenic and natural sources, Hg is transported around the globe and eventually deposited on the Earth's surface. Terrestrial ecosystems play an important role for the global cycling of Hg mainly for three reasons: (i) soils act as a sink for atmospherically deposited Hg and sequester large amounts of Hg due to the strong binding of Hg(II) to soil organic matter and mineral phases, (ii) re-emission from terrestrial ecosystems represents a source of Hg to the atmosphere as a result of reduction of Hg(II) to volatile elemental Hg(0), and (iii) runoff transport from soils represents a major source of Hg to aquatic environments where it is taken up by biota.

Biogeochemical reactions of Hg are associated with mass-dependent and mass-independent fractionation of its seven stable isotopes. The analysis of Hg stable isotopes may provide new insights into pathways and processes controlling the fate of Hg due to characteristic Hg isotope fractionation of different processes and potentially distinct signatures for different Hg sources. The goal of this thesis was to develop Hg stable isotopes as a tool to investigate terrestrial Hg cycling. The successful application of Hg stable isotopes requires both, the study of Hg isotope variations in terrestrial ecosystems in case studies, and the mechanistical investigation of processes causing Hg isotope fractionation under controlled laboratory conditions. Therefore, the following objectives were addressed: (i) to identify the pathway of atmospheric Hg deposition in boreal forest soils, (ii) to investigate the reductive re-emission of Hg from boreal forest soils, (iii) to develop an analytical method for Hg isotope measurements in natural waters and to investigate the source of Hg in the soil runoff, (iv) to investigate stable Hg isotope fractionation associated with Hg(II) sorption to mineral surfaces, and (v) to examine the isotope exchange kinetics of Hg(II).

In a field study, boreal forest soils in northern Sweden were investigated. The Hg stable isotope signatures of radiocarbon-dated boreal forest soils were measured and the source of atmospheric Hg deposition, reduction processes, and re-emission fluxes were investigated using a combined source/process tracing approach. The results suggested that deeper soil horizons accumulated precipitation-derived Hg over decades. The Hg isotope composition in organic soil horizons provided evidence for significant Hg re-emission driven by non-photochemical abiotic reduction by natural organic matter, a process not yet observed unambiguously in nature. The data suggested that water-saturated Histosols (peat soils) exhibited three times higher re-emission fluxes compared to well-drained Podzols and had re-emitted up to one third of previously deposited Hg to the atmosphere over a century. Thus, organic matter-driven re-emission of legacy Hg might be an important pathway previously not considered in global Hg models.

The runoff samples from boreal forest soils were measured with a new analytical approach based on ultrafiltration pre-enrichment allowing for the first time measurements of Hg isotope signatures in natural waters with high dissolved organic carbon concentrations. The results suggested that there was no fractionation during leaching of Hg from soils and that the uppermost organic soil horizons exhibited an at least five times higher mobility compared to underlying more decomposed organic soil horizons and contributed about 60 to 85% to the total Hg flux in the runoff. Therefore, a response of the terrestrial Hg runoff to a reduction in atmospheric Hg deposition within few decades could be expected.

The Hg isotope fractionation and the isotope exchange kinetics of Hg(II) sorption to goethite, an important iron oxide in soils, was investigated in batch experiments. Sorption of Hg(II) to goethite was associated with a preferential enrichment of light Hg isotopes on the mineral surface. The observed Hg isotope enrichment was in agreement with a theoretical equilibrium isotope effect during species equilibration in solution, suggesting that the isotope effect in solution was expressed during sorption through the adsorption of the cationic Hg species to the goethite surface. The isotope exchange experiments revealed that a significant amount of Hg(II) was sorbed to goethite in a non-exchangeable manner, suggesting that an isotope effect between dissolved and solid-bound Hg(II) can consist of: (i) a signal trapped in the non-exchangeable pool with a kinetic component from the initial adsorption, and (ii) a signal of the exchangeable pool consisting of the equilibrium isotope effect between the dissolved species and the solid-bound exchangeable Hg. These observations have general implications for isotope fractionation studies of other metals for which non-exchangeable sorption to mineral phases and isotope fractionation during species equilibration have been reported.

The results from the isotope exchange experiments between dissolved and solid-bound Hg(II) revealed that natural organic matter and thiol-resin also contained non-exchangeable Hg(II) pools. These observations suggest that the possibility of non-exchangeable binding must be considered to a greater extent in the assessment of the fate of Hg in the environment and the design of experimental studies.

The stable Hg isotope approaches and analytical methods used in this thesis offer the potential to gain further insights in the land/atmosphere exchange of Hg, the role of terrestrial Hg sources for aquatic biota, and the role of the terrestrial system in the global Hg cycle.

Zusammenfassung

Quecksilber (Hg) ist ein Schadstoff von globaler Bedeutung für die menschliche Gesundheit und die Umwelt. Quecksilber wird durch anthropogene und natürliche Quellen in die Atmosphäre ausgestossen, rund um den Globus transportiert und schlussendlich auf der Erdoberfläche abgelagert. Terrestrische Ökosysteme spielen eine zentrale Rolle für den globalen Quecksilberkreislauf, hauptsächlich aus drei Gründen: (i) Böden stellen durch die starke Bindung von Hg an natürliche organische Substanz und Mineraloberflächen eine wichtige Senke für atmosphärisch abgelagertes Quecksilber dar, (ii) die Reduktion von Hg(II) zu volatilem Hg(0) führt zu einer Reemission von Quecksilber aus terrestrischen Ökosystemen in die Atmosphäre, und (iii) der Austrag von Hg aus terrestrischen Ökosystemen stellt eine wichtige Quelle für aquatische Ökosysteme dar, in denen Hg von aquatischen Organismen aufgenommen werden kann.

Biogeochemische Reaktionen führen zu massenabhängiger und massenunabhängiger Fraktionierung der sieben stabilen Quecksilberisotope. Die Quecksilberisotopenanalyse kann durch die charakteristische Isotopenfraktionierung verschiedener Prozesse und mögliche Unterschiede in Quellensignaturen neue Erkenntnisse über das Verhalten von Quecksilber liefern. Das Ziel dieser Doktorarbeit war der Einsatz von stabilen Quecksilberisotopen als Methode, um das Verhalten von Quecksilber in terrestrischen Systemen zu untersuchen. Eine erfolgreiche Etablierung der Quecksilberisotopenanalyse benötigt zum einen Fallstudien, die die Unterschiede von Quecksilbersignaturen in terrestrischen Ökosystemen untersuchen und zum anderen Prozessstudien über Fraktionierungsmechanismen unter kontrollierten Laborbedingungen. Die Doktorarbeit beinhaltet folgende Aufgabenbereiche: (i) die Identifikation der Quellen von atmosphärischer Quecksilberdeposition in borealen Forstböden, (ii) die Untersuchung von reduktiver Hg-Reemission aus borealen Forstböden, (iii) die Entwicklung einer analytischen Methode zur Messung von Quecksilber-Isotopensignaturen in Oberflächengewässern und die Untersuchung der Quecksilberquellen im Abfluss aus Böden, (iv) die Untersuchung der stabilen Isotopenfraktionierung von Hg(II)-Sorption an mineralische Oberflächen, und (v) die Untersuchung der Kinetik von Hg(II)-Isotopenaustauschprozessen.

In einer Feldstudie wurden boreale Forstböden in Nordschweden untersucht. Die stabilen Quecksilberisotopensignaturen und das Radiokohlenstoffalter von Bodenproben wurden bestimmt und die Quellen der atmosphärischen Quecksilberdeposition, die Reduktionsprozesse und die Reemissionsflüsse untersucht. Die Resultate zeigten, dass die tieferen Bodenhorizonte über Jahrzehnte Quecksilber aus Niederschlag zu akkumulieren scheinen. Die Quecksilbersignatur in organischen Bodenhorizonten wies auf bedeutende Reemission von Quecksilber durch abiotische, nicht-photochemische Reduktion von Quecksilber durch natürliche organische Substanzen hin - ein Prozess der noch nie eindeutig in der Natur beobachtet wurde. Die Daten legen nahe, dass wassergesättigte Histosole (Moorböden) dreimal höhere Reemissionsflüsse als gut drainierte Podzole aufweisen. Demnach scheinen Histosole bis zu einem Drittel des vorgängig abgelagerten Quecksilbers innerhalb eines Jahrhunderts wieder an die Atmosphäre zu verlieren. Die Reduktion von Quecksilber durch organische Substanz scheint einen wichtigen Reemissionspfad darzustellen, der in bisherigen globalen Modellen nicht berücksichtigt wurde.

Die Abflussproben der borealen Forstböden wurden mittels einer neuen Messmethode, basierend auf einer Anreicherung mit Ultrafiltration, gemessen. Diese erlaubte zum ersten Mal die Analyse von Quecksilberisotopensignaturen in Wasserproben mit hohen Konzentrationen an gelöstem organischen Kohlenstoff. Die Resultate zeigten keine Hinweise für Isotopenfraktionierung während der Auswaschung von Quecksilber aus Böden sowie eine mindestens fünfmal höhere Mobilität des Quecksilbers im obersten organischen Bodenhorizont im Vergleich zu den tieferliegenden Horizonten. Demnach tragen die obersten Bodenhorizonte 60 - 85 % zum totalen Quecksilberabfluss bei. Bei einer Reduktion von atmosphärischer Deposition würde demzufolge eine Anpassung des Hg-Austrages aus terrestrischen Ökosystemen innerhalb von Jahrzehnten zu erwarten sein.

Die Fraktionierung der Quecksilberisotope und die Isotopenaustauschkinetik der Sorption von Hg(II) an Goethit, einem wichtigen Eisenoxid in Böden, wurde in Laborexperimenten untersucht. Die Sorption von Hg(II) an Goethit war mit einer präferentiellen Anreicherung von leichten Quecksilberisotopen an der Mineraloberfläche verbunden. Die beobachtete Isotopenanreicherung war in Übereinstimmung mit theoretischen Gleichgewichtsisotopeneffekten zwischen verschiedenen Lösungsspezies. Demnach wurde der Gleichgewichtsisotopeneffekt in Lösung durch die Adsorption der kationischen Lösungsspezies an der Mineraloberfläche exprimiert. Das Isotopenaustauschexperiment legte nahe, dass ein beträchtlicher Teil von sorbiertem Hg(II) irreversibel am Goethit gebunden war. Demzufolge scheint ein gemessener Isotopeneffekt zwischen einer Lösungsphase und einer sorbierten Phase aus (i) einem Signal im nicht austauschbaren

Pool, welches eine kinetische Komponente durch die initiale Adsorption enthält und (ii) einem Signal, welches den Gleichgewichtsisotopeneffekt zwischen den Lösungsspezies und der sorbierten austauschbaren Phase enthält, zu bestehen. Diese Beobachtungen haben allgemeingültige Implikationen für Isotopenfraktionierungsstudien von anderen Metallen, für welche irreversible Sorption an Mineraloberflächen oder Gleichgewichtsisotopeneffekte zwischen Lösungsspezies beschrieben wurden.

Die Resultate der Isotopenaustauschexperimente zwischen gelöstem und oberflächengebundenem Hg(II) zeigten, dass auch natürliche organisches Substanz und Thiolharze nicht austauschbare Hg(II)-Bindungen enthalten. Diese Beobachtungen weisen darauf hin, dass der Möglichkeit von nicht-austauschbaren Bindungen bei der Beurteilung vom Verhalten von Quecksilber in der Umwelt und beim Design von Experimenten eine grössere Beachtung geschenkt werden muss.

Die Ansätze und analytische Methoden der stabilen Quecksilberisotopenanalyse, die in dieser Doktorarbeit angewendet wurden, bieten die Möglichkeit, neue Erkenntnisse über den Quecksilberaustausch zwischen Land und Atmosphäre, über die Rolle von terrestrischen Quecksilberquellen für aquatische Lebewesen und über die Rolle der terrestrischen Ökosysteme für den globalen Quecksilberkreislauf zu gewinnen.

Résumé

Le mercure (Hg) est un polluant très préoccupant tant pour la santé que pour l'écosphère. Il est émis dans l'atmosphère par des sources anthropogènes et naturelles et peut être transporté autour du globe et éventuellement déposé sur la surface de la terre. Les écosystèmes terrestres jouent un rôle central dans le cycle global du mercure pour principalement trois raisons: (i) les sols agissent comme un dispositif de drainage pour le mercure déposé de l'atmosphère et retiennent de grandes quantités de Hg grâce à une fixation forte du Hg(II) à des substances organiques du sol, ainsi qu'à divers minéraux, (ii) la réémission par des écosystèmes terrestres vers l'atmosphère représente une source de Hg dûe à la réduction de Hg(II) à Hg(0) qui est volatil, et (iii) le transport par ruissellement au sol représente une source importante de Hg aux environnements aquatiques dans lesquels il est absorbé par des biotes.

Les réactions biogéochimiques de Hg sont associées au fractionnement soit dépendant soit indépendant de la masse des sept isotopes stables du mercure. L'analyse des isotopes du mercure peut ouvrir de nouvelles perspectives vers des voies et des mécanismes qui contrôlent sont sort, à cause du fractionnement caractéristique du Hg au cours de différents processus et potentiellement de différentes signatures par rapport aux sources.

Le but de cette Thèse est de développer l'emploi des isotopes stables du Hg comme un outil qui peut être utilisé pour investiguer le cycle terrestre du Hg. Le succès de l'application des isotopes stables du Hg demande d'une part l'étude des variations des isotopes de Hg dans des écosystèmes terrestres lors d'études de cas et d'autre part l'investigation des processus qui causent le fractionnement des isotopes du Hg sous les conditions contrôlées du laboratoire. Les objectifs de cette Thèse sont les suivants: (i) identifier le sources de la déposition du mercure atmosphérique sur les sols des forêts boréaux, (ii) investiguer la réémission réductive du mercure par les sols les forêts boréaux, (iii) développer une méthode analytique pour mesurer les isotopes du mercure dans les eaux naturelles, ainsi que rechercher la source du mercure dans les ruissellements des sols, (iv) examiner le fractionnement des isotopes stables du Hg associé à la sorption du Hg(II) sur la surface des minéraux, et (v) investiguer la cinétique de l'échange des isotopes du

mercure.

Dans le cadre d'une étude de terrain, des sols des forêts boréaux du nord de la Suède ont été examinés. Les signatures des isotopes stables du mercure des sols des forêts boréaux datés par la méthode au radiocarbone ont été analysées. La source de la déposition du Hg atmosphérique, les processus de réduction, ainsi que les flux de réémission ont été étudiés par une approche jointe de source/processus de tracement. Les résultats indiquent que les horizons les plus profonds ont accumulé du Hg provenant par la précipitation pendant des décennies. La composition isotopique du Hg dans les horizons de sol organique suggère une réémission remarquable de Hg produite par la réduction abiotique, non-photochimique par la matière organique naturelle. Ce processus n'a pas été clairement observé dans la nature. Les résultats indiquent que les histosols saturés en eau présentent des flux de réémission qui sont trois fois plus hauts que les podzols bien drainés et qu'ils ont réémis vers l'atmosphère au moins un tiers du Hg déjà déposé au cours d'un siècle. Par conséquence, la réémission du Hg existant causée par la matière organique semble représenter une voie importante, jusque-là inconsidérée dans les modèles globaux de Hg.

Les échantillons de ruissellement du sol des forêts boréaux ont été analysés par une nouvelle approche analytique basée sur le pré-enrichissement par ultrafiltration qui permet -pour la première fois- d'analyser les signatures isotopiques du Hg dans les eaux naturelles à concentration du carbone organique élevée. Les résultats démontrent qu'il n'y a pas de fractionnement des isotopes au cours du lessivage du mercure par les sols et que les horizons les plus supérieurs des sols organiques présentent une mobilité au moins cinq fois plus élevée par rapport à celle des horizons sous-jacent qui sont plus décomposés et ont contribué à environ $60 - 80$ % au flux total du Hg au ruissellement. Par conséquence, dans quelques décennies on peut s'attendre à une réduction de la déposition du Hg atmosphérique dûe au ruissellement terrestre du Hg.

Le fractionnement des isotopes du mercure et la cinétique de l'échange isotopique de la sorption du Hg(II) sur la goethite, un oxyde de fer important dans des sols, a été étudié dans des expériences de batch. La sorption du Hg(II) sur la goethite a été associée à un enrichissement préférentiel des isotopes légers du mercure sur la surface du minéral. L'enrichissement des isotopes du Hg observé est en accord avec l'effet d'équilibre isotopique théorique qui a lieu au cours de l'équilibrage des espèces en solution. Cette observation indique que l'effet isotopique en solution a été exprimé au cours de la sorption par l'adsorption des espèces cationiques du Hg sur la surface de la goethite. Les expériences sur l'échange isotopique ont montré qu'une quantité remarquable de Hg(II) était adsorbé sur la goethite d'une manière non-échangeable, ce qui suggère qu'un effet isotopique entre le Hg(II) en solution et le Hg(II) en phase solide peut se composer: (i) d'un signal piégé dans le bassin non-échangeable avec une composante cinétique par l'adsorption initiale et (ii) d'un signal du bassin échangeable qui se compose de l'effet isotopique d'équilibre entre les espèces en solution et le Hg échangeable en phase solide. Ces observations ont des implications générales pour les études de fractionnement des isotopes d'autres métaux, pour lesquels une sorption non-échangeable sur les minéraux, ainsi qu'un fractionnement isotopique au cours de l'équilibrage des espèces ont été mentionnés.

Les résultats des expériences sur l'échange des isotopes entre le Hg(II) en solution et celui en phase solide indiquent que la matière organique naturelle, ainsi que les résines thiolées contiennent aussi des bassins de Hg(II) non-échangeable. Ces observations soulignent que la possibilité de fixations non-échangeables doit être considérée en grande partie lors de l'évaluation du sort du mercure dans l'environnement, ainsi que dans la conception des études expérimentales.

Les approches et les méthodes analytiques des isotopes stables du mercure appliquées dans cette Thèse offrent un potentiel pour mieux comprendre l'échange du mercure entre le sol et l'atmosphère, pour saisir le rôle qui jouent les sources terrestres du Hg pour les biotes aquatiques, ainsi que le rôle des systèmes terrestres dans le cycle global du mercure.

Chapter 1

Introduction

1.1 Mercury - a global pollutant

Mercury (Hg) is a global pollutant of great concern for human and ecosystem health.[1] In the environment Hg can be methylated by anaerobic bacteria to methyl-Hg, a potent neurotoxin.[2] Because of bioaccumulation and biomagnification along the food chain humans are exposed to high concentrations of methyl-Hg through the consumption of fish and marine mammals.[2] In Scandinavia for example, fish in over 60% of all freshwater lakes contain methyl-Hg concentrations exceeding the general health guidelines of the EU for fish consumption.[3] Gaseous Hg(0) is emitted from natural (90 - 600 Mg year^{-1})[4,5] and anthropogenic sources (2000 Mg year^{-1}).[6] Gaseous elemental Hg(0), the dominant Hg form in the atmosphere, is transported around the globe and has a lifetime in the atmosphere on the order of one year.[1,7] Following oxidation of volatile gaseous Hg(0) to Hg(II), reactive Hg(II) is rapidly deposited on global aquatic and terrestrial surfaces also far away from the emission source (Figure 1.1).[1,7]

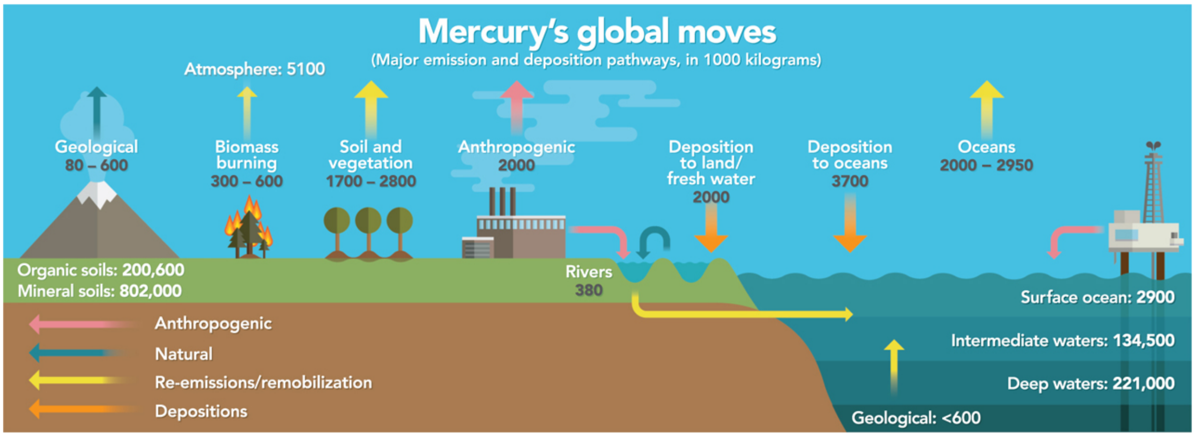
Mercury's global moves
(Major emission and deposition pathways, in 1000 kilograms)
Atmosphere: 5100
Geological
80 – 600
Biomass
burning
300 – 600
Soil and
vegetation
1700 – 2800
Anthropogenic
2000
Deposition
to land/
fresh water
2000
Deposition
to oceans
3700
Oceans
2000 – 2950
Organic soils: 200,600
Mineral soils: 802,000
Rivers
380
Surface ocean: 2900
Intermediate waters: 134,500
Deep waters: 221,000
Geological: <600
Anthropogenic
Natural
Re-emissions/remobilization
Depositions

Figure 1.1: Global cycling of mercury: Anthropogenic sources (red), natural sources (blue), and re-emission of legacy Hg (yellow) emit Hg to the atmosphere from where it is eventually deposited on the ocean and terrestrial earth surface (orange). (From Lubick and Malakoff, 2013.[8] Reprinted with permission from AAAS.)

Today, global inventories assume that each year 2000 Mg of Hg are emitted to the atmosphere through anthropogenic activities, primarily from coal combustion and artisanal and small-scale gold mining.[6] Additionally, significant amounts of Hg from commercial use (e.g., batteries, vinyl chloride monomer, and chlor-alkali production) have been historically and are still released to aquatic and terrestrial environments and the atmosphere.[9] Apart from an increased atmospheric Hg load, the release of commercial Hg products resulted in numerous contaminated sites with highly elevated Hg concentrations.[9]

In order to minimize human exposure to Hg, the global community has recently agreed to reduce anthropogenic Hg emission by signing the "Minamata Convention on Mercury" under the framework of the United Nations Environment Programme (UNEP). The monitoring of the efficiency of measures taken to reduce anthropogenic Hg emissions and the prediction of human Hg exposure in the future requires a detailed understanding of global Hg cycling. The re-emission of previously deposited Hg from ocean and terrestrial surfaces represents the largest Hg input to the atmosphere with estimated re-emission fluxes of 2000 - 2950 Mg year^{-1} for oceans and 1700 - 2800 Mg year^{-1} for terrestrial environments, respectively.[5] Recent models suggest that 60% of today's Hg deposition originate from the re-emission of legacy anthropogenic Hg.[10] Therefore, in order to predict future Hg concentrations in the atmosphere and eventually in fish it is essential to understand the Hg cycling in ocean and terrestrial environments.

1.2 Terrestrial mercury cycling

Soils contain the largest terrestrial pool of mercury[11–13] and play a dual role in the global Hg cycling; they act as sink for atmospheric Hg deposition[11,14] and as source through re-emission upon reduction.[15] Figure 1.2 illustrates the most important processes controlling the terrestrial Hg cycling. Several pathways lead to atmospheric Hg deposition to terrestrial surfaces; gaseous Hg(0) is taken up through stomata of plants, is oxidized in the plants and eventually deposited to the Earth surface as litterfall.[16,17] Alternatively, gaseous Hg(0) is oxidized to Hg(II) in the atmosphere and deposited to terrestrial surfaces either directly through precipitation as wet deposition or on foliage by dry deposition and washed to the soils as throughfall.[16,17] The dry deposition of gaseous Hg(0) has been suggested as sink for atmospheric Hg, however the mechanism and magnitude of this pathway remain unknown.[1,14] Soil runoff transports Hg from soils and represents a major Hg input to associated aquatic environments.[1] Furthermore it has been suggested that soil runoff is a major source of Hg to the Arctic Ocean, where Hg is eventually reduced and re-emitted to the atmosphere.[18]

Once deposited on foliage or taken up by plants, Hg(II) can be subject to photoreduction and subsequent re-emission of gaseous Hg(0). It has been reported that 45 % of Hg deposited to boreal uplands was re-emitted from the forest canopy to the atmosphere.[19]

In organic soils, the dominant Hg form is Hg(II), mainly bound to reduced sulfur groups of natural organic matter (NOM).[20] In mineral soils with low NOM contents

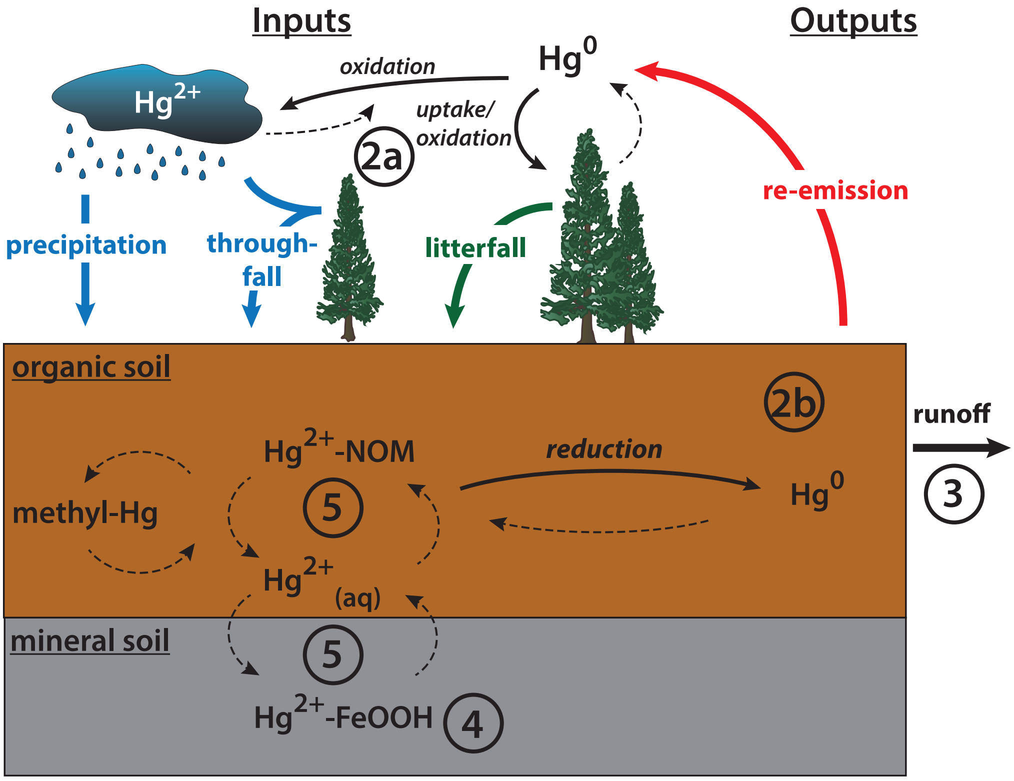
Inputs
Outputs
Hg^{2+}
oxidation
Hg^{0}
uptake/
oxidation
2a
re-emission
precipitation
through-
fall
litterfall
organic soil
2b
runoff
3
Hg^{2+}-NOM
reduction
Hg^{0}
methyl-Hg
5
Hg^{2+}
(aq)
mineral soil
5
Hg^{2+}-FeOOH
4

Figure 1.2: Conceptual model of terrestrial Hg cycling: Atmospheric Hg is deposited as oxidized Hg(II) via precipitation or throughfall or gaseous Hg(0) is taken up by stomata of plants and deposited as litterfall. In soils Hg(II) is subject to methylation/demethylation, adsorption/desorption and reduction/oxidation processes. All Hg species can be leached from the soils by surface or subsurface runoff. The numbers highlight the processes addressed in this thesis and represent the chapter numbers: (**2a**) sources of Hg deposition, (**2b**) Hg reduction and re-emission, (**3**) sources of Hg in soil runoff, (**4**) sorption of Hg(II) to goethite (α-FeOOH) as example for mineral-bound Hg(II), and (**5**) exchange kinetics between Hg(II) and natural organic matter (NOM) and goethite.

Hg(II) is dominantly sorbed to mineral surfaces such as iron oxides or clay minerals.[21,22] Under anaerobic conditions, Hg(II) is potentially methylated to methyl-Hg by microorganisms.[2] On the other hand, microbial demethylation is taking place, thus the concentrations of methyl-Hg in soils represent the net of the two processes (methylation and demethylation).[2]

Several mechanisms have been shown to cause Hg(II) reduction to Hg(0), which can eventually lead to re-emission of gaseous Hg(0) back to the atmosphere.[23] Hg(II) can be reduced through photochemical reduction,[24] microbially mediated reduction,[25,26] or non-photochemical abiotic reduction by mineral phases[27,28] or reduced NOM.[29–31] A recent study observed decreasing gaseous Hg(0) concentrations in mineral soil horizons compared to atmospheric concentrations, suggesting that the oxidation of gaseous Hg(0) might also be an important process in certain soils.[14]

Current global Hg models lack a mechanistic representation of the processes, largely because of insufficient understanding of the occurring processes.[9,32,33] Thus, the role of soils as long-term sinks for atmospherically deposited Hg and as source for Hg re-emission is still associated with large uncertainties. Because of analytical difficulties in the measurement of re-emission fluxes[34] and establishment of Hg mass balances in soils[17,35] many important questions concerning the reactivity of Hg in soils and re-emission/runoff processes remain unanswered. Recent developments of stable Hg isotope analysis offer the potential to address these questions using stable Hg isotope signatures.

1.3 Stable mercury isotopes

The different sources (e.g., anthropogenic and natural Hg) and the number of concurring processes make it difficult to interpret observed changes in concentrations. Hg speciation measurements and stable Hg isotope analysis provide additional dimensions carrying information about the history and fate of Hg in a sample. Biogeochemical reactions of Hg are associated with Hg stable isotope fractionation, allowing to gain new insights in the Hg cycling in the environment from Hg isotope signatures, which are not attainable by means of concentration measurements. Hg isotope signatures contain:

- **Source information;** The Hg isotope signatures caused by different isotope fractionation mechanisms provide a multidimensional fingerprint, which can be used as tool to assess the contribution of different sources in an environmental sample.

- **Process information;** Specific Hg isotope fractionation trajectories associated with different biogeochemical reactions allow the identification and quantification of occurring processes in an ecosystem.

Mercury has seven stable isotopes with the masses ^{196}Hg, ^{198}Hg, ^{199}Hg, ^{200}Hg, ^{201}Hg, ^{202}Hg, and ^{204}Hg. High precision stable Hg isotope analysis started in the early years of 2000 with the development of multicollector inductively coupled plasma mass spectrometry (MC-ICP-MS). Hg sample introduction using cold vapor generation by stannous chloride reduction in combination with thallium doping and sample standard bracketing for mass bias correction allowed Hg isotope ratio measurements at high enough precision to resolve small variations found in the environment.[36–38] In the following, many analytical developments have been made to measure stable Hg isotope signatures in environmental samples at low concentrations; e.g., for samples with high organic matter content,[39,40] natural waters,[41–43] and atmospheric gaseous Hg,[44,45] or to measure species-specific Hg isotope signatures of methyl-Hg.[46,47]

Many biogeochemical reactions are associated with mass-dependent fractionation (MDF), which scales proportional to the relative mass differences of the Hg isotopes (Figure 1.3).[48,49] In addition to MDF, the two odd mass isotopes (^{199}Hg and ^{201}Hg) can undergo mass-independent fractionation (MIF),[48] through magnetic isotope effects (MIE)[50] or nuclear volume fractionation (NVF)[51] (Figure 1.3). MDF is reported as the measured ratio of ^{202}Hg to ^{198}Hg relative to the bracketing standard NIST-3133 following standard nomenclature:[52,53]

$$\delta^{202}\mathrm{Hg} = \frac{(^{202}\mathrm{Hg}/^{198}\mathrm{Hg})_{\mathrm{sample}}}{(^{202}\mathrm{Hg}/^{198}\mathrm{Hg})_{\mathrm{NIST-3133}}} - 1 \tag{1.1}$$

MIF is reported as difference between the observed isotope signature to the expected MDF component (only valid for <10‰):

$$\Delta^{199}\mathrm{Hg} = \delta^{199}\mathrm{Hg} - (\delta^{202}\mathrm{Hg} \times 0.2520) \tag{1.2}$$

$$\Delta^{200}\mathrm{Hg} = \delta^{200}\mathrm{Hg} - (\delta^{202}\mathrm{Hg} \times 0.5024) \tag{1.3}$$

$$\Delta^{201}\mathrm{Hg} = \delta^{201}\mathrm{Hg} - (\delta^{202}\mathrm{Hg} \times 0.7520) \tag{1.4}$$

Isotopic differences between different pools are defined as enrichment factor ϵ^{202}Hg for MDF:

$$\epsilon^{202}\mathrm{Hg}_{\mathrm{pool1-pool2}} = \delta^{202}\mathrm{Hg}_{\mathrm{pool1}} - \delta^{202}\mathrm{Hg}_{\mathrm{pool2}} \tag{1.5}$$

and as enrichment factor E^{xxx}Hg for isotopic differences in MIF:

$$\mathrm{E}^{\mathrm{xxx}}\mathrm{Hg}_{\mathrm{pool1-pool2}} = \Delta^{\mathrm{xxx}}\mathrm{Hg}_{\mathrm{pool1}} - \Delta^{\mathrm{xxx}}\mathrm{Hg}_{\mathrm{pool2}} \tag{1.6}$$

where Δ^{xxx}Hg corresponds to Δ^{199}Hg, Δ^{200}Hg, or Δ^{201}Hg.

MIEs are manifested in radical pair reactions and exclusive for isotopes with a nuclear spin and magnetic momentum.[50,55] Only the odd mass Hg isotopes (^{199}Hg and ^{201}Hg) have a nuclear spin and magnetic momentum, thus MIEs are selective for ^{199}Hg

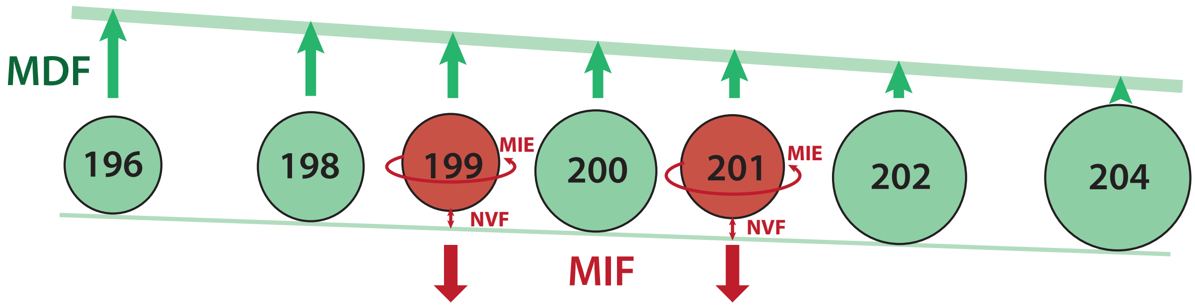

Figure 1.3: Mercury isotopes: All isotopes are subject to Mass Dependent Fractionation (MDF), the odd isotopes (^{199}Hg and ^{201}Hg) can undergo Mass Independent Fractionation (MIF) through Magnetic Isotope Effects (MIE) or Nuclear Volume Fractionation (NVF) (adapted from Wiederhold et al.[54]).

and ^{201}Hg. MIEs cause large MIF (more than 10 ‰ variation in Δ^{199}Hg)[48] and have been reported for photochemical reduction of Hg(II)[42,56–58] or photochemical demethylation of methyl-Hg.[56] Thereby it has been noted that photo-reduction of Hg(II) fractionated the odd mass isotopes at a ratio of Δ^{199}Hg/Δ^{201}Hg= 1 and photo-demethylation at a ratio of Δ^{199}Hg/Δ^{201}Hg= 1.36.[56]

NVF originates from the differences in the nuclear volume of Hg isotopes and thus scales with the nuclear charge radii.[51] Since the nuclear charge radii of the two odd mass Hg isotopes (^{199}Hg and ^{201}Hg) are smaller than the linear trend of even mass charge radii, NVF causes MIF on ^{199}Hg and ^{201}Hg.[51] Thereby the ratio of Δ^{199}Hg/Δ^{201}Hg is 1.6.[54] NVF has been observed during evaporation of gaseous Hg(0) from liquid Hg,[59,60] abiotic non-photochemical reduction of Hg(II) by natural organic matter (NOM) and stannous chloride,[61] or during sorption of Hg(II) to thiol-groups.[54] MIF caused by NVF is generally much smaller than from MIE and clear evidence for NVF in natural samples is still lacking.[62]

Recent observations of Hg isotope composition in precipitation samples reported MIF in even mass isotopes, indicated by positive Δ^{200}Hg values. The mechanism for this observation however remains unclear.[44,63–66]

The successful use of stable Hg isotopes as source and process tracer requires detailed knowledge about Hg isotope fractionation associated with biogeochemical processes controlling the Hg cycling in the investigated systems. Therefore, controlled laboratory experiments are important for the determination of stable Hg isotope fractionation factors and the controlling mechanisms.

For many processes controlling the terrestrial Hg cycling, stable Hg isotope fractionation factors have been published.[48] Stable Hg isotope fractionation associated with Hg(II) reduction has been studied for photochemical reduction,[56–58] microbial reduction,[67] and abiotic non-photochemical reduction by NOM.[61] Furthermore, Hg isotope fractionation factors for microbial[68] and abiotic[69] Hg(II) methylation and well as photochemical[56] and microbial[70] demethylation of methyl-Hg have been reported. Sorption of Hg(II) to NOM has been investigated by studying stable Hg isotope fractionation associated with Hg(II) sorption to thiol-resin.[54] For other important processes in soils such as gaseous Hg(0) oxidation, reduction or sorption of Hg(II) by/to mineral phases mechanistic studies on stable Hg isotope fractionation are missing.

In order to assess the potential of stable Hg isotopes to provide new insights in the terrestrial cycling of Hg, systematic studies on the distribution of stable Hg isotope signatures in soils are needed. At the start of this project only few publications existed, reporting stable Hg isotope signatures in soils mainly in a descriptive manner.[39,71,72] During the course of this thesis two studies have been published using stable Hg isotopes to assess the source and fate of Hg in soils. One focused on forest soils in Wisconsin, USA[66] and one on soil samples from an elevation gradient in subtropical China.[73] A synthesis of these studies with the results from this thesis is provided in the conclusions (Chapter 6).

1.4 Research approach and objectives

The goal of this thesis was to develop Hg stable isotope analysis as a new tool to investigate and understand relevant processes of Hg cycling in terrestrial environments. In order to achieve this goal the following complementary approaches were chosen: One focus was set on developing and establishing analytical methods to measure stable Hg isotopes in soil compartments and runoff and applying the techniques in a case study in boreal forest soils in northern Sweden. A second focus was set on the improvement of the basis for the interpretation of field observations by performing controlled mechanistic laboratory experiments. The determination of isotope fractionation factors associated with biogeochemical reactions thereby plays an important role. In the context of these experiments the question of ligand exchange and timescales required to reach equilibrium are important. For this purpose a different analytical approach using enriched stable Hg isotope tracers was applied. The following objectives were addressed:

- to identify the pathway of Hg deposition in boreal forest soil using stable Hg isotope signatures as source tracer for precipitation- and litter-derived Hg. (**2a** in Figure 1.2, Chapter 2).
- to investigate the reduction pathway and quantify reductive Hg loss and re-emission fluxes from boreal forest soils using Hg isotope fractionation trajectories as process tracer (**2b** in Figure 1.2, Chapter 2).
- to develop an analytical method for measuring stable Hg isotope signatures in aquatic samples with high dissolved organic carbon concentrations, investigate the source of Hg in soil runoff, and assess the pathway of Hg from soils to aquatic ecosystems (**3** in Figure 1.2, Chapter 3).
- to investigate stable Hg isotope fractionation associated with Hg(II) sorption to goethite, a representative for mineral surfaces (**4** in Figure 1.2, Chapter 4).
- to examine the isotope exchange kinetics of Hg(II) between organic ligands, goethite and natural organic matter (NOM) in order to understand the role of kinetics in terrestrial Hg cycling (**5** in Figure 1.2, Chapter 5).

References

[1] C. T. Driscoll, R. P. Mason, H. M. Chan, D. J. Jacob, and N. Pirrone. Mercury as a global pollutant: sources, pathways, and effects. *Environ. Sci. Technol.*, 47(10):4967–4983, 2013.

[2] H. Hsu-Kim, K. H. Kucharzyk, T. Zhang, and M. A. Deshusses. Mechanisms regulating mercury bioavailability for methylating microorganisms in the aquatic environment: a critical review. *Environ. Sci. Technol.*, 47(6):2441–2456, 2013.

[3] J. Munthe, I. Wangberg, S. Rognerud, E. Fjeld, M. Verta, P. Porvari, and M. Meili. Mercury in nordic ecosystems. Technical report, IVL Swedish Environmental Research Institute Ltd., 2007.

[4] N. Pirrone, S. Cinnirella, X. Feng, R. B. Finkelman, H. R. Friedli, J. Leaner, R. Mason, A. B. Mukherjee, G. B. Stracher, D. G. Streets, and K. Telmer. Global mercury emissions to the atmosphere from anthropogenic and natural sources. *Atmos. Chem. Phys.*, 10(13):5951–5964, 2010.

[5] R. P. Mason, A. L. Choi, W. F. Fitzgerald, C. R. Hammerschmidt, C. H. Lamborg, A. L. Soerensen, and E. M. Sunderland. Mercury biogeochemical cycling in the ocean and policy implications. *Environ. Res.*, 119(0):101–117, 2012.

[6] D. G. Streets, M. K. Devane, Z. F. Lu, T. C. Bond, E. M. Sunderland, and D. J. Jacob. All-time releases of mercury to the atmosphere from human activities. *Environ. Sci. Technol.*, 45(24):10485–10491, 2011.

[7] N. E. Selin, D. J. Jacob, R. M. Yantosca, S. Strode, L. Jaegle, and E. M. Sunderland. Global 3-D land-ocean-atmosphere model for mercury: Present-day versus preindustrial cycles and anthropogenic enrichment factors for deposition. *Glob. Biogeochem. Cycles*, 22(2), 2008.

[8] N. Lubick and D. Malakoff. With pact's completion, the real work begins. *Science*, 341(6153):1443–1445, 2013.

[9] H. M. Horowitz, D. J. Jacob, H. M. Amos, D. G. Streets, and E. M. Sunderland. Historical mercury releases from commercial products: global environmental implications. *Environ. Sci. Technol.*, 48(17):10242–10250, 2014.

[10] H. M. Amos, D. J. Jacob, D. G. Streets, and E. M. Sunderland. Legacy impacts of all-time anthropogenic emissions on the global mercury cycle. *Glob. Biogeochem. Cycles*, 27(2):410–421, 2013.

[11] D. F. Grigal. Mercury sequestration in forests and peatlands: A review. *J. Environ. Qual.*, 32(2):393–405, 2003.

[12] N. E. Selin. Global biogeochemical cycling of mercury: A review. *Annu. Rev. Environ. Resour.*, 34:43–63, 2009.

[13] D. Obrist, D. W. Johnson, S. E. Lindberg, Y. Luo, O. Hararuk, R. Bracho, J. J. Battles, D. B. Dail, R. L. Edmonds, R. K. Monson, S. V. Ollinger, S. G. Pallardy, K. S. Pregitzer, and D. E. Todd. Mercury distribution across 14 US forests. part I: Spatial patterns of concentrations in biomass, litter, and soils. *Environ. Sci. Technol.*, 45(9):3974–3981, 2011.

[14] D. Obrist, A. K. Pokharel, and C. Moore. Vertical profile measurements of soil air suggest immobilization of gaseous elemental mercury in mineral soil. *Environ. Sci. Technol.*, 48(4):2242–52, 2014.

[15] M. S. Gustin, S. E. Lindberg, and P. J. Weisberg. An update on the natural sources and sinks of atmospheric mercury. *Appl. Geochem.*, 23(3):482–493, 2008.

[16] V. L. St Louis, J. W. M. Rudd, C. A. Kelly, B. D. Hall, K. R. Rolfhus, K. J. Scott, S. E. Lindberg, and W. Dong. Importance of the forest canopy to fluxes of methyl mercury and total mercury to boreal ecosystems. *Environ. Sci. Technol.*, 35(15):3089–3098, 2001.

[17] J. D. Demers, C. T. Driscoll, T. J. Fahey, and J. B. Yavitt. Mercury cycling in litter and soil in different forest types in the Adirondack region, New York, USA. *Ecol. Appl.*, 17(5):1341–1351, 2007.

[18] J. A. Fisher, D. J. Jacob, A. L. Soerensen, H. M. Amos, A. Steffen, and E. M. Sunderland. Riverine source of arctic ocean mercury inferred from atmospheric observations. *Nat. Geosci.*, 5(7):499–504, 2012.

[19] J. A. Graydon, V. L. St Louis, S. E. Lindberg, K. A. Sandilands, J. W. M. Rudd, C. A. Kelly, R. Harris, M. T. Tate, D. P. Krabbenhoft, C. A. Emmerton, H. Asmath, and M. Richardson. The role of terrestrial vegetation in atmospheric Hg deposition: Pools and fluxes of spike and ambient Hg from the METAALICUS experiment. *Glob. Biogeochem. Cycles*, 26, 2012.

[20] U. Skyllberg, P. R. Bloom, J. Qian, C. M. Lin, and W. F. Bleam. Complexation of mercury(II) in soil organic matter: EXAFS evidence for linear two-coordination with reduced sulfur groups. *Environ. Sci. Technol.*, 40(13):4174–4180, 2006.

[21] M. C. Gabriel and D. G. Williamson. Principal biogeochemical factors affecting the speciation and transport of mercury through the terrestrial environment. *Environ. Geochem. Health*, 26(4):421–434, 2004.

[22] U. Skyllberg. *Mercury Biogeochemistry in Soils and Sediments*, volume 34 of *Developments in Soil Science*, pages 379–410. Elsevier B.V., Netherlands, 2010.

[23] H. Zhang and S. E. Lindberg. Processes influencing the emission of mercury from soils: A conceptual model. *J. Geophys. Res.-Atmos.*, 104(D17):21889–21896, 1999.

[24] M. Amyot, G. Mierle, D. R. S. Lean, and D. J. McQueen. Sunlight-induced formation of dissolved gaseous mercury in lake waters. *Environ. Sci. Technol.*, 28(13):2366–2371, 1994.

[25] R. P. Mason, F. M. M. Morel, and H. F. Hemond. The role of microorganisms in elemental mercury formation in natural-waters. *Water Air Soil Pollut.*, 80(1-4):775–787, 1995.

[26] H. A. Wiatrowski, P. M. Ward, and T. Barkay. Novel reduction of mercury(II) by mercury-sensitive dissimilatory metal reducing bacteria. *Environ. Sci. Technol.*, 40(21):6690–6696, 2006.

[27] H. A. Wiatrowski, S. Das, R. Kukkadapu, E. S. Ilton, T. Barkay, and N. Yee. Reduction of Hg(II) to Hg(0) by magnetite. *Environ. Sci. Technol.*, 43(14):5307–5313, 2009.

[28] S. E. Bone, J. R. Bargar, and G. Sposito. Mackinawite (FeS) reduces mercury(II) under sulfidic conditions. *Environ. Sci. Technol.*, 48(18):10681–10689, 2014.

[29] J. J. Alberts, J. E. Schindle, R. W. Miller, and D. E. Nutter. Elemental mercury evolution mediated by humic acid. *Science*, 184(4139):895–896, 1974.

[30] B. Allard and I. Arsenie. Abiotic reduction of mercury by humic substances in aquatic system - an important process for the mercury cycle. *Water Air Soil Pollut.*, 56:457–464, 1991.

[31] B. Gu, Y. Bian, C. L. Miller, W. Dong, X. Jiang, and L. Liang. Mercury reduction and complexation by natural organic matter in anoxic environments. *Proc. Natl. Acad. Sci. U.S.A.*, 108(4):1479–83, 2011.

[32] N. V. Smith-Downey, E. M. Sunderland, and D. J. Jacob. Anthropogenic impacts on global storage and emissions of mercury from terrestrial soils: Insights from a new global model. *J. Geophys. Res.-Biogeosci.*, 115, 2010.

[33] H. M. Amos, D. J. Jacob, D. Kocman, H. M. Horowitz, Y. Zhang, S. Dutkiewicz, M. Horvat, E. S. Corbitt, D. P. Krabbenhoft, and E. M. Sunderland. Global biogeochemical implications of mercury discharges from rivers and sediment burial. *Environ. Sci. Technol.*, 48(16):9514–9522, 2014.

[34] J. S. Denkenberger, C. T. Driscoll, B. A. Branfireun, C. S. Eckley, M. Cohen, and P. Selvendiran. A synthesis of rates and controls on elemental mercury evasion in the Great Lakes Basin. *Environ. Pollut.*, 161:291–298, 2012.

[35] D. F. Grigal, R. K. Kolka, J. A. Fleck, and E. A. Nater. Mercury budget of an upland-peatland watershed. *Biogeochemistry*, 50(1):95–109, 2000.

[36] D. S. Lauretta, B. Klaue, J. D. Blum, and P. R. Buseck. Mercury abundances and isotopic compositions in the Murchison (CM) and Allende (CV) carbonaceous chondrites. *Geochim. Cosmochim. Acta*, 65(16):2807–2818, 2001.

[37] C. N. Smith, S. E. Kesler, B. Klaue, and J. D. Blum. Mercury isotope fractionation in fossil hydrothermal systems. *Geology*, 33(10):825–828, 2005.

[38] D. Foucher and H. Hintelmann. High-precision measurement of mercury isotope ratios in sediments using cold-vapor generation multi-collector inductively coupled plasma mass spectrometry. *Anal. Bioanal. Chem.*, 384(7-8):1470–1478, 2006.

[39] A. Biswas, J. D. Blum, B. A. Bergquist, G. J. Keeler, and Z. Q. Xie. Natural mercury isotope variation in coal deposits and organic soils. *Environ. Sci. Technol.*, 42(22):8303–8309, 2008.

[40] R. Y. Sun, M. Enrico, L. E. Heimburger, C. Scott, and J. E. Sonke. A double-stage tube furnace-acid-trapping protocol for the pre-concentration of mercury from solid samples for isotopic analysis. *Anal. Bioanal. Chem.*, 405(21):6771–6781, 2013.

[41] J. B. Chen, H. Hintelmann, and B. Dimock. Chromatographic pre-concentration of Hg from dilute aqueous solutions for isotopic measurement by MC-ICP-MS. *J. Anal. At. Spectrom.*, 25(9):1402–1409, 2010.

[42] L. S. Sherman, J. D. Blum, K. P. Johnson, G. J. Keeler, J. A. Barres, and T. A. Douglas. Mass-independent fractionation of mercury isotopes in arctic snow driven by sunlight. *Nat. Geosci.*, 3(3):173–177, 2010.

[43] M. Strok, H. Hintelmann, and B. Dimock. Development of pre-concentration procedure for the determination of Hg isotope ratios in seawater samples. *Anal. Chim. Acta*, DOI: 10.1016/j.aca.2014.09.005.

[44] L. E. Gratz, G. J. Keeler, J. D. Blum, and L. S. Sherman. Isotopic composition and fractionation of mercury in great lakes precipitation and ambient air. *Environ. Sci. Technol.*, 44(20):7764–7770, 2010.

[45] X. Fu, L. E. Heimburger, and J. E. Sonke. Collection of atmospheric gaseous mercury for stable isotope analysis using iodine- and chlorine-impregnated activated carbon traps. *J. Anal. At. Spectrom.*, 29(5):841–852, 2014.

[46] V. N. Epov, S. Berail, M. Jimenez-Moreno, V. Perrot, C. Pecheyran, D. Amouroux, and O. F. X. Donard. Approach to measure isotopic ratios in species using multicollector-ICPMS coupled with chromatography. *Anal. Chem.*, 82(13):5652–5662, 2010.

[47] J. Masbou, D. Point, and J. E. Sonke. Application of a selective extraction method for methylmercury compound specific stable isotope analysis (MeHg-CSIA) in biological materials. *J. Anal. At. Spectrom.*, 28(10):1620–1628, 2013.

[48] J. D. Blum, L. S. Sherman, and M. W. Johnson. Mercury isotopes in earth and environmental sciences. *Annu. Rev. Earth Planet. Sci. Lett.*, 42(1):249–269, 2014.

[49] J. M. Eiler, B. Bergquist, I. Bourg, P. Cartigny, J. Farquhar, A. Gagnon, W. F. Guo, I. Halevy, A. Hofmann, T. E. Larson, N. Levin, E. A. Schauble, and D. Stolper. Frontiers of stable isotope geoscience. *Chem. Geol.*, 372:119–143, 2014.

[50] A. L. Buchachenko. Mercury isotope effects in the environmental chemistry and biochemistry of mercury-containing compounds. *Russ. Chem. Rev.*, 78(4):319–328, 2009.

[51] E. A. Schauble. Role of nuclear volume in driving equilibrium stable isotope fractionation of mercury, thallium, and other very heavy elements. *Geochim. Cosmochim. Acta*, 71(9):2170–2189, 2007.

[52] J. D. Blum and B. A. Bergquist. Reporting of variations in the natural isotopic composition of mercury. *Anal. Bioanal. Chem.*, 388(2):353–359, 2007.

[53] T. B. Coplen. Guidelines and recommended terms for expression of stable-isotope-ratio and gas-ratio measurement results. *Rapid Commun. Mass Spectrom.*, 25(17):2538–2560, 2011.

[54] J. G. Wiederhold, C. J. Cramer, K. Daniel, I. Infante, B. Bourdon, and R. Kretzschmar. Equilibrium mercury isotope fractionation between dissolved Hg(II) species and thiol-bound Hg. *Environ. Sci. Technol.*, 44(11):4191–4197, 2010.

[55] N. J. Turro. Influence of nuclear spin on chemical reactions: Magnetic isotope and magnetic field effects (a review). *Proc. Natl. Acad. Sci. U.S.A.*, 80(2):609–621, 1983.

[56] B. A. Bergquist and J. D. Blum. Mass-dependent and -independent fractionation of Hg isotopes by photoreduction in aquatic systems. *Science*, 318(5849):417–420, 2007.

[57] W. Zheng and H. Hintelmann. Mercury isotope fractionation during photoreduction in natural water is controlled by its Hg/DOC ratio. *Geochim. Cosmochim. Acta*, 73(22):6704–6715, 2009.

[58] W. Zheng and H. Hintelmann. Isotope fractionation of mercury during its photochemical reduction by low-molecular-weight organic compounds. *J. Phys. Chem. A*, 114(12):4246–4253, 2010.

[59] N. Estrade, J. Carignan, J. E. Sonke, and O. F. X. Donard. Mercury isotope fractionation during liquid-vapor evaporation experiments. *Geochim. Cosmochim. Acta*, 73(10):2693–2711, 2009.

[60] S. Ghosh, E. A. Schauble, G. Lacrampe Couloume, J. D. Blum, and B. A. Bergquist. Estimation of nuclear volume dependent fractionation of mercury isotopes in equilibrium liquid-vapor evaporation experiments. *Chem. Geol.*, 336:5–12, 2013.

[61] W. Zheng and H. Hintelmann. Nuclear field shift effect in isotope fractionation of mercury during abiotic reduction in the absence of light. *J. Phys. Chem. A*, 114(12):4238–4245, 2010.

[62] J. E. Sonke. A global model of mass independent mercury stable isotope fractionation. *Geochim. Cosmochim. Acta*, 75(16):4577–4590, 2011.

[63] J. B. Chen, H. Hintelmann, X. B. Feng, and B. Dimock. Unusual fractionation of both odd and even mercury isotopes in precipitation from Peterborough, ON, Canada. *Geochim. Cosmochim. Acta*, 90:33–46, 2012.

[64] L. S. Sherman, J. D. Blum, G. J. Keeler, J. D. Demers, and J. T. Dvonch. Investigation of local mercury deposition from a coal-fired power plant using mercury isotopes. *Environ. Sci. Technol.*, 46(1):382–90, 2012.

[65] P. M. Donovan, J. D. Blum, D. Yee, G. E. Gehrke, and M. B. Singer. An isotopic record of mercury in San Francisco bay sediment. *Chem. Geol.*, 349(0):87–98, 2013.

[66] J. D. Demers, J. D. Blum, and D. R. Zak. Mercury isotopes in a forested ecosystem: Implications for air-surface exchange dynamics and the global mercury cycle. *Glob. Biogeochem. Cycles*, 27(1):222–238, 2013.

[67] K. Kritee, J. D. Blum, M. W. Johnson, B. A. Bergquist, and T. Barkay. Mercury stable isotope fractionation during reduction of Hg(II) to Hg(0) by mercury resistant microorganisms. *Environ. Sci. Technol.*, 41(6):1889–1895, 2007.

[68] P. Rodriguez-Gonzalez, V. N. Epov, R. Bridou, E. Tessier, R. Guyoneaud, M. Monperrus, and D. Amouroux. Species-specific stable isotope fractionation of mercury during Hg(II) methylation by an anaerobic bacteria (Desulfobulbus propionicus) under dark conditions. *Environ. Sci. Technol.*, 43(24):9183–9188, 2009.

[69] M. Jimenez-Moreno, V. Perrot, V. N. Epov, M. Monperrus, and D. Amouroux. Chemical kinetic isotope fractionation of mercury during abiotic methylation of Hg(II) by methylcobalamin in aqueous chloride media. *Chem. Geol.*, 336:26–36, 2013.

[70] K. Kritee, T. Barkay, and J. D. Blum. Mass dependent stable isotope fractionation of mercury during mer mediated microbial degradation of monomethylmercury. *Geochim. Cosmochim. Acta*, 73(5):1285–1296, 2009.

[71] S. Ghosh, Y. F. Xu, M. Humayun, and L. Odom. Mass-independent fractionation of mercury isotopes in the environment. *Geochem. Geophys. Geosyst.*, 9, 2008.

[72] N. Estrade, J. Carignan, J. E. Sonke, and O. F. X. Donard. Measuring Hg isotopes in bio-geo-environmental reference materials. *Geostand. Geoanal. Res.*, 34(1):79–93, 2010.

[73] H. Zhang, R. S. Yin, X. B. Feng, J. Sommar, C. W. Anderson, A. Sapkota, X. W. Fu, and T. Larssen. Atmospheric mercury inputs in montane soils increase with elevation: evidence from mercury isotope signatures. *Sci. Rep.*, 3:3322, 2013.

Chapter 2

Mercury isotopes reveal organic matter-driven reductive Hg loss from boreal forest soils

M. Jiskra, J.G. Wiederhold, U. Skyllberg, R-M. Kronberg, I. Hajdas, and R. Kretzschmar,
Mercury isotopes reveal organic matter-driven reductive Hg loss from boreal forest soils.
in preparation

Abstract

Soils represent the largest terrestrial mercury (Hg) pool in exchange with the atmosphere. To predict how anthropogenic emissions affect global Hg cycling and eventually human Hg exposure, it is crucial to understand Hg deposition and re-emission of legacy Hg from soils. However, assessing re-emission fluxes remains difficult and suffers from large uncertainties, partly because of an insufficient understanding of the governing processes. We measured Hg stable isotope signatures of radiocarbon-dated boreal forest soils and modeled the source of atmospheric Hg deposition and re-emission pathways and fluxes using a combined source/process tracing approach. Our results suggest that deeper soil horizons accumulate precipitation-derived Hg over decades. We provide evidence for significant Hg re-emission from organic soil horizons due to non-photochemical abiotic reduction by natural organic matter, a process not yet observed unambiguously in nature. Our data suggest that water-saturated Histosols (peat soils) exhibit a three times higher reductive Hg loss compared to well-drained Podzols and re-emit up to one third of previously deposited Hg to the atmosphere over a century. Re-emission of legacy Hg following reduction by natural organic matter might be an important pathway previously not considered in global models, supporting the need for a process-based assessment of land/atmosphere Hg exchange.

2.1 Introduction

Current global Hg models suggest that land surfaces receive 3200 Mg a^{-1} through atmospheric deposition and re-emit 1700 to 2800 Mg a^{-1},[1–3] illustrating the dual role of soils in global Hg cycling. Long-range transported Hg^0 is oxidized in the atmosphere and deposited onto soils with precipitation or via plant surfaces as throughfall. Alternatively, gaseous Hg^0 is taken up through stomata, oxidized in the plants, and deposited on soils with litterfall. In soils, Hg^{2+} may be methylated or reduced to volatile Hg^0 which is eventually re-emitted back to the atmosphere (Figure 2.1).

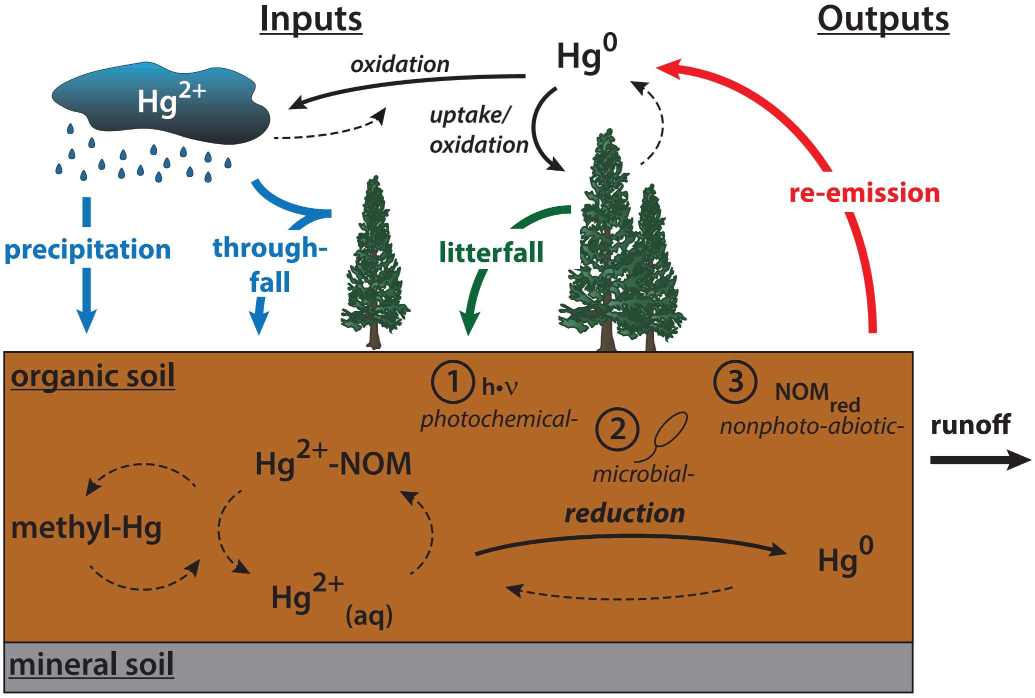
Inputs
Outputs
Hg^{2+}
oxidation
Hg^0
uptake/
oxidation
re-emission
precipitation
through-
fall
litterfall
organic soil
① h•ν
photochemical-
② microbial-
③ NOM_{red}
nonphoto-abiotic-
runoff
Hg^{2+}-NOM
methyl-Hg
reduction
Hg^0
$Hg^{2+}_{(aq)}$
mineral soil

Figure 2.1: Conceptual model of the terrestrial Hg cycle: Major input and output pathways. Atmospheric Hg is mainly deposited as oxidized Hg^{2+} via precipitation and throughfall or taken up by plant stomata and deposited with litterfall. In soils, Hg^{2+} can be reduced by different pathways: (**1**) photochemical, (**2**) microbial, or (**3**) non-photochemical abiotic reduction by natural organic matter (NOM), followed by re-emission back to the atmosphere. All Hg forms are subjected to leaching from soils with surface or subsurface runoff into aquatic ecosystems.

Quantitative estimates of Hg re-emission fluxes from terrestrial environments are scarce and suffer from considerable uncertainties due to large temporal and spatial variations in Hg fluxes and methodological limitations.[4] The establishment of Hg mass balances in soils remains challenging, because reliable estimates require knowledge of all Hg fluxes in parallel to total mass loss by carbon mineralization.[5,6]

Several processes have experimentally been shown to reduce Hg(II): direct and indirect photochemical reduction, microbially-mediated enzymatic reduction, or non-photochemical abiotic reduction by minerals and natural organic matter (NOM).[4,7–11] However, their relative importance for reductive Hg loss from terrestrial ecosystems remains poorly understood. Hg isotopes offer a new approach for identifying different Hg sources and loss processes through characteristic mass-dependent (MDF) and mass-independent (MIF) fractionation associated with each source and reduction pathway (Figure 2.2). Photochemical reduction in the presence of NOM preferentially reduces light isotopes leading to MDF and is associated with large positive MIF by magnetic isotope effects (MIE).[11] Microbial reduction also preferentially reduces light Hg isotopes, but without MIF.[10] NOM in the absence of sunlight preferentially reduces light isotopes and exhibits MIF caused by nuclear volume fractionation (NVF) in opposite direction to the MIE by photoreduction.[9]

By measuring Hg isotope signatures of litter and soil samples in combination with radiocarbon dating of the soil NOM, we were able to assess the atmospheric source of Hg in soils, Hg reduction pathways, and re-emission fluxes. Two major soil types commonly found in boreal forest ecosystems were sampled in Northern Sweden. Podzols are acidic soils with different layers of slowly decomposing NOM (O horizons), overlying the diagnostic mineral E and B horizons, typically developing in more well-drained landscape positions. Histosols (peat soils) consist primarily of NOM (H horizons, >40 cm thick) and commonly form by net accumulation of NOM under water-saturated conditions (wetlands). Podzols cover ≈15% and Histosols ≈7% of the northern circumpolar region.[12] The soils were separated into the organic surface horizons (Oe/He), the underlying Oa/Ha horizons comprised by older more decomposed NOM, and for Podzols the mineral horizons (E/B).

2.2 Methods

2.2.1 Soil samples

Samples were collected from typical boreal Norway spruce (>80 years old) forest soils, developed in glacial till from gneissic/granitic bedrock in a humid climate in a remote area north of the town Junsele in northern Sweden (N: 63°50', E: 17°00'). Composite samples (5 subsamples within 10 m^2) were taken by horizon (Oe/He, Oa/Ha, E/B) on a transect along the inclination of the landscape covering a range of hydrological conditions. Litter samples were collected after snowmelt as composite samples from the soil surface (25 subsamples within 100 m^2). The area receives an average annual precipitation of 530 mm and has a mean temperature of 2 °C (Jan: -11 °C, Jul: 15 °C, 1961-1990, Swedish Meteorological Institute, SMHI). All sampling locations were situated within an area of ≈1 km^2, therefore we assume that all soils were exposed to the same source and amount of atmospheric Hg deposition. The soil sampling and sample processing scheme is described in detail in the SI.

2.2.2 Analytical methods

For stable Hg isotope measurements, soil samples were combusted in a two-step oven system coupled to an oxidizing liquid trap of 1% $KMnO_4$. The Hg recovery was 94%±8.5% (1σ, n=72) and process blanks run after every 10 samples contained 0.04 ± 0.01 ng mL^{-1} Hg (1σ, n=9), corresponding to less than 1% of total concentrations in samples. The Hg isotope composition of the trap solutions was measured using cold vapor generation coupled to multicollector inductively coupled plasma mass spectrometry (CV-MC-ICPMS) employing sample-standard bracketing and Tl addition for mass bias correction. A detailed method description is provided in reference[29] and the SI.

Hg isotope data are measured and reported relative to the bracketing standard NIST-3133 for MDF as:

$$\delta^{202}\mathrm{Hg} = \frac{(^{202}\mathrm{Hg}/^{198}\mathrm{Hg})_{\mathrm{sample}}}{(^{202}\mathrm{Hg}/^{198}\mathrm{Hg})_{\mathrm{NIST-3133}}} - 1 \tag{2.1}$$

and for MIF as:

$$\Delta^{199}\mathrm{Hg} = \delta^{199}\mathrm{Hg} - (\delta^{202}\mathrm{Hg} \times 0.2520) \tag{2.2}$$

$$\Delta^{200}\mathrm{Hg} = \delta^{200}\mathrm{Hg} - (\delta^{202}\mathrm{Hg} \times 0.5024) \tag{2.3}$$

$$\Delta^{201}\text{Hg} = \delta^{201}\text{Hg} - (\delta^{202}\text{Hg} \times 0.7520) \tag{2.4}$$

Isotopic differences in MDF between different pools are defined as:

$$\epsilon^{202}\text{Hg}_{\text{pool1}-\text{pool2}} = \delta^{202}\text{Hg}_{\text{pool1}} - \delta^{202}\text{Hg}_{\text{pool2}} \tag{2.5}$$

Isotopic differences in MIF between different pools are defined as:

$$\text{E}^{\text{xxx}}\text{Hg}_{\text{pool1}-\text{pool2}} = \Delta^{\text{xxx}}\text{Hg}_{\text{pool1}} - \Delta^{\text{xxx}}\text{Hg}_{\text{pool2}} \tag{2.6}$$

where ^{xxx}Hg corresponds to ^{199}Hg, ^{200}Hg, or ^{201}Hg.

The isotopic enrichment factor was defined as:

$$\epsilon^{202}\text{Hg}_{\text{product/reactant}} = \alpha^{202}\text{Hg}_{\text{product/reactant}} - 1 \tag{2.7}$$

where $\alpha^{202}\text{Hg}_{\text{product/reactant}}$ corresponds to the fractionation factor reported in the corresponding publications.

Our in-house standard (ETH-Fluka) was measured regularly and had a reproducibility of δ^{202}Hg=-1.44±0.11‰, Δ^{199}Hg=0.07±0.05‰, Δ^{200}Hg=0.01±0.06‰ and Δ^{201}Hg=0.03‰ ±0.06‰ (2σ, n=21) in agreement with previously measured values.[29] A process standard (Montana Soil, NIST-2711) was combusted in the oven system after every 10 samples and reproduced at δ^{202}Hg=-0.12±0.10‰, Δ^{199}Hg=-0.23±0.07‰, Δ^{200}Hg=0.00±0.04‰ and Δ^{201}Hg=-0.18±0.02‰ (2σ, n=10), consistent with previously published values. Isotope measurements of peat samples low in ambient Hg and spiked with inorganic Hg(II) were in agreement with separate measurements of the inorganic Hg(II),[29] confirming the accuracy of our method for matrices prevalent in organic topsoils (SI).

2.2.3 Radiocarbon dating

Homogenized samples of bulk soil were combusted, graphitized and analyzed using Accelerator Mass Spectrometry (AMS; ETH Zurich). ^{14}C data are reported as fraction of modern ^{14}C (F^{14}C), i.e. concentration of ^{14}C normalized to the standard and corrected for mass fractionation using δ^{13}C. Radiocarbon ages of the bulk soil samples were determined according to Stuiver and Polach[30] and calendar ages were obtained using standard calibration curves (SI).

2.2.4 Hg isotope model

The source contributions and reductive losses in boreal forest soil samples were modeled by a Monte Carlo simulation approach, using the pseudorandom number generation function of the Matlab software (R2012a, MathWorks). The model consisted of two source components (litter- and precipitation derived Hg) and a reductive loss component incorporating MDF (δ^{202}Hg) and MIF (Δ^{199}Hg, Δ^{200}Hg, and Δ^{201}Hg). Litter-derived Hg was defined based on the collected litter samples and the end-member of precipitation-derived Hg was estimated based on all previously published measured precipitation data across North America (compiled in Blum et al.[16])(No data from Europe are available). Experimental fractionation factors for non-photochemical abiotic NOM reduction[9] and microbial reduction[10] were used for reductive loss estimations. Median model parameters for fraction precipitation ($f_{\text{precipitation}}$) and fraction of reductive loss (f_{reduced}) with the corresponding standard deviation are reported. Further information on the modeling approach and the mixing component scenarios is provided in the SI.

2.2.5 Hg re-emission flux calculation

The Hg pool (Hg_{pool}, μg m^{-2}) for each horizon was calculated using the Hg concentration, horizon thickness and soil bulk density. Using the modeled reductive loss (f_{reduced}) and mean age of the soil carbon (calibrated ^{14}C-age, a) we calculated the re-emission fluxes ($F_{\text{re-emission}}$, μg m^{-2} a^{-1}) for each horizon:

$$F_{\text{re-emission}} = \frac{(1 + f_{\text{reduced}}) \times \text{Hg}_{\text{pool}} \times f_{\text{reduced}}}{\text{calibrated } ^{14}\text{C-age}} \tag{2.8}$$

The overall re-emission flux was calculated from the sum of the organic horizons. Based on recent observations suggesting that mineral soil horizons might be net sinks for gaseous Hg^{0},[28] reductive re-emission from mineral horizons was not considered.

2.3 Hg isotope signatures of boreal forest soils

All soil and litter samples exhibited Hg concentrations of 17 to 313 ng g^{-1} and negative MDF (δ^{202}Hg= -2.56‰ to -1.55‰) and MIF (Δ^{199}Hg= -0.48‰ to -0.24‰) signatures (n=26) consistent with previously reported soil and litter data.[13,14] Litter samples exhibited the most negative MDF (δ^{202}Hg= -2.35‰±0.09‰) and MIF (Δ^{199}Hg= -0.44‰±0.03‰) (Figure 2.2a) similar to the values of the Podzol Oe horizons. Compared to the surface organic horizons (Oe/He), the underlying Oa/Ha horizons were enriched in heavy isotopes ($\epsilon^{202}\mathrm{Hg}_{\mathrm{Oa-Oe}}$= 0.37‰, p<0.02 and $\epsilon^{202}\mathrm{Hg}_{\mathrm{Ha-He}}$= 0.34‰, p<0.001, t-test)(Figure 2.2a). Podzol Oa horizons exhibited positive MIF enrichment ($\mathrm{E}^{199}\mathrm{Hg}_{\mathrm{Oa-Oe}}$= 0.11‰, p< 0.001, t-test), whereas Histosol Ha horizons showed negative MIF enrichment ($\mathrm{E}^{199}\mathrm{Hg}_{\mathrm{Ha-He}}$= -0.08‰, p< 0.02, t-test) compared to the overlying Oe/He horizons (Figure 2.2).

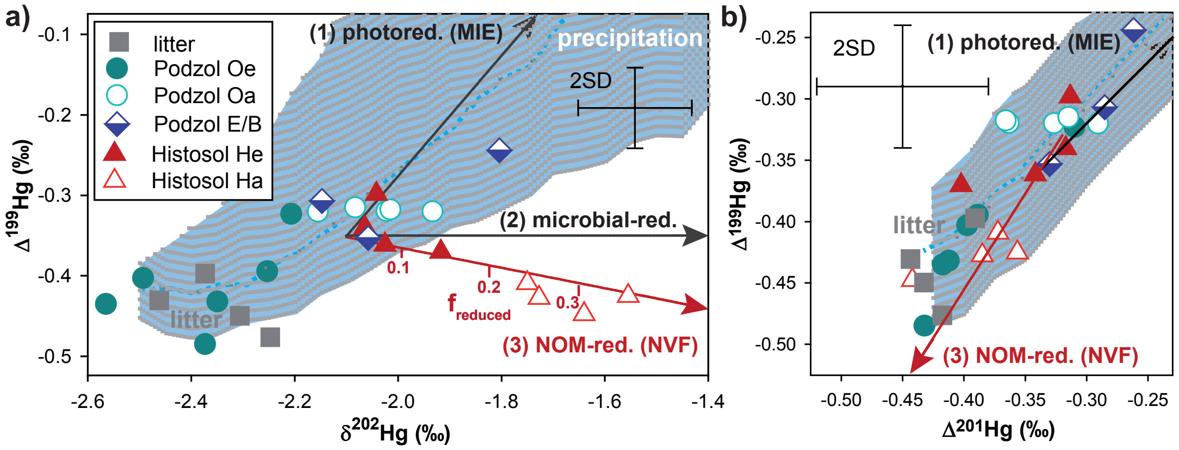

Figure 2.2: (**a**) Mass-independent fractionation (Δ^{199}Hg) vs. mass-dependent fractionation (δ^{202}Hg) and (**b**) mass-independent fractionations Δ^{199}Hg vs. Δ^{201}Hg in boreal litter and soil samples. The blue area represents the 5- to 95-percentile interval of mixing scenarios for litterfall- and precipitation-derived Hg (median= dotted line). The arrows represent the trajectories for (**1**) photochemical reduction (photored.),[11] (**2**) microbial reduction,[10] and (**3**) non-photochemical abiotic reduction by natural organic matter (NOM-red.)[9] with the respective amount of reductive loss (f_{reduced}).

We used a mixing model to determine relative contributions of litter-derived and precipitation-derived ($f_{\mathrm{precipitation}}$) Hg in soil samples. Previous publications applying Hg isotope source tracing in soils performed mixing calculations between atmospherically-deposited and geogenic Hg.[13, 14] However, based on the low mineral contents in the organic horizons and the low geogenic Hg concentrations in the underlying bedrock, the contribution of geogenic Hg to organic horizons was negligible in our study (SI). The modeled fraction of precipitation-derived Hg relative to total Hg increased in Podzols with soil depth from Oe (4%±3%), to Oa (14%±1%), and E/B (19%±7%) horizons. The calibrated radiocarbon ages in Podzols ranged from ≈10 years in litter to ≈60-120 years in E/B horizons (Figure 2.3b,c, Table S2.7). The positive correlation observed between the modeled $f_{\text{precipitation}}$ and the radiocarbon signature in Podzols ($F^{14}C$, $R^2=0.71$, $p<0.001$, Figure S2.9c) supports that precipitation-derived Hg is transported vertically and accumulated in lower Oa and mineral horizons over timescales of decades, as previously suggested based on elemental ratios.[15] Histosol samples with calibrated radiocarbon ages between ≈20 up to ≈1000 years exhibited relatively constant $f_{\text{precipitation}}$ of 12%±2% for He, and 10%±2% for Ha and did not follow time-dependent trends. This may be explained by the hydrological conditions in Histosols, where water saturation could at least temporarily hinder vertical transport. None of the measured soil samples exhibited even-mass Hg isotope anomalies (Δ^{200}Hg) outside analytical uncertainty, in contrast to all precipitation measurements published so far,[16] which supports the relatively small contribution of precipitation-derived Hg in soils. Our modeled source contributions are in agreement with previous estimates from isotope measurements,[13] but lower than concentration-based estimates,[6] confirming the dominant role of litter-derived Hg input to forest ecosystems.[17]

Some of our observed Hg isotope signatures, particularly from Histosols, could not be explained by litter/precipitation mixing (blue area in Figure 2.2), providing evidence for secondary processes. The trajectory for non-photochemical abiotic NOM reduction (**3**)[9] agreed well with the Hg isotope composition of the Histosol samples ($R^2=0.65$), whereas microbial (**2**)[10] and photochemical (**1**)[11] reduction have distinct fractionation trajectories (Figure 2.2). The MIF of NOM reduction, caused by NVF, is expected to fractionate the odd mass isotopes in a ratio of $\Delta^{199}\text{Hg}/\Delta^{201}\text{Hg}=1.6$,[9, 18] in agreement with the MIF data of Histosol samples (Figure 2.2b). The $\Delta^{199}\text{Hg}/\Delta^{201}\text{Hg}$ ratio of all soil samples was 1.02±0.13, consistent with previously reported data for soils[13,14,16] and likely dominated by MIE of photochemical reactions prior to deposition expected to fractionate with a ratio of $\Delta^{199}\text{Hg}/\Delta^{201}\text{Hg}=1$.[11] The average $\Delta^{199}\text{Hg}/\Delta^{201}\text{Hg}$ ratio of Histosol Ha horizons was 1.10, pointing towards a contribution of NVF-derived MIF, however the difference to Podzol samples (1.01) was not significant (p=0.06, t-test).

Non-photochemical abiotic reduction of Hg(II) by NOM was previously observed in laboratory experiments.[7,8] NOM plays a dual role for Hg redox reactions; on one hand providing electrons, but on the other hand decreasing rates of Hg(II) reduction and Hg(0) evasion by strong complexation and re-oxidation. Together with previously missing

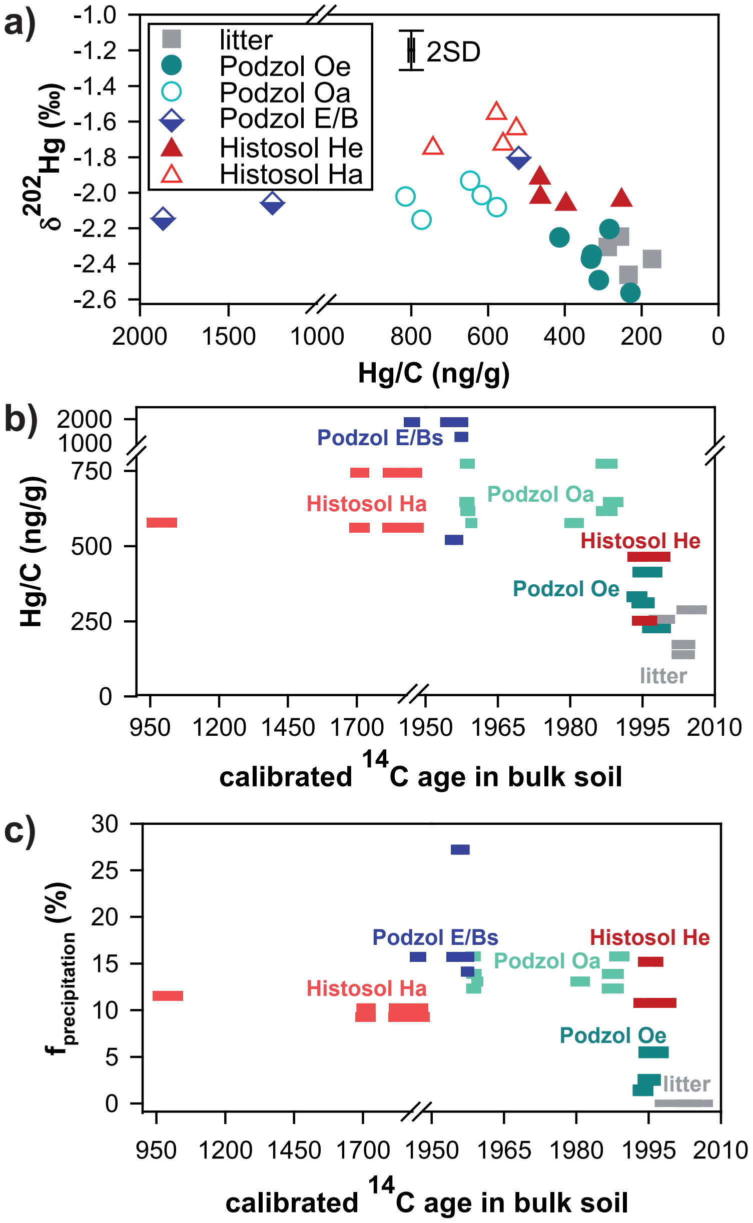

Figure 2.3: Time dependence of Hg isotope signatures in soil: (**a**) mass-dependent fractionation (δ^{202}Hg) vs. Hg/C ratio (**b**) Hg/C ratio vs. calibrated radiocarbon age in bulk soil, and (**c**) modeled fraction of precipitation-derived Hg from stable Hg isotope signatures vs. calibrated radiocarbon age of bulk soil. The width of the bars represents the calibrated age ranges (for certain radiocarbon signatures multiple age ranges are possible as indicated by multiple bars).

evidence for NOM-driven reduction under natural conditions this led to ambiguity about the importance of the process for global Hg cycling.[8] The remarkable correlation between the theoretical NOM-reduction trajectory and the Histosol data (Figure 2.2) suggests that

NOM reduction is an important process in boreal forest soils. Recent measurements of interstitial soil air, revealing the highest Hg^0 concentrations in organic-rich soil layers at high temperatures and low redox potentials,[19] support this hypothesis.

Photochemical Hg reduction, potentially active in foliage[13,20] and the uppermost soil layer, has a fractionation trajectory towards the isotope signature of precipitation-derived Hg (Figure 2.2: (**1**)) and would lead to an overestimation of $f_{\text{precipitation}}$ in the mixing calculation. The fractionation trajectory of direct microbial reduction (**2**), considered to be an important Hg reduction pathway in natural systems,[21,22] is similar to that of NOM reduction (**3**), except for the lack of MIF. We cannot exclude an influence of microbial reduction, however the isotopic enrichment factor reported for microbial reduction ($\epsilon^{202}Hg_{\text{product/reactant}}$= -0.4‰)[10] is much smaller than for NOM driven reduction ($\epsilon^{202}Hg_{\text{product/reactant}}$= -1.5‰).[9] Therefore, microbial reduction would result in higher reductive loss than suggested here; however, it cannot explain the observed Hg isotope range alone (Figure S2.8). Note that for indirect microbial Hg^{2+} reduction, using NOM as electron shuttle, a Hg isotope fractionation trajectory for NOM-driven reduction[9] is expected. Another process potentially causing Hg isotope fractionation in organic soil horizons is sorption of Hg(II) to NOM.[18] However, since almost all Hg was sorbed to NOM, we expect only very small net isotope effects from sorption. Mercury methylation and demethylation processes were not able to affect the bulk Hg isotopic composition, as methyl-Hg levels were low ($\leq$1.3% of Hg_{tot}, SI). Re-oxidation of Hg^0 could potentially cause significant Hg isotope fractionation, but this has not yet been investigated. In an ongoing study, we observed no isotope fractionation between soil horizons and corresponding creek runoff (Chapter 3).

Atmospheric Hg deposition was variable in time and decreased by about 50% in Scandinavia over the last two decades,[23] potentially affecting the Hg isotope signatures in the soil horizons. Reconstructions of Hg emission from coal combustion revealing relatively constant Hg isotope signatures,[24] do not indicate that there is a direct causal relationship between the coal emission signature and the Hg isotope variation in boreal forest soils discussed here. Peat bogs and lake sediments have been used as archives for Hg concentration and isotope composition to reveal historical atmospheric deposition and anthropogenic contamination,[25,26] however, our results suggest that such archives may be susceptible to overprinting by secondary processes like reductive Hg losses or accumulation of precipitation-derived Hg.

Based on the discussion above, the NOM reduction hypothesis appears to be the only plausible explanation for the observed Hg isotope signatures. Using the isotopic enrichment factor for NOM reduction,[9] we calculated reductive Hg losses. This approach can be considered as conservative estimate, because possible influences of microbial and photochemical reduction would result in higher Hg losses (Figure S2.7). For Podzol samples a reductive Hg loss relative to total previously deposited Hg of 4%±1% for Oe and 7%±2% for Oa and for Histosols a loss of 9%±3% for He and 28%±5% for Ha horizons was determined. The relative losses correspond to calculated Hg re-emission fluxes of 1.7 and 5.1 μg m^{-2} a^{-1} for Podzols and Histosols, respectively (Figure 2.4), in agreement with estimates based on Hg flux measurements for forest soils.[4,27]

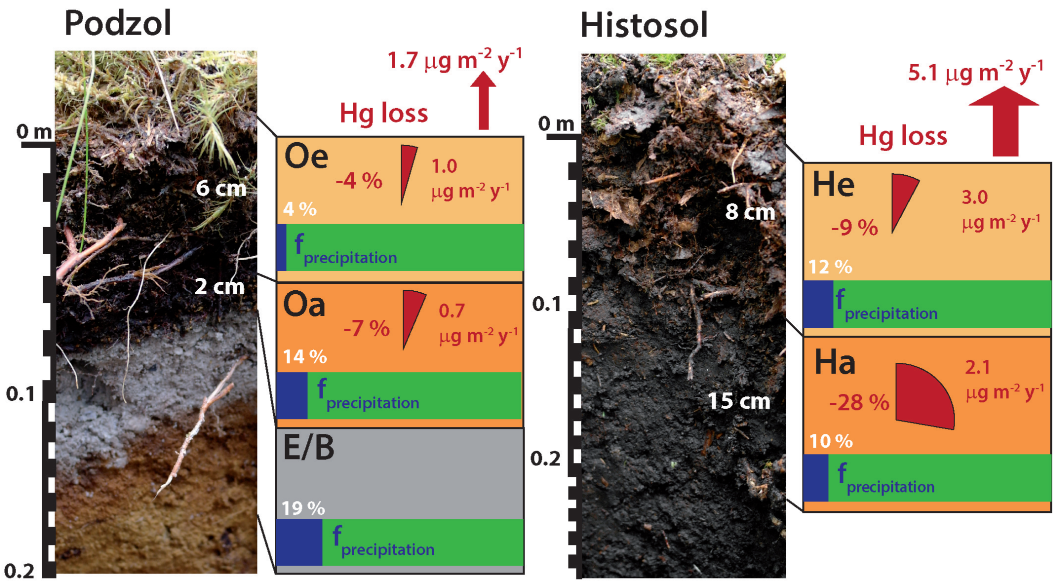
Podzol
0 m
6 cm
2 cm
0.1
0.2
1.7 µg m-2 y-1
Hg loss
Oe
-4 %
1.0 µg m-2 y-1
4 %
f precipitation
Oa
-7 %
0.7 µg m-2 y-1
14 %
f precipitation
E/B
19 %
f precipitation
Histosol
0 m
8 cm
0.1
15 cm
0.2
5.1 µg m-2 y-1
Hg loss
He
-9 %
3.0 µg m-2 y-1
12 %
f precipitation
Ha
-28 %
2.1 µg m-2 y-1
10 %
f precipitation

Figure 2.4: Summary of modeled results of different soil types (Podzols and Histosols): Fraction of precipitation-derived Hg ($f_{\text{precipitation}}$ as % of total Hg, the rest corresponds to litter-derived Hg) and modeled Hg loss by non-photochemical abiotic reduction by natural organic matter. Stable Hg isotope signatures suggest a threefold higher reductive Hg loss in Histosols as compared to Podzols.

2.4 Implications for global Hg cycling

Global models suggest that 60% of today's Hg deposition originate from re-emitted legacy anthropogenic Hg, making Hg re-emission from terrestrial surfaces one of the major sources of Hg emissions to the atmosphere.[3] Current global Hg models account for Hg evasion from soils by coupling the Hg loss to carbon respiration in soils, based on empirical correlations between Hg and C in some studies.[1,3] Our data suggest that poorly-drained Histosols exhibit a three times higher reductive Hg loss compared to Podzols, despite being characterized by high carbon accumulation rates. This finding indicates a higher mobility of Hg in reducing environments as previously expected. The significant Hg re-emission upon reduction by NOM, in addition to recent observations of gaseous Hg concentrations in mineral soils,[28] reveal the limitations of the coupling approach of Hg to C used in global Hg models.[1,3] We anticipate that with higher temperatures and precipitation at northern latitudes, driven by global warming leading to generally more anoxic conditions in peatlands and a melting of permafrost,[23] Hg reduction by NOM and subsequently Hg re-emission from organic soils will increase. Therefore, we demonstrate the need for a process-based ecosystem-specific assessment of Hg re-emissions to improve predictions of future global Hg cycling. Stable Hg isotope approaches as used in this study can provide new insights in the mechanisms and fluxes associated with land/atmosphere exchange of Hg.

Acknowledgments

We would like to thank Kurt Barmettler for his support in the soil chemistry laboratory and Colin Maden and Robin Smith for assistance in the isotope geochemistry laboratory. We are grateful to Urs Menet, Donat Niederer, Daniel Schnarwiler and Andreas Suesli for their help with manufacturing the two-stage combustion oven. We thank Alexander Brunner, Christa Bodmer and Alexandra Metzger for help with sample preparation and concentration analyses and Marita Skarpeli-Liati for field assistance. We acknowledge Daniel Obrist for helpful discussions. This research was funded by ETH Zurich (research grant ETH-15 09-2) and the Swedish Research Council for Environment and Spatial Planning (FORMAS, no. 29-2009-1207).

References

[1] Smith-Downey, N. V., Sunderland, E. M., and Jacob, D. J. Anthropogenic impacts on global storage and emissions of mercury from terrestrial soils: Insights from a new global model. *J. Geophys. Res.-Biogeosci.*, **115**:G03008, (2010).

[2] Mason, R. P. et al. Mercury biogeochemical cycling in the ocean and policy implications. *Environ. Res.*, **119**:101–117, (2012).

[3] Amos, H. M., Jacob, D. J., Streets, D. G., and Sunderland, E. M. Legacy impacts of all-time anthropogenic emissions on the global mercury cycle. *Glob. Biogeochem. Cycles*, **27**:410–421, (2013).

[4] Denkenberger, J. S. et al. A synthesis of rates and controls on elemental mercury evasion in the Great Lakes Basin. *Environ. Pollut.*, **161**:291–298, (2012).

[5] Grigal, D. F., Kolka, R. K., Fleck, J. A., and Nater, E.A. Mercury budget of an upland-peatland watershed. *Biogeochemistry*, **50**:95–109, (2000).

[6] Demers, J. D., Driscoll, C. T., Fahey, T. J., and Yavitt, J. B. Mercury cycling in litter and soil in different forest types in the Adirondack region, New York, USA. *Ecol. Appl.*, **17**:1341–1351, (2007).

[7] Alberts, J. J., Schindle, J.E., Miller, R. W., and Nutter, D. E. Elemental mercury evolution mediated by humic acid. *Science*, **184**:895–896, (1974).

[8] Gu, B. et al. Mercury reduction and complexation by natural organic matter in anoxic environments. *Proc. Natl. Acad. Sci. U.S.A.*, **108**:1479–83, (2011).

[9] Zheng, W. and Hintelmann, H. Nuclear field shift effect in isotope fractionation of mercury during abiotic reduction in the absence of light. *J. Phys. Chem. A*, **114**:4238–4245, (2010).

[10] Kritee, K., Blum, J. D., Johnson, M. W., Bergquist, B. A., and Barkay, T. Mercury stable isotope fractionation during reduction of Hg(II) to Hg(0) by mercury resistant microorganisms. *Environ. Sci. Technol.*, **41**:1889–1895, (2007).

[11] Bergquist, B. A. and Blum, J. D. Mass-dependent and -independent fractionation of Hg isotopes by photoreduction in aquatic systems. *Science*, **318**:417–420, (2007).

[12] *Soil Atlas of the Northern Circumpolar Region.* European Commission, Office of the Official Publications of the European Communities, Luxemburg, (2010).

[13] Demers, J. D., Blum, J. D., and Zak, R. D. Mercury isotopes in a forested ecosystem: Implications for air-surface exchange dynamics and the global mercury cycle. *Glob. Biogeochem. Cycles*, **27**:222–238, (2013).

[14] Zhang, H. et al. Atmospheric mercury inputs in montane soils increase with elevation: Evidence from mercury isotope signatures. *Sci. Rep.*, **3**:3322, (2013).

[15] Obrist, D. et al. Mercury distribution across 14 U.S. forests. Part I: Spatial patterns of concentrations in biomass, litter, and soils. *Environ. Sci. Technol.*, **45**:3974–3981, (2011).

[16] Blum, J. D., Sherman, L. S., and Johnson, M. W. Mercury isotopes in earth and environmental sciences. *Annu. Rev. Earth Planet. Sci. Lett.*, **42**:249–269, (2014).

[17] St Louis, V. L. et al. Importance of the forest canopy to fluxes of methyl mercury and total mercury to boreal ecosystems. *Environ. Sci. Technol.*, **35**:3089–3098, (2001).

[18] Wiederhold, J. G. et al. Equilibrium mercury isotope fractionation between dissolved Hg(II) species and thiol-bound Hg. *Environ. Sci. Technol.*, **44**:4191–4197, (2010).

[19] Moore, C. W. and Castro, M. S. Investigation of factors affecting gaseous mercury concentrations in soils. *Sci. Total Environ.*, **419**:136–43, (2012).

[20] Graydon, J. A. et al. The role of terrestrial vegetation in atmospheric Hg deposition: Pools and fluxes of spike and ambient Hg from the METAALICUS experiment. *Glob. Biogeochem. Cycles*, **26**:GB1022, (2012).

[21] Fritsche, J., Obrist, D., and Alewell, C. Evidence of microbial control of Hg(0) emissions from uncontaminated terrestrial soils. *J. Plant Nutr. Soil Sci.*, **171**:200–209, (2008).

[22] Poulain, A. J. et al. Potential for mercury reduction by microbes in the high Arctic. *Appl. Environ. Microbiol.*, **73**:2230–2238, (2007).

[23] Rydberg, J., Klaminder, J., Rosen, P., and Bindler, R. Climate driven release of carbon and mercury from permafrost mires increases mercury loading to sub-arctic lakes. *Sci. Total Environ.*, **408**:4778–4783, (2010).

[24] Sun, R. et al. Mercury stable isotope signatures of world coal deposits and historical coal combustion emissions. *Environ. Sci. Technol.*, **48**:7660–7668, 2014.

[25] Shotyk, W. et al. Anthropogenic contributions to atmospheric Hg, Pb and As accumulation recorded by peat cores from southern Greenland and Denmark dated using the 14C ”bomb pulse curve”. *Geochim. Cosmochim. Acta*, **67**:3991–4011, (2003).

[26] Biester, H., Bindler, R., Martinez-Cortizas, A., and Engstrom, D. R. Modeling the past atmospheric deposition of mercury using natural archives. *Environ. Sci. Technol.*, **41**:4851–4860, (2007).

[27] Lindberg, S. E., Hanson, P. J., Meyers, T. P., and Kim K. H. Air/surface exchange of mercury vapor over forests - The need for a reassessment of continental biogenic emissions. *Atmos. Environ.*, **32**:895–908, (1998).

[28] Obrist, D., Pokharel, A. K., and Moore, C. Vertical profile measurements of soil air suggest immobilization of gaseous elemental mercury in mineral soil. *Environ. Sci. Technol.*, **48**:2242–52, (2014).

[29] Jiskra, M., Wiederhold, J. G., Bourdon, B., and Kretzschmar R. Solution speciation controls mercury isotope fractionation of Hg(II) sorption to goethite. *Environ. Sci. Technol.*, **46**:6654–6662, 2012.

[30] Stuiver M. and Polach H. A. Reporting of C-14 data - discussion. *Radiocarbon*, **19**:355–363, 1977.

Chapter 3

Sources of mercury in boreal forest catchment runoff: Insights from Hg stable isotope signatures, radiocarbon signatures and Hg:C ratios

M. Jiskra, J.G. Wiederhold, U. Skyllberg, R-M. Kronberg, and R. Kretzschmar, Sources of mercury in boreal forest catchment runoff: Insights from Hg stable isotope signatures, radiocarbon signatures and Hg:C ratios. *in preparation*

Abstract

Terrestrial runoff represents a major source of mercury (Hg) to aquatic ecosystems. We measured Hg stable isotope signatures in the runoff of boreal forest catchments in northern Sweden, using a newly developed method based on ultrafiltration pre-enrichment suitable for natural waters with high dissolved organic carbon (DOC) concentration. We compared the runoff signatures with those of different soil horizons of the catchment and the results suggested no Hg isotope fractionation in association with leaching from soils. Using a mixing model we calculated the contribution of the soil horizons to the Hg in the runoff. Our results suggest that the surface organic horizons (Oe/He) exhibited the highest mobility of Hg and contributed about 60 - 85 % of the total Hg flux to the runoff. The underlying more humified Oa/Ha horizons displayed an at least 5 times lower mobility of Hg. The good agreement of the Hg isotope results with other source tracing approaches based on radiocarbon signatures and Hg:C ratios confirms a strong coupling of Hg and DOC dynamics in such boreal ecosystems. Given that Hg and DOC in the runoff is dominantly originating from the organic topsoils (Oe/He), we predict a response of terrestrial runoff to a reduction in atmospheric Hg deposition within a few decades.

3.1 Introduction

Humans are exposed to methyl-mercury (MeHg), the most toxic form of Hg, primarily through the consumption of fish.[1] In Scandinavia, over 60 % of all freshwater lakes contain fish with Hg conentrations exceeding the EU guideline for fish consumption.[2] Hg enters aquatic ecosystems by direct atmospheric deposition or via catchment runoff from terrestrial ecosystems.[1,3] The prediction of future Hg concentrations in the atmosphere, aquatic environments, and eventually in fish is essential for the assessment of future human Hg exposure through fish consumption. Anthropogenic Hg emissions have led to a 20 % increase in the soil Hg pool.[4] Efforts to reduce primary anthropogenic Hg emissions, agreed on by the Minamata Convention on Mercury coordinated by the United Nations Environment Programme (UNEP),[5] will result in reduced atmospheric deposition. With the decrease in atmospheric Hg deposition, one can expect an increasing relative contribution of Hg from terrestrial runoff to aquatic ecosystems. Thus, in order to predict the development of Hg concentrations in aquatic ecosystems it is essential to understand the Hg source and input pathways from terrestrial ecosystems and how they respond to changes in atmospheric Hg deposition.

The application of enriched Hg isotope tracers in a whole ecosystem study revealed a slow translocation of Hg(II) deposited on uplands from vegetation to topsoils and a slow response in the terrestrial runoff to the nearby lake and biota.[3,6]

Understanding the Hg transfer from boreal forests to aquatic ecosystems is of special importance because the highest fish Hg concentrations in Sweden and Finland have been observed in regions of boreal coniferous forests.[2] Dissolved organic carbon (DOC) forms stable complexes with Hg[7] and has an important role in the transport of Hg from terrestrial to aquatic ecosystems.[2,8–12] A strong coupling of terrestrial Hg runoff to DOC was also described in a study using terrestrial organic matter biomarkers as tracers for the source of Hg in lake sediments.[61, 62] MeHg from terrestrial sources was shown to exhibit a higher potential for bioaccumulation than MeHg in sediments.[13] Forest management practices were shown to affect aquatic ecosystems, e.g., through forest harvest after which increased Hg concentrations in water, zooplankton, and fish have been observed.[10,14–16] The processes driving increased Hg and MeHg fluxes after forest harvest remain poorly understood,[16] and have been the focus of an accompanying study.[17]

The analysis of natural Hg stable isotopes signatures provides a new tool to trace sources and transformations of ambient Hg in the environment. Hg stable isotopes have been successfully employed to trace Hg sources in fish,[18–21] e.g., by relating the Hg isotope signature of fish to the signatures of sediments and thereby inferring the contribution of anthropogenic pollution in fish[19] or the role of sediments as food source.[20] Furthermore, Hg stable isotopes were used to elucidate differences in MeHg sources between terrestrial and aquatic invertebrates.[22,23] The measurement of Hg isotope signatures in natural waters has not been possible previously due to the generally very low dissolved Hg concentrations. However, it is essential to know the Hg isotope signature in the water to fully understand processes governing Hg transformations and uptake into organisms. Only recently, analytical techniques have been developed for the measurement of stable Hg isotopes in natural water samples, based on acid digestion and pre-enrichment on an ion-exchange column[24,25] or stannous chloride reduction and purge and trap.[26] So far aqueous Hg isotope data have been mainly reported for precipitation samples (rain and snow)[26–31] exhibiting low DOC concentrations.

Here, we developed an alternative method based on a ultrafiltration technique used for pre-enrichment, suitable for water samples with high DOC concentrations combined with a two-step oven combustion system. This approach may prove useful in many natural aquatic environments, because the fate of Hg is often closely related to DOC and many relevant Hg transformations (e.g., methylation, demethylation, reduction) occur in DOC-rich environments. We investigated Hg stable isotope signatures of boreal forest catchment runoff in northern Sweden and compared it to different soil horizons studied previously[32] to address the following objectives: (i) to develop and validate a pre-enrichment system for the measurement of Hg isotope signatures in water samples with high DOC concentrations, (ii) to investigate the potential fractionation between Hg pools in soils and in water of the catchment runoff, (iii) to trace Hg in boreal catchment runoff back to soil horizons and investigate its relation to DOC dynamics assessed by radiocarbon signatures and Hg:C ratios, and (iv) to investigate the influence of forest harvest on Hg isotopes and Hg dynamics in forest soil runoff.

3.2 Experimental section

3.2.1 Materials and reagents

Polyethylene canisters (25 L) were cleaned in the laboratory with 0.24 M HCl/ 0.32 M HNO_3 (2×) and ultrapure water (>18 MΩ cm, 3×) and rinsed with sample water in the field (3×). All filtration steps were performed with a peristaltic pump (Masterflex I/P, Cole-Parmer) equipped with spallation-free pump-tubing (GORE Style 100SC, Cole-

Parmer). All tubings, manometer, valves and fittings were made of Teflon to avoid Hg and DOC sorption. 0.45 μm cross-flow filtration was performed with a 142 mm mixed cellulose ester membrane (HAWP14250, Merck Millipore) on a self-constructed Teflon filter-holder. For ultrafiltration, a hollow-fiber system was used (1 kDa cutoff, Polysulfone, UFP-1-C-9, GE Life Sciences). The filtration system was cleaned by circulating 0.05 M citric acid (pH 2-2.5) and NaOH (0.1 M) for 0.5 h each, to remove iron precipitates and organic matter, respectively, followed by repeated flushing with ultrapure water.

3.2.2 Study area

Samples were taken from four small catchments of boreal forests in northern Sweden close to Junsele (Figure S3.1, coordinates: 63°50' N, 17°00' E). Two sites were mature, >80-years-old spruce forest stands (reference site 1 and 2), from which the Hg isotope signature of soil samples had been measured previously.[32] Two sites were harvested two to three years prior to the sampling in 2011/2012 (clearcut site 1 and 2) and scarified to prepare the sites for planting. All soils were classified as either Podzols or Histosols[33] and have been actively drained by ditches dug in the early 1900's to increase forest productivity. Soil samples were taken from a transect perpendicular to the first-order stream in order to represent the soil variability, as described previously[32]. Composite samples consisting of 5 soil samples taken within 10 m^2 were divided into surface organic horizons (Oe/He), underlying Oa/Ha organic horizons exhibiting a higher degree of humification, and for Podzols mineral E+B horizons. Water samples from the first-order streams in the runoff of the four boreal forest catchments were collected in September 2012 for Hg isotope and radiocarbon analysis. In addition to the first-order streams, a larger stream draining all of the four catchments (LillC, Lillsele creek), and the inlet and outlet of a nearby lake (VK, Västa Kotrinvattnet) were sampled (Figure S3.1). Water samples for total Hg and dissolved organic carbon (DOC) analysis were taken at 9 occasions during 2011 and 2012 (Figure S3.2).[17] Soil samples were taken in july 2011.

3.2.3 Soil sample preparation

The soil sampling and oven combustion procedure has been described previously.[32] In short, composite samples were homogenized using a 4 mm cutting sieve, dried in an oven at 45°C and further homogenized using a rotary disk mill. The sample powder was used for elemental concentrations, Hg isotope, and radiocarbon analyses. For Hg isotope analysis, the samples were combusted in a two-stage combustion oven connected to an oxidizing liquid trap, as described previously.[32]

3.2.4 Water sample preparation

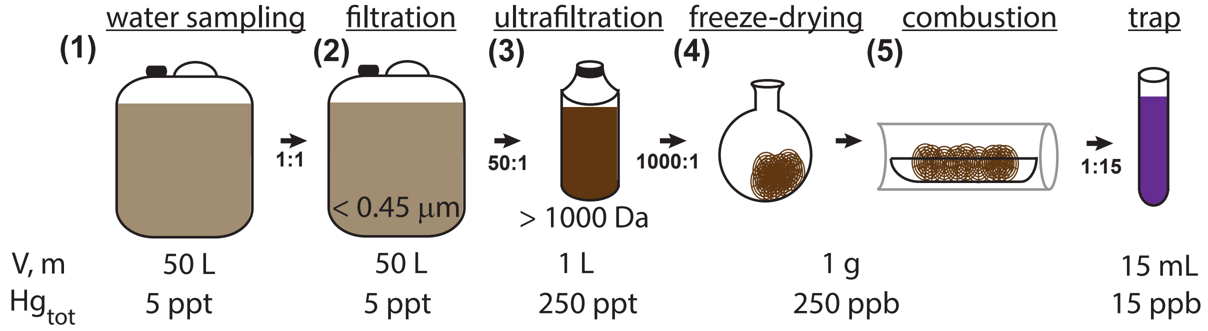

Figure 3.1: Schematic overview for the enrichment of Hg in water with high DOC concentration for Hg isotope analysis. Volumes (V) of water samples and mass (m) of solid sample and typical total Hg concentrations (Hg_{tot}). The ratios represent typical enrichments in Hg concentration during ultrafiltration and freeze-drying and dilution after combustion.

We developed a sample enrichment procedure for Hg associated with dissolved organic carbon (DOC) based on ultrafiltration. For aqueous samples with high DOC concentrations (13.7 to 58.5 mg L^{-1}) with background concentrations of Hg (3.9 to 14.0 ng L^{-1}) as found in boreal forest runoff of this study, all dissolved Hg is expected to be complexed to DOC, due to the high binding affinity of Hg to DOC.[7,34] A survey on natural freshwaters from the USA showed that the DOC fraction between $<0.45\mu$m and 10 kDa contained >50% of the total Hg filtered Hg ($<0.45\mu$m),[35] thus ultrafiltration allows for an enrichment of Hg and DOC. We assumed that a physical enrichment based on molecular size of the DOC would not introduce any methodological artifacts on the Hg isotope composition, even though only a part of the total Hg in the system was enriched together with the DOC.

A scheme of the pre-enrichment steps is given in Figure 3.1. 50 L of water sample were transported to the laboratory on the day of sampling and refrigerated at 4°C (step 1, Figure 3.1) until filtration was performed. Samples were filtered within 24 h using a 0.45 μm cutoff to remove particulate matter and bacteria (step 2, Figure 3.1). Water samples were then circulated through the ultrafiltration system, with water, dissolved ions, and low molecular weight DOC (<1 kDa) passing through the cutoff of the ultrafiltration membrane (permeate). Over time (≈6h) this led to an enrichment of DOC (<1 kDa) and concomitantly Hg in the remaining fraction (retentate, >1 kDa, $<0.45\mu$m) (step 3, Figure 3.1). Assuming a higher enrichment of DOC and thus Hg with a 1 kDa membrane, compared to a previously published survey which was performed with a 10 kDa cutoff,[35] the 1 L retentate could be expected to be associated with an up to 50 times increase in Hg concentration compared to the 50 L sample (Figure 3.1). The ≈1L retentate used for Hg isotope analysis was frozen and the remaining water was removed by freeze-drying (ALPHA 2-4 LDplus, Christ) (step 4, Figure 3.1). Finally the freeze-dried organic carbon was combusted in the two-stage oven system and total Hg trapped in an oxidizing liquid trap (step 5, Figure 3.1), as previously described for soil samples.[32]

To validate the enrichment method, water from a small lake in the peatland Seleger Moor (SM, Rifferswil, Switzerland) with high DOC concentrations (≈33 mg L^{-1}) and low Hg concentration (<<10 ng L^{-1}) was collected. The SM samples were filtered (0.45μm) and then spiked with 50, 100, and 250 ng L^{-1} of our inhouse Hg isotope standard (ETH-Fluka, 1000 ppm Hg(II) in 0.8 M HNO_3), conditioned for 24 h, and processed as described above. During ultrafiltration (step 3, Figure 3.1) the permeate fraction (<1kDa) and the retentate fraction (<0.45μm, >1kDa) were collected separately in addition to a fraction recovered from the ultrafiltration membrane by rinsing with 2L ultrapure water (rinse). The validation test showed a very good mass balance for the recovery of organic carbon (98% - 116%) and Hg (93% - 97%) (Table 3.1). About 10 % of the total organic carbon and Hg was associated with the rinse fraction, likely representing the dead volume in the ultrafiltration system and sorption to the membrane. The retentate of the SM sample spiked with 100 ng L^{-1} Hg and a retentate of a SM blank sample spiked with 1000 ng L^{-1} Hg after ultrafiltration were freeze-dried, combusted in the two-stage oven system and analyzed for Hg isotope signatures. The Hg isotope signature of the ETH-Fluka standard spiked to the SM water and processed by the ultrafiltration, freeze-drying and two-stage oven combustion method was within analytical uncertainty (2SD) to the results of the directly measured ETH-Fluka standard (Table 3.1), indicating that the enrichment procedure did not cause any Hg isotope fractionation. We therefore conclude that the sample enrichment using ultrafiltration is a suitable method to measure Hg isotope signatures of aqueous samples with high DOC concentrations.

Table 3.1: Validation of mercury enrichment method by ultrafiltration for the measurement of Hg isotope signatures in aqueous samples with high DOC concentrations: Samples from Seleger Moor (SM) in Switzerland spiked with different concentrations of Hg (in-house isotope standard, ETH-Fluka), size fraction, DOC and Hg concentration and percentage relative to total for the relevant fractions, and Hg isotope signatures.

	fraction	size	amount (L)	DOC (mg L^{-1})	DOC (% total)	Hg (ng L^{-1})	Hg (% total)	δ^{202}Hg (‰)	Δ^{199}Hg (‰)	Δ^{200}Hg (‰)	Δ^{201}Hg (‰)	Δ^{204}Hg (‰)
SM-blank	total	<0.45μm	10	33		<10						
	permeate	<1kDa	9	10	27	<10	nd					
	retentate	<0.45μm, >1kDa	1	147	44	11	nd					
SM-50ppt Hg	total	<0.45μm	10	33		49						
	permeate	<1kDa	9	9	25	<10	nd					
	retentate	<0.45μm, >1kDa	0.95	225	65	427	83					
	rinse	nd	2	16	10	27	11					
	recovery				**100**		**94**					
SM-100ppt Hg	total	<0.45μm	10.5	33		111						
	permeate	<1kDa	8.8	19	47	32	24					
	retentate	<0.45μm, >1kDa	1.08	213	66	672	63	-1.37	0.12	0.03	0.02	-0.04
	rinse	nd	2	6	3	36	6					
	recovery				**116**		**93**					
SM-250ppt Hg	total	<0.45μm	10	33		249						
	permeate	<1kDa	9	8	22	9	3					
	retentate	<0.45μm, >1kDa	0.89	239	65	2310	82					
	rinse	nd	2	17	10	143	12					
	recovery				**98**		**97**					
SM-1000ppt Hg	retentate	<0.45μm, >1kDa	0.94			1064		-1.35	0.09	0.04	0.02	-0.05
ETH-Fluka[a]	average							-1.44	0.07	0.01	0.03	0.00
	2 SD							±0.12	±0.06	±0.06	±0.06	±0.10
ETH-Fluka[a,b]	average							-1.38	0.08	0.02	0.03	-0.02
	2 SD							±0.09	±0.03	±0.02	±0.04	±0.05

[a] direct measurements of standard solution (ETH-Fluka), n=26

[b] Reference[36], n=16

nd= not determined

3.2.5 Analytical methods

Solutions of the oxidizing liquid trap, containing 1% $KMnO_4$ (w/v) in 10% H_2SO_4 (v/v) were pre-reduced using 0.66% (w/v) hydroxylamine-hydrochloride (H_2NOH-HCl) and diluted to 25 or 12.5 nmol L^{-1} Hg for isotope measurements. Hg isotope signatures were measured using cold vapor generation stannous chloride reduction (CV; HGX-200, Cetac) coupled to a multicollector inductively coupled plasma mass spectrometer (MC-ICPMS) as described in detail previously.[32,36,37] Briefly, all Hg masses were measured simultaneously for 108 integration cycles of 5 sec. Tl (NIST-997) masses 203 and 205, continuously introduced using a desolvating nebulizer (Apex, Elemental Scientific) were measured for instrumental mass bias correction. Hg isotope signatures are reported relative to the bracketing standard (NIST-3133) measured prior to and after each sample. Mass-dependent fractionation (MDF) is reported as δ^{202}Hg (eq: 3.1) and mass-independent fractionation (MIF) as Δ^{199}Hg, Δ^{200}Hg, Δ^{201}Hg, and Δ^{204}Hg (eq: 3.2 – 3.5) following previous recommendations.[38,39]

$$\delta^{202}\mathrm{Hg} = \frac{(^{202}\mathrm{Hg}/^{198}\mathrm{Hg})_{\mathrm{sample}}}{(^{202}\mathrm{Hg}/^{198}\mathrm{Hg})_{\mathrm{NIST-3133}}} - 1 \tag{3.1}$$

$$\Delta^{199}\mathrm{Hg} = \delta^{199}\mathrm{Hg} - (\delta^{202}\mathrm{Hg} \times 0.2520) \tag{3.2}$$

$$\Delta^{200}\mathrm{Hg} = \delta^{200}\mathrm{Hg} - (\delta^{202}\mathrm{Hg} \times 0.5024) \tag{3.3}$$

$$\Delta^{201}\mathrm{Hg} = \delta^{201}\mathrm{Hg} - (\delta^{202}\mathrm{Hg} \times 0.7520) \tag{3.4}$$

$$\Delta^{204}\mathrm{Hg} = \delta^{204}\mathrm{Hg} - (\delta^{202}\mathrm{Hg} \times 1.493) \tag{3.5}$$

The regularly measured in-house standard (ETH-Fluka) reproduced with δ^{202}Hg=-1.44‰ ±0.12‰, Δ^{199}Hg=0.07±0.05‰, Δ^{200}Hg=0.01±0.06‰ and Δ^{201}Hg=0.03±0.06‰ (2σ, n=21) and the process standard (Montana Soil, NIST-2711), combusted in the oven-enrichment system after every 10 samples reproduced at δ^{202}Hg=-0.12±0.10 ‰, Δ^{199}Hg=-0.23±0.07‰, Δ^{200}Hg=0.00±0.04‰ and Δ^{201}Hg=-0.18±0.02‰ (2σ, n=10), consistent with previously published values.[36,40,41] The accurate measurement of Hg isotope signatures in organic soil matrices was validated by measurements of peat samples low in ambient Hg spiked with inorganic Hg(II), consistent with direct measurements of the inorganic Hg(II)-salt (Table S3.7).[32]

Total dissolved Hg concentrations were measured using cold vapor atomic fluorescence spectrometry (CV-AFS; Millennium Merlin, PS Analytical) and DOC was measured using a total organic carbon analyzer (TOC, Dimatoc 2000, Dimatec). For solid samples, carbon and nitrogen were measured by a CHNS analyzer (LECO) and the total Hg concentration was measured by combustion atomic absorption spectrometry (LECO AMA-254). Element concentrations (Z>11) were measured by energy-dispersive X-ray fluorescence analysis (XRF; Spectro-X-Lab 2000, Spectro) of pressed pellets of powdered samples with wax (4g sample, 0.9 g wax).

Radiocarbon signatures were measured on the soil sample powders and freeze-dried organic carbon of the water samples after pre-enrichment. Samples were graphitized and high precision ^{14}C signatures measured on an accelerator mass spectrometer (AMS, ETH Zurich).[42] Since the majority of samples contained post-bomb carbon, the radiocarbon data are reported as fraction relative to modern carbon (F^{14}C) according to Reimer et al.[43]

3.2.6 Mixing models

We calculated the Hg contribution of different soil horizons to the catchment runoff with a mixing model using Hg isotope signatures, radiocarbon signatures, and Hg:C ratios as conservative tracers. We assumed that the Hg isotope signature, radiocarbon signature and Hg:C ratio in the dissolved phase was a mixture of the different sources, represented by the bulk soil horizon measurements and that there was no Hg isotope fractionation associated with leaching of Hg from the soils. Thus the signatures of the source pools (Oe/He, Oa/Ha, and E+B horizon) were treated as inert tracers. Whereas some observations reported identical Hg:C ratio in soil porewater and the respective solid phase,[8] the validity of this assumption is not universal.[10,34] We did not observe any statistical difference in F^{14}C between the bulk soil and the extracted humic acid fraction of selected soil samples (Figure S3.5), supporting that the F^{14}C leaching from a soil horizon is similar to its bulk F^{14}C signature. The limitations of the inert tracer approach will be addressed in the discussion. The distribution of the source signals was modeled based on the measured results (average and standard deviation, Table S3.4) using the pseudo-random number generation function of Matlab (R2012a, MathWorks) and the contributions of the soil samples were simulated with a Monte Carlo simulation approach (details in SI).

3.3 Results

All catchment runoff samples were characterized by an isotopically light δ^{202}Hg signature (MDF, δ^{202}Hg=-1.99‰ to -2.29‰) and a depletion in odd mass isotopes (MIF, Δ^{199}Hg=-0.33‰ to -0.42‰) (Figure 3.2 a,d,f and i). These values were within the range of the Hg isotope signatures measured for the organic soil samples (δ^{202}Hg=-1.55‰ to -2.56‰ and Δ^{199}Hg=-0.24‰ to -0.48‰)[32] (Figure 3.2 a,d,f and i, Table S3.2, S3.3). The water samples of the larger creek (LillC) and the lake inlet (VK-Inlet) had MDF (δ^{202}Hg = -2.01‰ and -1.76‰) and MIF (Δ^{199}Hg = -0.33‰ and -0.25‰) signatures, which were similar to the runoff samples from the boreal catchments (Table 3.2). The δ^{202}Hg signature of the lake outlet, representing the mixed lake water (VK-outlet) was similar to the lake inlet (δ^{202}Hg= -1.92‰), however its Δ^{199}Hg signature was different to all soil and runoff samples (Δ^{199}Hg = 0.04‰). All soil and natural water samples had a Δ^{199}Hg/Δ^{201}Hg ratio of ≈1 within analytical uncertainty and no sample exhibited any significant anomaly in Δ^{200}Hg (Table 3.2). The radiocarbon signature ($F^{14}C$) in the runoff (1.10 and 1.11 for reference site 1 and 2, respectively, Figure 3.2 b and g) indicated that the presence of post-bomb carbon was similar to the radiocarbon signatures measured for the organic topsoil horizons Oe/He (1.12±0.01 for both sites) and different from the underlying organic Oa/Ha (0.95±0.06 and 1.20±0.05) and mineral E+B (1.01±0.04 and 1.05±0.05) horizons (Table S3.4). The Hg:C ratios in the catchment runoff was generally lower (average of all 4 sites: 0.31 μg g^{-1}) than in the soils. The Hg:C ratio in soil increased with soil depth from the uppermost horizons (Oe/He, average: 0.42 μg g^{-1}) to the underlying organic Oa/Ha (average: 0.68 μg g^{-1}) and mineral E+B (average: 1.21 μg g^{-1}) horizons (Figure 3.2 c, e, h, and j, Table S3.4).

Table 3.2: Water samples: sampling date, dissolved organic carbon (DOC), total dissolved Hg (Hg_{tot}), mercury to carbon ratio (Hg:C), radiocarbon signature ($F^{14}C$) and mercury isotope signatures ($\pm 2\sigma$).

Name	Site	date	DOC (mg L^{-1})	Hg_{tot} (ng L^{-1})	Hg:C (μg/g)	$F^{14}C$	δ^{202}Hg (‰)	Δ^{199}Hg (‰)	Δ^{200}Hg (‰)	Δ^{201}Hg (‰)	Δ^{204}Hg (‰)
REF3	reference - 1	20.09.2012	30	9.2	0.31	1.101	-1.99±0.12	-0.33±0.05	-0.07±0.05	-0.36±0.07	-0.08±0.11
REF4	reference - 2	24.09.2012	20	6.8	0.34	1.111	-2.29±0.12	-0.38±0.05	-0.03±0.05	-0.29±0.07	0.09±0.11
CC3	clearcut - 1	24.09.2012	17	10.5	0.60		-2.05±0.12	-0.42±0.05	-0.12±0.05	-0.25±0.07	0.11±0.11
CC4	clearcut - 2	20.09.2012	34	10.6	0.31		-2.01±0.12	-0.39±0.05	-0.03±0.05	-0.41±0.07	-0.12±0.11
LillC	Lillsele creek	28.09.2012	24	6.6	0.27		-2.01±0.12	-0.33±0.05	-0.01±0.05	-0.35±0.07	0.12±0.11
VK-Inlet	lake inlet	28.09.2012	18	5.5	0.30		-1.76±0.12	-0.25±0.05	-0.01±0.05	-0.29±0.07	-0.06±0.11
VK-Outlet	lake outlet	28.09.2012	11	4.2	0.39		-1.92±0.12	0.04±0.05	-0.02±0.05	-0.04±0.07	-0.08±0.11

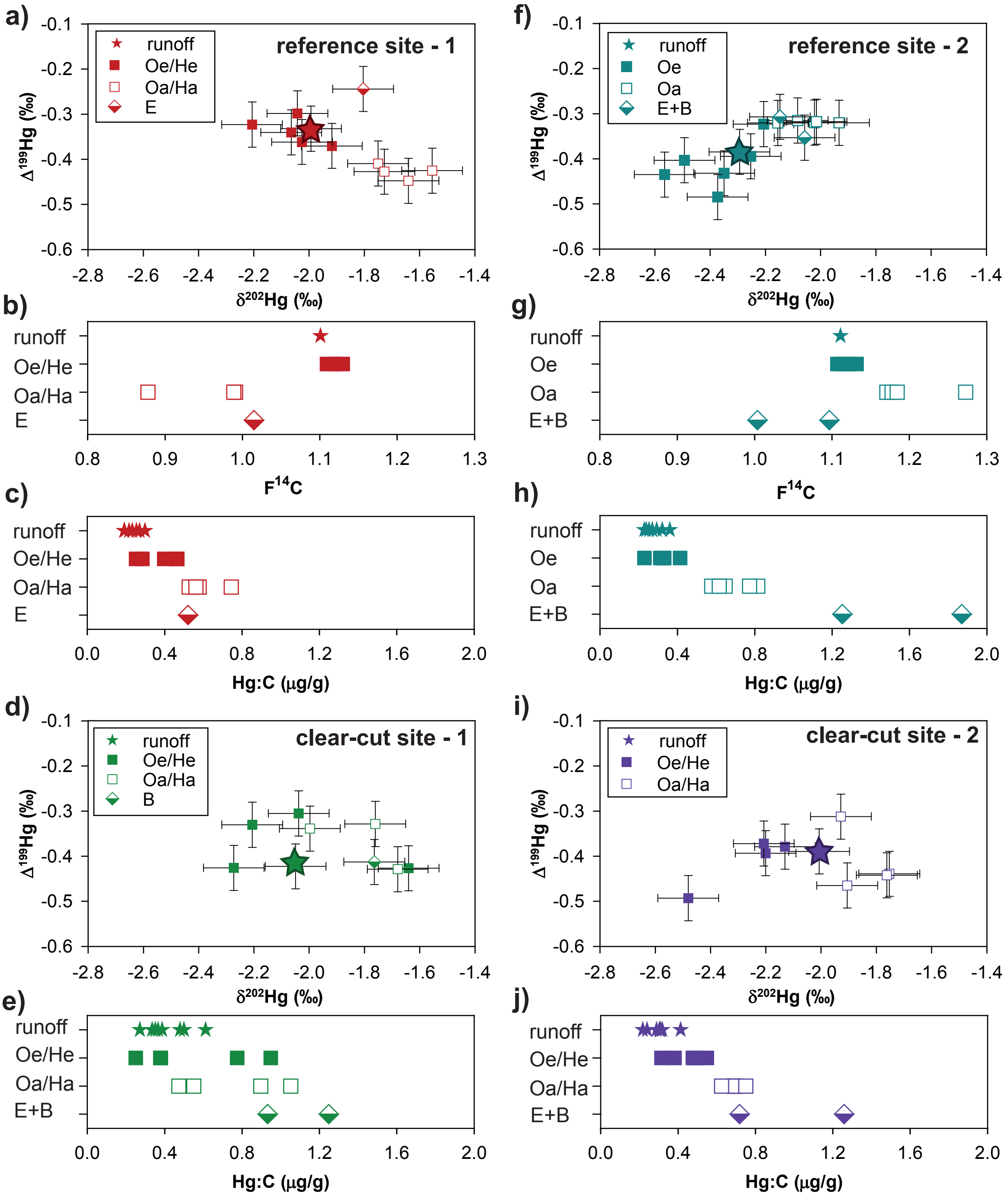

Figure 3.2: Water sample results (stars) of catchment runoff in comparison with major pools of boreal forest soils at four sites, two intact forests (reference site 1 and 2) and two harvested forest sites (clearcut site 1 and 2): Hg isotope signatures (δ^{202}Hg vs. Δ^{199}Hg, panels a, d, f and i), radiocarbon signature (F^{14}C, panels b and g) and Hg to carbon ratio (Hg:C, panels c, e, h and j).

3.4 Discussion

3.4.1 Hg isotope signatures

The δ^{202}Hg and Δ^{199}Hg signatures of the runoff samples were in the range of the Hg isotope signatures measured in the soils of the same boreal forest catchments[32] and consistent with other observations on soils, generally reporting negative δ^{202}Hg and Δ^{199}Hg.[31,44,45]

All runoff data were well described by a mixing of Hg isotope signatures from different soil horizons. The results of the mixing model suggest that for most of the sites the majority of the Hg originates from the surface Oe/He horizons with 71±17% and 58±18% for the reference sites 1 and 2, and 55±25% and 48±22% for the clear-cut sites 1 and 2, respectively (Figure 3.3, Table S3.6). The remaining fraction (28% - 52%) originated from the deeper more humified organic Ha/Oa horizon (12% - 52%) and the mineral E+B horizon (16% - 22%) (Table S3.6). The calculated relative contributions of the Oa/Ha and E+B horizons, however, have to be interpreted with caution, since their Hg isotope signatures were statistically indistinguishable.

Precipitation was previously observed to have a Hg isotope signature (δ^{202}Hg= 0.5‰ to -1.7‰ and Δ^{199}Hg=1.1‰ to -0.1‰, 5- to 95-percentile, <25 ng L^{-1}, n=58)[27–31] which is distinct from the soil and runoff samples. Thus, the contribution of precipitation to the runoff was not significant for the analyzed samples, which were all taken on days with no precipitation (Figure S3.2).

Potentially, the Hg in the catchment runoff could be affected by Hg isotope fractionation caused by secondary processes resulting in an offset of the runoff isotope signature compared to the soils. In case the mobilization of Hg from the soil would be controlled by an exchange of Hg between soil organic matter (SOM) and DOC, involving inorganic Hg(II) complexes in solution, an enrichment of heavy isotopes in the dissolved phase would be expected as observed for Hg(II) sorption to thiol-groups.[37] However, the process of Hg desorption from natural organic matter (NOM) has been shown to be very slow,[46] and therefore it appears more plausible that Hg is mobilized from soils while associated with NOM during DOC formation. Reductive loss of Hg during transport from the soil to the runoff could represent another plausible cause for Hg isotope fractionation; however, all known reduction mechanisms cause an enrichment of lighter isotopes in the reduced Hg^0 phase.[47–49] Because both potential secondary processes would lead to heavier δ^{202}Hg isotope signatures in the runoff, we see no evidence for secondary processes in the soil runoff characterized by relatively light δ^{202}Hg values (δ^{202}Hg=-1.99‰ to -2.29‰).

Therefore, we suggest that the Hg isotope signature in the runoff reflects the sources in the soils and that they can be used as tracer to elucidate source and flow pathways of Hg.

The sample of the larger stream (LillC), draining a larger catchment area including all four forest sites studied here, and the sample from the inlet to the lake (VK-Inlet, Västa Kotrinvattnet) had a Hg isotope signature similar to the first-order streams in the forest catchments (Table 3.2). Using a mixing model incorporating the source of precipitation,[32] we calculated only a small contribution of precipitation-derived Hg in the samples representing the larger catchment areas of 5±3% for LillC, 11±6% for VK-inlet and 15±10% for VK-outlet. Thus, the major fraction of 85% - 95% was attributed to terrestrial runoff from boreal forest soils. Significant anomalies on the even-mass isotopes (Δ^{200}Hg=0.27‰, average) were reported for precipitation.[27–31] The low contribution of precipitation-derived Hg in the runoff samples is thus in agreement with the absence of Δ^{200}Hg anomalies measured in the catchment runoff and lake samples. The difference in Δ^{199}Hg between the lake inlet (VK-inlet, Δ^{199}Hg = -0.25‰) and the lake outlet sample (VK-outlet, Δ^{199}Hg = 0.04‰) suggests that secondary photochemical processes have occurred, previously reported to cause large MIF,[26,47,50] taking place in the lake due to exposure to sunlight. Photochemical reduction of Hg(II) in the lake and a subsequent re-emission of volatile Hg^0 to the atmosphere represents a likely cause. It would require a reductive loss of ≈35±15% of Hg in the water body based on published fractionation factors for Hg(II) photoreduction in the presence of DOC[47] to cause the observed change in Δ^{199}Hg.

3.4.2 Radiocarbon signatures

The radiocarbon signature mixing model suggests that the DOC in the runoff is dominated by the surface horizon with 84±12% Oe/He and 64±28% Oe for reference site 1 and 2, respectively. The contribution of the underlying Oa/Ha horizons was calculated to be 8±10% and 16±17% for reference site 1 and 2, respectively. The modeled contribution of the mineral horizons (8±8% and 20±19% for reference site 1 and 2, respectively) might be overestimated due to the fact that the carbon concentrations in the mineral horizons were relatively low (10 to 50 g kg^{-1}) compared to the organic horizons (300 to 500 g kg^{-1}) but carbon pool sizes were not considered in the mixing model. The high fraction of DOC in runoff originating from Oe/He horizons is in agreement with a lysimeter study, reporting that Oe horizons of Podzols are the dominant source for DOC in soil leachates.[51]

Another study on boreal spruce forests in Sweden, however, indicated that DOC in soil solution collected from mineral B horizons was derived from the mineral horizon itself.[52] Despite the fact that there are large stocks of old carbon (100 to 1000 years) mainly in Ha horizons of Histosols,[32] the runoff was characterized by the presence of post-bomb carbon ($F^{14}C > 1$), and thus dominated by young DOC from the Oe/He horizons, in agreement with previous findings based on radiocarbon signatures.[53–55]

3.4.3 Hg:C ratios

Dissolved organic carbon (DOC) has a governing role for the mobility of Hg in soils, based on the high binding affinity of thiol groups in organic matter for Hg(II).[7] Several studies observed a correlation between dissolved Hg concentration and DOC concentration.[8–12,56] Based on this correlation, it has been suggested to trace the origin of Hg to soil horizons by comparing the Hg:C ratios in the runoff with Hg:C ratios of the solid phases.[8] However, other studies have observed independent dynamics of Hg and DOC, e.g., after snowmelt.[57] We observed an increase of the Hg:C ratios with soil depth, similar to previous observations.[6,8,58–60] Using the different Hg:C ratios in the soil horizons and runoff samples, we calculated contributions of Hg derived from the surface Oe/He horizons of 86±11% and 91±10% for reference sites 1 and 2, and 66±26% and 78±25% for clear-cut sites 1 and 2, respectively. The contributions of Oe/He horizons were consistently higher than the results from the Hg stable isotope and radiocarbon tracing approaches. There are several possible causes for this discrepancy between the different tracer approaches. The Hg:C ratio of the runoff used in the model reflects 8-9 measurements over the course of one year, whereas the Hg stable isotope signatures and radiocarbon signatures were measured on a single sampling occasion only. This could indicate that the contribution of Hg from the Oe/He topsoil is higher over the year as compared to the single sampling event in September 2012 exhibiting base-flow conditions. Second, there are indications for a systematic difference between Hg:C ratios in the solid phase compared to a lower Hg:C ratio in the solution phase (Figure S3.3), which would lead to an overestimation of the contribution from Oe/He horizons. A lower Hg:C ratio in the solution phase compared to Hg:C ratio of the soil could indicate the presence of HgS particles or Hg associated with FeS particles in the soil, exhibiting a very low solubility.[34]

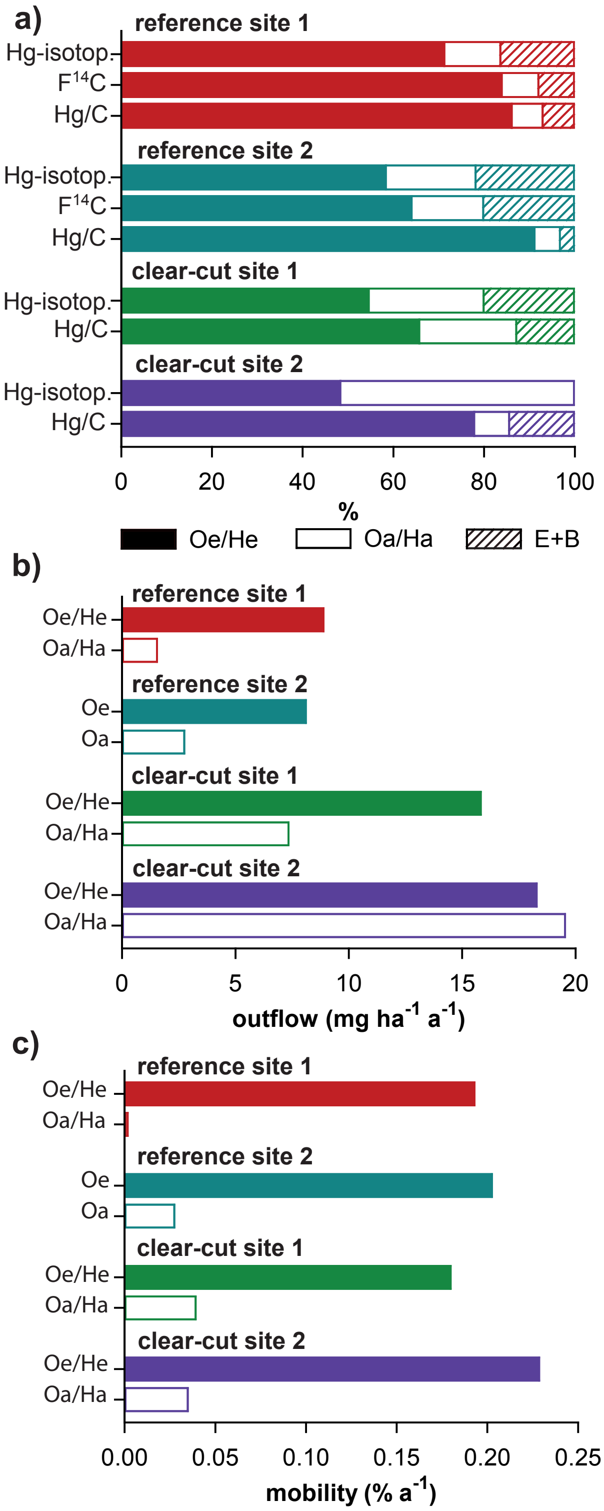

Figure 3.3: Role of soil horizons in catchment runoff: **(a)** contribution of soil horizons to catchment runoff based on Hg isotope signature, radiocarbon ($F^{14}C$) and Hg:C ratio as source tracer; **(b)** Hg outflow based on soil horizons based on Hg isotope signatures; **(c)** mobility relative to Hg pool sizes in different soil horizons.

3.4.4 Controls on Hg in boreal forest runoff

The modeled source contributions of Hg isotopes, a tracer for the Hg source, the radiocarbon signature, a tracer for the DOC source, and the Hg:C ratio were in good agreement (Figure 3.3a), suggesting a strong control of DOC dynamics on the mobilization of Hg. The samples were taken in September 2012 during base-flow conditions, where the DOC in the stream runoff is dominated by the riparian zone.[63] Based on the relatively constant Hg:C ratio over the whole sampling period (Figure S3.3, Table S3.4), we assumed that the temporal variability in the Hg source during base-flow conditions was limited. Using total Hg export calculations (Table S3.5),[17] we calculated the specific outflow for each organic horizon based on the source contribution modeled with the Hg isotope signatures (Figure 3.3b). The output of the Oe/He horizons was almost identical with 8.9 and 8.1 mg ha^{-1} a^{-1} for reference site 1 and 2, respectively. The outflow of the underlying Oa/Ha horizon was substantially lower (1.5 and 2.7 mg ha^{-1} a^{-1} for reference site 1 and 2, respectively). Based on estimates for the Hg pool sizes in the soils (Table S3.5),[17] we calculated the mobility of Hg from the different soil horizons as percentage of the annual outflow relative to the total soil horizon pool (Figure 3.3c). The organic topsoil horizons Oe/He showed a similar mobility at all four investigated sites of $\approx$0.2 % a^{-1}. The mobility of the underlying organic horizons was at least 5 times lower with $\approx$0.03 % a^{-1} for reference site 2 and the two clear-cut sites, and $\approx$0.002 % a^{-1} for reference site 1. The Oa/Ha horizons were characterized by a higher degree of humification, and might therefore have a reduced potential for mobilization of DOC and Hg. Furthermore, the hydraulic conductivity of boreal soils has been reported to decrease with soil depth, allowing higher lateral flow in the uppermost soil horizons.[64–67] The very low Hg mobility in the Histosol Ha horizon at reference site 1 could be related to an expected low hydrological connectivity of the horizon,[63] hampering the transport of water through the Ha horizon to the runoff. In contrast, the expected higher hydrological connectivity of Oe and Oa horizons of Podzols at reference site 2 can be assumed to allow transport. This would be in line with the constant fraction of precipitation-derived Hg in the Histosol profiles, compared to an accumulation of precipitation-derived Hg over time through vertical infiltration in the Podzol profiles.[32]

3.4.5 Effects of forest harvest

The harvesting of forest by clear-cutting has been shown to have significant effects on methyl-Hg concentrations in the catchment runoff and in biota of the associated aquatic ecosystems,[10,14–16] which was the focus of an accompanying study.[17] Forest clear-cut and site preparation has been shown to enhance the DOC mobilization and runoff flux compared to intact reference sites.[68,69] Higher Hg/DOC ratios in the runoff of clear-cut sites compared to reference sites have been observed in a comparison study of 47 forest stands in Sweden.[10] The increase of Hg:C ratio after clear-cut was explained by the mobilization of dissolved or colloidal HgS.[10] A recent long-term study, however, did not observe any changes in Hg:C ratio after forest harvest or site preparation.[70] Also a one-year survey at 20 forest catchments including the ones of this study did not reveal any statistically significant differences in Hg:C ratios between clear-cut and reference sites.[17] The Hg isotope signatures in the runoff of clear-cut sites indicated a higher contribution of Hg from underlying Oa/Ha horizons ($\approx$50%) as compared to the reference sites. This might suggest that forest harvest action led to an enhanced mobilization of Hg and DOC from underlying horizons. Since Hg:C ratios in the Oa/Ha horizons were higher than in Oe/He horizons, this offers an alternative explanation for higher Hg/DOC ratios observed in the runoff. In particular for forests with Histosols, where Ha horizons of reference sites exhibited a very low mobility (reference site 1, Figure 3.3c), the soil disturbance and mixing of deeper soil horizons by site scarification after harvest could potentially mobilize Hg, otherwise sequestered for long timescales under natural conditions. Similarly, radiocarbon signatures revealed a mobilization of old carbon from peat soils impacted by land-use change.[55] Furthermore, forest clear-cut was shown to cause warmer and wetter soil conditions, affecting the DOC mobilization and thus likely also Hg mobilization.[69] The rise in groundwater table, originating from a reduced evapotranspiration by the removal of the trees after the clear-cut,[16,69] could have led to a change in hydrological conditions increasing the lateral flow through the Ha horizons.[67]

3.4.6 Implications for the transport of terrestrial Hg to aquatic ecosystems

The development of the analytical method based on ultrafiltration pre-enrichment to measure Hg isotope signatures in natural waters with high DOC concentrations allowed us to perform the first investigation of Hg stable isotope signatures during transport of Hg from terrestrial to aquatic ecosystems. The fact that there was no evidence for Hg isotope fractionation during the transfer from soils to waters has important implications for the use of Hg isotopes in aquatic ecosystem studies and global cycling studies in general. If this finding would be consistent in other ecosystems beyond boreal forest catchments, measurements of Hg isotope signatures in terrestrial pools could be used as input source to aquatic ecosystems. Furthermore, the relatively constant Hg isotope signature measured in all runoff samples will allow using Hg isotopes for tracing different source contributions and transformation processes in aquatic systems, as illustrated for the example of the lake sample indicating photochemical reduction. The measurement of Hg isotope signatures in aqueous systems and the absence of Hg fractionation between terrestrial and aquatic systems closes an important knowledge gap towards incorporating MDF in global Hg isotope models,[71] allowing for a better understanding of Hg fluxes between terrestrial and aquatic ecosystems and the atmosphere in the future.

The high mobilization potential for Hg and DOC in organic topsoils, leading to a dominating contribution of Hg derived from the Oe/He topsoils in boreal soil runoff, suggests a response time of several decades to changes in atmospheric Hg deposition. Given that the uppermost organic horizons of Podzols and Histosols (Oe/He) have a mean radiocarbon age of ≈20 years, a decrease in atmospheric Hg deposition as a result of reduced anthropogenic Hg emissions can be expected to result in reduced Hg concentrations in terrestrial runoff with a lag phase of up to several decades. Soil disturbance, like e.g., forest harvest and site preparation might however counteract these trends and mobilize deeper sequestered Hg. The combination of Hg isotope signatures with radiocarbon signatures and Hg:C ratios provides a tool to further investigate the pathways of Hg and DOC from terrestrial to aquatic ecosystems, to quantify the source, and predict terrestrial Hg runoff in the future.

Acknowledgments

We would like to thank Kurt Barmettler for support in the soil chemistry laboratory and Colin Maden and Robin Smith for assistance in the isotope geochemistry laboratory. We are grateful to Urs Menet, Donat Niederer, Daniel Schnarwiler and Andreas Suesli for their help in the manufacturing of the two-stage combustion oven. We thank Irka Hajdas for measuring the radiocarbon signatures and Markus Meili for measuring Hg concentrations in water samples. We thank Alexander Brunner, Christa Bodmer, and Alexandra Metzger for help with sample preparation and concentration analyses. We acknowledge Daniel Obrist for helpful discussions. This research was funded by ETH

Zurich (research grant ETH-15 09-2) and the Swedish Research Council for Environment and Spatial Planning (FORMAS, no. 29-2009-1207).

References

[1] C. T. Driscoll, R. P. Mason, H. M. Chan, D. J. Jacob, and N. Pirrone. Mercury as a global pollutant: sources, pathways, and effects. *Environ. Sci. Technol.*, 47(10):4967–4983, 2013.

[2] J. Munthe, I. Wangberg, S. Rognerud, E. Fjeld, M. Verta, P. Porvari, and M. Meili. *Mercury in nordic ecosystems.* IVL Swedish Environmental Research Institute Ltd., 2007.

[3] R. C. Harris, J. W. M. Rudd, M. Amyot, C. L. Babiarz, K. G. Beaty, P. J. Blanchfield, R. A. Bodaly, B. A. Branfireun, C. C. Gilmour, J. A. Graydon, A. Heyes, H. Hintelmann, J. P. Hurley, C. A. Kelly, D. P. Krabbenhoft, S. E. Lindberg, R. P. Mason, M. J. Paterson, C. L. Podemski, A. Robinson, K. A. Sandilands, G. R. Southworth, V. L. S. Louis, and M. T. Tate. Whole-ecosystem study shows rapid fish-mercury response to changes in mercury deposition. *Proc. Natl. Acad. Sci. U.S.A.*, 104(42):16586–16591, 2007.

[4] N. V. Smith-Downey, E. M. Sunderland, and D. J. Jacob. Anthropogenic impacts on global storage and emissions of mercury from terrestrial soils: Insights from a new global model. *J. Geophys. Res.*, 115, 2010.

[5] UNEP. Minamata convention on mercury, united nations environment programme, 2013, (http://www.mercuryconvention.org).

[6] C. J. Oswald, A. Heyes, and B. A. Branfireun. Fate and transport of ambient mercury and applied mercury isotope in terrestrial upland soils: insights from the METAALICUS watershed. *Environ. Sci. Technol.*, 48(2):1023–31, 2014.

[7] U. Skyllberg, P. R. Bloom, J. Qian, C. M. Lin, and W. F. Bleam. Complexation of mercury(II) in soil organic matter: EXAFS evidence for linear two-coordination with reduced sulfur groups. *Environ. Sci. Technol.*, 40(13):4174–4180, 2006.

[8] S. Akerblom, M. Meili, L. Bringmark, K. Johansson, D. Kleja, and B. Bergkvist. Partitioning of Hg between solid and dissolved organic matter in the humus layer of boreal forests. *Water Air Soil Pollut.*, 189(1-4):239–252, 2008.

[9] J. A. Dittman, J. B. Shanley, C. T. Driscoll, G. R. Aiken, A. T. Chalmers, and J. E. Towse. Ultraviolet absorbance as a proxy for total dissolved mercury in streams. *Environ. Pollut.*, 157(6):1953–1956, 2009.

[10] U. Skyllberg, M. B. Westin, M. Meili, and E. Bjorn. Elevated concentrations of methyl mercury in streams after forest clear-cut: A consequence of mobilization from soil or new methylation? *Environ. Sci. Technol.*, 43(22):8535–8541, 2009.

[11] A. L. Riscassi and T. M. Scanlon. Controls on stream water dissolved mercury in three mid-Appalachian forested headwater catchments. *Water Resour. Res.*, 47, 2011.

[12] J. D. Demers, J. B. Yavitt, C. T. Driscoll, and M. R. Montesdeoca. Legacy mercury and stoichiometry with C, N, and S in soil, pore water, and stream water across the upland-wetland interface: The influence of hydrogeologic setting. *J. Geophys. Res.-Biogeo.*, 118(2):825–841, 2013.

[13] S. Jonsson, U. Skyllberg, M. B. Nilsson, E. Lundberg, A. Andersson, and E. Bjorn. Differentiated availability of geochemical mercury pools controls methylmercury levels in estuarine sediment and biota. *Nat. Commun.*, 5:4624, 2014.

[14] E. Garcia and R. Carignan. Impact of wildfire and clear-cutting in the boreal forest on methyl mercury in zooplankton. *Can. J. Fish. Aquat. Sci.*, 56(2):339–345, 1999.

[15] E. Garcia and R. Carignan. Mercury concentrations in northern pike (Esox lucius) from boreal lakes with logged, burned, or undisturbed catchments. *Can. J. Fish. Aquat. Sci.*, 57:129–135, 2000.

[16] K. Bishop, C. Allan, L. Bringmark, E. Garcia, S. Hellsten, L. Hogbom, K. Johansson, A. Lomander, M. Meili, J. Munthe, M. Nilsson, P. Porvari, U. Skyllberg, R. Sorensen, T. Zetterberg, and S. Akerblom. The effects of forestry on Hg bioaccumulation in nemoral/boreal waters and recommendations for good silvicultural practice. *Ambio*, 38(7):373–380, 2009.

[17] R.M. Kronberg. *The Boreal Journey of Methyl Mercury- From Forest Harvest to Black Alder Swamps.* PhD thesis, Swedish University of Agricultural Sciences, 2014.

[18] D. B. Senn, E. J. Chesney, J. D. Blum, M. S. Bank, A. Maage, and J. P. Shine. Stable isotope (N, C, Hg) study of methylmercury sources and trophic transfer in the northern gulf of Mexico. *Environ. Sci. Technol.*, 44(5):1630–1637, 2010.

[19] V. Perrot, V. N. Epov, M. V. Pastukhov, V. I. Grebenshchikova, C. Zouiten, J. E. Sonke, S. Husted, O. F. X. Donard, and D. Amouroux. Tracing sources and bioaccumulation of mercury in fish of lake Baikal- Angara river using Hg isotopic composition. *Environ. Sci. Technol.*, 44(21):8030–8037, 2010.

[20] G. E. Gehrke, J. D. Blum, D. G. Slotton, and B. K. Greenfield. Mercury isotopes link mercury in San Francisco bay forage fish to surface sediments. *Environ. Sci. Technol.*, 45(4):1264–1270, 2011.

[21] S. Y. Kwon, J. D. Blum, C. Y. Chen, D. E. Meattey, and R. P. Mason. Mercury isotope study of sources and exposure pathways of methylmercury in estuarine food webs in the northeastern U.S. *Environ Sci Technol*, 48(17):10089–97, 2014.

[22] M. T. Tsui, J. D. Blum, S. Y. Kwon, J. C. Finlay, S. J. Balogh, and Y. H. Nollet. Sources and transfers of methylmercury in adjacent river and forest food webs. *Environ. Sci. Technol.*, 46(20):10957–64, 2012.

[23] M. T. Tsui, J. D. Blum, J. C. Finlay, S. J. Balogh, Y. H. Nollet, W. J. Palen, and M. E. Power. Variation in terrestrial and aquatic sources of methylmercury in stream predators as revealed by stable mercury isotopes. *Environ. Sci. Technol.*, 48(17):10128–10135, 2014.

[24] J. B. Chen, H. Hintelmann, and B. Dimock. Chromatographic pre-concentration of Hg from dilute aqueous solutions for isotopic measurement by MC-ICP-MS. *J. Anal. At. Spectrom.*, 25(9):1402–1409, 2010.

[25] M. Strok, H. Hintelmann, and B. Dimock. Development of pre-concentration procedure for the determination of Hg isotope ratios in seawater samples. *Analytica Chimica Acta*, (DOI: 10.1016/j.aca.2014.09.005).

[26] L. S. Sherman, J. D. Blum, K. P. Johnson, G. J. Keeler, J. A. Barres, and T. A. Douglas. Mass-independent fractionation of mercury isotopes in Arctic snow driven by sunlight. *Nat. Geosci.*, 3(3):173–177, 2010.

[27] L. E. Gratz, G. J. Keeler, J. D. Blum, and L. S. Sherman. Isotopic composition and fractionation of mercury in great lakes precipitation and ambient air. *Environ. Sci. Technol.*, 44(20):7764–7770, 2010.

[28] J-B. Chen, H. Hintelmann, X. Feng, and B. Dimock. Unusual fractionation of both odd and even mercury isotopes in precipitation from Peterborough, ON, Canada. *Geochim. Cosmochim. Acta*, 90(0):33–46, 2012.

[29] L. S. Sherman, J. D. Blum, G. J. Keeler, J. D. Demers, and J. T. Dvonch. Investigation of local mercury deposition from a coal-fired power plant using mercury isotopes. *Environ. Sci. Technol.*, 46(1):382–390, 2012.

[30] P. M. Donovan, J. D. Blum, D. Yee, G. E. Gehrke, and M. B. Singer. An isotopic record of mercury in San Francisco bay sediment. *Chem. Geol.*, 349(0):87–98, 2013.

[31] J. D. Demers, J. D. Blum, and D. R. Zak. Mercury isotopes in a forested ecosystem: Implications for air-surface exchange dynamics and the global mercury cycle. *Glob. Biogeochem. Cycles*, 27(1):222–238, 2013.

[32] M. Jiskra, J. G. Wiederhold, U. Skyllberg, R.M. Kronberg, I. Hajdas, and R. Kretzschmar. Mercury isotopes reveal organic matter-driven reductive Hg loss from boreal forest soils. submitted.

[33] IUSS Working Group WRB. 2014. World Reference Base for Soil Resources 2014. International soil classification system for naming soils and creating legends for soil maps. Technical Report World Soil Resources Reports No. 106, FAO, Rome.

[34] U. Skyllberg. *Chemical speciation of mercury in soil and sediment*, pages 219–258. John Wiley & Sons, 2012.

[35] C. L. Babiarz, J. P. Hurley, S. R. Hoffmann, A. W. Andren, M. M. Shafer, and D. E. Armstrong. Partitioning of total mercury and methylmercury to the colloidal phase in freshwaters. *Environ. Sci. Technol.*, 35(24):4773–4782, 2001.

[36] M. Jiskra, J. G. Wiederhold, B. Bourdon, and R. Kretzschmar. Solution speciation controls mercury isotope fractionation of Hg(II) sorption to goethite. *Environ. Sci. Technol.*, 46(12):6654–62, 2012.

[37] J. G. Wiederhold, C. J. Cramer, K. Daniel, I. Infante, B. Bourdon, and R. Kretzschmar. Equilibrium mercury isotope fractionation between dissolved Hg(II) species and thiol-bound Hg. *Environ. Sci. Technol.*, 44(11):4191–4197, 2010.

[38] J. Blum and B. Bergquist. Reporting of variations in the natural isotopic composition of mercury. *Anal. Bioanal. Chem.*, 388(2):353–359, 2007.

[39] T. B. Coplen. Guidelines and recommended terms for expression of stable-isotope-ratio and gas-ratio measurement results. *Rapid Commun. Mass Spectrom.*, 25(17):2538–2560, 2011.

[40] N. Estrade, J. Carignan, J. E. Sonke, and O. F. X. Donard. Mercury isotope fractionation during liquid-vapor evaporation experiments. *Geochim. Cosmochim. Acta*, 73(10):2693–2711, 2009.

[41] R. S. Smith, J. G. Wiederhold, A. D. Jew, G. E. Brown Jr, B. Bourdon, and R. Kretzschmar. Small-scale studies of roasted ore waste reveal extreme ranges of stable mercury isotope signatures. *Geochim. Cosmochim. Acta*, 137(0):1–17, 2014.

[42] L. Wacker, G. Bonani, M. Friedrich, I. Hajdas, B. Kromer, M. Nemec, M. Ruff, M. Suter, H. A. Synal, and C. Vockenhuber. Micadas: routine and high-precision radiocarbon dating. *Radiocarbon*, 52(2):252–262, 2010.

[43] P. J. Reimer, T. A. Brown, and R. W. Reimer. Discussion: Reporting and calibration of post-bomb C-14 data. *Radiocarbon*, 46(3):1299–1304, 2004.

[44] A. Biswas, J. D. Blum, B. A. Bergquist, G. J. Keeler, and Z. Q. Xie. Natural mercury isotope variation in coal deposits and organic soils. *Environ. Sci. Technol.*, 42(22):8303–8309, 2008.

[45] H. Zhang, R. S. Yin, X. B. Feng, J. Sommar, C. W. Anderson, A. Sapkota, X. W. Fu, and T. Larssen. Atmospheric mercury inputs in montane soils increase with elevation: evidence from mercury isotope signatures. *Sci. Rep.*, 3:3322, 2013.

[46] M. Jiskra, D. Saile, J. G. Wiederhold, B. Bourdon, E. Bjorn, and R. Kretzschmar. Kinetics of Hg(II) exchange between organic ligands, goethite, and natural organic matter studied with an enriched stable isotope approach. *Environ. Sci. Technol.*, page DOI:10.1021/es503483m, 2014.

[47] B. A. Bergquist and J. D. Blum. Mass-dependent and -independent fractionation of Hg isotopes by photoreduction in aquatic systems. *Science*, 318(5849):417–420, 2007.

[48] K. Kritee, J. D. Blum, M. W. Johnson, B. A. Bergquist, and T. Barkay. Mercury stable isotope fractionation during reduction of Hg(II) to Hg(0) by mercury resistant microorganisms. *Environ. Sci. Technol.*, 41(6):1889–1895, 2007.

[49] W. Zheng and H. Hintelmann. Nuclear field shift effect in isotope fractionation of mercury during abiotic reduction in the absence of light. *J. Phys. Chem. A*, 114(12):4238–4245, 2010.

[50] W. Zheng and H. Hintelmann. Isotope fractionation of mercury during its photochemical reduction by low-molecular-weight organic compounds. *J. Phys. Chem. A*, 114(12):4246–4253, 2010.

[51] M. Froberg, D. Berggren, B. Bergkvist, C. Bryant, and H. Knicker. Contributions of Oi, Oe and Oa horizons to dissolved organic matter in forest floor leachates. *Geoderma*, 113(3-4):311–322, 2003.

[52] M. Froberg, D. Berggren, B. Bergkvist, C. Bryant, and J. Mulder. Concentration and fluxes of dissolved organic carbon (DOC) in three norway spruce stands along a climatic gradient in Sweden. *Biogeochemistry*, 77(1):1–23, 2006.

[53] S. L. Schiff, R. Aravena, S. E. Trumbore, M. J. Hinton, R. Elgood, and P. J. Dillon. Export of DOC from forested catchments on the precambrian shield of central Ontario: Clues from C-13 and C-14. *Biogeochemistry*, 36(1):43–65, 1997.

[54] S. M. Palmer, D. Hope, M. F. Billett, J. J. C. Dawson, and C. L. Bryant. Sources of organic and inorganic carbon in a headwater stream: Evidence from carbon isotope studies. *Biogeochemistry*, 52(3):321–338, 2001.

[55] C. J. Hulatt, H. Kaartokallio, M. J. Oinonen, E. Sonninen, C. A. Stedmon, and D. N. Thomas. Radiocarbon dating of fluvial organic matter reveals land-use impacts in boreal peatlands. *Environ. Sci. Technol.*, DOI:10.1021/es5030004, 2014.

[56] C. J. Oswald and B. A. Branfireun. Antecedent moisture conditions control mercury and dissolved organic carbon concentration dynamics in a boreal headwater catchment. *Water Resour. Res.*, 50(8):6610–6627, 2014.

[57] J. Schelker, D. A. Burns, M. Weiler, and H. Laudon. Hydrological mobilization of mercury and dissolved organic carbon in a snow-dominated, forested watershed: Conceptualization and modeling. *J. Geophys. Res.-Biogeosci.*, 116, 2011.

[58] D. Obrist, D. W. Johnson, and S. E. Lindberg. Mercury concentrations and pools in four Sierra Nevada forest sites, and relationships to organic carbon and nitrogen. *Biogeosciences*, 6(5):765–777, 2009.

[59] D. Obrist, D. W. Johnson, S. E. Lindberg, Y. Luo, O. Hararuk, R. Bracho, J. J. Battles, D. B. Dail, R. L. Edmonds, R. K. Monson, S. V. Ollinger, S. G. Pallardy, K. S. Pregitzer, and D. E. Todd. Mercury distribution across 14 US forests. Part I: Spatial patterns of concentrations in biomass, litter, and soils. *Environ. Sci. Technol.*, 45(9):3974–3981, 2011.

[60] J. I. Juillerat, D. S. Ross, and M. S. Bank. Mercury in litterfall and upper soil horizons in forested ecosystems in Vermont, USA. *Environ. Toxicol. Chem.*, 31(8):1720–1729, 2012.

[61] R. Teisserenc, M. Lucotte, and S. Houel. Terrestrial organic matter biomarkers as tracers of Hg sources in lake sediments. *Biogeochemistry*, 103(1-3):235–244, 2011.

[62] R. Teisserenc, M. Lucotte, R. Canuel, M. Moingt, and D. Obrist. Combined dynamics of mercury and terrigenous organic matter following impoundment of Churchill falls hydroelectric reservoir, Labrador. *Biogeochemistry*, 118(1-3):21–34, 2014.

[63] H. Laudon, M. Berggren, A. Agren, I. Buffam, K. Bishop, T. Grabs, M. Jansson, and S. Kohler. Patterns and dynamics of dissolved organic carbon (DOC) in boreal streams: The role of processes, connectivity, and scaling. *Ecosystems*, 14(6):880–893, 2011.

[64] L. Lundin. *Soil moisture and ground water in till soil and the significance of soil type for runoff.* PhD thesis, Uppsala University, 1982.

[65] A. Rodhe. On the generation of stream runoff in till soils. *Nord. Hydrol.*, 20(1):1–8, 1989.

[66] K. H. Bishop, H. Grip, and A. Oneill. The origins of acid runoff in a hillslope during storm events. *J. Hydrol.*, 116(1-4):35–61, 1990.

[67] K. Bishop, J. Seibert, S. Koher, and H. Laudon. Resolving the double paradox of rapidly mobilized old water with highly variable responses in runoff chemistry. *Hydrol. Process.*, 18(1):185–189, 2004.

[68] J. Schelker, K. Eklof, K. Bishop, and H. Laudon. Effects of forestry operations on dissolved organic carbon concentrations and export in boreal first-order streams. *J. Geophys. Res.-Biogeosci.*, 117, 2012.

[69] J. Schelker, T. Grabs, K. Bishop, and H. Laudon. Drivers of increased organic carbon concentrations in stream water following forest disturbance: Separating effects of changes in flow pathways and soil warming. *J. Geophys. Res.-Biogeosci.*, 118(4):2013JG002309, 2013.

[70] K. Eklof, J. Schelker, R. Sorensen, M. Meili, H. Laudon, C. von Bromssen, and K. Bishop. Impact of forestry on total and methyl-mercury in surface waters: distinguishing effects of logging and site preparation. *Environ. Sci. Technol.*, 48(9):4690–4698, 2014.

[71] J. E. Sonke. A global model of mass independent mercury stable isotope fractionation. *Geochim. Cosmochim. Acta*, 75(16):4577–4590, 2011.

Chapter 4

Solution speciation controls mercury isotope fractionation of Hg(II) sorption to goethite

M. Jiskra, J.G. Wiederhold, B. Bourdon, and R. Kretzschmar, Solution speciation controls mercury isotope fractionation of Hg(II) sorption to goethite. *Environ. Sci. Technol.*, **2012**, 46,12, 6654 - 6662.

Abstract

The application of Hg isotope signatures as tracers for environmental Hg cycling requires the determination of isotope fractionation factors and mechanisms for individual processes. Here, we investigated Hg isotope fractionation of Hg(II) sorption to goethite in batch systems under different experimental conditions. We observed a mass-dependent enrichment of light Hg isotopes on the goethite surface relative to dissolved Hg (ϵ^{202}Hg of -0.30‰ to -0.44‰) which was independent of the pH, chloride and sulfate concentration, type of surface complex, and equilibration time. Based on previous theoretical equilibrium fractionation factors, we propose that Hg isotope fractionation of Hg(II) sorption to goethite is controlled by an equilibrium isotope effect between Hg(II) solution species, expressed on the mineral surface by the adsorption of the cationic solution species. In contrast, the formation of outer-sphere complexes and subsequent conformation changes to different inner-sphere complexes appeared to have insignificant effects on the observed isotope fractionation. Our findings emphasize the importance of solution speciation in metal isotope sorption studies and suggest that the dissolved Hg(II) pool in soils and sediments, which is the most mobile and bioavailable, should be isotopically heavy, as light Hg isotopes are preferentially sequestered during binding to both mineral phases and natural organic matter.

4.1 Introduction

Soils worldwide contain a total pool of 1.15×10^6 tons of Hg and represent the most important terrestrial sink for atmospherically deposited Hg from natural and anthropogenic sources.[1] Mercury in soils can be exported to aquatic environments, re-emitted as Hg^0 to the atmosphere, or methylated under anoxic conditions to form neurotoxic and bioaccumulating methylmercury.[2] However, the largest Hg pool in soils is bound to organic and mineral soil phases, where it is immobilized.[1] In organic topsoils, Hg is mainly bound to reduced organic sulfur groups,[3] whereas in soils and sediments with low organic matter contents, mineral phases such as iron and other metal (oxyhydr)oxides and clay minerals play an important role as sorbents.[4,5] In addition, iron (oxyhydr)oxides form colloidal particles in natural aquatic and terrestrial environments and can thus act as carriers of sorbed metals such as Hg by colloidal transport.[6]

The fractionation of stable Hg isotopes in nature has gained much attention in recent years,[7–9] as it provides a promising tracer for environmental Hg cycling. Mercury isotopes have been shown to exhibit mass-dependent fractionation (MDF) as well as mass-independent fractionation (MIF), caused by nuclear volume fractionation (NVF)[10] or magnetic isotope effect (MIE),[11] together generating a multidimensional isotope signature. To apply stable Hg isotopes as a tool to understand the fate of Hg in the environment, one needs to understand Hg isotope fractionation factors and mechanisms of individual biogeochemical pathways. With this mechanistic information, it will be possible to deconvolute different sources and processes using measured stable Hg isotope ratios in natural samples. So far, Hg isotope fractionation has been studied experimentally for photoreduction of Hg^{2+} and methylmercury,[12,13] abiotic and biotic methylation of Hg,[14,15] abiotic and biotic reduction of Hg^{2+},[16,17] photolytic and microbial methylmercury degradation[18,19] volatilization of elemental liquid Hg,[20,21] and aqueous to gas phase transfer of elemental Hg.[22] In a previous study, we investigated equilibrium isotope fractionation between dissolved Hg(II) species and thiol-bound Hg as a model system for sorption of Hg(II) to natural organic matter.[23] No data are available yet for stable isotope fractionation of Hg sorption to mineral phases. However, stable isotope fractionation during sorption to minerals has been described for other metals. Sorption studies for Cu(II),[24,25] Zn(II),[25,26] and Fe(II)[27,28] to mineral phases (iron and manganese (oxyhydr)oxides) revealed that sorption was in most cases associated with an enrichment of heavy isotopes on mineral surfaces relative to the dissolved phase. The observed isotope fractionation was explained by the lower vibrational frequencies of the sorption complexes with heavy isotopes and thus a lower zero-point energy compared with complexes with light isotopes.[29] In contrast, an isotope fractionation toward light isotopes on the mineral surface for experiments[30] and preliminary Cd data;[31] a mechanistic interpretation is however lacking. Mo(VI) and U(VI), both predominantly present in anionic form, showed a preferential sorption of light isotopes to manganese (oxyhydr)oxides.[32,33] The interpretation of these isotope effects is still under debate: in the case of U(VI), the isotope fractionation was attributed to a change in coordination environment between the dissolved and sorbed phases.[33] For Mo(VI) it has been proposed that the isotope fractionation is caused by an equilibrium isotope effect between different solution species, where only the minor species is actively sorbing.[34,35] However, a newer study postulates a fractionation between the dissolved Mo and a polynuclear surface precipitate.[36]

In this study we present the first data for Hg isotope fractionation during sorption processes to mineral surfaces. Goethite (α-FeOOH) was chosen as the sorbent because it is the most abundant iron (oxyhydr)oxide in soils[37] and Hg(II) sorption to goethite has been studied with both macroscopic[38,39] and spectroscopic[40,41] techniques. The objectives of this study were (i) to investigate stable Hg isotope fractionation associated with sorption of Hg(II) to goethite under different environmentally relevant pH conditions and chloride and sulfate concentrations and after different equilibration times and (ii) to elucidate the mechanisms driving Hg isotope fractionation of sorption on the basis of experimental results, previously presented surface complexation studies, and theoretical calculations for equilibrium fractionation factors of Hg species.

4.2 Experimental section

4.2.1 Materials and reagents

The goethite was synthesized following a standard method (preparation from an alkaline system) described by Schwertmann and Cornell[42] and was already used and characterized in previous studies.[43,44] The structure of the synthesized goethite was confirmed by X-ray diffraction (XRD), and a surface area of 38 m^2 g^{-1} was measured using the N2-BET (Brunauer-Emmett-Teller) method.[43] All chemicals used in this study were analytical grade and used without further treatment, if not indicated otherwise. A detailed list of reagents, chemical impurities, and preparation procedures is provided in the Supporting Information.

Table 4.1: Parameters of the Experimental Series: number of batches in the experimental series (n), goethite concentration (g L^{-1}), initial Hg concentration (μM), pH, solution matrix (MOPS (2.5 mM), SO_4^{2-} (0.95 M), and Cl^- (0.5 mM)), equilibration time (t_{eq}, h), expected dominating Hg(II) surface complex with "b" for bidentate and "m" for monodentate, and isotopic enrichment factors of stable Hg isotopes on the goethite surface relative to the solution for mass-dependent fractionation (ϵ^{202}Hg) and mass-independent fractionation (E^{199}Hg) with 1σ uncertainties.[a]

series	**n**	**goethite concn.** (g L^{-1})	**Hg concn.** (μM)	**pH**	**solution** matrix	$\mathbf{t_{eq}}$ (h)	**Hg(II) surface complex**	ϵ^{202}**Hg** (‰)	σ (‰)	$\boldsymbol{E}^{199}$**Hg** (‰)	σ (‰)
pH	5	5	5	3.1 – 6		72	$b^{40,45}$	-0.37	0.03	0.03	0.011
MGR-18 h	4	0.5 – 20	25	7	MOPS	18	$b^{40,45}$	-0.36	0.03	-0.02	0.013
MGR-72 h	4	0.5 – 20	25	7	MOPS	72	$b^{40,45}$	-0.32	0.03	-0.02	0.013
MGR-720 h	3	0.5 – 9	25	7	MOPS	720	$b^{40,45}$	-0.42	0.04	-0.03	0.015
MGR-sulfate	3	0.5 – 9	25	7	MOPS, SO_4^{2-}	72	m^{41}	-0.30	0.04	0.01	0.015
pH-Cl	3	5	5	5 – 6	Cl^-	72	m^{41}	-0.32	0.04	0.00	0.015
MGR-Cl	3	0.5 – 9	10	7	MOPS, Cl^-	72	m^{41}	-0.44	0.04	-0.03	0.015

[a] See the Supporting Information for details. Each experimental series was performed with different fractions of total Hg sorbed, which was varied by different mercury-to-goethite ratios (MGR series) or by different pH values (pH series).

4.2.2 Batch experiments

Two types of sorption experiments were performed in batch reactors to assess the Hg isotope fractionation at different fractions of the total Hg sorbed to goethite. In the pH series, the sorbed fraction of Hg was varied by adjusting the suspension pH to values between 3.1 and 6, and in the mercury-to-goethite ratio (MGR) series, the ratio between total Hg and goethite was varied at constant pH 7. Goethite (between 0.5 and 20 g L^{-1}; see Table 4.1) was added to acid-washed 30 mL Teflon centrifuge tubes and was dispersed by ultrasonication in 20 mL of matrix solution. The experiments at pH 7 were performed in a buffer solution containing 2.5 mM 3-morpholinopropanesulfonic acid (MOPS), whereas the suspensions in the pH series were unbuffered. Experiments were conducted in the absence and presence of chloride and sulfate, respectively, which influences the speciation of Hg(II) in solution and on the surface.[41,46] For chloride-bearing experiments, the solution matrix contained 0.5 mM NaCl, and for sulfate-bearing experiments, 0.95 M $Na_2SO_4{}^{2-}$ was added, as listed in Table 4.1. The pH was adjusted by titration with diluted HNO_3 or NaOH. Aliquots of a mercury(II) nitrate stock solution were then added to the goethite suspension to yield an initial Hg concentration of 5−25 μM and equilibrated for 18, 72, or 720 h on an end-overend shaker at room temperature in the dark. To separate the sorbed and dissolved pools, the equilibrated samples were centrifuged at 3000 rpm for 15 min. The supernatants were decanted and filtered through 0.2 μm Nylon filters to obtain the dissolved pool. The goethite, containing the sorbed Hg, was dissolved in 6 M HCl at 80 °C. All samples were stabilized with 1% BrCl (v/v) (0.2 M BrCl in HClconcd.) and stored at 4 °C prior to analysis.

4.2.3 Analytical methods

Hg concentrations were measured by cold vapor atomic fluorescence spectrometry (CV-AFS; Millennium Merlin, PS Analytical, U.K.). Samples were diluted to 2.5−25 nM for concentration measurements. Standards prepared in triplicate were reproduced within ±3.6% (2σ), which is reported as the uncertainty of the concentration measurements. Hg isotope ratios were measured by cold vapor generation (HGX-200, Cetac, Omaha, NE, U.S.) coupled to multicollector inductively coupled plasma mass spectrometry (MC-ICPMS; Nu instruments, Wrexham, U.K.). In addition to standard bracketing, mass bias was corrected by Tl addition using a desolvating nebulizer. This method was previously described in detail[23] and further information is provided in the Supporting Information. All isotope ratios of samples and secondary standards were measured relative to NIST-

3133, which was used as the bracketing standard. We report Hg isotope data following the nomenclature suggested by Blum and Bergquist,[47] adapted to recent recommendations of IUPAC:[48]

$$\delta^{202}\mathrm{Hg} = \frac{(^{202}\mathrm{Hg}/^{198}\mathrm{Hg})_{\mathrm{sample}}}{(^{202}\mathrm{Hg}/^{198}\mathrm{Hg})_{\mathrm{NIST-3133}}} - 1 \tag{4.1}$$

$$\Delta^{199}\mathrm{Hg} = \delta^{199}\mathrm{Hg} - (\delta^{202}\mathrm{Hg} \times 0.2520) \tag{4.2}$$

The mass-independent fractionation, expressed here as Δ^{199}Hg, represents the deviation of the isotope ratio from the massdependent fractionation line, where 0.2520 was used as the kinetic mass-dependent scaling factor for δ^{199}Hg, calculated analogously to δ^{202}Hg on the basis of ^{199}Hg/^{198}Hg. Please note that the use of the equilibrium mass-dependent scaling factor (0.2539) would not alter our results in a significant manner, and we decided to use the kinetic factor for reasons of consistency with the nomenclature used in field studies.[47] Our in-house standard (ETH Fluka) was regularly measured between samples and reproduced at $\delta^{202}\mathrm{Hg}_{\mathrm{NIST-3133}}$ = -1.38 ± 0.09‰ and Δ^{199}Hg = +0.08 ± 0.03‰ (2σ, n = 16). For the UM-Almadèn standard (provided by Joel Blum, University of Michigan), we obtained isotope ratios of $\delta^{202}\mathrm{Hg}_{\mathrm{NIST-3133}}$ = -0.55 ± 0.02‰ and Δ^{199}Hg = -0.02 ± 0.05‰ (2σ, n = 4), which are in excellent agreement with published values ($\delta^{202}\mathrm{Hg}_{\mathrm{NIST-3133}}$ = -0.54 ± 0.08‰, Δ^{199}Hg = -0.01 ± 0.05‰ (2σ, n = 4)).[12] Multiple measurements of the mercury(II) nitrate salt used in the sorption experiments resulted in values of $\delta^{202}\mathrm{Hg}_{\mathrm{NIST-3133}}$ = -0.69 ± 0.09‰ and Δ^{199}Hg = +0.01 ± 0.03‰ (2σ, n = 4). The ETH Fluka inhouse standard and mercury(II) nitrate salt were both reproduced within ±0.09‰ (2σ) for δ^{202}Hg and ±0.03‰ (2σ) for Δ^{199}Hg, which are considered to be the analytical precisions for all reported measurements. To simplify further data analysis and presentation, Hg isotope ratios of all experimental data are reported in the following relative to the composition of the mercury(II) nitrate salt used in all experiments, representing the starting condition:

$$\delta^{202}\mathrm{Hg} = \delta^{202}\mathrm{Hg}^{\mathrm{sample}}_{\mathrm{NIST-3133}} - \delta^{202}\mathrm{Hg}^{\mathrm{mercury(II)\ nitrate\ salt}}_{\mathrm{NIST-3133}} \tag{4.3}$$

The fractionation of Hg isotopes on the goethite surface relative to the solution is expressed as enrichment factor ϵ for MDF:

$$\epsilon^{202}\mathrm{Hg}_{\mathrm{sorbed-dissolved}} = \delta^{202}\mathrm{Hg}_{\mathrm{sorbed}} - \delta^{202}\mathrm{Hg}_{\mathrm{dissolved}} \tag{4.4}$$

and as enrichment factor E for MIF:

$$E^{199}\text{Hg} = \epsilon^{199}\text{Hg} - (\epsilon^{202}\text{Hg} \times 0.2520) \tag{4.5}$$

Calculating the enrichment factors (ϵ^{202}Hg and E^{199}Hg) as the difference in the isotope signatures between the sorbed and the dissolved pools averaged over the number of batches in an experimental series (n = 3-5) allowed us to ensure mass balance criteria. The uncertainties of the enrichment factors, reported as 1 standard deviation, σ, were calculated from the error propagation of the difference calculation on the basis of the above-reported analytical precisions (±0.09‰ (2σ) for δ^{202}Hg and ±0.03‰ (2σ) for Δ^{199}Hg). All statistical tests were performed on the basis of a 95% confidence level. Further details on data analysis, mass balance criteria, error propagation, and statistical tests are provided in the Supporting Information.

4.3 Results and discussion

4.3.1 Sorption of Hg to goethite

In accordance with previous studies,[38,39,49] the sorption of Hg(II) to goethite exhibited a strong pH dependence characterized by a distinct increase of the sorbed fraction with increasing pH, for instance, from 15% at pH 3.6 to 64% at pH 5.3 (Figure S4.2, Table S4.4a). Addition of chloride resulted in a pronounced decrease in Hg sorption compared to that in the chloride-free series (Figures S4.2 and S4.3), which is due to the formation of stable Hg(II)-chloro complexes in solution.[46] The variation of the MGR at constant pH 7 resulted in Hg surface coverages between 0.025 and 0.30 μmol m^{-2}. In the MGR-sulfate series, Hg showed a slightly lower sorption affinity compared to that in the series in the absence of chloride and sulfate (Figure S4.3). Comparing the experiments with different equilibration times (18, 72, and 720 h), we observed an increase in the sorbed fraction of about 10-17% between 18 and 720 h of equilibration (Figure S4.4). Similar observations were previously reported for a time series from 2 h up to 8 weeks with an increase in the Hg fraction sorbed to goethite without any clear end point.[50] EXAFS spectroscopy on Hg(II) sorbed to goethite at a surface coverage (Γ) of 0.4 μmol m^{-2} provided no evidence for surface precipitation of Hg.[40,41] As the surface coverage in our experiments never exceeded 0.3 μmol m^{-2}, we conclude that surface precipitation is unlikely and Hg was sorbed as outersphere and/or inner-sphere complexes.

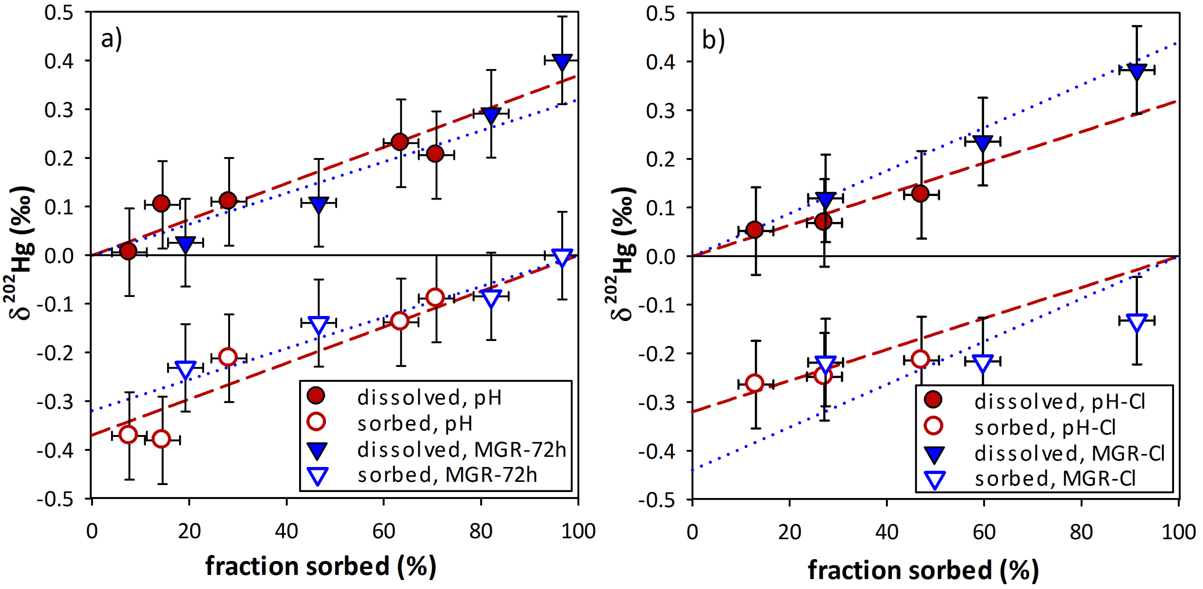

Figure 4.1: δ^{202}Hg of the sorbed (open symbols) and dissolved (closed symbols) pools as a function of the Hg fraction sorbed (%). Experiments in the absence of chloride (**a**) and with 0.5 mM chloride (**b**) were performed with 72 h of equilibration time. The sorbed fraction was varied by changing the pH (pH and pH-Cl series) and by changing the mercury-to-goethite ratio (MGR-72 h and MGR-Cl series). The equilibrium fractionation lines, derived from the calculated enrichment factors (see Table 4.1), are shown as dotted lines for the MGR series and dashed lines for the pH series.

4.3.2 Stable Hg isotope fractionation

In all experiments, Hg sorbed to goethite was found to be enriched in light Hg isotopes. Figure 4.1a displays the δ^{202}Hg isotope signature as a function of the fraction of total Hg which was sorbed to goethite in the experimental series with no chloride and variable pH (pH series, Table 4.1) and for an experimental series with varying mercury-to-goethite ratio (MGR-72 h series). Both data sets exhibited an increase of δ^{202}Hg in the dissolved phase with increasing fraction of sorbed Hg. The sorbed pool was correspondingly enriched in light Hg isotopes, as indicated by negative δ^{202}Hg values. The δ^{202}Hg signatures of the sorbed and dissolved Hg pools in the presence of 0.5 mM chloride followed the same trends (Figure 4.1b). The enrichment factors ϵ^{202}Hg, calculated from the difference between the sorbed and dissolved δ^{202}Hg averaged over the number of batches in one experimental series (n = 3–5), fell in a narrow range between -0.30 ± 0.04‰ and -0.44 ± 0.04‰ (Table 4.1). A statistical test comparing the determined enrichment factors (ϵ^{202}Hg; see the Supporting Information) of the MGR-72 h series in the absence of chloride and the MGR-Cl series with 0.5 mM Cl^- revealed no significant differences. Furthermore, the isotopic results of the two approaches used to vary the fraction of sorbed Hg (pH and MGR series) were not significantly different from each other, both in the absence of chloride and with 0.5 mM Cl^-. Figure 4.2 shows the comparison between the experimental series with 0.95 M sulfate (MGR-sulfate) and with no sulfate (MGR-72 h). The enrichment factors for the MGRsulfate and for the MGR-72 h series (see Table 4.1) were not significantly different from each other. Figure 4.3 shows a time series of Hg(II) sorption to goethite with equilibration times of 18, 72, and 720 h. Even though there was a significant increase in the fraction of sorbed Hg with time (Figure S4.4, Supporting Information), the comparison of the time series revealed no statistically significant difference between their enrichment factors (ϵ^{202}Hg). Therefore, although the adsorption of Hg was continuing, we observed no dependence of the Hg isotope fractionation on the equilibration time. The comparison of two alternative model approaches did not yield conclusive results concerning the reversibility of the sorption process (see the Supporting Information). None of the experimental series showed mass-independent fractionation expressed by E^{199}Hg being significantly different from zero (Figure 4.4b, Table 4.1; Table S4.2, Supporting Information).

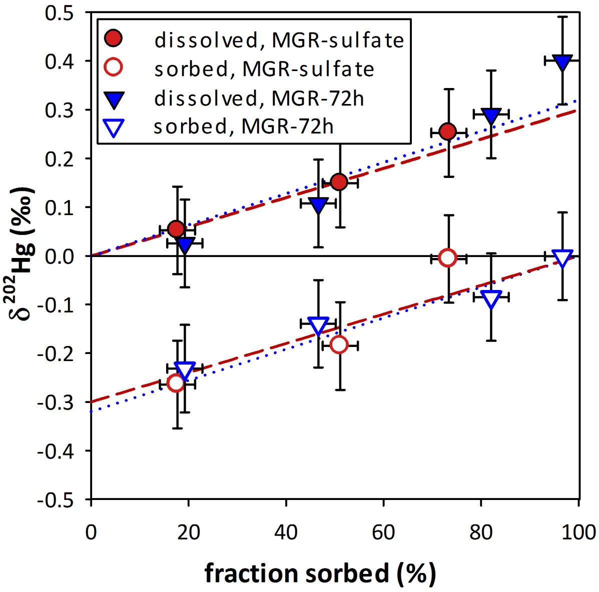

Figure 4.2: δ^{202}Hg of the sorbed (open symbols) and dissolved (closed symbols) pools as a function of the fraction sorbed (%). Experiments were performed with 0.95 M sulfate (circles, MGR-sulfate series) and in the absence of sulfate (triangles, MGR-72 h series). The equilibrium fractionation lines, derived from the calculated enrichment factors, are shown as dashed lines for the MGR-sulfate series and dotted lines for the MGR-72 h series without sulfate (see Table 4.1).

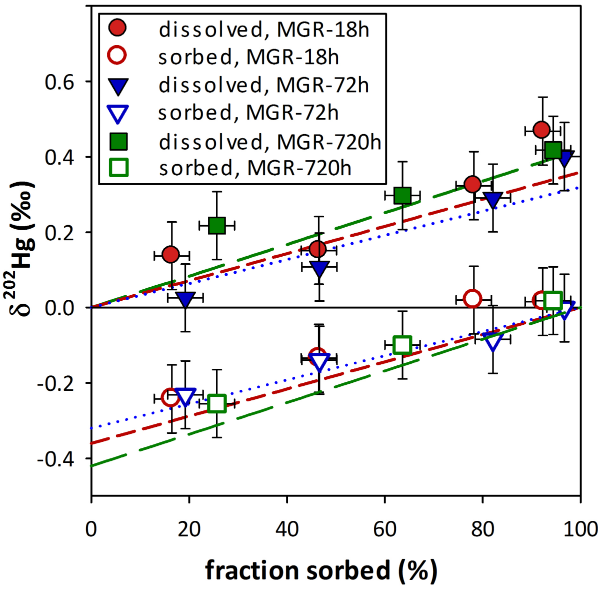

Figure 4.3: Hg isotope fractionation during sorption of Hg(II) to goethite as a function of the equilibration time (18, 72, and 720 h; see Table 1). δ^{202}Hg of the sorbed (open symbols) and dissolved (closed symbols) pools as a function of the fraction sorbed (%). The equilibrium fractionation lines, derived from the calculated enrichment factors, are shown as short-dashed lines for the MGR-18 h series, as dotted lines for the MGR-72 h series, and as long-dashed lines for the MGR-720 h series (see Table 4.1).

4.3.3 Possible Hg isotope fractionation mechanisms

Previous studies identified the cationic Hg(II) species ($HgOH^+$ and $HgCl^+$) as the sorption active solution species as discussed further below.[39,51] Following this, the sorption of Hg(II) to a mineral surface, in this case goethite (α-FeOOH), can be described by the following reaction steps, which all might be potentially associated with an isotopic enrichment (IE):

$$\mathrm{HgL_n} \overset{IE_{SE}}{\longleftrightarrow} \mathrm{HgL_{n-1}}^+ + \mathrm{L}^- \tag{4.6}$$

$$\equiv\mathrm{FeOH} + \mathrm{HgL_{n-1}}^+ \overset{IE_{OS}}{\longleftrightarrow} \equiv\mathrm{FeOH{-}HgL_{OS}}^+ \tag{4.7}$$

$$\equiv\mathrm{FeOH{-}HgL_{OS}}^+ \overset{IE_{IS}}{\longleftrightarrow} \equiv \mathrm{FeOH\text{-}HgL_{IS}} + \mathrm{H}^+ \tag{4.8}$$

Neutral dissolved Hg(II) species (HgL_n) dissociate to the cationic Hg(II) species HgL_{n-1}^+ and the ligand (L^-, in our experiments OH^- or Cl^-) (eq 4.6). This species equilibration (SE) in solution might be associated with an equilibrium isotope effect (IESE). The sorption active Hg(II) cationic species HgL_{n-1}^{+} adsorbs to the goethite surface to form an outer-sphere complex ($\equiv$FeOH—HgL_{OS}^{+}) (eq 4.7) followed by the dehydration of the outer-sphere complex and a deprotonation of the goethite surface hydroxyl group to form an inner-sphere complex ($\equiv$FeO-Hg_{IS}) (eq 4.8). The conformation change between the bonding environment of the Hg(II) cation in solution and the outer-sphere complex could potentially cause an isotopic enrichment (IE_{OS}), as well as the conformation change between the outer-sphere complex and the inner-sphere complex during dehydration (IE_{IS}).

4.3.4 Isotope fractionation during species equilibration in solution (IE_{SE})

Species equilibration under the experimental conditions presented here usually involves hydroxide as the ligand and can therefore be denoted for the most part as hydrolysis, with the exception of the dissociation of $HgCl_2$, where chloride is the leaving ligand. Based on the observed strong correlation between the metal's first hydrolysis constant and the surface complexation constant for metal sorption to mineral surfaces, the concept of hydrolysis as the first reaction step in the adsorption of Hg(II) to goethite was established.[52] Following this, the adsorption of Hg(II) to mineral phases was successfully modeled by the solution concentration of $HgOH^+$ and $HgCl^+$ in the absence and presence of chloride, respectively, which were considered as the sorption active species.[39,51] On the basis of calculations performed using Visual MINTEQ[53] (database NIST 46.7), in the absence of Cl^- and at pH 7, $HgOH^+$ occurs with an abundance of 0.06% and all the remaining Hg is present as $Hg(OH)_2$. With 0.5 mM Cl^- at pH 7, $HgCl^+$ is present with an abundance of 0.006% and the main solution species are $HgClOH^0$ (49.6%), $Hg(OH)_2{}^0$ (37.0%), and $HgCl_2{}^0$ (13.4%). It is important to consider that, after the removal of cationic species from solution by adsorption to surfaces, a re-equilibration takes place which replenishes the small stock of cationic species by dissociation of the dominant neutral Hg(II) species, which is very fast with a dehydration rate constant (k_w) for Hg(II) of 9.3×10^{10} s^{-1}.[54] Thus, the small pool size of the cationic Hg(II) species in solution does not preclude that adsorption of larger amounts of Hg(II) to surfaces can proceed via the positively charged species which exhibit a higher affinity for surface binding. On the basis of this fast equilibration between cationic and neutral Hg species, an equilibrium isotope effect between those species can be transferred to the goethite surface as the low-abundance cations interact dominantly with the mineral surface.

4.3.5 Calculated predictions of MDF and NVF

We calculated the isotopic enrichment factor of cationic species relevant in our experiments on the basis of theoretical equilibrium isotope fractionation factors for individual Hg species relative to elemental Hg vapor (calculated in the gas phase) published by Wiederhold et al.[23] The equilibrium enrichment factors consist of an MDF component based on density functional theory and an NVF component based on relativistic Dirac-Coulomb calculations following the work of Schauble.[10] The sum of the MDF and NVF components resulted in the predicted isotopic enrichment factor for each Hg species (MDF + NVF). On the basis of the assumption that 1000 ln $\beta^{202-198} \approx \epsilon^{202}\mathrm{Hg}$, the enrichment factor of the cationic species $\epsilon^{202}\mathrm{Hg}_{\mathrm{cat}}$ (HgOH^+ or HgCl^+) was calculated from the difference between the 1000 ln $\beta_{\mathrm{cat}}^{202-198}$ of the cationic species and the average of the 1000 ln $\beta_{\mathrm{n_i}}^{202-198}$ of the neutral species $\mathrm{n_i}$, where $f_{\mathrm{n_i}}$ is their relative abundance:

$$\epsilon^{202}\mathrm{Hg}_{\mathrm{cat}} = 1000 \ln \beta_{\mathrm{cat}}^{202-198} - \sum_{\mathrm{i}} (f_{\mathrm{n_i}} \times 1000 \ln \beta_{\mathrm{n_i}}^{202-198}) \tag{4.9}$$

NVF is related to the nuclear charge radii of the Hg isotopes which do not scale linearly with mass; therefore, NVF is associated with MIF. The expected mass-independent enrichment in $E^{199}\mathrm{Hg}$ is calculated from the cationic enrichment factor of the nuclear volume component ($\epsilon^{202}\mathrm{Hg}_{\mathrm{NVF}}$) using the scaling factors of $^{199/198}\mathrm{Hg}$ relative to $^{202/198}\mathrm{Hg}$,[23] where $\mathrm{SF}_{\mathrm{MDF}}$ is the kinetic mass-dependent scaling factor of 0.252 and $\mathrm{SF}_{\mathrm{NVF}}$ is the nuclear volume scaling factor of 0.0525 using nuclear charge radii from Landolt-Boernstein:[55]

$$\mathrm{E}^{199}\mathrm{Hg} = (\epsilon^{202}\mathrm{Hg}_{\mathrm{NVF}} \times \mathrm{SF}_{\mathrm{NVF}}) - (\epsilon^{202}\mathrm{Hg}_{\mathrm{NVF}} \times \mathrm{SF}_{\mathrm{MDF}}) \tag{4.10}$$

Figure 4.4a shows the calculated Hg isotope enrichment factor of the cationic species HgOH^+ and HgCl^+ relative to the main solution species for the experimental series at pH 7. The 95% confidence interval for all experimental series at pH 7 in the absence of chloride overlapped with the calculated enrichment factor (MDF + NVF) for HgOH^+ ($\epsilon^{202}\mathrm{Hg}$ = -0.37‰). The calculated enrichment factor for HgCl^+ ($\epsilon^{202}\mathrm{Hg}$ = -0.28‰), although not within the 95% confidence interval of the chloride experiment (-0.36‰ to -0.52‰), was still in reasonable agreement with the experimental series. The NVF component of the calculations predicts an MIF of -0.08‰ in $E^{199}\mathrm{Hg}$ both for the HgOH^+ and the HgCl^+ experiments, as illustrated by the NVF values in Figure 4.4b. However, none of the experimental series showed any mass-independent fractionation expressed by $\mathrm{E}^{199}\mathrm{Hg}$ being statistically different from zero (Figure 4.4b, Table 4.1; Table S4.2, Supporting Information). This discrepancy between the experimental findings and the theoretical calculations for the Hg species is not yet fully understood. We can only speculate that there might be a certain overestimation of the NVF component or the resulting extent of MIF in the calculations. Errors on the species calculations might result from uncertainties of input parameters (nuclear charge radii), the neglected influence of solvation effects, or the adequacy of the model; a quantification of these errors however was not feasible (see the Supporting Information of Wiederhold et al.[23] for a detailed discussion on errors). The species calculations for lower pH are not shown here, but they were in qualitative agreement with the results at pH 7, although there are large uncertainties due to a lack of calculated 1000 ln $\beta^{202-198}$ values for some species present at lower pH (e.g., Hg^{2+}).

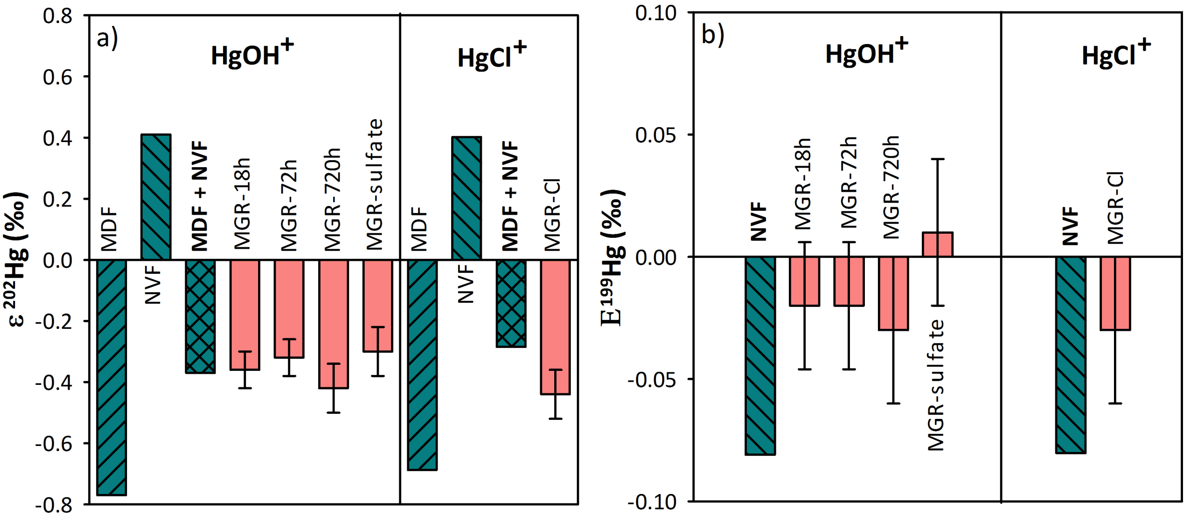

Figure 4.4: Calculated isotopic enrichment factors (ϵ^{202}Hg and E^{199}Hg) of cationic Hg species relative to the dominant solution species at pH 7 (derived from previously published data[23]) plotted as hatched bars. In the absence of chloride the isotopic fractionation was calculated for $HgOH^+$, in the presence of chloride for $HgCl^+$. The calculations include two components from mass-dependent fractionation (MDF) and nuclear volume fractionation (NVF). The sum of these results is the expected net effect (MDF + NVF). Plain bars represent experimental enrichment factors (**a**, ϵ^{202}Hg for MDF; **b**, E^{199}Hg for MIF, Table 4.1) of the Hg pool sorbed to goethite relative to dissolved Hg.

4.3.6 Isotope fractionation during surface complex formation ($\mathrm{IE_{OS}}$, $\mathrm{IE_{IS}}$)

As mentioned above, the change in conformation between the dissolved Hg species and the sorption complexes (outer-sphere and inner-sphere complex) could cause isotope fractionation as proposed in the example of Mo and U.[32,33] There are no calculations of enrichment factors for surface-bound Hg species available, and an assessment of potentially different Hg isotope signatures of outer-sphere and inner-sphere complexes was not possible, as only total sorbed Hg was measured. However, previous studies have identified different types of inner-sphere surface complexes for different experimental conditions presented here. Hg(II) sorbed to goethite forms bidentate inner-sphere complexes over the entire pH range investigated, as shown by extended X-ray absorption fine structure (EXAFS) spectroscopy.[40,45] High sulfate concentrations (≈1 M) were found to trigger the formation of ternary monodentate complexes ($\equiv$Fe-O-Hg-SO_4),[41] whereas the solution speciation of Hg is not significantly altered by sulfate addition. Calculations with stability constants using Visual MINTEQ and literature data[46] predicted a $>10^6$ times lower abundance of $HgSO_4$ and $Hg(SO_4)_2{}^{2-}$ compared to the predominant $Hg(OH)_2$ species (over 99.99% at pH 7), which was in agreement with previous calculations.[40] There was no statistical difference between Hg isotope fractionation of Hg(II) sorption to goethite in systems expected to form bidentate surface complexes (MGR-72 h series, Figure 4.2) and monodentate complexes (MGR-sulfate series, Figure 4.2), which indicates that the conformation of inner-sphere complexes ($\mathrm{IE_{IS}}$) does not significantly influence the Hg isotope fractionation. This finding is supported by the experiments in the presence of chloride, as the Hg isotope enrichment did not significantly vary compared with that in the absence of Cl^-, although a change in surface complexation toward ternary monodentate inner-sphere complexes ($\equiv$Fe-O-Hg-Cl) was expected on the basis of previous studies.[41,56]

4.3.7 Control of Hg isotope fractionation

The measured isotopic enrichment between the sorbed and dissolved pools can be expressed as a function of the isotopic enrichment of the cationic species during equilibration in solution ($\epsilon^{202}\mathrm{Hg_{SE}}$) and the isotopic enrichment during sorption of the cationic species ($\epsilon^{202}\mathrm{Hg_{sorption}}$) (derivation shown in the Supporting Information):

$$\epsilon^{202}\mathrm{Hg_{sorbed-dissolved}} = \epsilon^{202}\mathrm{Hg_{sorption}} + (1 - f_{\mathrm{cat}})\ \epsilon^{202}\mathrm{Hg_{SE}} \tag{4.11}$$

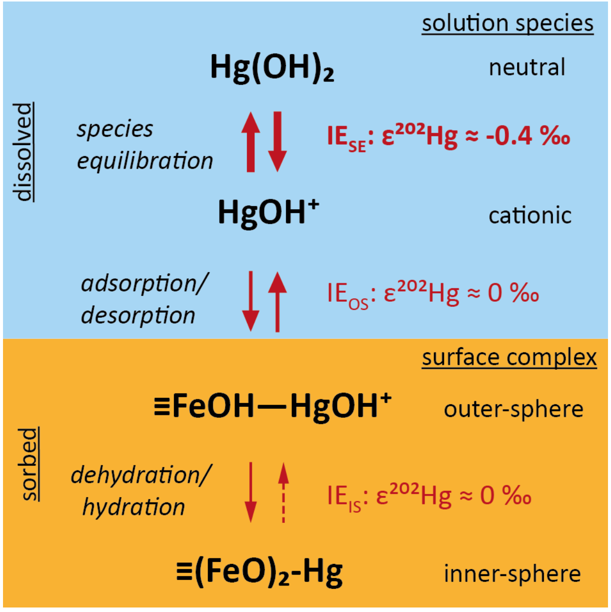
solution species
Hg(OH)₂
neutral
dissolved
species equilibration
IE_SE: ε202Hg ≈ -0.4 ‰
HgOH+
cationic
adsorption/ desorption
IE_OS: ε202Hg ≈ 0 ‰
surface complex
≡FeOH—HgOH+
outer-sphere
sorbed
dehydration/ hydration
IE_IS: ε202Hg ≈ 0 ‰
≡(FeO)₂-Hg
inner-sphere

Figure 4.5: Proposed reaction scheme controlling Hg isotope fractionation of Hg(II) sorption to goethite. The equilibrium isotope effect between Hg(II) solution species is transferred to the goethite surface through the sorption active cationic species, which are isotopically lighter than the neutral solution species. Subsequent conformation changes between dissolved species and outer-sphere complexes as well as during dehydration to form inner-sphere complexes appear to have an insignificant effect on the overall isotopic fractionation.

The scaling term representing the relative fraction of cationic species $(1 - f_{\mathrm{cat}})$ was close to 1 in both experimental series (MGR-72 h and MGR-Cl) as the cationic species occurred at very low abundances at pH 7 ($f_{\mathrm{cat(HgOH^+)}} = 0.06\%$, $f_{\mathrm{cat(HgCl^+)}} = 0.006\%$). As shown in Figure 4.4, the observed isotope fractionation between the sorbed and dissolved Hg pools ($\epsilon^{202}\mathrm{Hg}_{\mathrm{sorbed-dissolved}}$) is in good agreement with the predicted isotope enrichment of the cationic species during species equilibration ($\epsilon^{202}\mathrm{Hg}_{\mathrm{SE}}$). Therefore, we conclude that the isotope fractionation of Hg(II) sorption ($\epsilon^{202}\mathrm{Hg}_{\mathrm{sorbed-dissolved}}$) is controlled by an equilibrium isotope effect between Hg(II) solution species, expressed on the goethite surface by the adsorption of the cationic solution species. The isotopic fractionation during sorption of the cationic species ($\epsilon^{202}\mathrm{Hg}_{\mathrm{sorption}}$), consisting of possible effects during conformation change between the cationic solution species and the outer-sphere complex ($\mathrm{IE_{OS}}$) as well as during the dehydration of the outer-sphere complex to form an inner-sphere complex ($\mathrm{IE_{IS}}$), appears to have an insignificant contribution. This is supported by the fact that the isotopic enrichment factors for experimental conditions forming monodentate inner-sphere complexes (MGR-sulfate and MGR-Cl series) were statistically indistinguishable from those for experiments forming bidentate complexes (e.g., MGR-72 h series). In addition, the finding that the observed isotope effect was insensitive to the equilibration time provided further evidence that the different reaction steps at the mineral surface, some of which are expected to exhibit much slower kinetics compared with species equilibration in solution and thus explaining why the sorption had not yet reached a maximum, did not exert an important influence on the Hg isotope distribution in our system. Figure 4.5 shows the proposed schematic overview of the reaction steps involved in the sorption of Hg(II) to goethite and their associated Hg isotope enrichment factors for the example of $HgOH^+$ sorption.

4.3.8 Implications for other metal isotope and surface complexation studies.

We think that the detailed mechanistic insights provided by this study will have implications for other metal isotope systems as well as for the general understanding of metal sorption processes to mineral surfaces. On one hand, the postulated importance of equilibrium isotope fractionation during hydrolysis, or in more general terms equilibration of solution species which are involved to different extents in sorption processes, may influence the isotope fractionation during sorption for other metals as well. Apart from Hg(II), the correlation between the metal's hydrolysis constant and the metal's surface complexation constant was shown for other metal cations (Ag^+, Pb^{2+}, Cd^{2+}, Zn^{2+}, Co^{2+}, Cu^{2+}, Ni^{2+}),[52,57] most of which possess several stable isotopes. Theoretical investigations of stable isotope fractionation between solution species were recently published for some metal isotope systems (e.g., Ni, Zn).[58–60] A comparison with experimental data for metal isotope fractionation during sorption to a mineral phase could potentially help in further identifying the mechanisms causing metal isotope fractionation for these elements too and may provide further validation for the concept presented here. On the other hand, stable isotope fractionation during sorption of other metals could also be influenced to a larger extent by surface reactions depending on the relative importance of the factors and processes described in equation 4.11, which could be different compared with the specific example of Hg(II) presented here. In the context of surface complexation, this study demonstrates that stable isotope fractionation studies can offer new insights into reaction mechanisms at mineral surfaces and provide further evidence for existing surface complexation models.

4.3.9 Implications for stable Hg isotopes as environmental tracer

The observed MDF and the absence of MIF during sorption of Hg(II) to goethite have been shown to be constant over a range of pH, as well as chloride and sulfate concentrations which trigger the formation of different surface complexes. Although the experiments were performed at higher concentrations than generally found in the environment, the constant Hg isotope fractionation over a large range of surface coverages (between 0.002 and 0.3 μmol m^{-2}) allows the transfer of our results to environmental systems, as there is no indication of a concentration dependence of the determined enrichment factors. This lack of dependence upon concentration, chemical conditions, and equilibration time will facilitate the interpretation of natural Hg isotope fractionation in soils and sediments driven by sorption processes.

Previous field studies have reported systematic differences between Hg isotope compositions of different environmental compartments or Hg pools. For instance, a consistent offset of 0.60 ± 0.16‰ between fish and sediment samples (δ^{202}Hg, corrected for photochemical effects deduced from MIF) was reported from the San Francisco Bay,[61] and water leachates were found to be enriched by 0.70 ± 0.13‰ in δ^{202}Hg compared with soil samples from a mining site in China.[62] We suggest, based on the results of this study as well as the previously published work on Hg(II)-thiol binding,[23] that sorption processes may be at least partially responsible for these observed systematic offsets and influence the isotope signature of natural Hg pools to a significant extent. Sorption of Hg(II) to goethite as well as sorption of Hg(II) to thiol groups,[23] studied as a model system for binding to natural organic matter, revealed a very similar isotopic enrichment of light Hg isotopes onto the surfaces. Based on these laboratory studies, we expect that light Hg isotopes are preferentially sequestered in soils and sediments with enrichment factors in a relatively narrow range of about -0.3‰ to -0.6‰ in δ^{202}Hg for both thiol-bound and mineral-bound Hg(II). As a consequence, the mobile phase, eventually leaching from soils and sediments, is expected to be correspondingly enriched in heavy Hg isotopes. Furthermore, the proposed enrichment of heavy Hg isotopes in the mobile Hg(II) pool should also be considered when dealing with Hg isotope fractionation during bioaccumulation, as the mobile fraction is bioavailable.

Acknowledgments

We thank Kurt Barmettler for help in the soil chemistry laboratory, Felix Oberli for help with the Hg isotope measurements, Robin S. Smith for various support, Felix Maurer for statistical advice, and three anonymous reviewers for helpful comments. This research was funded by ETH Zurich (Grant ETH-15 09-2), which is gratefully acknowledged.

References to Chapter 4

[1] N. E. Selin. Global biogeochemical cycling of mercury: A review. *Annu. Rev. Environ. Resour.*, 34:43–63, 2009.

[2] U. Skyllberg, M. B. Westin, M. Meili, and E. Bjorn. Elevated concentrations of methyl mercury in streams after forest clear-cut: A consequence of mobilization from soil or new methylation? *Environ. Sci. Technol.*, 43(22):8535–8541, 2009.

[3] U. Skyllberg. *Chemical Speciation of Mercury in Soil and Sediment*, pages 219–258. John Wiley & Sons, Inc., 2011.

[4] M. C. Gabriel and D. G. Williamson. Principal biogeochemical factors affecting the speciation and transport of mercury through the terrestrial environment. *Environ. Geochem. Health*, 26(4):421–434, 2004.

[5] U. Skyllberg. *Mercury Biogeochemistry in Soils and Sediments*, volume 34 of *Developments in Soil Science*, pages 379–410. Elsevier B.V., Netherlands, 2010.

[6] R. Kretzschmar and T. Schafer. Metal retention and transport on colloidal particles in the environment. *Elements*, 1(4):205–210, 2005.

[7] B. A. Bergquist and J. D. Blum. The odds and evens of mercury isotopes: applications of mass-dependent and mass-independent isotope fractionation. *Elements*, 5(6):353–357, 2009.

[8] J. D. Blum. *Applications of Stable Mercury Isotopes to Biogeochemistry*, pages 229–245. Advances in Isotope Geochemistry. Springer Berlin Heidelberg, 2011.

[9] H. Hintelmann and W. Zheng. *Tracking Geochemical Transformations and Transport of Mercury through Isotope Fractionation*, pages 293–327. John Wiley & Sons, Inc., 2011.

[10] E. A. Schauble. Role of nuclear volume in driving equilibrium stable isotope fractionation of mercury, thallium, and other very heavy elements. *Geochim. Cosmochim. Acta*, 71(9):2170–2189, 2007.

[11] A. L. Buchachenko. Mercury isotope effects in the environmental chemistry and biochemistry of mercury-containing compounds. *Russ. Chem. Rev.*, 78(4):319–328, 2009.

[12] B. A. Bergquist and J. D. Blum. Mass-dependent and -independent fractionation of Hg isotopes by photoreduction in aquatic systems. *Science*, 318(5849):417–420, 2007.

[13] W. Zheng and H. Hintelmann. Isotope fractionation of mercury during its photochemical reduction by low-molecular-weight organic compounds. *J. Phys. Chem. A*, 114(12):4246–4253, 2010.

[14] P. Rodriguez-Gonzalez, V. N. Epov, R. Bridou, E. Tessier, R. Guyoneaud, M. Monperrus, and D. Amouroux. Species-specific stable isotope fractionation of mercury during Hg(II) methylation by an anaerobic bacteria (Desulfobulbus propionicus) under dark conditions. *Environ. Sci. Technol.*, 43(24):9183–9188, 2009.

[15] D. Malinovsky and F. Vanhaecke. Mercury isotope fractionation during abiotic transmethylation reactions. *Int. J. Mass Spectrom.*, 307(1-3):214–224, 2011.

[16] W. Zheng and H. Hintelmann. Nuclear field shift effect in isotope fractionation of mercury during abiotic reduction in the absence of light. *J. Phys. Chem. A*, 114(12):4238–4245, 2010.

[17] K. Kritee, J. D. Blum, M. W. Johnson, B. A. Bergquist, and T. Barkay. Mercury stable isotope fractionation during reduction of Hg(II) to Hg(0) by mercury resistant microorganisms. *Environ. Sci. Technol.*, 41(6):1889–1895, 2007.

[18] D. Malinovsky, K. Latruwe, L. Moens, and F. Vanhaecke. Experimental study of mass-independence of Hg isotope fractionation during photodecomposition of dissolved methylmercury. *J. Anal. At. Spectrom.*, 25(7):950–956, 2010.

[19] K. Kritee, T. Barkay, and J. D. Blum. Mass dependent stable isotope fractionation of mercury during mer mediated microbial degradation of monomethylmercury. *Geochim. Cosmochim. Acta*, 73(5):1285–1296, 2009.

[20] N. Estrade, J. Carignan, J. E. Sonke, and O. F. X. Donard. Mercury isotope fractionation during liquid-vapor evaporation experiments. *Geochim. Cosmochim. Acta*, 73(10):2693–2711, 2009.

[21] S. Ghosh, E. A. Schauble, G. Lacrampe Couloume, J. D. Blum, and B. A. Bergquist. Estimation of nuclear volume dependent fractionation of mercury isotopes in equilibrium liquid-vapor evaporation experiments. *Chem. Geol.*, 336:5–12, 2013.

[22] W. Zheng, D. Foucher, and H. Hintelmann. Mercury isotope fractionation during volatilization of Hg(0) from solution into the gas phase. *J. Anal. At. Spectrom.*, 22(9):1097–1104, 2007.

[23] J. G. Wiederhold, C. J. Cramer, K. Daniel, I. Infante, B. Bourdon, and R. Kretzschmar. Equilibrium mercury isotope fractionation between dissolved Hg(II) species and thiol-bound Hg. *Environ. Sci. Technol.*, 44(11):4191–4197, 2010.

[24] O. S. Pokrovsky, J. Viers, E. E. Emnova, E. I. Kompantseva, and R. Freydier. Copper isotope fractionation during its interaction with soil and aquatic microorganisms and metal oxy(hydr)oxides: Possible structural control. *Geochim. Cosmochim. Acta*, 72(7):1742–1757, 2008.

[25] L. S. Balistrieri, D. M. Borrok, R. B. Wanty, and W. I. Ridley. Fractionation of Cu and Zn isotopes during adsorption onto amorphous Fe(III) oxyhydroxide: Experimental mixing of acid rock drainage and ambient river water. *Geochim. Cosmochim. Acta*, 72(2):311–328, 2008.

[26] F. Juillot, C. Marechal, M. Ponthieu, S. Cacaly, G. Morin, M. Benedetti, J. L. Hazemann, O. Proux, and F. Guyot. Zn isotopic fractionation caused by sorption on goethite and 2-lines ferrihydrite. *Geochim. Cosmochim. Acta*, 72(19):4886–4900, 2008.

[27] C. Mikutta, J. G. Wiederhold, O. A. Cirpka, T. B. Hofstetter, B. Bourdon, and U. Von Gunten. Iron isotope fractionation and atom exchange during sorption of ferrous iron to mineral surfaces. *Geochim. Cosmochim. Acta*, 73(7):1795–1812, 2009.

[28] B. L. Beard, R. M. Handler, M. M. Scherer, L. Wu, A. D. Czaja, A. Heimann, and C. M. Johnson. Iron isotope fractionation between aqueous ferrous iron and goethite. *Earth Planet. Sci. Lett.*, 295(1-2):241–250, 2010.

[29] E. A. Schauble, M. Meheut, and P. S. Hill. Combining metal stable isotope fractionation theory with experiments. *Elements*, 5(6):369–374, 2009.

[30] O. S. Pokrovsky, J. Viers, and R. Freydier. Zinc stable isotope fractionation during its adsorption on oxides and hydroxides. *J. Colloid Interface Sci.*, 291(1):192–200, 2005.

[31] L. E. Wasylenki, G. Montanez, and A. D. Anbar. Cd isotope fractionation during adsorption varies with salinity. In *AGU, 90(52), Fall Meet. Suppl.* Eos Trans.

[32] J. Barling and A. D. Anbar. Molybdenum isotope fractionation during adsorption by manganese oxides. *Earth Planet. Sci. Lett.*, 217(3-4):315–329, 2004.

[33] G. A. Brennecka, L. E. Wasylenki, J. R. Bargar, S. Weyer, and A. D. Anbar. Uranium isotope fractionation during adsorption to Mn-oxyhydroxides. *Environ. Sci. Technol.*, 45(4):1370–1375, 2011.

[34] C. Siebert, T. F. Nagler, F. von Blanckenburg, and J. D. Kramers. Molybdenum isotope records as a potential new proxy for paleoceanography. *Earth Planet. Sci. Lett.*, 211(1-2):159–171, 2003.

[35] C. L. Weeks, A. D. Anbar, L. E. Wasylenki, and T. G. Spiro. Density functional theory analysis of molybdenum isotope fractionation. *J. Phys. Chem. A*, 111(49):12434–8, 2007.

[36] L. E. Wasylenki, C. L. Weeks, J. R. Bargar, T. G. Spiro, J. R. Hein, and A.l D. Anbar. The molecular mechanism of Mo isotope fractionation during adsorption to birnessite. *Geochim. Cosmochim. Acta*, 75(17):5019–5031, 2011.

[37] R. M. Cornell and U. Schwertmann. *The Iron Oxides.* Wiley-VCH Verlag, Heidelberg, Germany, 2004.

[38] E. A. Forbes, A. M. Posner, and J. P. Quirk. Specific adsorption of inorganic Hg(II) species and Co(II) complex ions on goethite. *J. Colloid Interface Sci.*, 49(3):403–409, 1974.

[39] N. J. Barrow and V. C. Cox. The effects of pH and chloride concentration on mercury sorption. I. by goethite. *J. Soil Sci.*, 43(2):295–304, 1992.

[40] C. S. Kim, J. J. Rytuba, and Jr. Brown, G. E. EXAFS study of mercury(II) sorption to Fe- and Al-(hydr)oxides I. effects of pH. *J. Colloid Interface Sci.*, 271(1):1–15, 2004.

[41] C. S. Kim, J. Rytuba, and Jr. Brown, G. E. EXAFS study of mercury(II) sorption to Fe- and Al-(hydr)oxides - II. effects of chloride and sulfate. *J. Colloid Interface Sci.*, 270(1):9–20, 2004.

[42] U. Schwertmann and R.M. Cornell. *Iron Oxides in the Laboratory - Preparation and Characterisation.* Wiley-VCH, Weinheim, 2nd, edition, 2000.

[43] P. U. Reichard, S. M. Kraemer, S. W. Frazier, and R. Kretzschmar. Goethite dissolution in the presence of phytosiderophores: rates, mechanisms, and the synergistic effect of oxalate. *Plant Soil*, 276(1-2):115–132, 2005.

[44] J. G. Wiederhold, S. M. Kraemer, N. Teutsch, P. M. Borer, A. N. Halliday, and R. Kretzschmar. Iron isotope fractionation during proton-promoted, ligand-controlled, and reductive dissolution of goethite. *Environ. Sci. Technol.*, 40(12):3787–3793, 2006.

[45] C. R. Collins, D. M. Sherman, and K. V. Ragnarsdottir. Surface complexation of Hg^{2+} on goethite: Mechanism from EXAFS spectroscopy and density functional calculations. *J. Colloid Interface Sci.*, 219(2):345–350, 1999.

[46] K. J. Powell, P. L. Brown, R. H. Byrne, T. Gajda, G. Hefter, S. Sjoberg, and H. Wanner. Chemical speciation of Hg(II) with environmental inorganic ligands. *Aust. J. Chem.*, 57(10):993–1000, 2004.

[47] J. Blum and B. Bergquist. Reporting of variations in the natural isotopic composition of mercury. *Anal. Bioanal. Chem.*, 388(2):353–359, 2007.

[48] T. B. Coplen. Guidelines and recommended terms for expression of stable-isotope-ratio and gas-ratio measurement results. *Rapid Commun. Mass Spectrom.*, 25(17):2538–2560, 2011.

[49] S. S. Mathur and D. A. Dzombak. *Chapter 16 Surface complexation modeling: goethite*, volume 11, pages 443–468. Elsevier, 2006.

[50] L. Fischer, G. W. Brummer, and N. J. Barrow. Observations and modelling of the reactions of 10 metals with goethite: adsorption and diffusion processes. *Eur. J. Soil Sci.*, 58(6):1304–1315, 2007.

[51] D. Sarkar, M. E. Essington, and K. C. Misra. Adsorption of mercury(II) by variable charge surfaces of quartz and gibbsite. *Soil Sci. Soc. Am. J.*, 63(6):1626–1636, 1999.

[52] D. A. Dzombak and F.M. Morel. *Surface complexation modeling: hydrous ferric oxide.* Wiley, New York, 1990.

[53] J.P. Gustafsson. Visual minteq 3.0, 2011.

[54] Ralph G. Wilkins. *Kinetics and Mechanism of Reactions of Transition Metal Complexes.* Wiley-VCH Verlag, 2nd edition, 2003.

[55] G.; Fricke and K.; Heilig. *80-Hg Mercury*, volume 20, chapter Nuclear Charge Radii. Springer, Heidelberg, 2004.

[56] L. Gunneriusson and S. Sjoberg. Surface complexation in the H^+-goethite ([alpha]-FeOOH)-Hg (II)-chloride system. *J. Colloid Interface Sci.*, 156(1):121–128, 1993.

[57] N. J. Barrow, J. Gerth, and G. W. Brummer. Reaction kinetics of the adsorption and desorption of nickel, zinc and cadmium by goethite. II modelling the extent and rate of reaction. *J. Soil Sci.*, 40(2):437–450, 1989.

[58] T. Fujii, F. Moynier, N. Dauphas, and M. Abe. Theoretical and experimental investigation of nickel isotopic fractionation in species relevant to modern and ancient oceans. *Geochim. Cosmochim. Acta*, 75(2):469–482, 2011.

[59] J. R. Black, A. Kavner, and E. A. Schauble. Calculation of equilibrium stable isotope partition function ratios for aqueous zinc complexes and metallic zinc. *Geochim. Cosmochim. Acta*, 75(3):769–783, 2011.

[60] T. Fujii, F. Moynier, P. Telouk, and M. Abe. Experimental and theoretical investigation of isotope fractionation of zinc between aqua, chloro, and macrocyclic complexes. *J. Phys. Chem. A*, 114(7):2543–2552, 2010.

[61] G. E. Gehrke, J. D. Blum, D. G. Slotton, and B. K. Greenfield. Mercury isotopes link mercury in San Francisco bay forage fish to surface sediments. *Environ. Sci. Technol.*, 45(4):1264–1270, 2011.

[62] R. Yin, X. Feng, J. Wang, Z. Bao, B. Yu, and J. Chen. Mercury isotope variations between bioavailable mercury fractions and total mercury in mercury contaminated soil in Wanshan mercury mine, SW China. *Chem. Geol.*, 336(0):80–86, 2013.

Chapter 5

Kinetics of Hg(II) exchange between organic ligands, goethite, and natural organic matter studied with an enriched stable isotope approach

M. Jiskra, D. Saile, J.G. Wiederhold, B. Bourdon, E. Björn, and R. Kretzschmar, Kinetics of Hg(II) exchange between organic ligands, goethite, and natural organic matter studied with an enriched stable isotope approach. *Environ. Sci. Technol.*, accepted manuscript, DOI:10.1021/es503483m

Abstract

The mobility and bioavailability of toxic Hg(II) in the environment strongly depends on its interactions with natural organic matter (NOM) and mineral surfaces. Using an enriched stable isotope approach, we investigated the exchange of Hg(II) between dissolved species (inorganically complexed or cysteine-, EDTA-, or NOM-bound) and solid-bound Hg(II) (carboxyl-/thiol-resin or goethite) over 30 days under constant conditions (pH, Hg and ligand concentrations). The Hg(II)-exchange was initially fast, followed by a slower phase, and depended on the properties of the dissolved ligands and sorbents. The results were described by a kinetic model allowing the simultaneous determination of adsorption and desorption rate coefficients. The timescales required to reach equilibrium with the carboxyl-resin varied greatly from 1.2 d for $Hg(OH)_2$ to 16 d for Hg(II)-cysteine complexes and approximately 250 d for EDTA-bound Hg(II). Other experiments could not be described by an equilibrium model, suggesting that a significant fraction of total-bound Hg was present in a non-exchangeable form (thiol-resin and NOM: 53-58%; goethite: 22-29%). Based on the slow and incomplete exchange of Hg(II) described in this study, we suggest that kinetic effects must be considered to a greater extent in the assessment of the fate of Hg in the environment and the design of experimental studies, e.g., for stability constant determination or metal isotope fractionation during sorption.

5.1 Introduction

Mercury is of great concern for human and ecosystem health due to its ability to be methylated and accumulated along the food chain as toxic methyl-Hg[1]. The mobility and reactivity of Hg(II) in aquatic and terrestrial ecosystems is controlled to a large degree by interactions with dissolved ligands, natural organic matter (NOM), inorganic sulfides, and mineral surfaces.[1–3] A widely used method to assess the bioavailability of Hg is based on a thermodynamic approach, where equilibrium concentrations of dissolved Hg(II)-species (e.g., $HgS^0{}_{(aq)}$) are calculated[4]. This approach relies on accurate stability constants and the system being at equilibrium, an assumption which has not been thoroughly investigated[1]. Recent findings, suggesting that Hg(II)-species such as Hg(II)-cysteine complexes are actively taken up by bacterial cells,[5–7] or that Hg(II)-(NOM)-sulfide nanoparticles are available for methylation,[8–11] indicate that kinetics have a major effect on the bioavailability of Hg[12,13], which is not yet fully understood.

Furthermore, many observations on the fate of Hg(II) in experiments and natural systems cannot be explained by thermodynamic approaches. Several studies reported a decrease of labile Hg(II)[14], reducible Hg(II),[15,16] or Hg bioavailability[17] with increasing exposure time of Hg(II) to NOM. These observations were explained by a slow competitive ligand exchange from labile reactive/bioavailable Hg-NOM complexes to strong non-reactive Hg-NOM complexes.[14–17] Hintelmann et al.[18,19] found that Hg(II) newly added to sediments exhibited higher methylation rates than ambient Hg. Jonsson et al.[12,13] reported orders of magnitude different methylation rates depending on the solid/adsorbed phase of Hg(II) and concluded that a combination of thermodynamics and kinetics of Hg(II) dissolution/desorption processes control the methylation and bioavailability of different Hg pools.

Irreversible sorption of Hg(II) and other heavy metals to soils has been described previously[20–23] and was explained by high-affinity binding sites of NOM[21] and lattice or pore diffusion in mineral phases;[21,23] however, the exact mechanisms for the observed sorption hysteresis remained unclear.

These observations raise the question under which conditions purely thermodynamic approaches are justified and where kinetic controls or irreversible sorption play a substantial role for the environmental fate of Hg. Radioisotope and enriched stable isotope approaches were shown to be a powerful tool to investigate exchange kinetics,[24–26] and to assess pool-sizes of exchangeable metals in soils.[27–30] However, measuring isotope exchange kinetics through the activity of radioactive isotopes in solution[24] does not allow distinguishing between isotope exchange and net adsorption, unless the total concentration of the metal in solution is measured with a second analytical technique, often resulting in considerable uncertainties. In contrast, modern mass spectrometry in combination with enriched stable isotopes allows the simultaneous measurement of isotope ratios and concentrations, providing a more reliable approach for distinguishing between isotope exchange and net sorption processes.[30]

Here, we present an approach using enriched stable Hg isotopes to simultaneously investigate adsorption and desorption kinetics of Hg(II) with minimized disturbances of the chemical conditions. In a first phase (preconditioning), we sorbed natural abundance Hg to a solid phase. In a second phase (isotope exchange), we replaced the remaining natural abundance Hg in solution by an equal amount of an enriched Hg isotope tracer and investigated the isotope exchange by monitoring the change in isotope ratio in the solution over time. The objectives were (i) to investigate the adsorption and desorption rate coefficients of dissolved inorganically complexed $Hg(II)_{aq}$ or dissolved organic-ligand-bound Hg(II) with solid-bound Hg(II), (ii) to determine the timescales required to reach equilibrium, (iii) to assess the role of ligand type and coordination on the exchange of Hg(II), and (iv) to assess the pool sizes and discuss potential binding mechanisms of non-exchangeable Hg(II).

5.2 Experimental section

5.2.1 Materials and reagents

All chemicals used in this study were analytical grade and solutions were prepared with ultrapure water (>18.2 MΩ cm, Millipore). Goethite (α-FeOOH), an important iron oxyhydroxide mineral in soils, and two resins with different surface functional groups were used as solid sorbents. The first was a cation exchange resin with carboxyl functional groups on an acrylic polymer backbone (Bio-Rex 70, Bio-Rad). The second was a resin with thiol functional groups on a styrene copolymer backbone (Ambersep GT74, Rohm & Haas). Both resins were in the form of beads with a diameter ranging from 0.3 to 1.2 mm for the carboxyl-resin and from 0.45 to 0.7 mm for the thiol-resin, and they could be easily separated from solution by decantation. The coordination of Hg(II) sorption to thiol-resin has been previously described[31] and this resin was used as model compound for studying sorptive interactions between Hg(II) and organic thiol groups.[31–33] Goethite was synthesized according to a standard procedure (from alkaline solution) by Schwertmann and Cornell[34] and has been used and characterized in previous studies.[35, 36, 37] The structure of the freeze-dried goethite was verified by X-ray diffraction (XRD) and a N_2-BET specific surface area of 38 m^2 g^{-1} was determined[35]. Suwannee River NOM (1R101N, IHSS, St. Paul, MN, U.S.) was used as representative for dissolved NOM. Suwannee River NOM has a total sulfur content of 6.5 g kg^{-1}, of which 28% has been reported to be reduced S (S_{red} =56.8 μmol g^{-1})[38].

L-cysteine (Cys, 97%, Aldrich) and ethylenediaminetetraacetic acid (EDTA, 99%, Merck) are low molecular weight (LMW) organic ligands with high affinities for Hg(II),[39,40] occurring in nanomolar to submicromolar concentrations in the environment.[41,42] However, the main reason for choosing cysteine and EDTA as model organic ligands was their wide application in experimental studies and their difference in Hg(II) complexation. Cysteine has been shown to enhance Hg(II) uptake in microorganisms[5–7], enhance renal toxicity when co-administered with Hg(II)[43] and oxidize Hg(0)[44]. EDTA has been extensively used as competing LMW-ligand for the determination of Hg(II)-NOM stability constants.[45–47] Cysteine forms 1:2-type ($Hg(Cys)_2$) and 1:3-type ($Hg(Cys)_3$) complexes with Hg(II) under the conditions applied in this study.[48,49] Hg(II) is primarily coordinated to the thiol-group and can be further stabilized by the carboxyl-group in the $Hg(Cys)_2$ complex.[49] EDTA forms polydentate complexes with Hg(II) in which Hg is coordinated with carboxyl/amino functional groups (O/N-coordination).[40]

Stock solutions of Hg(II) with natural abundance (NA) isotope composition (NA-Hg) were prepared from a 1000 mg L^{-1} Hg standard solution (Merck). Enriched stable Hg isotope tracers were purchased in oxide form (200-HgO, with 96.41% ^{200}Hg, Oak Ridge National Laboratory) and in metallic form (198-Hg, with 91.75% ^{198}Hg, Trace Sciences International Corp.). Enriched isotope tracer solutions were prepared by dissolution of 200-HgO in 5% HNO_3 and oxidation of metallic 198-Hg with 69% HNO_3 and dilution, respectively. We use the notation ”xxx-Hg” for materials or solutions enriched in a specific isotope ^{xxx}Hg. Further information on the exchange resins and enriched Hg isotope tracers are provided in the Supporting Information (SI).

5.2.2 Batch experiments

Experiments were performed to investigate the isotope exchange between dissolved inorganically complexed Hg(II) ($Hg(II)_{aq}$) and solid-bound Hg(II) (carboxyl-, thiol-resin, or goethite) (Figure 5.1a) and between Hg(II) complexed to dissolved organic ligands (EDTA, cysteine or NOM) and solid-bound Hg(II) (carboxyl- or thiol-resin) (Figure

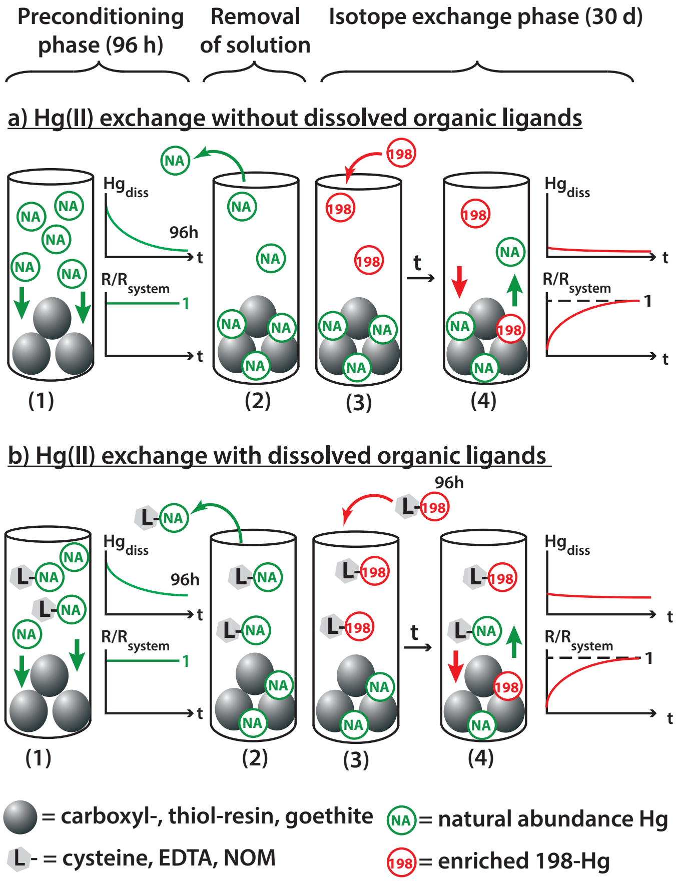
Preconditioning phase (96 h)
Removal of solution
Isotope exchange phase (30 d)
a) Hg(II) exchange without dissolved organic ligands
NA
198
Hgdiss
96h
t
R/Rsystem
1
(1)
(2)
(3)
(4)
b) Hg(II) exchange with dissolved organic ligands
L-NA
L-198
= carboxyl-, thiol-resin, goethite
L- = cysteine, EDTA, NOM
NA = natural abundance Hg
198 = enriched 198-Hg

Figure 5.1: Setup for Hg(II) isotope exchange experiments without dissolved organic ligands **(a)** and with dissolved organic ligands **(b)**. In the preconditioning phase **(1)** natural abundance NA-Hg was mixed with **(a)** solid phases (carboxyl-, thiol-resin or goethite) and **(b)** with dissolved organic ligands (cysteine, EDTA, and Suwannee river natural organic matter (NOM)) and solid phases (carboxyl- and thiol-resin) and allowed to adsorb for 96 h. Then the dissolved NA-Hg(II) species in solution were removed **(2)** and replaced by a similar concentration of enriched 198-Hg(II) isotope tracer **(3)**. The 198-Hg tracer addition caused a sudden drop in the isotope ratio in solution (R) which was normalized to the isotope ratio of the whole system (R_{system}). In the isotope exchange phase **(4)**, the exchange kinetics as expressed by the approach of R towards R_{system} was investigated over 30 d.

5.1b). All experiments were conducted in 10 mL Teflon centrifuge tubes as individual batch reactors (duplicate for each time-point). The tubes were filled with 9.5 mL sample solution and sealed with Teflon screw caps, leaving a <0.5 mL headspace of air. For carboxyl-, and thiol-resin experiments, performed at pH 4.0 to 4.2, the buffering capacity of the exchange resins was sufficient to maintain a constant pH (±0.05 to ±0.15 pH units). Goethite experiments were less buffered and the suspension pH was 5.4±0.6

and 5.9±0.4 without and with 0.5 mmol L^{-1} chloride, respectively (Table 5.1). In the pH range of 4 to 7 and in absence of dissolved organic ligands and chloride, $Hg(II)_{aq}$ was predominantly present in solution as $Hg(OH)_2$ with a minor contribution of cationic Hg species ($HgOH^+$, Hg^{2+})[50]. The pH was chosen for experimental considerations due to the high buffer capacity of the carboxyl-resin at pH 4 and represents typical conditions found in organic-rich terrestrial environments.

In the preconditioning phase (phase **1** in Figure 5.1) a solution between 1 and 105 μmol L^{-1} of natural abundance NA-Hg(II) was added to carboxyl- and thiol-resins (10 ± 0.2 mg wet mass, 59±2% and 56±2% water content) and goethite (25 ± 1 mg dry mass) (Table 5.1). The Hg(II) loadings on the carboxyl- and thiol-resins were chosen below the sorption capacity of the resins (Figure S5.3), to achieve dissolved Hg concentrations of ≈25 nmol L^{-1} after the preconditioning phase. The Hg loadings in this study are higher than expected under environmental conditions, however, they allowed the assessment of the variety of the binding sites, beyond the high-affinity binding sites which are present at low abundances. In experiments with dissolved organic ligands (Figure 5.1b), those were added simultaneously with the NA-Hg(II) solution and the resins. The suspensions were mixed on an end-over-end shaker at room temperature (23±2 °C) in the dark. Over the preconditioning time of 96 h dissolved NA-Hg(II) was allowed to interact with the dissolved ligands and solid sorbents present, resulting in a decrease in dissolved Hg(II) concentration due to adsorption of Hg(II) to solid phases (Figure S4). After the preconditioning time the solution phase was removed (phase **2** in Figure 5.1) and the dissolved NA-Hg(II) concentration was measured. The solid-bound Hg(II) fractions (f_{sorbed}) varied between 38% and 99.97% depending on the ligands and sorbents present (Table 5.1). The solutions of resin-experiments were removed from the resin with a syringe and filtered through a 0.45 μm nylon membrane filter (Perfect-Flow, Wicom). The goethite suspensions were first centrifuged (≈3300 g for 15 min) and then the supernatant was filtered as in the resin experiments. Samples were stabilized with BrCl (0.2M in $HCl_{concd.}$) to 1% (v/v) in solutions without dissolved organic ligands and to 10% (v/v) in solutions with dissolved organic ligands to break down Hg(II)-organic complexes prior to analysis. Solutions of a 198-Hg isotope tracer were prepared with similar concentrations to the total dissolved NA-Hg measured after the preconditioning phase. When more than 99% Hg was adsorbed, 1% of the total NA-Hg amount was added as 198-Hg because of analytical precision considerations. In these experiments, the higher concentration of 198-Hg at the beginning of the isotopes exchange phase led to a fast initial net adsorption (Figure 5.3a). In experiments with dissolved organic ligands, solutions with the same ligand concentrations as in the preconditioning phase (Table 5.1) were mixed with 198-Hg and preconditioned for 96 h prior to addition to the resin. For the isotope exchange experiments the 198-Hg solutions were added to the solid phases (phase **3** in Figure 5.1). The addition of the 198-Hg solution caused a sudden drop of the ^{202}Hg/^{198}Hg isotope ratio (R) in solution, since the dissolved Hg(II) pool was enriched in ^{198}Hg compared to the total Hg in the system. The isotope exchange (phase **4** in Figure 5.1) between dissolved inorganically complexed 198-Hg(II) (Figure 5.1a) or 198-Hg(II) complexed to dissolved organic ligands (Figure 5.1b) and solid-bound NA-Hg(II) was monitored by measuring R in solution over time as it evolved toward the known isotope ratio of the total system (R_{system}). The isotope exchange was stopped after different exchange times (3 h to 30 d) by separating the dissolved and solid pool as described for the preconditioning phase and R and concentration of total dissolved Hg (Hg_{diss}) were measured. To calculate Hg recoveries (Table 5.1), the solid-bound Hg(II) was desorbed with 5 mL HCl for 24 h (12M for resins and 9M for goethite) and the concentration of Hg(II) sorbed after the exchange phase was measured.

Table 5.1: Parameters of experimental series: Dissolved ligand type and concentration ([L], μmol L^{-1}), solid phase type (C-resin= carboxyl-resin, T-resin= thiol-resin) and concentration ([solid], g L^{-1}), pH, initial NA-Hg concentration ([NA-Hg], μmol L^{-1}) and enriched 198-Hg tracer concentration added for the isotope exchange phase ([198-Hg], μmol L^{-1}), fraction of Hg sorbed after the preconditioning phase (f_{sorb}, %) and total Hg recovery[a], errors are $\pm 1\sigma$.

series	**Dissolved ligand**	**[L]** (μmol L^{-1})	**solid**	**[solid]** (g L^{-1})	**pH**	**NA-Hg]** (μmol L^{-1})	**[198-Hg]** (μmol L^{-1})	**f_{sorb}** (%)	**recovery** (%)
Hg(II)$_{aq}$ – C-resin	no	-	C-resin	1.05	4.0±0.05	9.97	0.094	99.6±0.5	110±5
Hg(II)$_{aq}$ – T-resin	no	-	T-resin	1.05	4.0±0.15	103.20	0.944	99.97±0.004	97±2
Hg(II)-EDTA – C-resin	EDTA	2	C-resin	1.05	4.1±0.05	10.62	1.747	83±2	100±1
Hg(II)-cysteine – C-resin	cysteine	2	C-resin	1.05	4.2±0.12	8.62	0.482	94±0.6	100±2
Hg(II)-NOM – C-resin	SR-NOM	43.9[b]	C-resin	1.05	4.1±0.05	12.22	1.555	83±2	71±6
Hg(II)-NOM – T-resin	SR-NOM	439[b]	T-resin	1.05	4.0±0.08	105.20	2.541	97±0.2	81±2
Hg(II)$_{aq}$ – goethite	no	-	goethite	2.64	5.4±0.6	0.81	0.103	88±7	87±5
Hg(II)-Cl$_{aq}$ – goethite	chloride	500	goethite	2.64	5.9±0.4	0.94	0.624	39±15	100±7

[a] calculated for sum of NA-Hg and 198-Hg

[b] mg NOM L^{-1}

5.2.3 Analytical methods

Hg_{diss} and R were determined by cold vapor (CV) generation using stannous chloride reduction (HGX-200, Cetac) coupled to a quadrupole inductively coupled plasma mass spectrometer (q-ICPMS; Agilent 7500, Agilent Technologies). All masses were measured in the analog detector mode. Signal intensities were corrected for background by subtraction of the blank signal measured prior to each sample. Data were corrected for instrumental mass fractionation by applying a linear mass bias correction, calculated from NA-Hg standard measurements performed after every 10 samples. All samples were diluted to Hg concentrations between 0.5 and 25 nmol L^{-1}. The ratio $^{202}Hg/^{198}Hg$ (R) was measured for 45 cycles of 0.6 s and calculated from the background and mass bias corrected ratio of the signal intensities. The analytical precision was tested with artificially spiked standards revealing that this method is capable of resolving 0.005 nM 198-Hg (1% of total Hg) in a 0.5 nM NA-Hg solution (t-test, p= 0.0077), fulfilling the analytical requirements for this study. Hg_{diss} was measured by a reverse isotope dilution approach.[51,52,53,54] A known amount of 200-Hg isotope standard (usually 25 nmol L^{-1}) was added to the samples. Signal intensities of mass 198, 200 and 202 were recorded for 30 cycles of 0.3 s. Concentrations were calculated from instrumental mass bias and background corrected signals applying a matrix inversion approach.[52,54] Hg concentrations of general characterization experiments (sorption isotherms and adsorption kinetics, Figures S5.3 and S5.4) were measured using atomic fluorescence spectrometry (CV-AFS; Millenium Merlin, PS Analytical). DOC concentrations were measured using UV absorbance (UV-visible Spectrophotometer, Cary 50, Varian) at 245 nm relative to the NOM stock solution. Proton adsorption and desorption kinetics were measured with a pH electrode.

5.2.4 Data reporting

The total dissolved Hg(II) concentration (Hg_{diss}) was calculated from the concentration of enriched 198-Hg isotope tracer ($C(198\text{-}Hg)_{diss}$) and the concentration of natural abundance Hg ($C(NA\text{-}Hg)_{diss}$).

$$Hg_{diss} = C(198\text{-}Hg)_{diss} + C(NA\text{-}Hg)_{diss} \tag{5.1}$$

All measured isotope ratios in solution (R) are reported relative to the ratio of the whole individual batch system (R_{system}):

$$\frac{\mathrm{R}}{\mathrm{R_{system}}} = \frac{(^{202}\mathrm{Hg}/^{198}\mathrm{Hg})_{\mathrm{diss}}}{(^{202}\mathrm{Hg}/^{198}\mathrm{Hg})_{\mathrm{system}}} \tag{5.2}$$

where $\mathrm{R_{system}} = (^{202}\mathrm{Hg}/^{198}\mathrm{Hg})_{\mathrm{system}}$ is calculated from the amount of Hg ($\mathrm{n}(^{202}\mathrm{Hg})_{\mathrm{precond}}$ and $\mathrm{n}(^{198}\mathrm{Hg})_{\mathrm{precond}}$) added as NA-Hg in the preconditioning phase, the amount of Hg ($\mathrm{n}(^{202}\mathrm{Hg})_{\mathrm{removed}}$ and $\mathrm{n}(^{198}\mathrm{Hg})_{\mathrm{removed}}$) removed and the amount of Hg ($\mathrm{n}(^{202}\mathrm{Hg})_{\mathrm{tracer}}$ and $\mathrm{n}(^{198}\mathrm{Hg})_{\mathrm{tracer}}$) added as 198-Hg in the isotope exchange phase:

$$(^{202}\mathrm{Hg}/^{198}\mathrm{Hg})_{\mathrm{system}} = \frac{n(^{202}\mathrm{Hg})_{\mathrm{precond}} - n(^{202}\mathrm{Hg})_{\mathrm{removed}} + n(^{202}\mathrm{Hg})_{\mathrm{tracer}}}{n(^{198}\mathrm{Hg})_{\mathrm{precond}} - n(^{198}\mathrm{Hg})_{\mathrm{removed}} + n(^{198}\mathrm{Hg})_{\mathrm{tracer}}} \tag{5.3}$$

5.2.5 Kinetic modeling

The evolution of R and $\mathrm{Hg_{diss}}$ over time during the isotope exchange phase was modeled for $^{202}\mathrm{Hg}$ representing the natural abundance Hg (NA-Hg) remaining in the system and for $^{198}\mathrm{Hg}$ representing the enriched 198-Hg tracer added in the exchange phase. R in solution at time t was calculated following equation 5.4 where $\mathrm{N_{aq}^{202}}$ and $\mathrm{N_{aq}^{198}}$ represent the amount (nmol) of $^{202}\mathrm{Hg}$ and $^{198}\mathrm{Hg}$ in solution:

$$\mathrm{R_{aq}(t)} = \frac{\mathrm{N_{aq}^{202}(t)}}{\mathrm{N_{aq}^{198}(t)}} \tag{5.4}$$

The modeled R is reported relative to the isotope ratio of the system, following the definition described in equation 5.3. The modeled total dissolved Hg concentration ($\mathrm{Hg_{diss}}$) was calculated as follows:

$$\mathrm{Hg_{diss}^{aq}(t)} = \frac{\mathrm{N_{aq}^{202}(t)}}{^{202}\mathrm{ab_{NA-Hg}}} + \frac{\mathrm{N_{aq}^{198}(t)}}{^{198}\mathrm{ab_{198-Hg}}} \tag{5.5}$$

where $^{202}\mathrm{ab_{NA-Hg}}$ and $^{198}\mathrm{ab_{198-Hg}}$ correspond to the relative abundance of $^{202}\mathrm{Hg}$ in NA-Hg and of $^{198}\mathrm{Hg}$ in the enriched 198-Hg tracer, respectively (Table S5.2).

The one-pool equilibrium model (model 1a in Figure 5.2), where dissolved inorganically complexed Hg(II) is exchanging with one pool of solid-bound Hg (Hg(II)-$\mathrm{S_1}$) to equilibrium was described by equations 5.6 and 5.7:

$$\frac{\mathrm{dN_{aq}^{202}}}{\mathrm{dt}} = -\mathrm{k^{ads}} \times \mathrm{N_{aq}^{202}} + \mathrm{k^{des}} \times \mathrm{N_{S1}^{202}} \tag{5.6}$$

$$\frac{\mathrm{dN_{aq}^{198}}}{\mathrm{dt}} = -\mathrm{k^{ads}} \times \mathrm{N_{aq}^{198}} + \mathrm{k^{des}} \times \mathrm{N_{S1}^{198}} \tag{5.7}$$

where N_{S1}^{202} and N_{S1}^{198} represent the amounts (nmol) of ^{202}Hg and ^{198}Hg sorbed to solid surfaces and k^{ads} and k^{des} are the adsorption and desorption rate coefficients, respectively. Rate coefficients for ^{202}Hg and ^{198}Hg were set to be equal, as kinetic isotope fractionation is not resolvable with the analytical precision used and can be considered insignificant in the framework of this study.

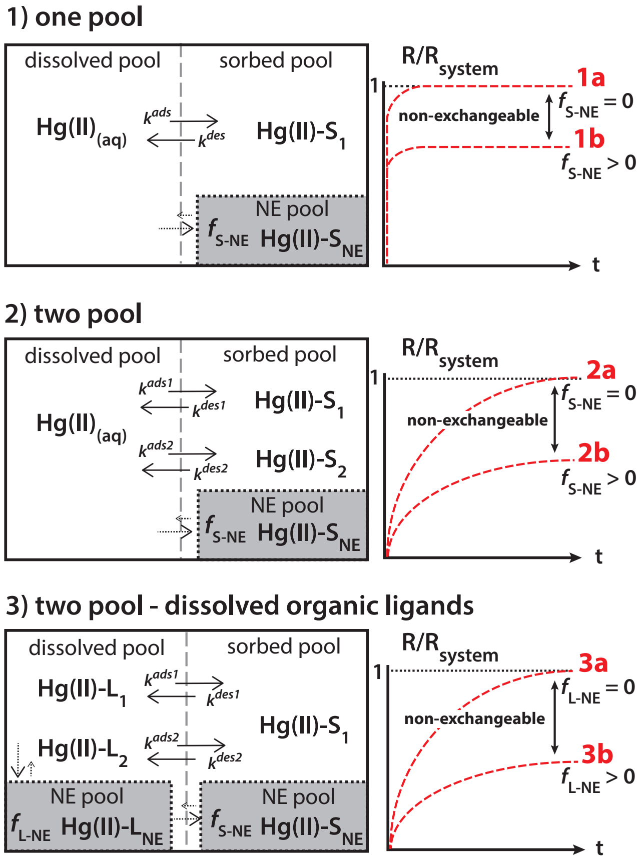
1) one pool

2) two pool

3) two pool - dissolved organic ligands

dissolved pool
sorbed pool
Hg(II)(aq)
kads
kdes
Hg(II)-S1
NE pool
fS-NE Hg(II)-SNE
R/Rsystem
1
1a
non-exchangeable
fS-NE = 0
1b
fS-NE > 0
t
kads1
kdes1
kads2
kdes2
Hg(II)-S2
2a
2b
Hg(II)-L1
Hg(II)-L2
fL-NE Hg(II)-LNE
3a
fL-NE = 0
3b
fL-NE > 0

Figure 5.2: Models describing the isotope exchange phase. In model **1** one pool of inorganically-complexed dissolved Hg(II)$_{(\mathrm{aq})}$ exchanges with one pool of solid-bound Hg(II)-S$_1$. In model **2** two solid-bound Hg pools (Hg(II)-S$_1$ and Hg(II)-S$_2$) are exchanging at different rates with dissolved Hg(II)$_{(\mathrm{aq})}$. In the presence of dissolved organic ligands (model **3**) two dissolved organic-ligand-bound Hg pools (Hg(II)-L$_1$ and Hg(II)-L$_2$) are exchanging with one solid-bound pool (Hg(II)-S$_1$). Isotope exchange experiments approaching equilibrium **(1a, 2a, and 3a)** are characterized by R/R$_{\mathrm{system}}$ values approaching 1. Experiments reaching a R/R$_{\mathrm{system}}$ plateau below 1 **(1b, 2b, and 3b)** indicate the presence of Hg(II) in a non-exchangeable (NE) pool of solid-bound Hg(II) ($f_{\mathrm{S-NE}}$ >0) or for dissolved NOM ligands **(3b)** a non-exchangeable dissolved pool ($f_{\mathrm{L-NE}}$ >0). The non-exchangeab pools were considered to be constant in size and not interacting with exchangeable Hg during the isotope exchange phase, after they had been filled in the preconditioning phase.

The initial conditions of the model were set to the measured experimental conditions at the beginning of the isotope exchange phase (Table S5.3, details in SI). For experiments with a fast initial isotope exchange followed by a second slower exchange phase, a two-pool model (model 2, Figure 5.2) with a faster and a slower exchanging sorbed pool provided a better representation of the measured data. In experiments with dissolved organic ligands a model with two dissolved pools exchanging with solid-bound Hg(II) at different rates (model 3, Figure 5.2) was shown to provide the best fit. The differential equations for the two-pool models which are similar to equations 5.6 and 5.7 are provided in the SI. The Hg loading on the solid phases and the pH were not considered in the model and therefore, the rate coefficients are dependent on the experimental conditions.

In cases where R did not approach R_{system}, representing isotopic equilibrium, but reached a plateau at $R/R_{system}<1$, the equilibrium models were not able to describe the experimental results without the presence of an additional non-exchangeable (NE) Hg(II) pool. Potential Hg(II) diffusion into the non-exchangeable pool during the isotope exchange phase was found to have a minor effect on the interpretation of our results (SI). Therefore, the pool size of non-exchangeable Hg(II) was considered constant in size. The pool size of non-exchangeable solid-bound Hg was described as a fraction of the solid bound NA-Hg(II) ($f_{\mathrm{S-NE}}$) and subtracted from the initial amount of solid-bound NA-Hg(II) for modeling the isotope exchange phase. The pool size of non-exchangeable dissolved organic-ligand-bound Hg(II) ($f_{\mathrm{L-NE}}$) was described accordingly and subtracted from the initial amount of dissolved 198-Hg(II).

The adsorption and desorption rate coefficients ($k^{ads1,2}$ and $k^{des1,2}$), pool sizes of non-exchangeable Hg ($f_{\mathrm{S-NE}}$ and $f_{\mathrm{L-NE}}$), and the fraction of the faster exchanging pool ($f1$) were simulated using a Monte Carlo approach based on a uniformly distributed pseudorandom number generation in MATLAB (R2012a, MathWorks).[55] The simulations were evaluated based on the sum of squared residuals comparing the model simulations at each experimental time-point with the corresponding measured values. The reported parameters correspond to the best fit, yielding the lowest sum of squared residuals for the measured R and Hg_{diss} for each series. Small differences in the optimal parameters for describing R and Hg_{diss} were found, potentially caused by different analytical procedures or potential mechanisms not considered in the models (e.g., adsorption of Hg-ligand complexes to resin or container wall). The optimization fit for ”R only” was taken for an accurate estimation of the timescales to reach equilibrium.

5.3 Results and discussion

5.3.1 Hg(II)-exchange between dissolved inorganic complexes and resins

The isotope exchange between $Hg(II)_{aq}$ and carboxyl-resin-bound Hg(II) was fast, indicated by a rapid increase in R, reaching $R/R_{system}=1$ within less than 4 d (Figure 5.3b). The results of the $Hg(II)_{aq}$ − carboxyl-resin isotope exchange experiment were well described by the one-pool equilibrium model (model 1a, Figure 5.2), where one pool of carboxyl-resin-bound Hg(II) exchanges with $Hg(II)_{aq}$ until equilibrium is reached. The Hg(II) adsorption and desorption rate coefficients of the best model fit (Table 5.2) were considerably lower than for proton sorption (Figure S5.5). According to the model providing the best fit for R, the $Hg(II)_{aq}$ − carboxyl-resin system reached equilibrium ($R/R_{system} = 1$) after 1.2 d.

The isotope exchange phase between $Hg(II)_{aq}$ and thiol-resin-bound Hg(II) was characterized by a fast initial increase in R followed by a slower increase aproaching a plateau at R/R_{system} ≈0.9 after 16 d, after which it remained constant until the end of the experiment (Figure 5.3b). A plateau at $R/R_{system}<1$ suggests the presence of a pool of non-exchangeable Hg(II) bound to the thiol-resin. The one-pool model with an additional non-exchangeable pool (1b, Figure 5.2) and the two pool equilibrium model (2a, Figure 5.2) poorly matched the results of the $Hg(II)_{aq}$ − thiol-resin experiment (Figure S5.6). The results were best described by a model with two pools of solid-bound Hg(II) exchanging at different rates and a third pool of non-exchangeable solid-bound Hg(II) (Model 2b, Figure 5.2), with the fitted parameters given in Table 5.2. Based on the best model fit, the fast exchanging pool ($f1$) accounted for only ≈0.25% of the total sorbed Hg, however the determined rate coefficients for the fast exchanging pool have to be treated with caution since it was only represented in the first few samples (Table 5.2). 42% of the total thiol-resin-bound Hg(II) exchanged at slower rates. The remaining 57% were accounted to non-exchangeable Hg(II), corresponding to a Hg(II) loading of 56 nmol mg^{-1} thiol-resin. It is important to realize that a value of 0.9 for R/R_{system} does not correspond to a 90% approach to equilibrium. This is because the pool sizes of dissolved and solid-bound Hg are very different.

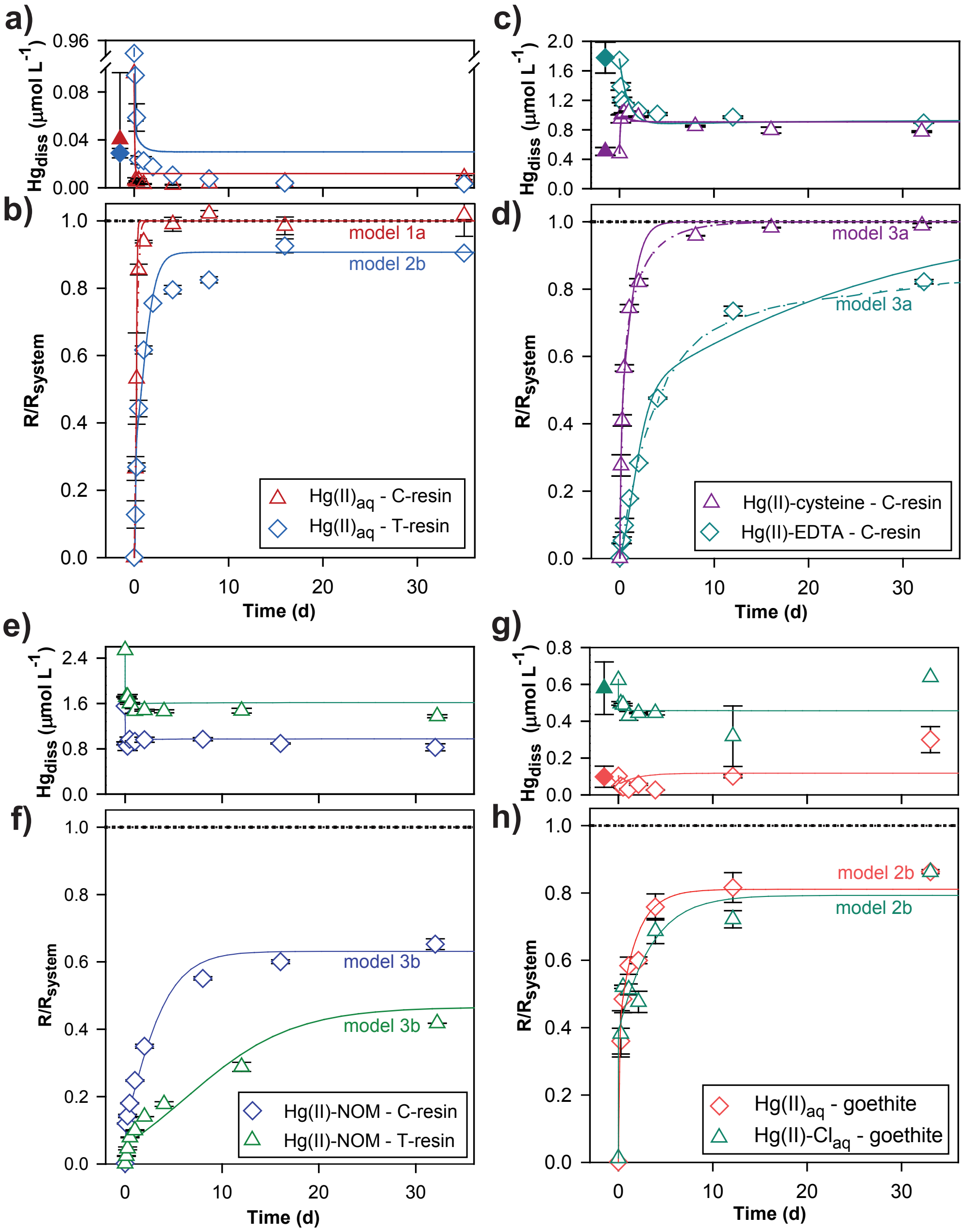

Figure 5.3: Total dissolved Hg concentration (Hg_{diss}) in μmol L^{-1} and isotope ratio (R/R_{system}) in solution over 30d isotope exchange phase (open symbols) of different experiments: **(a, b)** between $Hg(II)_{aq}$ and carboxyl (C-) or thiol (T-) resin-bound Hg(II), **(c, d)** between dissolved Hg(II)-cysteine or Hg(II)-EDTA and C-resin-bound Hg(II) and, **(e, f)** between dissolved Suwannee River NOM-bound Hg(II) and C- or T-resin-bound Hg(II), and **(g, h)** between $Hg(II)_{aq}$ and Hg(II) sorbed to goethite. Error bars represent the range of duplicate batch experiments for the open symbols (smaller than symbol size if not visible). The solid lines represent the best fits of modeled concentration and isotope ratio (models refer to Figure 5.2) and dashed lines represent the best fit for the equilibrium timescale determination (R only, see text). The closed symbols represent Hg_{diss} after the 96 h preconditioning phase ($\pm\sigma$).

Table 5.2: Parameters of model fits: model type according to Figure 5.2, adsorption and desorption rate coefficients (k^{ads1}, k^{ads2}, k^{des1} and k^{des2}), initial size of fast exchangeable pool relative to total exchangeable pool ($f1$), Pool size of non-exchangeable Hg (f_{NE}), time to reach equilibrium (t_{eq}), and coefficient of determination for the isotope ratio fit (R^2 (R)) and the concentration fit (R^2 ($Hg_{dissolved}$)). (C-resin= carboxyl-resin , T-resin= thiol-resin)

series	**model**	$\mathbf{k^{ads1}}$ (h^{-1})	$\mathbf{k^{ads2}}$ (h^{-1})	$\mathbf{k^{des1}}$ (h^{-1})	$\mathbf{k^{des2}}$ (h^{-1})	$\boldsymbol{f1}$ (%)	$\boldsymbol{f_{NE}}$ (%)	$\mathbf{t_{eq}}$ (d)	$\mathbf{R^2}$ **(R)**	$\mathbf{R^2}$ **($\mathbf{Hg_{diss}}$)**
$\mathbf{Hg(II)_{aq}}$ − C-resin	1a	7.7×10^{-1}	-	8.2×10^{-4}	-	100	0	≈1.2 [b]	0.972	0.925
$\mathbf{Hg(II)_{aq}}$ − T-resin	2b	1.9×10^{-1}	1.0	6.9×10^{-2}	6.0×10^{-4}	0.5	57	$\gg30$ [a]	0.984	0.996
Hg(II)-EDTA − C-resin	3a	2.2×10^{-3}	5.3×10^{-5}	4.3×10^{-2}	2.7×10^{-3}	11	0	≈250 [b,c]	0.989	0.629
Hg(II)-cysteine − C-resin	3a	4.9×10^{-2}	2.8×10^{-4}	3.8×10^{-1}	3.8×10^{-2}	42	0	≈16 [b]	0.994	0.850
Hg(II)-NOM − C-resin	3b	3.3	1.8×10^{-2}	6.7×10^{-3}	6.8×10^{-5}	97	58	$\gg30$ [a]	0.993	0.908
Hg(II)-NOM − T-resin	3b	7.6	7.6×10^{-3}	2.1×10^{-2}	2.2×10^{-5}	90	53	$\gg30$ [a]	0.968	0.872
$\mathbf{Hg(II)_{aq}}$ − goethite	2b	5.9×10^{-1}	5.0×10^{-3}	1.4×10^{-1}	2.0×10^{-2}	27	29	$\gg30$ [a]	0.975	0.634
$\mathbf{Hg(II)\text{-}Cl_{aq}}$ − goethite	2b	4.6	4.1×10^{-3}	6.7	1.1×10^{-2}	47	22	$\gg30$ [a]	0.962	0.616

[a] no estimation possible based on 30 d exchange experiment.

[b] derived from isotope ratio optimization only (R only)

[c] extrapolated

5.3.2 Hg(II)-exchange between dissolved organic ligands and carboxyl-resin

The Hg(II)-exchange between the dissolved organic ligands (cysteine and EDTA) and carboxyl-resin was slower as compared to $Hg(II)_{aq}$ (Figures 5.3c and d). The exchange of Hg-cysteine, where equilibrium was reached after about 2 weeks was considerably faster than the exchange of Hg-EDTA experiment, which did not reach equilibrium within 30 d. We suggest that the faster isotope exchange observed for Hg-cysteine compared to Hg-EDTA was controlled by the different Hg coordination; for Hg-cysteine, mono- or bidentate bonds have to be broken for Hg(II) to exchange with resin-bound Hg, which has likely a higher probability than the breaking of the polydentate complexation in Hg-EDTA. Whereas one-pool models provided a poor fit, the results of both experimental series with dissolved organic-LMW ligands could be well represented by models with two pools of dissolved organic-ligand-bound Hg(II) (model 3a, Figure 5.2) with the best-fit parameters given in Table 5.2.

According to the model fit, the isotope exchange between dissolved Hg-cysteine complexes and carboxyl-resin-bound Hg(II) was in equilibrium after ≈16 d. For the Hg-EDTA experiment, the best-fit model resulted in an equilibration time of ≈250 d; however, this should be interpreted with caution since it represents an extrapolation beyond the duration of our experiments (30 d). The slow isotope exchange of Hg(II)-EDTA complexes is in agreement with previous findings for competitive exchange between Fe(III)-EDTA and Ca(II)-EDTA[56]. In comparison, the predicted timescale for Hg(II)-EDTA complexes to reach equilibrium with carboxyl-resin-bound Hg(II) of ≈250 d would be about twice as long as for the Ca(II)-Fe(III)-EDTA system in solution.

5.3.3 Hg(II)-exchange between dissolved NOM and resins

The isotope exchange between dissolved NOM-bound Hg(II) and Hg(II) bound to carboxyl- or thiol-resin (Figure 5.3f) was even slower than that observed for the experiments with dissolved LMW-organic ligands and equilibrium was not reached within 30 d, in agreement with previous observations.[57] The isotope ratio in solution of the Hg(II)-NOM experiment with carboxyl-resin reached a plateau at R/R_{system} ≈0.6 after about two weeks, suggesting the presence of non-exchangeable Hg(II). Since Hg(II) bound to carboxyl-resin was reversible in the absence of dissolved organic ligands, this suggests that NOM contained a pool of non-exchangeable Hg(II). NOM in competition with the thiol-resin had a lower Hg(II) loading (4.2 nmol Hg mg^{-1} NOM) compared to NOM in competition with the carboxyl-resin (24 nmol Hg mg^{-1} NOM), which has a lower affinity for Hg(II) than the thiol-resin. The dissolved Hg concentration decreased in both experimental series during the initial isotope exchange phase (Figure 5.3e), concomitant with a 15% decrease in NOM concentration relative to the initial NOM over the course of the experiment (Figure S5.7), indicating possibly adsorption of Hg(II)-NOM complexes to the resins, as described previously[58]. Since the total analytical recovery of Hg in the experimental series with NOM was relatively poor (71% for the NOM-carboxyl series and 81% for the NOM-thiol series, Table 5.1), we cannot exclude some loss of Hg from these systems, potentially through reduction of Hg(II) to Hg(0) by NOM,[59, 60] although our experiments were conducted under oxic conditions in the dark. Model simulations considering the potential loss of Hg (using recovered Hg as initial condition, Figure S5.8) did not reveal any relevant difference for the interpretation of the results.

The results of the isotope exchange were best represented by a model with two exchangeable pools of ligand-bound Hg(II) and one additional pool of non-exchangeable Hg(II)-NOM complexes (model 3b, Figure 5.2). According to the best-fit model, 53% of the dissolved Hg(II)-NOM complexes in competition with the thiol-resin and 58% in competition with the carboxyl-resin were non-exchangeable, corresponding to 2.2 and 14 nmol Hg(II) per mg Suwannee River NOM for the thiol- and carboxyl-resin experiment, respectively. This implies that between 4.4 to 28 nmol mg^{-1} thiol groups per Suwannee River NOM (assuming a 2:1 thiol:Hg complexation[31]) are capable of complexing Hg(II) irreversibly. This value is in agreement with the 11 - 17 nmol mg^{-1} high affinity binding sites, calculated from the spectroscopic quantification of reduced sulfur (S_{red}) in Suwannee River NOM[38], based on the assumption that 20 - 30% of the S_{red} is present as thiol.[31] Also Haitzer et al.[61] calculated a concentration of 5 nmol mg^{-1} high affinity binding sites in NOM, however, a recent study using a fluorescent probe equilibrated for 2 hours quantified a thiol-content of 0.7 nmol mg^{-1} in Suwannee River NOM.[62] The non-exchangeable Hg(II)-binding to NOM as compared to Hg(II)-cysteine, where we observed an isotope exchange equilibrium after 16 d, though in both ligand complexes Hg(II) is bound to thiol-groups, could potentially be explained by the difference in coordination of Hg(II). Whereas Hg(II) forms monodentate thiol complexes with cysteine, Hg(II) in NOM is associated to at least two thiol groups[31] and forms bidentate complexes, likely exhibiting a slower exchange rate than monodentate complexes. The additional complexation of Hg(II) in NOM by a third thiol-group, previously suggested by spectroscopic evidence[31, 63] as well as from deprotonation characteristics[64] would further promote this effect. Support for this concept can be derived from the experiment with Hg(II)-EDTA complexes, where the polydentate Hg(II)-binding by EDTA strongly reduced the exchange with the carboxyl-resin. Steric hindrance of the large NOM molecules could potentially further slow down the exchange of Hg-NOM.

5.3.4 Hg(II)-exchange between dissolved inorganic complexes and goethite

The isotope exchange of both experimental series without and with 0.5 mM chloride was initially fast followed by a slower exchange phase reaching a plateau at R/R_{system} ≈ 0.8 after 12 d (Figures 5.3g and h). In the presence of chloride, dissolved Hg(II) occurs as chloro complexes (e.g., $HgCl_2$)[50], previously shown to reduce Hg(II) sorption to goethite.[65, 37] Chloride was further shown to favor the formation of ternary monodentate Hg(II) surface complexes on goethite, whereas in the absence of chloride bidentate Hg(II) surface complexes where shown to dominate.[66, 67] The variations in total Hg concentrations over the course of the experiments (Figure 5.3g) were probably caused by pH instabilities (Table 5.1) because the system was not buffered. Preliminary experiments at pH 7 with a 3-morpholinopropanesulfonic acid (MOPS) buffer showed a continuous net adsorption over the 30 d experiment, as previously reported[37,68], and the isotopic exchange characteristics and the non-exchangeable Hg(II) sorption to goethite was in agreement with the unbuffered data presented here (Figure S5.9).

The results of the isotope exchange phase for both goethite experiments were best described by a model with two exchanging pools (model 2b, Figure 5.2) of goethite-sorbed Hg(II) (presumably a fast outer-sphere complex pool and slower inner-sphere complex pool) and one pool of non-exchangeable Hg(II). Thereby the sorption rate coefficients of the fast exchanging pool have to be treated with caution since the fast initial phase was poorly covered by the sampling scheme. The model results for the experiment without chloride revealed that 29% of the total Hg(II) sorbed to goethite was non-exchangeable, corresponding to 0.19 nmol Hg mg^{-1} goethite (5.0 nmol m^{-2} surface area). The experimental series with 0.5 mM chloride was modeled with an non-exchangeable pool of 22%, corresponding to a non-exchangeable pool of 0.1 nmol Hg mg^{-1} goethite (2.8 nmol m^{-2}). This suggests that, although different Hg(II) complexes were described in the presence of chloride (monodentate) compared to without chloride (bidentate),[66, 67] there were only minor effects of chloride on the amount of non-exchangeable Hg(II). The diffusion into pores of the goethite appeared to be the most probable cause for the observed non-exchangeable pool of Hg(II), since incorporation of Hg(II) into the lattice structure can be excluded for metals with large ionic radii.[23]

5.3.5 Implications of exchange kinetics for laboratory experiments

The time required to reach equilibrium is an essential parameter for the design of experiments considered as thermodynamically-controlled, e.g., for the determination of sorption isotherms[69] or stability constants.[47, 46, 70, 45, 33] Hg(II) has a high affinity for reduced sulfur and was found to be complexed in NOM with two thiol groups at low Hg/NOM ratios, whereas at higher Hg/NOM ratios the coordination of Hg(II) to C/N-atoms was found to dominate[31]. Accordingly, the apparent stability constant (K) for Hg(II) complexation with NOM was shown to decrease with increasing Hg/NOM ratio, suggesting different binding sites in NOM exhibiting different binding affinities for Hg(II).[45] Assuming a 1:2 complexation of Hg(II) with organic thiol-groups in NOM ($Hg^{2+} + 2\ L^{-} = HgL_2$), log K values between 28.5 and 40.4 were reported.[33,46,61,64] Studies determining the stability constant of Hg(II)-NOM complexes typically applied equilibration times between 12 h and 13 d,[33,45–47,61,64,70] however the justification for the chosen equilibration times remained arguable.

Our isotope exchange data suggest that equilibration times chosen in many of the previous experiments may have been too short to reach equilibrium. The observation of a positive correlation of stability constants with equilibration times applied in previous studies (Figure S5.10) supports this argument. Short equilibration times would have the consequence that Hg(II) is partially associated with low affinity binding sites, e.g., carboxyl groups, which are more abundant than high affinity thiol groups and therefore the probability of Hg(II) to first interact with carboxyl groups is higher. This effect, caused by long timescales required for Hg(II) to exchange to the thermodynamically more stable thiol groups, would reduce the observed stability constant similar to the effect observed by increasing the Hg/DOC ratio.[45] These findings suggest that higher stability constants of the reported range (LogK (HgL_2) = 28.5 - 40.4) are probably more representative for Hg(II) binding to thiol-groups in NOM. This would be in agreement with the previous suggestion that Hg complexation by NOM could be modeled by stability constants for LMW thiol complexes[71] (e.g. for cysteine: logK = 42.7, $Hg^{2+} + 2\ L^{2-} = HgL_2^{2-}$, I = 1M).[39]

5.3.6 Implications for isotope fractionation experiments

The investigation of natural Hg isotope variations in environmental samples has a great potential for studying sources and transformation processes in biogeochemical Hg cycling. To interpret Hg isotope signatures of field samples, it is essential to understand the underlying mechanisms causing the observed variations by stable isotope fractionation.[72] Here, we showed that a considerable fraction of Hg(II) was irreversibly bound to thiol-resin, NOM and, goethite with respect to isotope exchange on the investigated timescales of up to one month. In previous studies investigating Hg isotope fractionation during sorption of Hg(II) to thiol-resin[32] and goethite,[37] preconditioning times between 18h and 30d were employed. Similar timescales have been applied in stable isotope fractionation studies investigating the interaction of other metals, such as Cr,[73] Fe,[74] Cu,[75,76] Zn,[77,78] Mo,[79] Cd,[80] Tl,[81] and U[82] with mineral surfaces and NOM. In the case of Hg(II) sorption to goethite, no dependence of isotope fractionation on preconditioning time could be observed[37]. This observation, however, does not imply that the measured isotope signatures represent exclusively equilibrium isotope effects. We suggest that results from isotope fractionation studies between dissolved and sorbed phases, where part of the isotopes are bound to a non-exchangeable pool, are composed of two signals: (i) a kinetic isotope effect from the first initial adsorption to the non-exchangeable pool, and (ii) an equilibrium isotope effect between the dissolved and the exchangeable pool.

Based on constant metal concentration and/or isotope signature in solution over time, previous studies concluded that the observed isotope fractionation must derive from an equilibrium isotope effect.[76–79,81,82] We suggest that this argumentation needs to be revisited since the possibility of a kinetic isotope fractionation signal, trapped in a non-exchangeable pool, has not been considered before. In the case of Hg isotope fractionation during sorption of Hg(II) to thiol-resin[32] and to goethite,[37] kinetic isotope effects have presumably played a minor role, since the observed isotope effects were in good agreement with theoretical equilibrium isotope effects calculated for the relevant Hg(II) species in the specific system.

Therefore, in order to derive an equilibrium isotope fractionation factor from the isotopic difference between a dissolved and a sorbed pool, it is essential to experimentally show that the investigated system is in isotopic equilibrium. Isotope exchange experiments using enriched isotopes as previously applied[26,74] and presented here represent a suitable method to assess the timescales required to reach equilibrium. Alternatively, the three-isotope method[83,84] employing an enriched spike allows the simultaneous determination of equilibrium fractionation factors and timescales needed to reach equilibrium.

Finally, this postulated coexistence of two isotopic signals in different sorbed pools needs to be considered in the interpretation of measured metal isotope data from laboratory and field studies.

5.3.7 Environmental implications

The finding that Hg(II) can be bound in a non-exchangeable manner to NOM and mineral surfaces, over timescales of months has at least two important implications for the fate of Hg(II) in the environment: (i) systems which are at equilibrium are capable of sequestering Hg(II) over long timescales, in forms that are likely unavailable for uptake into organisms, and (ii) in systems which are not at equilibrium, Hg(II) associated partially to low-affinity binding sites (e.g., high abundance carboxyl groups in NOM) may exchange rapidly with dissolved Hg(II) and can lead to a higher availability and reactivity of Hg(II) than expected from the thermodynamic stability with high-affinity binding sites in NOM. Environmental changes such as a drop in pH or redox potential and organic matter degradation might result in a higher reactivity of Hg(II) as expected from desorption rates investigated under constant conditions in this study. In conclusion, kinetic constraints have to be considered to a greater extent in future studies investigating and modeling the fate of Hg(II) in natural systems.

Acknowledgments

We thank Kurt Barmettler for technical assistance in the Soil Chemistry laboratory. We are grateful to Ulf Skyllberg for his valuable input and three anonymous reviewers for their helpful comments. M.J. acknowledges the FIMIN Reseach Network Programme funded by the European Science Foundation for an Exchange Visit Grant. This research was funded by a research grant from ETH Zurich (ETH-15 09-2).

References to Chapter 5

[1] H. Hsu-Kim, K. H. Kucharzyk, T. Zhang, and M. A. Deshusses. Mechanisms regulating mercury bioavailability for methylating microorganisms in the aquatic environment: a critical review. *Environ. Sci. Technol.*, 47(6):2441–2456, 2013.

[2] M. C. Gabriel and D. G. Williamson. Principal biogeochemical factors affecting the speciation and transport of mercury through the terrestrial environment. *Environ. Geochem. Health*, 26(4):421–434, 2004.

[3] G. R. Aiken, H. Hsu-Kim, and J. N. Ryan. Influence of dissolved organic matter on the environmental fate of metals, nanoparticles, and colloids. *Environ. Sci. Technol.*, 45(8):3196–201, 2011.

[4] J. M. Benoit, C. C. Gilmour, R. P. Mason, and A. Heyes. Sulfide controls on mercury speciation and bioavailability to methylating bacteria in sediment pore waters. *Environ. Sci. Technol.*, 33(6):951–957, 1999.

[5] J. K. Schaefer and F. M. M. Morel. High methylation rates of mercury bound to cysteine by geobacter sulfurreducens. *Nat. Geosci.*, 2(2):123–126, 2009.

[6] J. K. Schaefer, S. S. Rocks, W. Zheng, L. Liang, B. Gu, and F. M. M. Morel. Active transport, substrate specificity, and methylation of Hg(II) in anaerobic bacteria. *Proc. Natl. Acad. Sci. U.S.A.*, 108(21):8714–8719, 2011.

[7] J. K. Schaefer, A. Szczuka, and F. M. M. Morel. Effect of divalent metals on Hg(II) uptake and methylation by bacteria. *Environ. Sci. Technol.*, 48(5):3007–3013, 2014.

[8] A. M. Graham, G. R. Aiken, and C. C. Gilmour. Dissolved organic matter enhances microbial mercury methylation under sulfidic conditions. *Environ. Sci. Technol.*, 46(5):2715–2723, 2012.

[9] T. Zhang, B. Kim, C. Leyard, B. C. Reinsch, G. V. Lowry, M. A. Deshusses, and H. Hsu-Kim. Methylation of mercury by bacteria exposed to dissolved, nanoparticulate, and microparticulate mercuric sulfides. *Environ. Sci. Technol.*, 46(13):6950–6958, 2012.

[10] A. M. Graham, G. R. Aiken, and C. C. Gilmour. Effect of dissolved organic matter source and character on microbial Hg methylation in Hg-S-DOM solutions. *Environ. Sci. Technol.*, 47(11):5746–5754, 2013.

[11] T. Zhang, K. H. Kucharzyk, B. Kim, M. A. Deshusses, and H. Hsu-Kim. Net methylation of mercury in estuarine sediment microcosms amended with dissolved, nanoparticulate, and microparticulate mercuric sulfides. *Environ. Sci. Technol.*, 48(16):9133–9141, 2014.

[12] S. Jonsson, U. Skyllberg, M. B. Nilsson, P. O. Westlund, A. Shchukarev, E. Lundberg, and E. Bjorn. Mercury methylation rates for geochemically relevant Hg-II species in sediments. *Environ. Sci. Technol.*, 46(21):11653–11659, 2012.

[13] S. Jonsson, U. Skyllberg, M. B. Nilsson, E. Lundberg, A. Andersson, and E. Bjorn. Differentiated availability of geochemical mercury pools controls methylmercury levels in estuarine sediment and biota. *Nat. Commun.*, 5:4624, 2014.

[14] H. Hsu and D. L. Sedlak. Strong Hg(II) complexation in municipal wastewater effluent and surface waters. *Environ. Sci. Technol.*, 37(12):2743–2749, 2003.

[15] C. L. Miller, L. Y. Liang, and B. H. Gu. Competitive ligand exchange reveals time dependant changes in the reactivity of Hg-dissolved organic matter complexes. *Environ. Chem.*, 9(6):495–501, 2012.

[16] C. L. Miller, G. Southworth, S. Brooks, L. Liang, and B. Gu. Kinetic controls on the complexation between mercury and dissolved organic matter in a contaminated environment. *Environ. Sci. Technol.*, 43(22):8548–8553, 2009.

[17] S. A. Chiasson-Gould, J. M. Blais, and A. J. Poulain. Dissolved organic matter kinetically controls mercury bioavailability to bacteria. *Environ. Sci. Technol.*, 48(6):3153–61, 2014.

[18] H. Hintelmann, K. Keppel-Jones, and R. D. Evans. Constants of mercury methylation and demethylation rates in sediments and comparison of tracer and ambient mercury availability. *Environ. Toxicol. Chem.*, 19(9):2204–2211, 2000.

[19] H. Hintelmann and R. Harris. Application of multiple stable mercury isotopes to determine the adsorption and desorption dynamics of Hg(II) and MeHg to sediments. *Mar. Chem.*, 90(1-4):165–173, 2004.

[20] B. R. Coughlin and A. T. Stone. Nonreversible adsorption of divalent metal ions (Mn^{II}, Co^{II}, Ni^{II}, Cu^{II}, and Pb^{II}) onto goethite: Effects of acidification, Fe^{II} addition, and picolinic acid addition. *Environ. Sci. Technol.*, 29(9):2445–2455, 1995.

[21] Y. J. Yin, H. E. Allen, C. P. Huang, D. L. Sparks, and P. F. Sanders. Kinetics of mercury(II) adsorption and desorption on soil. *Environ. Sci. Technol.*, 31(2):496–503, 1997.

[22] L. Liao, H. M. Selim, and R. D. DeLaune. Mercury adsorption-desorption and transport in soils. *J. Environ. Qual.*, 38(4):1608–1616, 2009.

[23] N. J. Barrow, G. W. Brümmer, and L. Fischer. Rate of desorption of eight heavy metals from goethite and its implications for understanding the pathways for penetration. *Eur. J. Soil Sci.*, 63(3):389–398, 2012.

[24] P. Benes, P. Picat, M. Cernik, and J. M. Quinault. Kinetics of radionuclide interaction with suspended-solids in modeling the migration of radionuclides in rivers. 1. parameters for 2-step kinetics. *J. Radioanal. Nucl. Chem.*, 159(2):175–186, 1992.

[25] P. Ciffroy, J. M. Garnier, and M. K. Pham. Kinetics of the adsorption and desorption of radionuclides of Co, Mn, Cs, Fe, Ag and Cd in freshwater systems: experimental and modelling approaches. *J. Environ. Radioact.*, 55(1):71–91, 2001.

[26] C. M. Johnson, J. L. Skulan, B. L. Beard, H. Sun, K. H. Nealson, and P. S. Braterman. Isotopic fractionation between Fe(III) and Fe(II) in aqueous solutions. *Earth Planet. Sci. Lett.*, 195(1-2):141–153, 2002.

[27] E. Smolders, K. Brans, A. Foldi, and R. Merckx. Cadmium fixation in soils measured by isotopic dilution. *Soil Sci. Soc. Am. J.*, 63(1):78–85, 1999.

[28] S. D. Young, A. Tye, A. Carstensen, L. Resende, and N. Crout. Methods for determining labile cadmium and zinc in soil. *Eur. J. Soil Sci.*, 51(1):129–136, 2000.

[29] R. E. Hamon, D. R. Parker, and E. Lombi. Advances in isotopic dilution techniques in trace element research: a review of methodologies, benefits, and limitations. *Adv. Agron.*, 99:289–343, 2008.

[30] Y. Sivry, J. Riotte, V. Sappin-Didier, M. Munoz, PO. Redon, L. Denaix, and B. Dupré. Multi-elementary (Cd, Cu, Pb, Zn, Ni) stable isotopic exchange kinetic (SIEK) method to characterize polymetallic contaminations. *Environ. Sci. Technol.*, 45(15):6247–6253, 2011.

[31] U. Skyllberg, P. R. Bloom, J. Qian, C. M. Lin, and W. F. Bleam. Complexation of mercury(II) in soil organic matter: EXAFS evidence for linear two-coordination with reduced sulfur groups. *Environ. Sci. Technol.*, 40(13):4174–4180, 2006.

[32] J. G. Wiederhold, C. J. Cramer, K. Daniel, I. Infante, B. Bourdon, and R. Kretzschmar. Equilibrium mercury isotope fractionation between dissolved Hg(II) species and thiol-bound Hg. *Environ. Sci. Technol.*, 44(11):4191–4197, 2010.

[33] W. Dong, Y. Bian, L. Liang, and B. Gu. Binding constants of mercury and dissolved organic matter determined by a modified ion exchange technique. *Environ. Sci. Technol.*, 45(8):3576–3583, 2011.

[34] U. Schwertmann and R.M. Cornell. *Iron Oxides in the Laboratory - Preparation and Characterisation.* Wiley-VCH, Weinheim, 2nd, edition, 2000.

[35] P. U. Reichard, S. M. Kraemer, S. W. Frazier, and R. Kretzschmar. Goethite dissolution in the presence of phytosiderophores: rates, mechanisms, and the synergistic effect of oxalate. *Plant Soil*, 276(1-2):115–132, 2005.

[36] J. G. Wiederhold, S. M. Kraemer, N. Teutsch, P. M. Borer, A. N. Halliday, and R. Kretzschmar. Iron isotope fractionation during proton-promoted, ligand-controlled, and reductive dissolution of goethite. *Environ. Sci. Technol.*, 40(12):3787–3793, 2006.

[37] M. Jiskra, J. G. Wiederhold, B. Bourdon, and R. Kretzschmar. Solution speciation controls mercury isotope fractionation of Hg(II) sorption to goethite. *Environ. Sci. Technol.*, 46(12):6654–62, 2012.

[38] T. Karlsson, P. Persson, and U. Skyllberg. Extended X-ray absorption fine structure spectroscopy evidence for the complexation of cadmium by reduced sulfur groups in natural organic matter. *Environ. Sci. Technol.*, 39(9):3048–3055, 2005.

[39] J. Stary and K. Kratzer. Radiometric determination of stability-constants of mercury species complexes with L-cysteine. *J. Radioanal. Nucl. Chem.*, 126(1):69–75, 1988.

[40] G. Anderegg. Polynuclear complexes of the EDTA analogues. *Anal. Chim. Acta*, 394(2-3):345–352, 1999.

[41] J. Z. Zhang, F. Y. Wang, J. D. House, and B. Page. Thiols in wetland interstitial waters and their role in mercury and methylmercury speciation. *Limnol. Oceanogr.*, 49(6):2276–2286, 2004.

[42] W. Stumm and J. J. Morgan. *Aquatic Chemistry: Chemical Equilibria and Rates in Natural Waters.* Series: Environmental science and technology. New York, Wiley, third ed. edition, 1996.

[43] R. K. Zalups and D. W. Barfuss. Nephrotoxicity of inorganic mercury co-administered with L-cysteine. *Toxicology*, 109(1):15–29, 1996.

[44] W. Zheng, H. Lin, B. F. Mann, L. Liang, and B. Gu. Oxidation of dissolved elemental mercury by thiol compounds under anoxic conditions. *Environ. Sci. Technol.*, 47(22):12827–12834, 2013.

[45] M. Haitzer, G. R. Aiken, and J. N. Ryan. Binding of mercury(II) to dissolved organic matter: The role of the mercury-to-DOM concentration ratio. *Environ. Sci. Technol.*, 36(16):3564–3570, 2002.

[46] F. J. Black, K. W. Bruland, and A. R. Flegal. Competing ligand exchange-solid phase extraction method for the determination of the complexation of dissolved inorganic mercury(II) in natural waters. *Anal. Chim. Acta*, 598(2):318–333, 2007.

[47] J. D. Gasper, G. R. Aiken, and J. N. Ryan. A critical review of three methods used for the measurement of mercury (Hg^{2+})-dissolved organic matter stability constants. *Appl. Geochem.*, 22(8):1583–1597, 2007.

[48] F. Jalilehvand, B. O. Leung, M. Izadifard, and E. Damian. Mercury(II) cysteine complexes in alkaline aqueous solution. *Inorg. Chem.*, 45(1):66–73, 2006.

[49] J. Watts, E. Howell, and J. K. Merle. Theoretical studies of complexes between Hg(II) ions and L-cysteinate amino acids. *Int. J. Quantum Chem.*, 114(5):333–339, 2014.

[50] K. J. Powell, P. L. Brown, R. H. Byrne, T. Gajda, G. Hefter, S. Sjoberg, and H. Wanner. Chemical speciation of Hg(II) with environmental inorganic ligands. *Aust. J. Chem.*, 57(10):993–1000, 2004.

[51] M. Sargent, R. Harte, and C. Harrington. *Guidelines for Achieving High Accuracy in Isotope Dilution Mass Spectrometry (IDMS)*, volume 1. The Royal Society of Chemistry, 2002.

[52] J. Qvarnstrom and W. Frech. Mercury species transformations during sample pre-treatment of biological tissues studied by HPLC-ICP-MS. *J. Anal. At. Spectrom.*, 17(11):1486–1491, 2002.

[53] H. Hintelmann and N. Ogrinc. *Determination of stable mercury isotopes by ICP/MS and their application in environmental studies*, volume 835 of *ACS Symposium Series*, pages 321–338. Amer. Chem. Soc., Washington, 2003.

[54] T. Larsson, E. Bjorn, and W. Frech. Species specific isotope dilution with on line derivatisation for determination of gaseous mercury species. *J. Anal. At. Spectrom.*, 20(11):1232–1239, 2005.

[55] J. Voss. *An Introduction to Statistical Computing: A Simulation-based Approach.* John Wiley & Sons, United Kingdom, 2014.

[56] H. Xue, L. Sigg, and F. G. Kari. Speciation of EDTA in natural waters: exchange kinetics of Fe-EDTA in river water. *Environ. Sci. Technol.*, 29(1):59–68, 1995.

[57] U. Skyllberg, K. Xia, P. R. Bloom, E. A. Nater, and W. F. Bleam. Binding of mercury(II) to reduced sulfur in soil organic matter along upland-peat soil transects. *J. Environ. Qual.*, 29(3):855–865, 2000.

[58] E. M. Thurman, R. L. Malcolm, and G. R. Aiken. Prediction of capacity factors for aqueous organic solutes adsorbed on a porous acrylic resin. *Anal. Chem.*, 50(6):775–779, 1978.

[59] J. J. Alberts, J. E. Schindle, R. W. Miller, and D. E. Nutter. Elemental mercury evolution mediated by humic acid. *Science*, 184(4139):895–896, 1974.

[60] B. Gu, Y. Bian, C. L. Miller, W. Dong, X. Jiang, and L. Liang. Mercury reduction and complexation by natural organic matter in anoxic environments. *Proc. Natl. Acad. Sci. U.S.A.*, 108(4):1479–1483, 2011.

[61] M. Haitzer, G. R. Aiken, and J. N. Ryan. Binding of mercury(II) to aquatic humic substances: Influence of pH and source of humic substances. *Environ. Sci. Technol.*, 37(11):2436–2441, 2003.

[62] B. Rao, C. Simpson, H. Lin, L. Liang, and B. Gu. Determination of thiol functional groups on bacteria and natural organic matter in environmental systems. *Talanta*, 119(0):240–247, 2014.

[63] K. L. Nagy, A. Manceau, J. D. Gasper, J. N. Ryan, and G. R. Aiken. Metallothionein-like multinuclear clusters of mercury(II) and sulfur in peat. *Environ. Sci. Technol.*, 45(17):7298–7306, 2011.

[64] A. R. Khwaja, P. R. Bloom, and P. L. Brezonik. Binding constants of divalent mercury (Hg^{2+}) in soil humic acids and soil organic matter. *Environ. Sci. Technol.*, 40(3):844–849, 2006.

[65] N. J. Barrow and V. C. Cox. The effects of pH and chloride concentration on mercury sorption. I. by goethite. *J. Soil Sci.*, 43(2):295–304, 1992.

[66] C. S. Kim, J. J. Rytuba, and Jr. Brown, G. E. EXAFS study of mercury(II) sorption to Fe- and Al-(hydr)oxides I. effects of pH. *J. Colloid Interface Sci.*, 271(1):1–15, 2004.

[67] C. S. Kim, J. Rytuba, and Jr. Brown, G. E. EXAFS study of mercury(II) sorption to Fe- and Al-(hydr)oxides - II. effects of chloride and sulfate. *J. Colloid Interface Sci.*, 270(1):9–20, 2004.

[68] L. Fischer, G. W. BrG'Ommer, and N. J. Barrow. Observations and modelling of the reactions of 10 metals with goethite: adsorption and diffusion processes. *Eur. J. Soil Sci.*, 58(6):1304–1315, 2007.

[69] G. Limousin, J. P. Gaudet, L. Charlet, S. Szenknect, V. Barthes, and M. Krimissa. Sorption isotherms: A review on physical bases, modeling and measurement. *Appl. Geochem.*, 22(2):249–275, 2007.

[70] C. H. Lamborg, C. M. Tseng, W. F. Fitzgerald, P. H. Balcom, and C. R. Hammerschmidt. Determination of the mercury complexation characteristics of dissolved organic matter in natural waters with "reducible Hg" titrations. *Environ. Sci. Technol.*, 37(15):3316–3322, 2003.

[71] U. Skyllberg. Competition among thiols and inorganic sulfides and polysulfides for Hg and MeHg in wetland soils and sediments under suboxic conditions: Illumination of controversies and implications for MeHg net production. *J. Geophys. Res.*, 113, 2008.

[72] J. E. Sonke, L. E. Heimburger, and A. Dommergue. Mercury biogeochemistry: paradigm shifts, outstanding issues and research needs. *C. R. Geosci.*, 345(5-6):213–224, 2013.

[73] A. S. Ellis, T. M. Johnson, and T. D. Bullen. Using chromium stable isotope ratios to quantify Cr(VI) reduction: lack of sorption effects. *Environ. Sci. Technol.*, 38(13):3604–3607, 2004.

[74] J. L. L. Morgan, L. E. Wasylenki, J. Nuester, and A. D. Anbar. Fe isotope fractionation during equilibration of Fe-organic complexes. *Environ. Sci. Technol.*, 44(16):6095–6101, 2010.

[75] M. Bigalke, S. Weyer, and W. Wilcke. Copper isotope fractionation during complexation with insolubilized humic acid. *Environ. Sci. Technol.*, 44(14):5496–5502, 2010.

[76] B. M. Ryan, J. K. Kirby, F. Degryse, K. Scheiderich, and M. J. McLaughlin. Copper isotope fractionation during equilibration with natural and synthetic ligands. *Environ. Sci. Technol.*, 48(15):8620–8626, 2014.

[77] F. Juillot, C. Marechal, M. Ponthieu, S. Cacaly, G. Morin, M. Benedetti, J. L. Hazemann, O. Proux, and F. Guyot. Zn isotopic fractionation caused by sorption on goethite and 2-lines ferrihydrite. *Geochim. Cosmochim. Acta*, 72(19):4886–4900, 2008.

[78] D. Jouvin, P. Louvat, F. Juillot, C. N. Marechal, and M. F. Benedetti. Zinc isotopic fractionation: why organic matters. *Environ. Sci. Technol.*, 43(15):5747–5754, 2009.

[79] L. E. Wasylenki, B. A. Rolfe, C. L. Weeks, T. G. Spiro, and A. D. Anbar. Experimental investigation of the effects of temperature and ionic strength on Mo isotope fractionation during adsorption to manganese oxides. *Geochim. Cosmochim. Acta*, 72(24):5997–6005, 2008.

[80] L. E. Wasylenki, J. W. Swihart, and S. J. Romaniello. Cadmium isotope fractionation during adsorption to Mn oxyhydroxide at low and high ionic strength. *Geochim. Cosmochim. Acta*, 140(0):212–226, 2014.

[81] S. G. Nielsen, L. E. Wasylenki, M. Rehkamper, C. L. Peacock, Z. C. Xue, and E. M. Moon. Towards an understanding of thallium isotope fractionation during adsorption to manganese oxides. *Geochim. Cosmochim. Acta*, 117:252–265, 2013.

[82] G. A. Brennecka, L. E. Wasylenki, J. R. Bargar, S. Weyer, and A. D. Anbar. Uranium isotope fractionation during adsorption to Mn-oxyhydroxides. *Environ. Sci. Technol.*, 45(4):1370–1375, 2011.

[83] Y. Matsuhisa, J. R. Goldsmith, and R. N. Clayton. Mechanisms of hydrothermal crystallization of quartz at 250°c and 150 kbar. *Geochim. Cosmochim. Acta*, 42(2):173–182, 1978.

[84] A. J. Frierdich, B. L. Beard, T. R. Reddy, M. M. Scherer, and C. M. Johnson. Iron isotope fractionation between aqueous Fe(II) and goethite revisited: New insights based on a multi-direction approach to equilibrium and isotopic exchange rate modification. *Geochim. Cosmochim. Acta*, 139(0):383–398, 2014.

Chapter 6

Conclusions and outlook

The goal of this thesis was to develop Hg stable isotopes as tool to investigate terrestrial Hg cycling. Thereby two complementary approaches were chosen. In Chapter 2 and 3 stable Hg isotopes in boreal forest soils were investigated in a field study. In Chapter 4 and 5 Hg stable isotope fractionation and kinetic Hg(II) exchange between dissolved and solid-bound Hg(II) was studied in laboratory experiments. This chapter provides a synthesis of the outcome of this thesis with most recent literature. Thereby the results will be discussed in the perspective of which insights stable Hg isotopes can provide on terrestrial Hg cycling and what the implications are for metal isotope fractionation studies in general. Furthermore, an outlook on further research needs and potential limitations of the approaches chosen in this thesis is provided.

6.1 Mechanistic studies of stable isotope fractionation during sorption

Stable isotope fractionation during metal sorption to mineral phases has been studied for several metal isotope systems. For sorption of Cu(II),[1,2] Zn(II),[2,3] and Fe(II)[4,5] to iron- and aluminum-oxides a preferential sorption of heavy metal isotopes was reported. These observations were interpreted by an equilibrium isotope effect based on the theory that the sorbed metal ions have a stronger bonding environment and thus lower zero-point energy compared to dissolved ions, favoring the preferential sorption of heavy isotopes to the mineral surface.[2,6] Studies on sorption of anionic metal species[7–9] and an increasing number of observations on cationic metal species[10–12] reported a preferential sorption of lighter isotopes to mineral surfaces, indicating a more complex cause of stable isotope fractionation observed during sorption.

Figure 6.1 provides an overview of possible isotope effects causing stable isotope fractionation during sorption for the example of Hg(II) sorption to goethite. The two major findings of stable Hg isotope fractionation experiments during Hg(II) sorption to goethite (Chapter 4) and the isotope exchange experiments (Chapter 5) were:

1. Sorption of Hg(II) to goethite, investigated in Chapter 4, was associated with a preferential sorption of light Hg isotopes to the solid surface. We concluded that the observed isotope fractionation between dissolved Hg(II) and solid-bound Hg(II) was originating from an equilibrium isotope effect between different solution species, where the cationic species, occurring in low abundance in solution, is sorbing to the

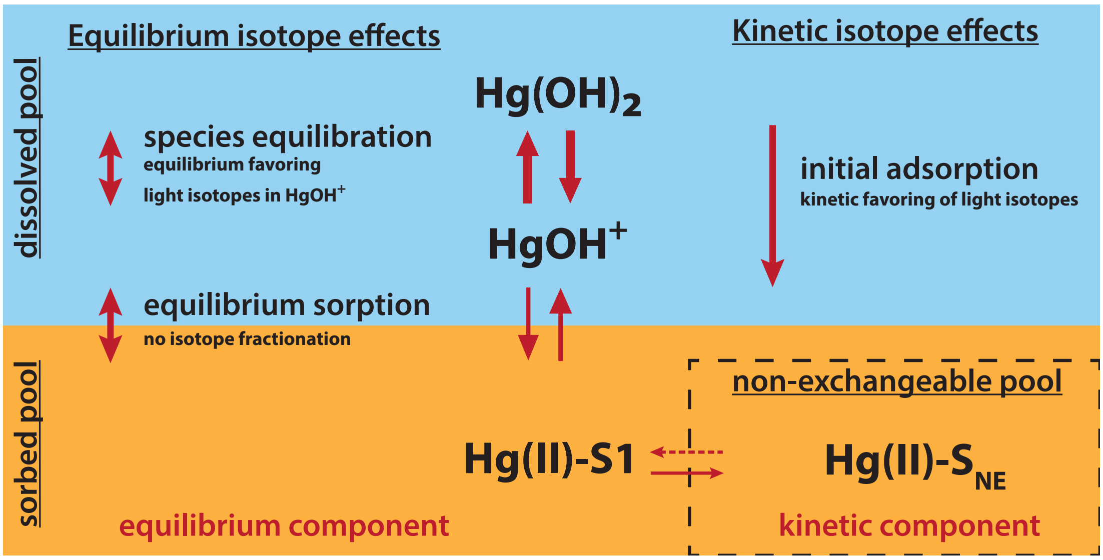
Equilibrium isotope effects
Kinetic isotope effects
dissolved pool
Hg(OH)2
species equilibration
equilibrium favoring
light isotopes in HgOH+
initial adsorption
kinetic favoring of light isotopes
HgOH+
equilibrium sorption
no isotope fractionation
non-exchangeable pool
sorbed pool
Hg(II)-S1
Hg(II)-SNE
equilibrium component
kinetic component

Figure 6.1: Schematic overview about the control of equilibrium and kinetic isotope effects on stable isotope fractionation during metal sorption to solid phases: Example of Hg(II) sorption to goethite. Hg(II)-S1 and Hg(II)-S_{NE} represent the exchangeable and non-exchangeable solid-bound Hg pool, respectively.

goethite surface. In principle, any metal with different solution species can exhibit an isotope fractionation between the dissolved phase and the sorbed phase if the species equilibration in solution is associated with an equilibrium isotope effect and there are different sorption affinities for the different species. The net isotope effect between the sorbed and dissolved pool ($\epsilon_{\text{sorbed}-\text{dissolved}}$) thereby depends on the equilibrium isotope effect of species equilibration ($\epsilon_{\text{species equilibration}}$), the equilibrium isotope effect during sorption ($\epsilon_{\text{sorption}}$), and on the fraction of the actively sorbing species (f_{ASS}) according to equation 6.1 (adapted from equation 4.11 in chapter 4).

$$\epsilon^{202}\text{Hg}_{\text{sorbed}-\text{dissolved}} = \epsilon^{202}\text{Hg}_{\text{sorption}} + (1 - f_{\text{ASS}})\epsilon^{202}\text{Hg}_{\text{species equilibration}} \tag{6.1}$$

The solution speciation is mainly a function of pH and dissolved ligands (e.g., chloride). Depending on the speciation of the metal an equilibrium isotope effect of species equilibration can be expressed on the solid-bound pool during sorption. At neutral pH the actively sorbing cationic Hg(II) species occur at very low abundances, therefore the equilibrium isotope effect between the dominant neutral $Hg(OH)_2$ species and the low abundant $Hg(OH)^+$ species can be entirely expressed during sorption (Chapter 4). Zn on the other hand is predominantly present as Zn^{2+} in solution around pH 7,[13] thus in this case solution speciation can be neglected as potential cause for isotope fractionation.

2. The isotope exchange between dissolved $Hg(II)_{aq}$ and goethite-bound Hg(II), investigated in Chapter 5, revealed that a significant fraction of solid-bound Hg was sorbed to a non-exchangeable pool. We concluded that in the presence of a non-exchangeable pool an isotope effect between dissolved and solid-bound Hg(II) can consist of: (i) a signal trapped in the non-exchangeable pool with a kinetic component from the initial adsorption, and (ii) a signal of the exchangeable pool consisting of the equilibrium isotope effect between the dissolved species and the solid-bound exchangeable Hg (Figure 6.1).

The implications of the findings on sorption to goethite and NOM are not limited to Hg(II). For many bivalent metals irreversible sorption to goethite has been reported,[14,15] and solution speciation of several metals[16–20] was theoretically shown to be associated with a fractionation of the stable metal isotopes. Therefore the two potentially co-existing pools of solid-bound metal ions exhibiting different isotope fractionation signals (Figure 6.1) should be considered in further studies on metal isotope fractionation during sorption.

6.1.1 Outlook on future studies on metal isotope fractionation during sorption

In order to postulate an equilibrium isotope effect from the experimentally measured difference in isotope signatures between a dissolved and adsorbed phase, one needs to demonstrate that isotopic equilibrium was established. Constant dissolved concentration or constant isotope signatures over time, previously interpreted as proof for isotopic equilibrium[3,7,21–24] provide a non-conclusive assessment since the potential presence of a non-exchangeable pool is not considered. The determination of isotopic equilibrium requires more sophisticated diagnostic approaches like isotope exchange experiments performed in chapter 5 or elsewhere[25,26] or the three-isotope method allowing a simultaneous determination of equilibrium fractionation factors and timescales required to reach equilibrium.[27,28]

Given that there are many processes potentially causing metal isotope fractionation between dissolved and sorbed phases (Figure 6.1) the evaluation of the cause for an observed isotope effect in an experiment is challenging. Theoretical calculations of equilibrium fractionation factors are increasingly available for different dissolved species[16–20,29] and recently also for solid phases.[30,31] A combination of experimental results with spectroscopic observations and theoretical calculations offers the most integrative and promising approach to elucidate the mechanism causing metal stable isotope fractionation during sorption.

The difficulty to reach equilibrium in experimental studies highlights the question on the importance of equilibrium conditions for the fate of metals in the environment. Many problems concerning metal pollution dynamics in the environment have time scales similar to the time scales employed in laboratory experiments. Therefore, if equilibrium isotope fractionation factors are employed for the interpretation of environmental problems the question has to be raised again whether equilibrium conditions are prevailing or whether kinetic effects or non-exchangeable pools have to be considered for the interpretation of environmental observations.

6.2 Assessing terrestrial mercury cycling with stable Hg isotopes

The stable Hg isotope composition of soils from North America and China was reported to be enriched in light Hg isotopes (negative δ^{202}Hg values) and depleted in odd-mass isotopes (negative Δ^{199}Hg values),[32–34] which is in agreement with the Hg isotope signatures measured in boreal forest soils from northern Sweden in this thesis (Chapter 2 and Chapter 3). Hg isotope signatures of geogenic background appear to be distinct from Hg isotope signatures measured in precipitation and foliage,[35] suggesting the potential to trace the source contributions of precipitation- and litter-derived Hg and geogenic background. Demers et al.[33] and Zhang et al.[34] have successfully applied mixing models to calculate the contribution of geogenic and atmospherically-derived Hg in soils. In the organic soil horizons of boreal forest soils investigated in this thesis the contribution of Hg from geogenic background was negligible, suggesting that in these organic soils the large majority of Hg in the soil horizons derived from atmospheric deposition. The separation of atmospheric deposition into precipitation-derived and litter-derived Hg, which was also applied in the study of Demers et al.,[33] allowed to describe the source of Hg in the boreal forest soil samples, which appeared to be not affected by secondary processes.

Figure 6.2a provides an overview of biogeochemical processes in soils and their MDF, given as enrichment factors ϵ^{202}Hg (Equation 1.5). Demers et al.[33] concluded from parallel measurements of atmospheric Hg and Hg in foliage, that the uptake of Hg through stomata of plants was associated with a fractionation of -2.9‰ in δ^{202}Hg. Sorption of Hg(II) to thiol groups[29] and goethite (Chapter 4), microbial methylation of Hg(II) to methyl-Hg,[36] and reduction of Hg(II) to volatile Hg(0)[37–39] were experimentally shown to be associated with an enrichment of light Hg isotopes in the product. Hg re-emission from soils has been measured with a flux chamber in Wisconsin, USA and did not show any significant Hg isotope fractionation compared to atmospheric isotope composition.[33] The residual Hg isotope composition in boreal forest soils investigated in this thesis (Chapter 2), provided evidence for significant organic matter-driven reductive Hg loss, which would be expected to result in an enrichment of light Hg isotopes in the re-emitted Hg. Finally, the runoff from boreal forest soils did not provide any evidence for systematic fractionation of Hg isotopes during leaching compared to the source soil pool (Chapter 3).

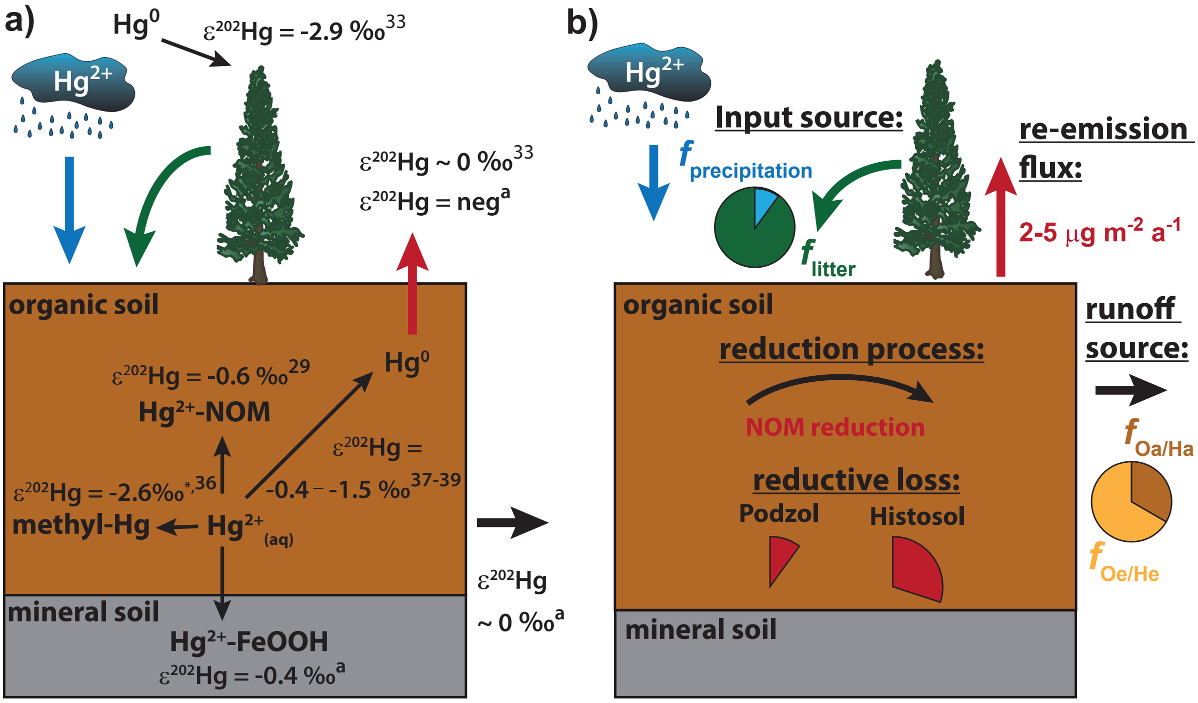
a)
Hg⁰
ε²⁰²Hg = -2.9 ‰³³
Hg²⁺
ε²⁰²Hg ~ 0 ‰³³
ε²⁰²Hg = negᵃ
organic soil
ε²⁰²Hg = -0.6 ‰²⁹
Hg²⁺-NOM
Hg⁰
ε²⁰²Hg =
-0.4 - -1.5 ‰³⁷⁻³⁹
ε²⁰²Hg = -2.6‰*,³⁶
methyl-Hg
Hg²⁺(aq)
mineral soil
Hg²⁺-FeOOH
ε²⁰²Hg = -0.4 ‰ᵃ
ε²⁰²Hg
~ 0 ‰ᵃ
b)
Hg²⁺
Input source:
f precipitation
f litter
re-emission flux:
2-5 µg m⁻² a⁻¹
organic soil
reduction process:
NOM reduction
reductive loss:
Podzol
Histosol
mineral soil
runoff source:
f Oa/Ha
f Oe/He

Figure 6.2: Synthesis of stable Hg isotope fractionation associated with terrestrial mercury cycling: (**a**) MDF enrichment factors (ϵ^{202}Hg) of known processes/reactions. Data from Literature (see reference numbers) and this thesis: a, * under exponential growth conditions. (**b**) Major findings of this thesis (Chapter 2 and 3). Using Hg stable isotopes the source of atmospheric Hg input, the source of Hg in soil runoff, and reduction pathways were investigated and reductive loss and re-emission fluxes were quantified.

Figure 6.2b summarizes major findings about the fate of Hg in boreal forest soils gained from the investigation of stable Hg isotopes signatures, which in particular provided insights to:

1. The source of atmospheric Hg deposition. Based on distinct Hg isotope source signatures for litter-derived and precipitation-derived Hg, the contribution of different Hg deposition pathways to the soil Hg pool could be calculated with a mixing model. The results suggested that litter-derived Hg dominated the Hg-deposition (up to 95 % in organic topsoils) and that the fraction of precipitation-derived Hg increased with soil age up to 20 % in deeper mineral soil horizons of Podzols (Chapter 2).

2. The Hg source in the runoff from boreal forest soils. The comparison of the Hg isotope signature in catchment runoff with Hg pools of the different soil horizons revealed that the runoff is dominated by Hg from the organic topsoils ($60 - 85$ %). The underlying more decomposed organic soil horizons exhibited an at least 5 times lower Hg mobility compared to the uppermost soil horizons (Chapter 3).

3. Secondary processes causing reductive Hg loss from boreal forest soils. The variation of stable Hg isotope signatures in boreal forest soils provided strong evidence for organic matter-driven reductive Hg loss. Using the distinct fractionation trajectory for non-photochemical abiotic reduction by organic matter in model calculations, the reductive loss could be quantified suggesting that in poorly drained Histosols up to 30 % of previously deposited Hg is re-emitted to the atmosphere, corresponding to re-emission fluxes of $\approx 5\ \mu\text{g m}^{-2}\ \text{a}^{-1}$.

The establishment of a mass balance for Hg in soils based on concentration and flux measurements represents a great challenge because all potential Hg fluxes have to be determined. Additionally, in organic soils the total mass loss by carbon mineralization has to be considered. Despite the limited number of studies performed on terrestrial Hg,[33,34] the investigation of Hg stable isotopes in soils has already provided important new insights in the sources of Hg deposition and secondary loss processes. Hg stable isotope analysis offers a high potential to assess processes and fluxes controlling the fate of Hg in terrestrial ecosystems, which are hardly assessable by means of concentration measurements. However, the exploitation of the potential of Hg stable isotope analysis warrants more in-depth studies to further constrain the mechanisms controlling Hg stable isotope signatures in terrestrial environments.

6.2.1 Outlook for terrestrial Hg cycling

In order to investigate secondary processes in soils by means of Hg stable isotope fractionation, it is essential to constrain the Hg isotope signatures of the sources and their relative contributions. For the assessment of the geogenic background, the Hg isotope composition of mineral soils do not represent a reliable end-member because observations based on Hg stable isotope signatures (Chapter 2) and elemental ratios[40] suggested that precipitation-derived Hg had been accumulated in mineral soil horizons over time. The Hg isotope composition of the geogenic background should be therefore assessed by the analysis of bedrock material.

The successful evaluation of stable Hg isotope signatures in terrestrial environments depends on accurate Hg isotope fractionation factors for biogeochemical reactions. Most fractionation factors known today were experimentally determined in aqueous systems and transferred to terrestrial systems. A better constrain of terrestrial Hg cycling will be achieved with systematic studies of terrestrial processes, e.g. the photochemical reduction of Hg in plant leaves.[33] In particular the Hg isotope fractionation associated with oxidation of gaseous Hg remains unknown. The understanding of Hg isotope fractionation associated with Hg oxidation during foliar uptake of different plant species and during gaseous elemental Hg deposition will result in a significant decrease of the uncertainties associated with the interpretation of Hg stable isotope signatures in soils.

Flux chamber measurements of gaseous Hg re-emission from forest soils in Wisconsin, USA revealed no significant difference compared to the atmospheric Hg isotope signatures.[33] Poorly drained Histosols on the other hand indicated significant fractionation during Hg loss due to organic matter-driven reduction (Chapter 2). The different findings warrant for more investigations of different terrestrial ecosystems in order to evaluate under which conditions significant Hg re-emission from soils occurs and what role organic-matter driven reductive Hg loss plays for global atmospheric Hg cycling. Hg isotope measurements of gaseous Hg in the atmosphere and from soil re-emission will allow to further investigate the land/atmosphere exchange of Hg.

In order to conclusively elucidate the development of mercury pools in soils a historical record of the Hg isotope composition of deposition is needed. The reconstruction of Hg deposition will involve the development of a historical record of atmospheric Hg isotope signatures and the understanding of the Hg fractionation processes associated with Hg deposition. To reconstruct the atmospheric Hg isotope composition, the evolution of Hg emission composition is required, involving anthropogenic sources, e.g., coal combustion,[41] natural emissions, and re-emissions from terrestrial and ocean surfaces. The measurement of historical archives such as e.g., peat cores could help to reconstruct Hg deposition, however they might be susceptible to secondary processes as discussed in Chapter 2. Thus, the successful interpretation of historical deposition archives relies on the understanding of secondary processes.

The transfer of Hg from terrestrial ecosystems to aquatic biota represents an important pathway for human Hg exposure through fish consumption. The measurement of Hg isotope signatures in catchment runoff provided important insights in the source of Hg (Chapter 3). To get more conclusive information of the transport pathways, whole ecosystem studies from catchments and runoff characterization to the aquatic ecosystem and biota are needed. The development of analytical techniques to measure the species-specific stable Hg isotope composition of methyl-Hg in soils and sediments and in natural waters could provide new insights in the transport pathway and bioaccumulation of methyl-Hg.

References

[1] O. S. Pokrovsky, J. Viers, E. E. Emnova, E. I. Kompantseva, and R. Freydier. Copper isotope fractionation during its interaction with soil and aquatic microorganisms and metal oxy(hydr)oxides: Possible structural control. *Geochim. Cosmochim. Acta*, 72(7):1742–1757, 2008.

[2] L. S. Balistrieri, D. M. Borrok, R. B. Wanty, and W. I. Ridley. Fractionation of Cu and Zn isotopes during adsorption onto amorphous Fe(III) oxyhydroxide: Experimental mixing of acid rock drainage and ambient river water. *Geochim. Cosmochim. Acta*, 72(2):311–328, 2008.

[3] F. Juillot, C. Marechal, M. Ponthieu, S. Cacaly, G. Morin, M. Benedetti, J. L. Hazemann, O. Proux, and F. Guyot. Zn isotopic fractionation caused by sorption on goethite and 2-lines ferrihydrite. *Geochim. Cosmochim. Acta*, 72(19):4886–4900, 2008.

[4] C. Mikutta, J. G. Wiederhold, O. A. Cirpka, T. B. Hofstetter, B. Bourdon, and U. Von Gunten. Iron isotope fractionation and atom exchange during sorption of ferrous iron to mineral surfaces. *Geochim. Cosmochim. Acta*, 73(7):1795–1812, 2009.

[5] B. L. Beard, R. M. Handler, M. M. Scherer, L. L. Wu, A. D. Czaja, A. Heimann, and C. M. Johnson. Iron isotope fractionation between aqueous ferrous iron and goethite. *Earth Planet. Sci. Lett.*, 295(1-2):241–250, 2010.

[6] E. A. Schauble, M. Meheut, and P. S. Hill. Combining metal stable isotope fractionation theory with experiments. *Elements*, 5(6):369–374, 2009.

[7] G. A. Brennecka, L. E. Wasylenki, J. R. Bargar, S. Weyer, and A. D. Anbar. Uranium isotope fractionation during adsorption to Mn-oxyhydroxides. *Environ. Sci. Technol.*, 45(4):1370–1375, 2011.

[8] J. Barling and A. D. Anbar. Molybdenum isotope fractionation during adsorption by manganese oxides. *Earth Planet. Sci. Lett.*, 217(3-4):315–329, 2004.

[9] O. S. Pokrovsky, A. Galy, J. Schott, G. S. Pokrovski, and S. Mantoura. Germanium isotope fractionation during Ge adsorption on goethite and its coprecipitation with Fe oxy(hydr)oxides. *Geochim. Cosmochim. Acta*, 131(0):138–149, 2014.

[10] O. S. Pokrovsky, J. Viers, and R. Freydier. Zinc stable isotope fractionation during its adsorption on oxides and hydroxides. *J. Colloid Interface Sci.*, 291(1):192–200, 2005.

[11] C. Ockert, N. Gussone, S. Kaufhold, and B. M. A. Teichert. Isotope fractionation during Ca exchange on clay minerals in a marine environment. *Geochim. Cosmochim. Acta*, 112:374–388, 2013.

[12] L. E. Wasylenki, J. W. Swihart, and S. J. Romaniello. Cadmium isotope fractionation during adsorption to Mn oxyhydroxide at low and high ionic strength. *Geochim. Cosmochim. Acta*, 140(0):212–226, 2014.

[13] W. Stumm and J. J. Morgan. *Aquatic Chemistry: Chemical Equilibria and Rates in Natural Waters.* Series: Environmental science and technology. New York [etc.] : Wiley, third ed. edition, 1996.

[14] Barbara R. Coughlin and Alan T. Stone. Nonreversible adsorption of divalent metal ions (Mn^{II}, Co^{II}, Ni^{II}, Cu^{II}, and Pb^{II}) onto goethite: Effects of acidification, Fe^{II} addition, and picolinic acid addition. *Environ. Sci. Technol.*, 29(9):2445–2455, 1995.

[15] N. J. Barrow, G. W. Brümmer, and L. Fischer. Rate of desorption of eight heavy metals from goethite and its implications for understanding the pathways for penetration. *Eur. J. Soil Sci.*, 63(3):389–398, 2012.

[16] E. A. Schauble. Role of nuclear volume in driving equilibrium stable isotope fractionation of mercury, thallium, and other very heavy elements. *Geochim. Cosmochim. Acta*, 71(9):2170–2189, 2007.

[17] P. S. Hill, E. A. Schauble, and E. D. Young. Effects of changing solution chemistry on Fe^{3+}/Fe^{2+} isotope fractionation in aqueous Fe-Cl solutions. *Geochim. Cosmochim. Acta*, 74(23):6669–6689, 2010.

[18] T. Fujii, F. Moynier, P. Telouk, and M. Abe. Experimental and theoretical investigation of isotope fractionation of zinc between aqua, chloro, and macrocyclic complexes. *J. Phys. Chem. A*, 114(7):2543–2552, 2010.

[19] J. R. Black, A. Kavner, and E. A. Schauble. Calculation of equilibrium stable isotope partition function ratios for aqueous zinc complexes and metallic zinc. *Geochim. Cosmochim. Acta*, 75(3):769–783, 2011.

[20] T. Fujii, F. Moynier, N. Dauphas, and M. Abe. Theoretical and experimental investigation of nickel isotopic fractionation in species relevant to modern and ancient oceans. *Geochim. Cosmochim. Acta*, 75(2):469–482, 2011.

[21] D. Jouvin, P. Louvat, F. Juillot, C. N. Marechal, and M. F. Benedetti. Zinc isotopic fractionation: why organic matters. *Environ. Sci. Technol.*, 43(15):5747–5754, 2009.

[22] L. E. Wasylenki, B. A. Rolfe, C. L. Weeks, T. G. Spiro, and A. D. Anbar. Experimental investigation of the effects of temperature and ionic strength on Mo isotope fractionation during adsorption to manganese oxides. *Geochim. Cosmochim. Acta*, 72(24):5997–6005, 2008.

[23] S. G. Nielsen, L. E. Wasylenki, M. Rehkamper, C. L. Peacock, Z. C. Xue, and E. M. Moon. Towards an understanding of thallium isotope fractionation during adsorption to manganese oxides. *Geochim. Cosmochim. Acta*, 117:252–265, 2013.

[24] B. M. Ryan, J. K. Kirby, F. Degryse, K. Scheiderich, and M. J. McLaughlin. Copper isotope fractionation during equilibration with natural and synthetic ligands. *Environ. Sci. Technol.*, 48(15):8620–6, 2014.

[25] C. M. Johnson, J. L. Skulan, B. L. Beard, H. Sun, K. H. Nealson, and P. S. Braterman. Isotopic fractionation between Fe(III) and Fe(II) in aqueous solutions. *Earth Planet. Sci. Lett.*, 195(1-2):141–153, 2002.

[26] J. L. L. Morgan, L. E. Wasylenki, J. Nuester, and A. D. Anbar. Fe isotope fractionation during equilibration of Fe-organic complexes. *Environ. Sci. Technol.*, 44(16):6095–6101, 2010.

[27] Y. Matsuhisa, J. R. Goldsmith, and R. N. Clayton. Mechanisms of hydrothermal crystallization of quartz at 250°C and 150 kbar. *Geochim. Cosmochim. Acta*, 42(2):173–182, 1978.

[28] A. J. Frierdich, B. L. Beard, T. R. Reddy, M. M. Scherer, and C. M. Johnson. Iron isotope fractionation between aqueous Fe(II) and goethite revisited: New insights based on a multi-direction approach to equilibrium and isotopic exchange rate modification. *Geochim. Cosmochim. Acta*, 139(0):383–398, 2014.

[29] J. G. Wiederhold, C. J. Cramer, K. Daniel, I. Infante, B. Bourdon, and R. Kretzschmar. Equilibrium mercury isotope fractionation between dissolved Hg(II) species and thiol-bound Hg. *Environ. Sci. Technol.*, 44(11):4191–4197, 2010.

[30] E. A. Schauble. Modeling nuclear volume isotope effects in crystals. *Proc. Natl. Acad. Sci. U. S. A.*, 110(44):17714–17719, 2013.

[31] M. Meheut and E. A. Schauble. Silicon isotope fractionation in silicate minerals: Insights from first-principles models of phyllosilicates, albite and pyrope. *Geochim. Cosmochim. Acta*, 134:137–154, 2014.

[32] A. Biswas, J. D. Blum, B. A. Bergquist, G. J. Keeler, and Z. Q. Xie. Natural mercury isotope variation in coal deposits and organic soils. *Environ. Sci. Technol.*, 42(22):8303–8309, 2008.

[33] J. D. Demers, J. D. Blum, and D. R. Zak. Mercury isotopes in a forested ecosystem: Implications for air-surface exchange dynamics and the global mercury cycle. *Glob. Biogeochem. Cycles*, 27(1):222–238, 2013.

[34] H. Zhang, R. S. Yin, X. B. Feng, J. Sommar, C. W. Anderson, A. Sapkota, X. W. Fu, and T. Larssen. Atmospheric mercury inputs in montane soils increase with elevation: evidence from mercury isotope signatures. *Sci. Rep.*, 3:3322, 2013.

[35] J. D. Blum, L. S. Sherman, and M. W. Johnson. Mercury isotopes in earth and environmental sciences. *Annu. Rev. Earth Planet. Sci. Lett.*, 42(1):249–269, 2014.

[36] P. Rodriguez-Gonzalez, V. N. Epov, R. Bridou, E. Tessier, R. Guyoneaud, M. Monperrus, and D. Amouroux. Species-specific stable isotope fractionation of mercury during Hg(II) methylation by an anaerobic bacteria (Desulfobulbus propionicus) under dark conditions. *Environ. Sci. Technol.*, 43(24):9183–9188, 2009.

[37] B. A. Bergquist and J. D. Blum. Mass-dependent and -independent fractionation of Hg isotopes by photoreduction in aquatic systems. *Science*, 318(5849):417–420, 2007.

[38] K. Kritee, J. D. Blum, M. W. Johnson, B. A. Bergquist, and T. Barkay. Mercury stable isotope fractionation during reduction of Hg(II) to Hg(0) by mercury resistant microorganisms. *Environ. Sci. Technol.*, 41(6):1889–1895, 2007.

[39] W. Zheng and H. Hintelmann. Nuclear field shift effect in isotope fractionation of mercury during abiotic reduction in the absence of light. *J. Phys. Chem. A*, 114(12):4238–4245, 2010.

[40] D. Obrist, D. W. Johnson, S. E. Lindberg, Y. Luo, O. Hararuk, R. Bracho, J. J. Battles, D. B. Dail, R. L. Edmonds, R. K. Monson, S. V. Ollinger, S. G. Pallardy, K. S. Pregitzer, and D. E. Todd. Mercury distribution across 14 US forests. part I: Spatial patterns of concentrations in biomass, litter, and soils. *Environ. Sci. Technol.*, 45(9):3974–3981, 2011.

[41] R. Sun, J. E. Sonke, L. E. Heimburger, H. E. Belkin, G. Liu, D. Shome, E. Cukrowska, C. Liousse, O. S. Pokrovsky, and D. G. Streets. Mercury stable isotope signatures of world coal deposits and historical coal combustion emissions. *Environ. Sci. Technol.*, 48(13):7660–7668, 2014.

Supporting Information to Chapter 2

Materials and methods

Soil Sampling

Soil samples were taken from two boreal forest catchments close to Junsele (N: 63°50', E: 17°00') in northern Sweden (Figure S3.5). For each catchment five sampling points composed of 5 individual profiles dug within 10 m^2 were chosen along a transect following the inclination of the landscape. Soils were classified according to the world reference base for soil resources.[1] The samples were cut from the profiles with a knife and divided into the overlying Oe/He and underlying Oa/Ha horizons (for Ha only the top 15 cm were considered). For each sample, the dimensions were measured (for volume calculation) and then the samples were pooled to one composite sample. The soil samples were stored in refrigerated boxes and sieved for homogenization using a 4 mm cutting sieve within 48h after sampling. The mineral soil samples were sieved through a 1.6 mm sieve. Then the samples were dried in a ventilated oven at 45 °C for 72h. The dried samples were weighed to determine the water loss. Aliquots of the dried samples were further homogenized using a rotary disk mill. The fine powder was finally analyzed for total element and Hg isotope composition. Carbon and nitrogen were measured using a CHNS analyzer (LECO). Total Hg concentrations were measured by combustion atomic absorption spectrometry (LECO AMA 254). The sample powders were pressed to wax pellets for concentration measurements of additional elements (atomic number Z>11) using energy-dispersive X-ray fluorescence analysis (Spectro-X-Lab 2000, Spectro).

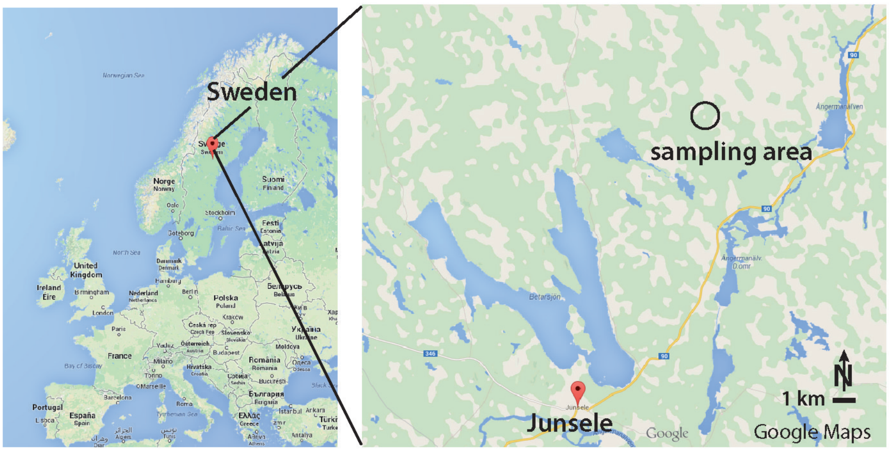

Figure S2.1: Map of soil sampling site.

Methyl-mercury in bulk soil samples

Subsamples of all organic soil samples were taken after sieving and homo-genization for MeHg determination using isotope dilution GC-ICP-MS in the context of another research project focussing on land-use change.[2] The organic soil samples contained on average a MeHg concentration of 1.1 ng g^{-1} (maximum: 4.0 ng g^{-1}), corresponding to 0.5% (maximum: 1.3%) of the total Hg concentration (Hg_{tot}).

Radiocarbon dating

Homogenized samples of bulk soil were combusted, graphitized and analyzed using Accelerator Mass Spectrometry (AMS; ETH Zurich).[3] ^{14}C data are reported as fraction of modern ^{14}C ($F^{14}C$), i.e. concentration of ^{14}C normalized to the standard and corrected for mass fractionation using $\delta^{13}C$. Radiocarbon ages are reported according to Stuiver and Polach[4] and for samples containing post-bomb carbon the $F^{14}C$ is reported according to Reimer et al.[5]. Calibrations of the radiocarbon data were performed using the OxCal software (version 4.2.3, Bronk Ramsey, 2013). All pre-bomb carbon data ($F^{14}C$ <1) were calibrated using the IntCal13 atmospheric ^{14}C curve[6]. Samples with $F^{14}C$ >1 were calibrated using the post-bomb NH1 atmospheric ^{14}C curve[7]. Figure 3c shows the calibrated ^{14}C age against the fraction of precipitation inferred from stable Hg isotope measurements. Please note that carbon in the soil samples represents a mixture of old and young carbon, therefore the interpretation of a bulk age should be used with caution.

Role of Hg from geogenic background

We estimated the content of mineral material in the organic topsoils from the measured Si concentration in each sample, assuming a SiO_2 concentration of 60 % (w/w) for granite, the predominant bedrock at the sampling area. Alriksson et al.[8] reported average Hg concentrations of 13 ng g^{-1} (SE= ± 0.7 ng g^{-1}, n= 200) for mineral C horizons in Sweden. The reported concentrations showed a positive correlation with carbon content, suggesting potential Hg contributions of atmospheric origin. Despite this, we used 13 ng g^{-1} as geogenic background Hg concentration. The contribution of geogenic Hg to the total Hg in the samples was calculated to be on average 0.36% (max= 1.8%). The Hg isotope composition previously reported for rocks has shown no significant MIF and also the variation in MDF was limited[9]. Therefore we concluded that the contribution of Hg from geogenic origin can be neglected for the organic topsoil samples and thus we did not incorporate a geogenic endmember in the mixing scenarios.

Oven combustion system

Hg enrichment was performed in a two-step combustion oven connected to a oxidizing liquid trap, adapted from[10] as illustrated in Figure S2.3. Sample powders were introduced in a quartz boat in the first combustion oven. The first oven was heated stepwise (start temp: 50°C, ramp 1: 1.8°C min^{-1} (50-160°C), ramp 2: 1.0°C min^{-1} (160-235°C), hold for 30 min, ramp 3: 1.0°C min^{-1} (235-320°C), ramp 4: 2.0°C min^{-1} (320-600°C)) until a final temperature of 600°C. The second combustion oven was kept at 1000°C to ensure complete combustion of volatile organic compounds from the sample. The quartz oven tube was flushed with Hg-free air (purified by Au-trap) with $\approx$80 mL min^{-1}. The air inlet contained a heater (350°C, 25W) to prevent condensation or back diffusion of organics or Hg. After the second combustion oven the air was led through a Teflon tubing, heated with an external resistance heater (105 °C, 4 W), to the oxidizing liquid trap. The liquid trap system was evacuated to 950 mbar. A glass pipette tip was used as gas inlet to the oxidizing liquid trap, which contained a 15 ml solution of 1% (w/v) $KMnO_4$ in 10% H_2SO_4. All glassware (quarz boats, pipette tips and glass vials) were acid washed for at least 24 h in 6 M HCl, rinsed three times with H_2O_{MQ} and dried in a clean room. Samples were run in batches of 8, followed by one process blank measurement and one Montana soil (NIST-2711) standard measurement. The Hg recovery of samples and standards was 94%±8.5% (1σ, n=72) and process blank levels were 0.04 ± 0.01 ng L^{-1} Hg (1σ, n=9).

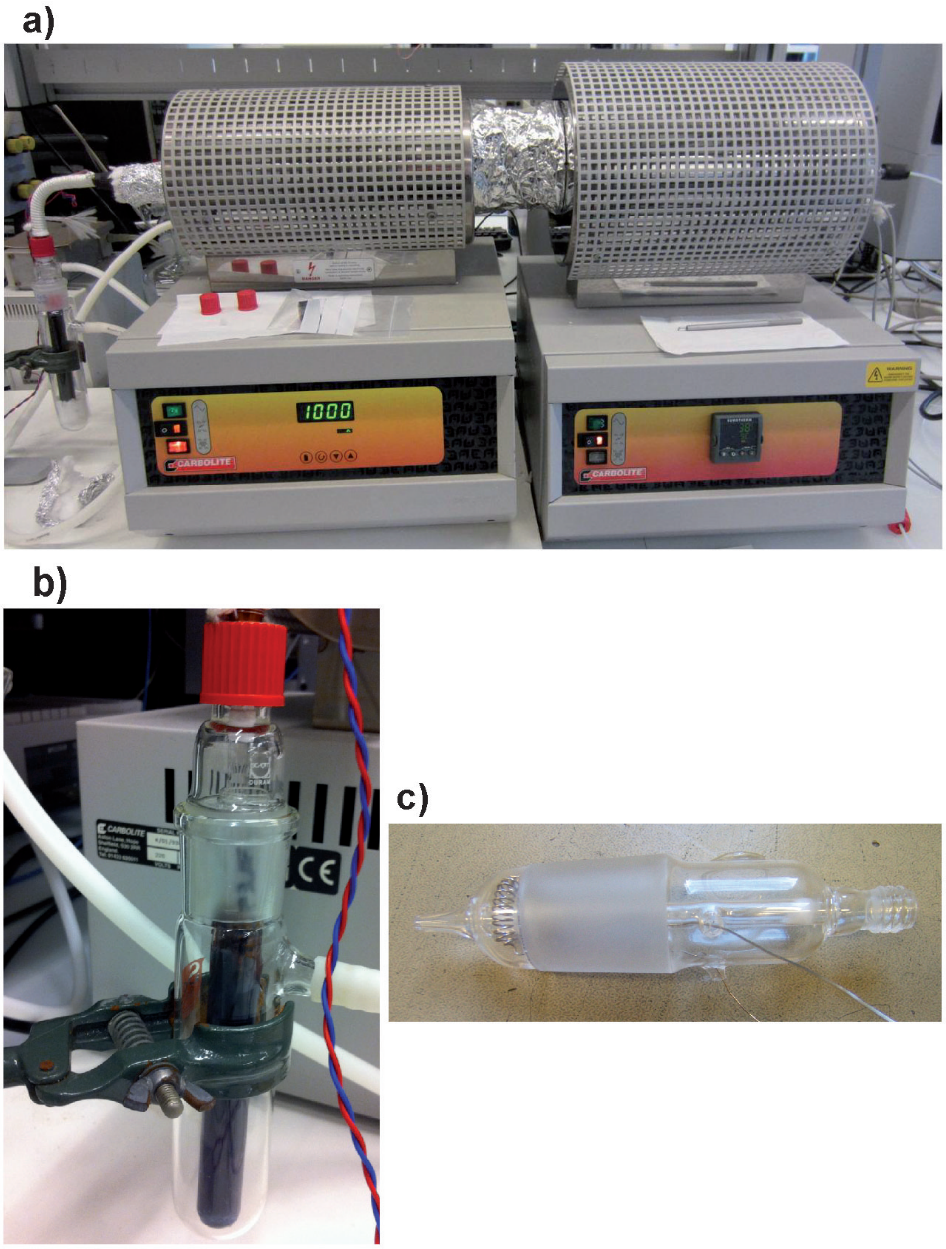
a)
1000
CARBOLITE
CARBOLITE
b)
c)

Figure S2.2: Pictures of two step combustion system used for Hg enrichment. (**a**) overview, (**b**) oxidizing liquid trap, and (**c**) air inlet

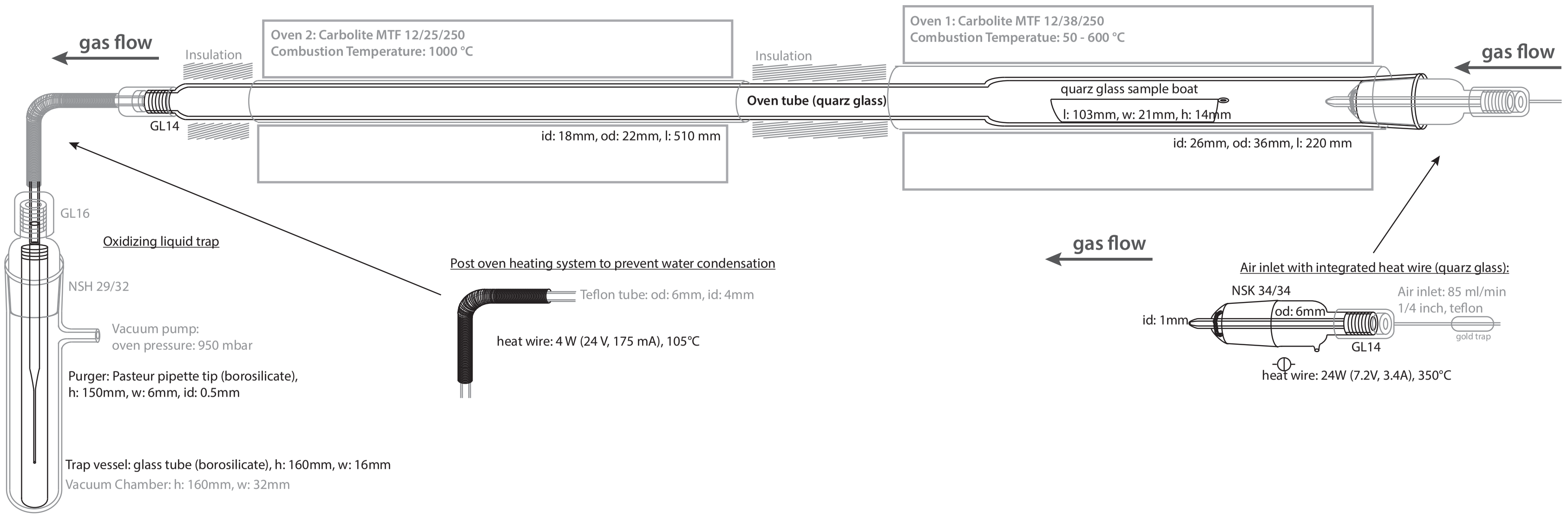
gas flow
Insulation
Oven 2: Carbolite MTF 12/25/250
Combustion Temperature: 1000 °C
Insulation
Oven 1: Carbolite MTF 12/38/250
Combustion Temperatue: 50 - 600 °C
gas flow
quarz glass sample boat
l: 103mm, w: 21mm, h: 14mm
Oven tube (quarz glass)
GL14
id: 18mm, od: 22mm, l: 510 mm
id: 26mm, od: 36mm, l: 220 mm
GL16
Oxidizing liquid trap
gas flow
Post oven heating system to prevent water condensation
Air inlet with integrated heat wire (quarz glass):
NSH 29/32
Teflon tube: od: 6mm, id: 4mm
NSK 34/34
Air inlet: 85 ml/min
1/4 inch, teflon
id: 1mm
od: 6mm
Vacuum pump:
oven pressure: 950 mbar
heat wire: 4 W (24 V, 175 mA), 105°C
GL14
gold trap
heat wire: 24W (7.2V, 3.4A), 350°C
Purger: Pasteur pipette tip (borosilicate),
h: 150mm, w: 6mm, id: 0.5mm
Trap vessel: glass tube (borosilicate), h: 160mm, w: 16mm
Vacuum Chamber: h: 160mm, w: 32mm

Figure S2.3: Schematic drawing of two step combustion system used for Hg enrichment.

Hg isotope measurements

Hg trap solutions were stored at 4°C in the dark. Prior to Hg isotope measurements, $KMnO_4$ and residues of precipitated MnO_2 were reduced by the addition of 0.66% (w/v) hydroxylamine-hydrochloride (H_2NOH-HCl). Subsamples were taken and diluted to concentrations of approximately 0.5 nmol L^{-1} (0.1 ppb) for concentration measurements by cold vapor atomic fluorescence spectrometry (CV-AFS, Millenium Merlin, PS Analytical, U.K.). Hg isotope ratio measurements were performed using a method adapted from previously published methods[11],[12]. Samples were diluted to 25 nmol L^{-1} (5 ppb) and matched to signal intensities within 10% of the bracketing standard. Hg was introduced to the multicollector inductively coupled plasma mass spectrometer (MC-ICPMS; Nu instruments, Wrexham, U.K.) using cold vapor generation by stannous chloride reduction (HGX-200; Cetac, Omaha, NE, U.S.). Tl NIST-997 standard was continuously introduced using a desolvating nebulizer (Apex; Elemental Scientific, Omaha, U.S.) and was used for instrumental mass bias correction. The collectors of the MC-ICPMS were set to all Hg (196, 198, 199, 200, 201, 202 and 204) and Tl masses (203 and 205). Signal intensities detected on masses 194 and 206, collected to check for Pt and Pb respectively, were indifferent from the detector baseline, implying that no interferences occurred on the Hg masses common with Pt and Pb. Isotope ratios were measured after a 5 min uptake and stabilization phase. The data were collected in three blocks of 36 measurements integrating over 5 s each. Prior to each block the detector baselines were measured by electrostatic analyzer (ESA) deflection. After each measurement the sample was washed out with 1% BrCl for 3 min, after which the ^{202}Hg intensities dropped to 5 mV, representing about 1 % of the beam intensities at 25 nmol L^{-1} measuring concentration. Prior to each measurement session (no longer than 20 h), a gain calibration of the collectors was performed, settings were tuned for optimum signal intensity, signal stability, and peak shapes.

Mixing model

The Hg isotope signature of precipitation was estimated based on measured precipitation data across North America compiled from[13–17]. The precipitation data were divided into three categories concerning anthropogenic contribution of Hg; low: 0-10 ng L^{-1}, medium: 10-25 ng L^{-1} and high >25 ng L^{-1} Hg or clear indication for heavy anthropogenic contamination described in the publication. Since highly contaminated precipitation signatures were only measured close to coal-fired powerplants, these were not considered in our precipitation source estimate for the remote area in northern Sweden.[15] For the endmember of precipitation derived Hg used for the calculations shown in the main manuscript low and medium samples were used (0-25 ng L^{-1}), however simulations with only low or medium concentrated Hg did not significantly change the results.

Table S2.1: Hg isotope composition of precipitation separated in anthropogenic contamination categories derived from literature ([13–17]). The mean values and 1 σ standard deviation of the population are reported.

categorie	Hg_{tot} (ng L^{-1})	$\delta^{202}Hg$ ‰	$\Delta^{199}Hg$ ‰	$\Delta^{200}Hg$ ‰	$\Delta^{201}Hg$ ‰	n
low	0-10	-0.74 ± 0.50	0.48 ± 0.30	0.37 ± 0.28	0.45 ± 0.31	33
medium	10-25	-0.32 ± 0.43	0.33 ± 0.20	0.17 ± 0.06	0.35 ± 0.19	25
high	> 25	-1.87 ± 1.48	0.25 ± 0.20	0.10 ± 0.07	0.12 ± 0.21	39

A linear regression model was used to describe the relation between $\Delta^{199}Hg$ and $\delta^{202}Hg$ (Figure S2a), between $\Delta^{200}Hg$ and $\Delta^{199}Hg$, and between $\Delta^{201}Hg$ and $\Delta^{199}Hg$. The Hg isotope composition of rain samples used in the mixing calculations was estimated based on the parameters of the linear regression and the variance (1σ) of the residuals, which was modeled using the normal distributed pseurorandom number generation function of MatLab.

Table S2.2: Model parameters for precipitation endmember scenarios.

categorie			correlation	intercept	1σ
low	$\delta^{202}Hg$	=		- 0.74‰	± 0.50‰
	$\Delta^{199}Hg$	=	-0.28 $*\delta^{202}Hg$	+ 0.28‰	± 0.26‰
	$\Delta^{200}Hg$	=	-0.19 $*\Delta^{199}Hg$	+ 0.47‰	± 0.28‰
medium	$\delta^{202}Hg$	=		- 0.32‰	± 0.43‰
	$\Delta^{199}Hg$	=	-0.17 $*\delta^{202}Hg$	+ 0.28‰	± 0.18‰
	$\Delta^{200}Hg$	=	0.21 $* \Delta^{199}Hg$	+0.10‰	± 0.05‰
low and medium	$\delta^{202}Hg$	=		-0.61‰	± 0.45‰
	$\Delta^{199}Hg$	=	-0.26 $*\delta^{202}Hg$	+0.29‰	± 0.21‰
	$\Delta^{200}Hg$	=	0.34 $* \Delta^{199}Hg$	+0.06‰	± 0.06‰
	$\Delta^{201}Hg$	=	0.91 $* \Delta^{199}Hg$		± 0.13‰

As endmember for the litter derived Hg, we used the average and variance of the 4 measured litter samples. The Hg isotope signature was similar to the lowest range of Hg isotope signatures previously reported for foilage (δ^{202}Hg=-2.53 ‰, Δ^{199}Hg=-0.40 ‰)[17] and the ^{14}C age was the youngest of all measured soil samples. The fraction of litter (f_{litter}) was varied between 0 and 1.

Table S2.3: Litter endmember

			intercept	1σ
litter	δ^{202}Hg	=	-2.35‰	± 0.092‰
	Δ^{199}Hg	=	-0.44‰	± 0.03‰
	Δ^{200}Hg	=	-0.06‰	± 0.05‰
	Δ^{201}Hg	=	-0.42‰	± 0.02‰

$$\delta^{202}\text{Hg}_{\text{mixed}} = \text{f}_{\text{litter}} \times \delta^{202}\text{Hg}_{\text{litter}} + (1 - \text{f}_{\text{litter}}) \times \delta^{202}\text{Hg}_{\text{rain}} \tag{S2.1}$$

$$\Delta^{\text{xxx}}\text{Hg}_{\text{mixed}} = \text{f}_{\text{litter}} \times \Delta^{\text{xxx}}\text{Hg}_{\text{litter}} + (1 - \text{f}_{\text{litter}}) \times \Delta^{\text{xxx}}\text{Hg}_{\text{rain}} \tag{S2.2}$$

The fraction of precipitation-derived Hg was directly inferred from f_{litter} following the relationship:

$$\text{f}_{\text{precipitation}} = 1 - \text{f}_{\text{litter}} \tag{S2.3}$$

The isotope signatures of the soil sample after reductive loss (Hg_{soil}) was calculated from the mixed Hg isotope signature (Hg_{mixed}), where $\text{f}_{\text{reduced}}$ corresponds to the fraction of reductive Hg loss and α^{202}Hg to the fractionation factor for the corresponding reduction pathway (Table S2.4).

$$\delta^{202}\text{Hg}_{\text{soil}} = ((\delta^{202}\text{Hg}_{\text{mixed}} + 1) \times \text{f}_{\text{reduced}})^{(\alpha^{202}\text{Hg}-1)} - 1 \tag{S2.4}$$

$$\epsilon^{202}\text{Hg}_{\text{redloss}} = \delta^{202}\text{Hg}_{\text{mixed}} - \delta^{202}\text{Hg}_{\text{soil}} \tag{S2.5}$$

The MIF was calculated as follows:

$$\Delta^{\text{xxx}}\text{Hg}_{\text{soil}} = \Delta^{\text{xxx}}\text{Hg}_{\text{mixed}} - \text{E}^{\text{xxx}}\text{Hg} \tag{S2.6}$$

Table S2.4: Isotopic enrichment factors of reductive pathways

photo-reduction[18]		
$\alpha^{202}\mathrm{Hg}_{\mathrm{photo}}$	=	0.9994
$\epsilon^{202}\mathrm{Hg}_{\mathrm{photo}}$	=	-0.6‰
$\mathrm{E}^{199}\mathrm{Hg}_{\mathrm{photo}}$	=	$0.75 \times \epsilon^{202}\mathrm{Hg}_{\mathrm{redloss}}$
$\mathrm{E}^{200}\mathrm{Hg}_{\mathrm{photo}}$	=	0
$\mathrm{E}^{201}\mathrm{Hg}_{\mathrm{photo}}$	=	$0.91 \times \epsilon^{202}\mathrm{Hg}_{\mathrm{redloss}}$
microbial-reduction[19]		
$\alpha^{202}\mathrm{Hg}_{\mathrm{microb}}$	=	0.99848
$\epsilon^{202}\mathrm{Hg}_{\mathrm{microb}}$	=	-0.4‰
$\mathrm{E}^{199}\mathrm{Hg}_{\mathrm{microb}}$	=	0
$\mathrm{E}^{200}\mathrm{Hg}_{\mathrm{microb}}$	=	0
$\mathrm{E}^{201}\mathrm{Hg}_{\mathrm{microb}}$	=	0
NOM-reduction[20]		
$\alpha^{202}\mathrm{Hg}_{\mathrm{NOM}}$	=	0.9996
$\epsilon^{202}\mathrm{Hg}_{\mathrm{NOM}}$	=	-1.52‰
$\mathrm{E}^{199}\mathrm{Hg}_{\mathrm{NOM}}$	=	$-0.12 \times \epsilon^{202}\mathrm{Hg}_{\mathrm{redloss}}$
$\mathrm{E}^{200}\mathrm{Hg}_{\mathrm{NOM}}$	=	0
$\mathrm{E}^{201}\mathrm{Hg}_{\mathrm{NOM}}$	=	$-0.08 \times \epsilon^{202}\mathrm{Hg}_{\mathrm{redloss}}$

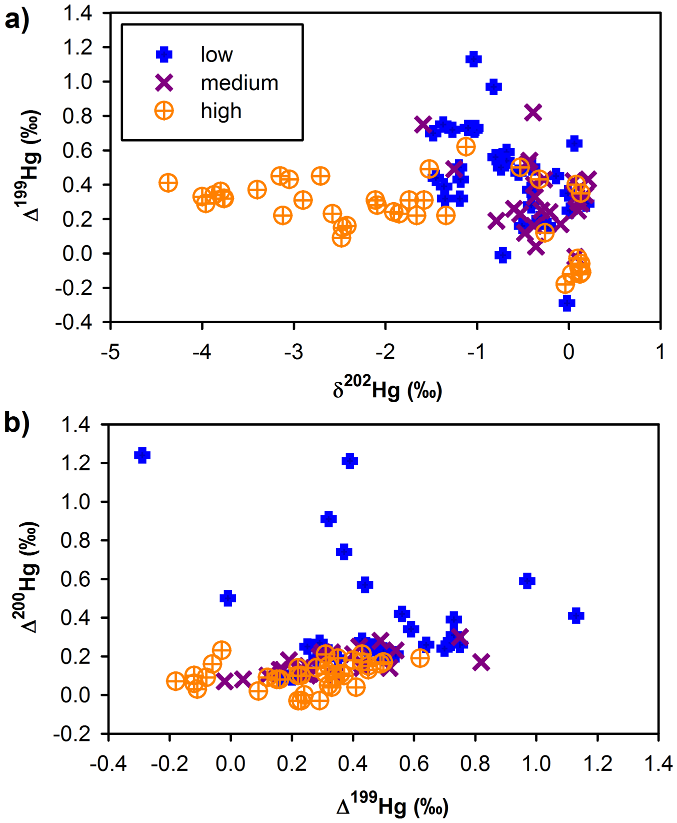

Figure S2.4: Hg isotope signatures of precipitation samples compiled from [13–17] depending on Hg concentration (low= <10 ng L^{-1}; medium= 10 - 25 ng L^{-1}; high= >25 ng L^{-1}) **(a)** Δ^{199}Hg vs. δ^{202}Hg and **(b)** Δ^{200}Hg vs. Δ^{199}Hg.

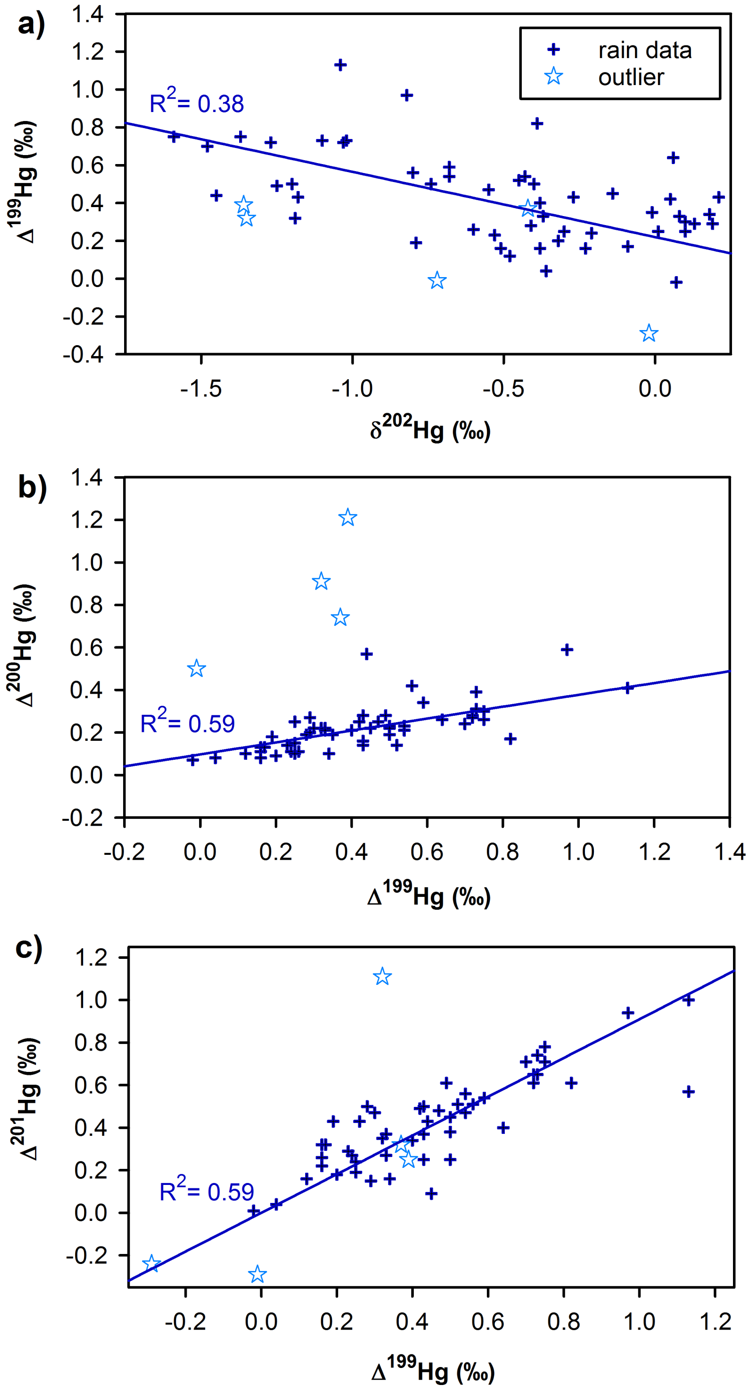

Figure S2.5: Linear regression of precipitation data (low and medium) compiled from [13–17]: **(a)** Δ^{199}Hg vs. δ^{202}Hg, **(b)** Δ^{200}Hg vs. Δ^{199}Hg, and **(c)** Δ^{201}Hg vs. Δ^{199}Hg. The stars represent outliers not considered in the regression. (The slopes of the regressions are given in Table S2)

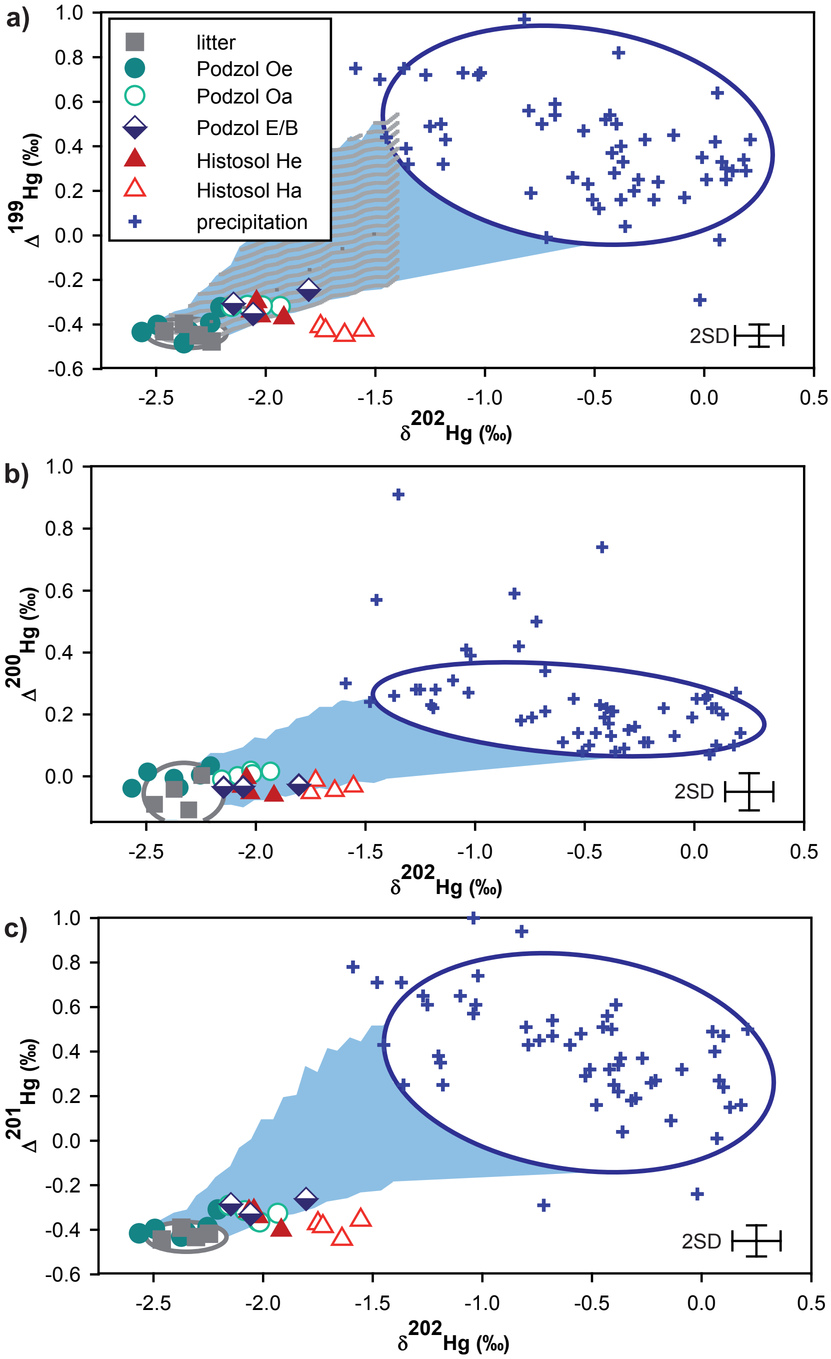

Figure S2.6: Modeled mixing scenarios (blue area) between Hg in litter (squares) and precipitation (crosses) shown in **(a)** Δ^{199}Hg vs. δ^{202}Hg, **(b)** Δ^{200}Hg vs. δ^{202}Hg, and **(c)** Δ^{201}Hg vs. δ^{202}Hg.

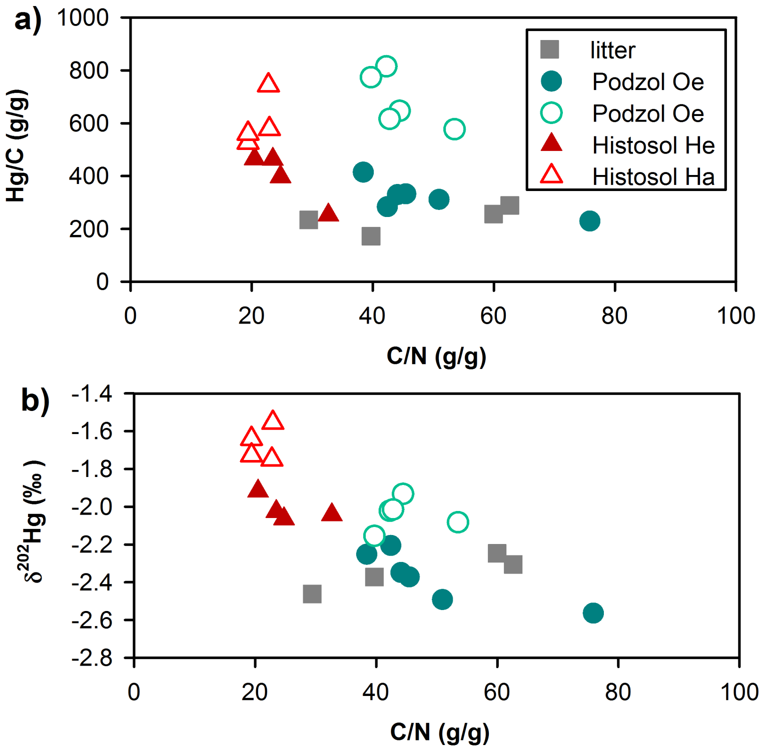

Figure S2.7: **(a)** Increase of Hg/C ratio with decreasing C/N ratio, **(b)** δ^{202}Hg vs. carbon to nitrogen ratio (C/N).

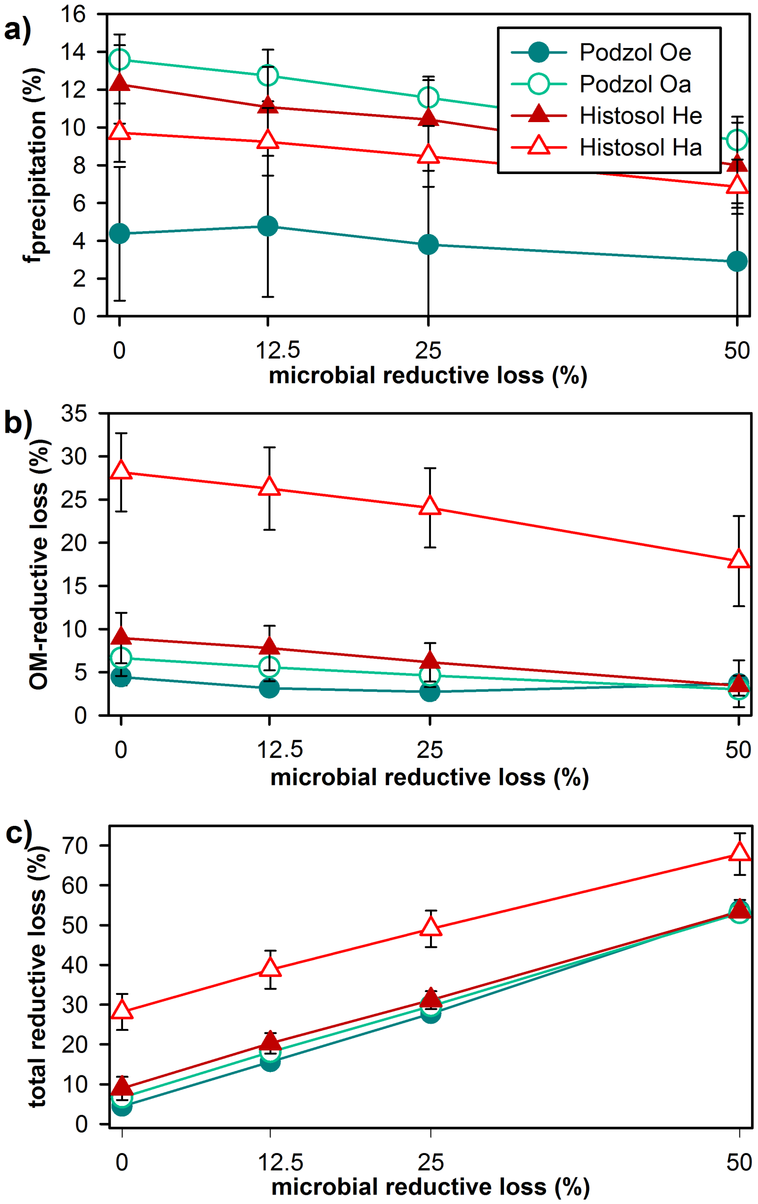

Figure S2.8: Influence of microbial reduction on modeled (**a**) fraction of precipitation in soil sample, (**b**) fraction of reductive loss by abiotic non-photochemical NOM reduction, and (**c**) total reductive loss.

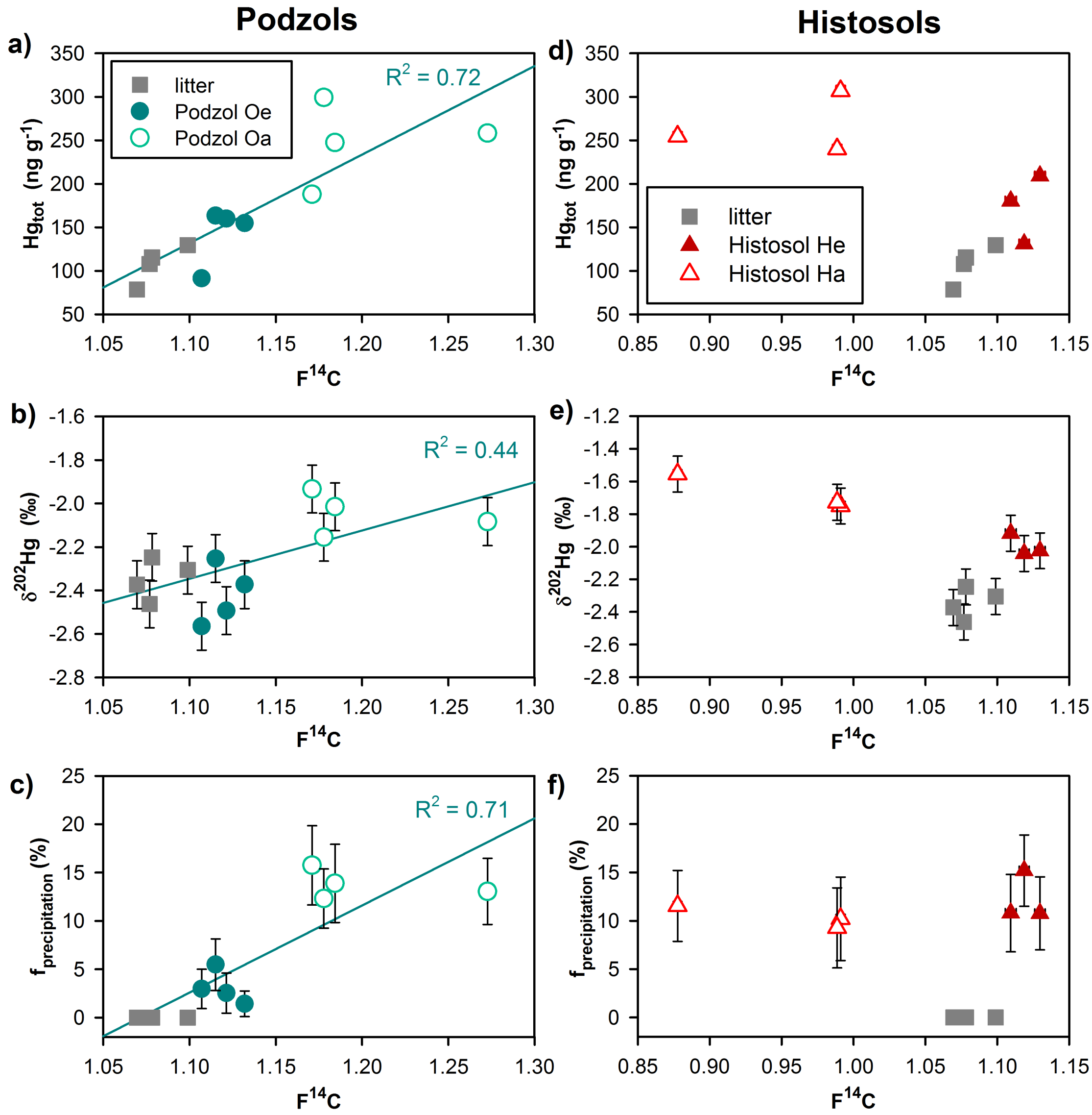

Figure S2.9: Correlation between radiocarbon signature ($F^{14}C$) and Hg concentration (**a**,**d**), MDF(**b**,**e**) and modeled fraction of precipitation-derived Hg (**c**,**f**). Errors represent 2σ for δ^{202}Hg and 1σ for $f_{\text{precipitation}}$.

Table S2.5: Concentration data of soil samples: horizon thickness (cm), total Hg concentration (ng g^{-1}), carbon and nitrogen concentration (% weight), C/N ratio (g g^{-1}) and Hg/C ratio (ng g^{-1}) and Si concentration (μg g^{-1})

Sample	horizon (cm)	Hg tot (ng g^{-1})	C (%)	N (%)	C/N (g g^{-1})	Hg/C (ng g^{-1})	Si (μg g^{-1})
litter-1	<1	108	46.0	1.56	29.5	69	2452
litter-2	<1	79	45.5	1.15	39.6	68	2883
litter-3	<1	130	45.0	0.72	62.5	180	5634
litter-4	<1	115	45.0	0.75	60.0	154	4525
Podzol-Oe-1	5	121	42.5	1.00	42.4	284	5582
Podzol-Oe-2	10	91	40.0	0.53	75.9	229	4539
Podzol-Oe-3	10	160	51.4	1.01	51.0	311	9977
Podzol-Oe-4	6	163	39.5	1.03	38.4	414	12210
Podzol-Oe-5	4	147	44.6	1.01	44.1	329	11100
Podzol-Oe-6	6	155	46.7	1.03	45.5	332	7340
Podzol-Oa-1	2	188	29.1	0.65	44.5	646	74810
Podzol-Oa-2	2	258	44.8	0.84	53.5	577	19680
Podzol-Oa-3	2	313	38.5	0.91	42.3	815	16740
Podzol-Oa-4	2	299	38.7	0.97	39.7	773	21020
Podzol-Oa-5	2	247	40.2	0.94	42.8	616	41040
Podzol-E-1	2	26	4.9	0.15	32.7	520	245500
Podzol-E-2	6	17	0.9	<0.1	nd	1870	285000
Podzol-B-1	nd	31	2.4	<0.1	nd	1253	214400
Histosol-He-1	5	180	38.8	1.90	20.5	465	3428
Histosol-He-2	10	209	45.1	1.92	23.5	464	3861
Histosol-He-3	8	171	43.1	1.74	24.7	397	3335
Histosol-He-4	10	131	51.9	1.59	32.7	252	2639
Histosol-Ha-1	68	255	44.1	1.92	22.9	578	26720
Histosol-Ha-2	68	307	41.3	1.82	22.7	744	30020
Histosol-Ha-3	40	225	42.8	2.21	19.4	526	14750
Histosol-Ha-4	45	240	42.8	2.21	19.4	561	7662

nd= not determined

Table S2.6: Hg isotope data of soil samples

Sample	δ^{202}Hg (‰)	δ^{201}Hg (‰)	δ^{200}Hg (‰)	δ^{199}Hg (‰)	δ^{204}Hg (‰)	Δ^{199}Hg (‰)	Δ^{200}Hg (‰)	Δ^{201}Hg (‰)	Δ^{204}Hg (‰)	Δ^{199}Hg/ Δ^{201}Hg
litter-1	-2.46	-2.29	-1.33	-1.05	-3.63	-0.43	-0.09	-0.44	0.05	0.97
litter-2	-2.37	-2.18	-1.23	-1.00	-3.47	-0.40	-0.04	-0.39	0.07	1.02
litter-3	-2.31	-2.17	-1.27	-1.03	-3.38	-0.45	-0.11	-0.43	0.06	1.04
litter-4	-2.25	-2.11	-1.13	-1.04	-3.31	-0.48	0.00	-0.42	0.05	1.14
Podzol-Oe-1	-2.21	-1.97	-1.08	-0.88	-3.28	-0.32	0.03	-0.31	0.01	1.04
Podzol-Oe-2	-2.56	-2.35	-1.33	-1.08	-3.79	-0.44	-0.04	-0.42	0.04	1.04
Podzol-Oe-3	-2.49	-2.27	-1.24	-1.03	-3.71	-0.40	0.01	-0.40	0.01	1.01
Podzol-Oe-4	-2.25	-2.08	-1.13	-0.96	-3.39	-0.39	0.00	-0.39	-0.03	1.02
Podzol-Oe-5	-2.35	-2.18	-1.22	-1.02	-3.53	-0.43	-0.04	-0.41	-0.02	1.05
Podzol-Oe-6	-2.37	-2.22	-1.16	-1.98	-3.72	-0.48	-0.01	-0.43	-0.02	1.12
Podzol-Oa-1	-1.93	-1.78	-0.96	-0.81	-2.93	-0.32	0.02	-0.33	-0.05	0.98
Podzol-Oa-2	-2.08	-1.88	-1.05	-0.84	-3.07	-0.32	0.00	-0.31	0.04	1.00
Podzol-Oa-3	-2.02	-1.88	-1.00	-0.83	-3.00	-0.32	0.02	-0.36	0.02	0.88
Podzol-Oa-4	-2.16	-1.91	-1.09	-0.86	-3.23	-0.32	-0.01	-0.29	-0.02	1.10
Podzol-Oa-5	-2.01	-1.88	-1.00	-0.83	-3.03	-0.32	0.01	-0.37	-0.03	0.87
Podzol-E-1	-1.80	-1.62	-0.93	-0.70	-2.70	-0.24	-0.03	-0.26	-0.01	0.93
Podzol-E-2	-2.15	-1.90	-1.11	-0.85	-3.27	-0.31	-0.03	-0.29	-0.06	1.08
Podzol-B-1	-2.06	-1.88	-1.07	-0.87	-3.08	-0.35	-0.03	-0.33	-0.01	1.07
Histosol-He-1	-1.92	-1.84	-1.03	-0.85	-2.87	-0.37	-0.06	-0.40	-0.01	0.92
Histosol-He-2	-2.03	-1.86	-1.07	-0.87	-3.08	-0.36	-0.05	-0.34	-0.05	1.06
Histosol-He-3	-2.06	-1.87	-1.07	-0.86	-3.08	-0.34	-0.03	-0.32	0.00	1.07
Histosol-He-4	-2.04	-1.85	-1.03	-0.81	-2.97	-0.30	-0.01	-0.31	0.08	0.95
Histosol-Ha-1	-1.55	-1.53	-0.81	-0.82	-2.23	-0.43	-0.03	-0.36	0.09	1.19
Histosol-Ha-2	-1.75	-1.69	-0.93	-0.85	-2.55	-0.41	-0.05	-0.37	0.06	1.10
Histosol-Ha-3	-1.64	-1.68	-0.87	-0.86	-2.41	-0.45	-0.05	-0.44	0.04	1.01
Histosol-Ha-4	-1.73	-1.68	-0.88	-0.86	-2.48	-0.43	-0.01	-0.39	0.10	1.11

Table S2.7: Fraction of precipitation in soil samples based on models ($f_{precipitation}$) wit standard deviation ($\pm 1\sigma$), ^{14}C concentration as fraction modern (F^{14}C) with standard deviation ($\pm 1\sigma$), the calibrated mean age and age range (years) with the probability of the range.

Sample	F^{14}C	$\pm 1\sigma$	δ^{13}C	$\pm 1\sigma$	mean age (years)	age range (years)	$f_{precipitation}$	$\pm 1\sigma$	$f_{reduced}$	$\pm 1\sigma$	Hg_{pool} (μg m^{-2})	$F_{re-emission}$ (μg m^{-2} a^{-1})
litter-1	1.077	0.004	-29.7	1.0	2004	2002-2005	0		0			
litter-2	1.070	0.004	-32.2	1.0	2005	2003-2008	0		0			
litter-3	1.099	0.004	-33.9	1.0	1999	1997-2001	0		0			
litter-4	1.078	0.004	-29.8	1.0	2003	2002-2005	0		0			
Podzol-Oe-1	nd						11.1	3.4	4.4	3.3	149	
Podzol-Oe-2	1.107	0.003	-29.4	1.0	1998	1996-2000	3.0	2.0	3.6	2.5	115	0.33
Podzol-Oe-3	1.121	0.004	-35.2	1.1	1994	1994-1997	2.5	2.1	4.1	3.2	431	1.13
Podzol-Oe-4	1.115	0.004	-28.6	1.0	1995	1994-1998	5.5	2.7	4.5	3.4	273	0.81
Podzol-Oe-5	nd						2.8	2.2	3.7	3.1	163	
Podzol-Oe-6	1.132	0.004	-31.7	1.0	1994	1993-1995	1.4	1.3	6.3	3.5	359	1.49
Podzol-Oa-1	1.171	0.004	-28.3	1.0	1989	1958-1959;1988-1990	15.8	4.1	9.8	5.5	178	0.87
Podzol-Oa-2	1.273	0.004	-26.9	1.1	1981	1959-1960;1920-1982	13.1	3.4	6.5	4.8	280	0.65
Podzol-Oa-3	nd						13.0	3.1	7.2	4.7	331	
Podzol-Oa-4	1.178	0.004	-27.6	1.0	1988	1958-1959;1986-1989	12.3	3.1	4.8	3.6	358	0.77
Podzol-Oa-5	1.184	0.004	-28.4	1.0	1988	1958-1959;1986-1989	13.9	4.0	4.8	2.9	315	0.68
Podzol-E-1	1.015	0.004	-25.3	1.0	1956	1955-1957	27.2	6.0	nd	nd	nd	nd
Podzol-E-2	1.004	0.004	-27.3	1.0	1956	1888-1912; 1954-1958	15.7	4.2	nd	nd	nd	nd
Podzol-B-1	1.097	0.004	-27.2	1.0	1957	1957-1958	14.1	4.8	nd	nd	nd	nd
Histosol-He-1	1.109	0.004	-28.4	1.0	1997	1996-2000	10.8	4.0	13.0	6.2	214	2.36
Histosol-He-2	1.130	0.004	-29.0	1.0	1994	1993-1995	10.8	3.8	9.0	5.1	812	4.70
Histosol-He-3	nd						12.4	3.6	7.6	4.7	349	
Histosol-He-4	1.119	0.003	-33.9	1.1	1995	1994-1997	15.2	3.7	6.2	4.3	433	1.84
Histosol-Ha-1	0.878	0.003	-28.2	1.0	991	951-1029	11.5	3.7	33.4	4.5	1561	0.69
Histosol-Ha-2	0.991	0.003	-27.4	1.0	1810	1694-1728; 1812-1912	10.2	4.3	23.5	6.2	2486	3.59
Histosol-Ha-3	nd						7.9	3.8	30.4	5.3	1484	
Histosol-Ha-4	0.989	0.003	-23.5	1.1	1865	1690-1729;1810-1925	9.3	4.1	25.4	5.9	1034	2.25

nd= not determined

Table S2.8: Results of standards processed and measured together with the soil samples reported in this study. All measured values are in agreement with previously reported values (see references).

Standard	Name	form/matrix	n		δ^{202}Hg (‰)	Δ^{199}Hg (‰)	Δ^{200}Hg (‰)	Δ^{201}Hg (‰)	Δ^{204}Hg (‰)	Reference
secondary standard	ETH-Fluka		26	average	-1.43	0.07	0.01	0.03	0.01	[12,21]
				2σ	0.12	0.05	0.05	0.07	0.11	
procedural standard	NIST SRM 2711	Montana soil	11	average	-0.12	-0.23	0.00	-0.18	0.01	[21,22]
				2σ	0.10	0.07	0.04	0.03	0.09	
procedural standard	Federsee-spike	Histosol[a]	2	average	-0.76	-0.01	0.00	-0.05	-0.03	
				2σ	0.09	0.08	0.04	0.12	0.04	

[a]= Histosol material has been characterized by Hoffmann et al.[23] and spiked to 2.9 μg g^{-1} with $Hg(NO_3)_2$-salt previously measured by Jiskra et al.[12].

References

[1] IUSS Working Group WRB. 2014. World Reference Base for Soil Resources 2014. International soil classification system for naming soils and creating legends for soil maps. Technical Report World Soil Resources Reports No. 106, FAO, Rome.

[2] L. Lambertsson, E. Lundberg, M. Nilsson, and W. Frech. Applications of enriched stable isotope tracers in combination with isotope dilution GC-ICP-MS to study mercury species transformation in sea sediments during in situ ethylation and determination. *J. Anal. At. Spectrom.*, 16(11):1296–1301, 2001.

[3] L. Wacker, G. Bonani, M. Friedrich, I. Hajdas, B. Kromer, M. Nemec, M. Ruff, M. Suter, H. A. Synal, and C. Vockenhuber. Micadas: routine and high-precision radiocarbon dating. *Radiocarbon*, 52(2):252–262, 2010.

[4] M. Stuiver and H. A. Polach. Reporting of C-14 data - discussion. *Radiocarbon*, 19(3):355–363, 1977.

[5] P. J. Reimer, T. A. Brown, and R. W. Reimer. Discussion: Reporting and calibration of post-bomb C-14 data. *Radiocarbon*, 46(3):1299–1304, 2004.

[6] P. J. Reimer, E. Bard, A. Bayliss, J. W. Beck, P. G. Blackwell, C. B. Ramsey, C. E. Buck, H. Cheng, R. L. Edwards, M. Friedrich, P. M. Grootes, T. P. Guilderson, H. Haflidason, I. Hajdas, C. Hatte, T. J. Heaton, D. L. Hoffmann, A. G. Hogg, K. A. Hughen, K. F. Kaiser, B. Kromer, S. W. Manning, M. Niu, R. W. Reimer, D. A. Richards, E. M. Scott, J. R. Southon, R. A. Staff, C. S. M. Turney, and J. van der Plicht. INTCAL13 and MARINE13 radiocarbon age calibration curves 0-50,000 years cal BP. *Radiocarbon*, 55(4):1869–1887, 2013.

[7] Q. Hua, M. Barbetti, and A. Z. Rakowski. Atmospheric radiocarbon for the period 1950-2010. *Radiocarbon*, 55(4):2059–2072, 2013.

[8] A. Alriksson. Regional variability of Cd, Hg, Pb and C concentrations in different horizons of swedish forest soils. *Water, Air and Soil Pollution: Focus*, 1(3-4):325–341, 2001.

[9] J. D. Blum, L. S. Sherman, and M. W. Johnson. Mercury isotopes in earth and environmental sciences. *Annu. Rev. Earth Planet. Sci. Lett.*, 42(1):249–269, 2014.

[10] A. Biswas, J. D. Blum, B. A. Bergquist, G. J. Keeler, and Z. Q. Xie. Natural mercury isotope variation in coal deposits and organic soils. *Environ. Sci. Technol.*, 42(22):8303–8309, 2008.

[11] J. G. Wiederhold, C. J. Cramer, K. Daniel, I. Infante, B. Bourdon, and R. Kretzschmar. Equilibrium mercury isotope fractionation between dissolved Hg(II) species and thiol-bound Hg. *Environ. Sci. Technol.*, 44(11):4191–4197, 2010.

[12] M. Jiskra, J. G. Wiederhold, B. Bourdon, and R. Kretzschmar. Solution speciation controls mercury isotope fractionation of Hg(II) sorption to goethite. *Environ. Sci. Technol.*, 46(12):6654–6662, 2012.

[13] L. E. Gratz, G. J. Keeler, J. D. Blum, and L. S. Sherman. Isotopic composition and fractionation of mercury in great lakes precipitation and ambient air. *Environ. Sci. Technol.*, 44(20):7764–7770, 2010.

[14] JB. Chen, H. Hintelmann, XB. Feng, and B. Dimock. Unusual fractionation of both odd and even mercury isotopes in precipitation from Peterborough, ON, Canada. *Geochim. Cosmochim. Acta*, 90(0):33–46, 2012.

[15] L. S. Sherman, J. D. Blum, G. J. Keeler, J. D. Demers, and J. T. Dvonch. Investigation of local mercury deposition from a coal-fired power plant using mercury isotopes. *Environ. Sci. Technol.*, 46(1):382–90, 2012.

[16] P. M. Donovan, J. D. Blum, D. Yee, G. E. Gehrke, and M. B. Singer. An isotopic record of mercury in San Francisco Bay sediment. *Chem. Geol.*, 349(0):87–98, 2013.

[17] J. D. Demers, J. D. Blum, and D. R. Zak. Mercury isotopes in a forested ecosystem: Implications for air-surface exchange dynamics and the global mercury cycle. *Glob. Biogeochem. Cycles*, 27(1):222–238, 2013.

[18] B. A. Bergquist and J. D. Blum. Mass-dependent and -independent fractionation of Hg isotopes by photoreduction in aquatic systems. *Science*, 318(5849):417–420, 2007.

[19] K. Kritee, J. D. Blum, M. W. Johnson, B. A. Bergquist, and T. Barkay. Mercury stable isotope fractionation during reduction of Hg(II) to Hg(0) by mercury resistant microorganisms. *Environ. Sci. Technol.*, 41(6):1889–1895, 2007.

[20] W. Zheng and H. Hintelmann. Nuclear field shift effect in isotope fractionation of mercury during abiotic reduction in the absence of light. *J. Phys. Chem. A*, 114(12):4238–4245, 2010.

[21] R. S. Smith, J. G. Wiederhold, A. D. Jew, G. E. Brown Jr, B. Bourdon, and R. Kretzschmar. Small-scale studies of roasted ore waste reveal extreme ranges of stable mercury isotope signatures. *Geochim. Cosmochim. Acta*, 137(0):1–17, 2014.

[22] N. Estrade, J. Carignan, J. E. Sonke, and O. F. X. Donard. Measuring Hg isotopes in bio-geo-environmental reference materials. *Geostand. Geoanal. Res.*, 34(1):79–93, 2010.

[23] M. Hoffmann, C. Mikutta, and R. Kretzschmar. Bisulfide reaction with natural organic matter enhances arsenite sorption: Insights from X-ray absorption spectroscopy. *Environ. Sci. Technol.*, 46(21):11788–11797, 2012.

Supporting Information to Chapter 3

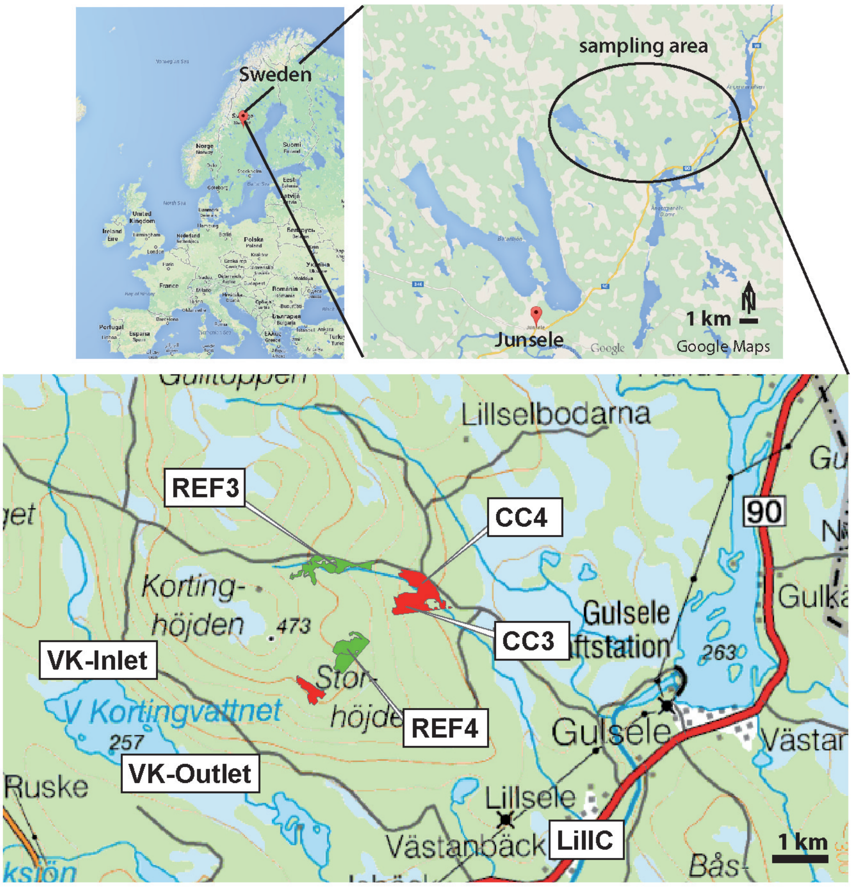
Sweden
sampling area
1 km
N
Junsele
Google Maps
REF3
CC4
CC3
VK-Inlet
VK-Outlet
REF4
LillC
Lillselbodarna
Korting-
höjden
473
Stor-
höjden
V Kortingvattnet
257
Ruske
Gulsele
Gulsele
263
90
Lillsele
Västanbäck
Västar
Bås-
1 km

Figure S3.1: Map of water sampling sites. The different water sampling locations are indicated at the lower panel. The four boreal forest catchments (reference sites in green (REF3, REF4) and clear-cut sites in red (CC3, CC4) drain in the same river (LillC). The nearby lake Vasta Kotingvattnet was sampled at the inlet (VK-Inlet) and outlet (VK-Outlet).

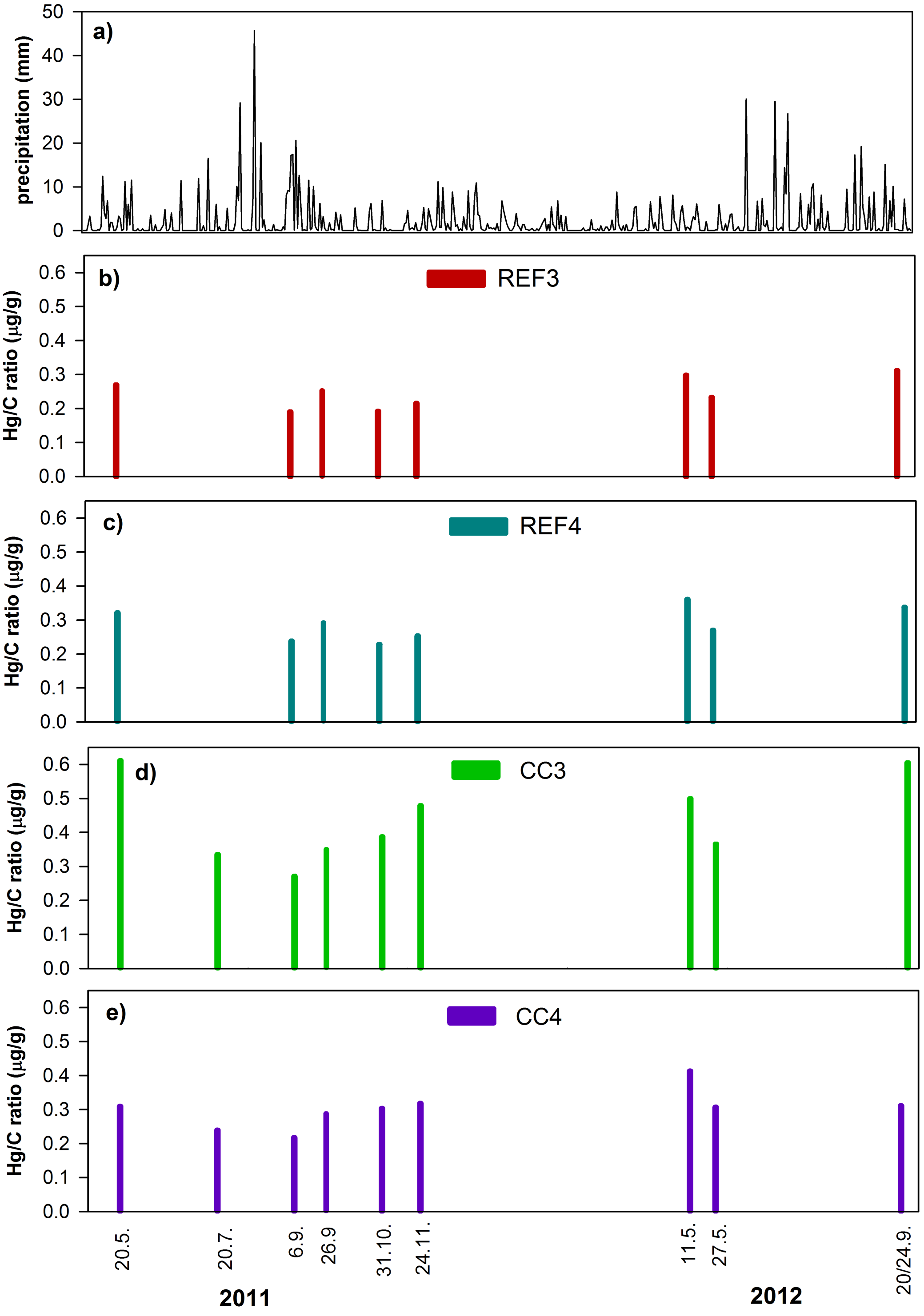

Figure S3.2: **a**) Precipitation at Junsele SMHI over whole sampling campaign from May 2011 to September 2012 (Data from Swedish Meterological Institute, SMHI). Hg/C ratios of the four sites: **b**) REF3 - Storhojden 1, **c**) REF4 - Storhojden 2, **d**) CC3 - Gulltoppen 1, and **d**) CC4 - Gulltoppen 2. (Data from Kronberg[1]).

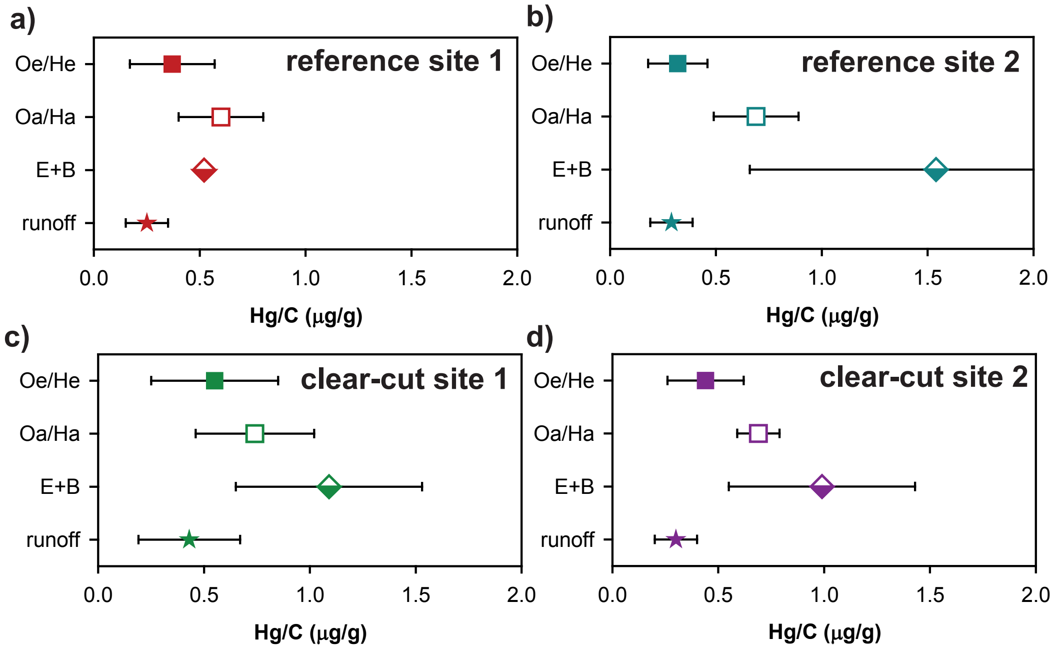

Figure S3.3: Hg/C ratios of boreal forest sites used in mixing models: The symbols represent the average and the error bars 2 standard deviation of the measured values.

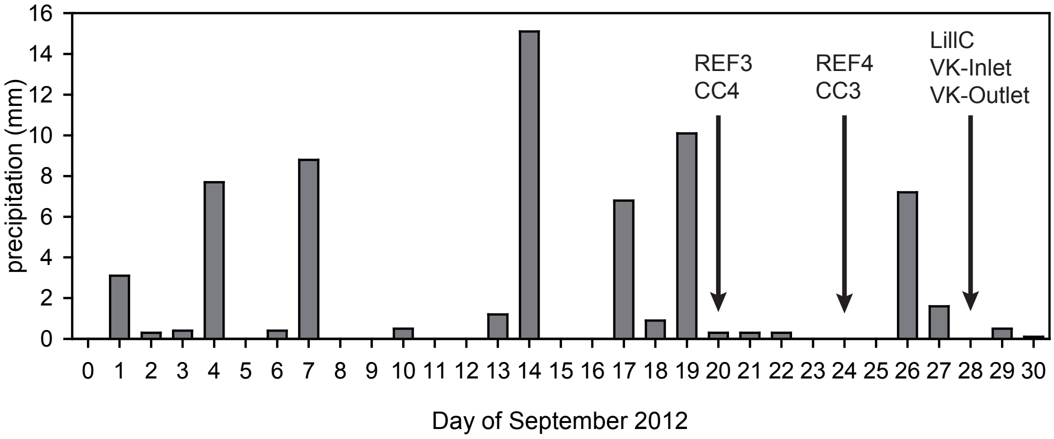

Figure S3.4: Precipitation at Junsele SMHI station during September 2012. The arrows indicate the days of sampling (Data from Swedish Meterological Institute, SMHI).

Radiocarbon dating

In addition to the radiocarbon dating of the bulk soil samples we performed humic acid extractions for selected samples. We followed an extraction procedure for the humic acid fraction adapted from the International Humic Substances Society (IHSS).[2] 10 g of soil sample was added to 100 ml 0.1 M HCl and shaken on a horizontal shaker for 1 h. Then pH was adjusted to 7 with 1 M NaOH and 0.1 M NaOH was added to reach a solid to solution ratio of 1:10. The soil samples were shaken for 4.5 h followed by sedimentation over night under N_2 atmosphere. The samples were centrifuged at 1000 rpm for 12 min and the humic acid extract decanted. The humic acid extracts were freeze-dried. The recovered powder after freeze-drying represented 0.5 - 4 % of the total sample mass and was used for dariocarbon analysis.

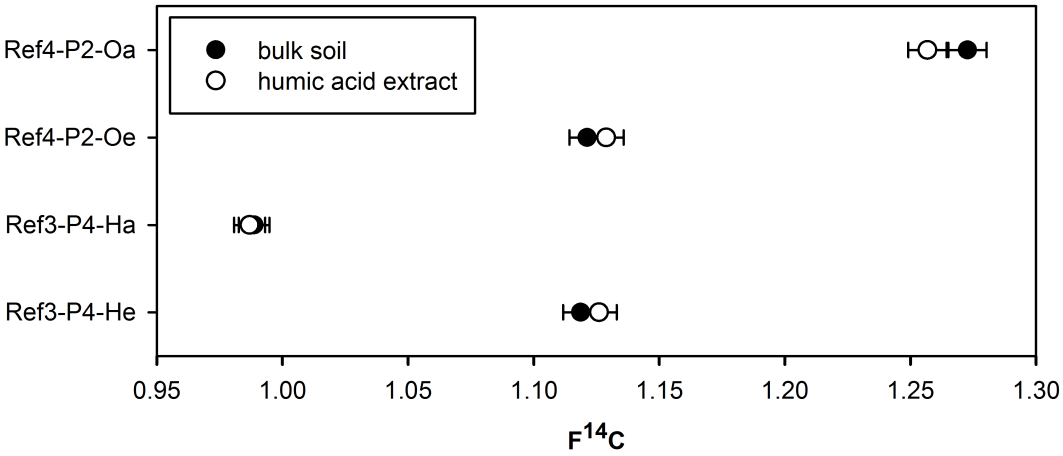

Figure S3.5: Comparison of radiocarbon signatures from bulk soils and humic acid extracts: The error bars represent two standard deviations of the analytical precision.

Table S3.1: Concentration data of soil samples from clear-cut sites: Horizon thickness, total Hg concentration (Hg tot), carbon (C) and nitrogen (N) concentration (% weight), C/N ratio, Hg:C ratio and Si concentration.

Sample	horizon (cm)	Hg tot (ng g^{-1})	C (%)	N (%)	C/N (g g^{-1})	Hg:C (μg g^{-1})	Si (mg g^{-1})
CC3							
CC3-P1-He	4	378	39.9	1.7	26.6	0.95	24
CC3-P2-He	4	164	43.6	1.3	38.4	0.38	9
CC3-P3-Oe	8	107	43.0	0.9	56.7	0.25	6
CC3-P4-Oe	5	143	37.6	1.1	39.4	0.38	19
CC3-P5-Oe	9	312	40.3	1.3	36.0	0.77	18
CC3-P1-Ha	23	340	32.3	1.3	28.3	1.05	48
CC3-P2-Ha	30	262	29.2	1.3	26.6	0.90	77
CC3-P3-Oa	4	216	45.7	1.1	49.4	0.47	7
CC3-P4-Oa	8	182	33.1	1.4	27.0	0.55	40
CC3-P5-E	3	18	1.9	0.0	104.9	0.93	262
CC3-P5-B	nd	60	4.8	0.1	51.3	1.25	178
CC4							
CC4-P1-He	7	235	42.9	1.6	31.4	0.55	11
CC4-P2-He	6	246	50.1	1.5	40.1	0.49	8
CC4-P3-He	5	176	46.2	1.3	42.0	0.38	6
CC4-P4-He	7	137	43.7	1.3	39.5	0.31	5
CC4-P5-Oe	4	199	41.8	1.3	37.2	0.48	12
CC4-P1-Ha	30	220	31.3	1.6	22.2	0.70	34
CC4-P2-Ha	25	278	40.3	1.8	25.9	0.69	19
CC4-P3-Ha	35	260	38.0	1.8	24.6	0.69	18
CC4-P4-Ha	24	213	34.2	1.8	22.5	0.62	29
CC4-P5-Oa	3	273	36.4	1.0	41.8	0.75	22
CC4-P5-E	7	11	0.8	0.0	nd	1.26	271
CC4-P5-B	nd	15	2.0	0.0	nd	0.72	211

nd = not determined

Table S3.2: Hg isotope data of soil samples reproduced from Jiskra et al.[3]

Samplename	name ref[3]	δ^{202}Hg (‰)	δ^{201}Hg (‰)	δ^{200}Hg (‰)	δ^{199}Hg (‰)	δ^{204}Hg (‰)	Δ^{199}Hg (‰)	Δ^{200}Hg (‰)	Δ^{201}Hg (‰)	Δ^{204}Hg (‰)	F^{14}C
REF3											
Ref3-P1-He	Histosol-He-1	-1.92	-1.84	-1.03	-0.85	-2.87	-0.37	-0.06	-0.40	-0.01	1.109
Ref3-P2-He	Histosol-He-2	-2.03	-1.86	-1.07	-0.87	-3.08	-0.36	-0.05	-0.34	-0.05	1.130
Ref3-P3-He	Histosol-He-3	-2.06	-1.87	-1.07	-0.86	-3.08	-0.34	-0.03	-0.32	0.00	
Ref3-P4-He	Histosol-He-4	-2.04	-1.85	-1.03	-0.81	-2.97	-0.30	-0.01	-0.31	0.08	1.119
Ref3-P5-Oe	Podzol-Oe-1	-2.21	-1.97	-1.08	-0.88	-3.28	-0.32	0.03	-0.31	0.01	
Ref3-P1-Ha	Histosol-Ha-1	-1.55	-1.53	-0.81	-0.82	-2.23	-0.43	-0.03	-0.36	0.09	0.878
Ref3-P2-Ha	Histosol-Ha-2	-1.75	-1.69	-0.93	-0.85	-2.55	-0.41	-0.05	-0.37	0.06	0.991
Ref3-P3-Ha	Histosol-Ha-3	-1.64	-1.68	-0.87	-0.86	-2.41	-0.45	-0.05	-0.44	0.04	
Ref3-P4-Ha	Histosol-Ha-4	-1.73	-1.68	-0.88	-0.86	-2.48	-0.43	-0.01	-0.39	0.10	0.989
Ref3-P5-E	Podzol-E-1	-1.80	-1.62	-0.93	-0.70	-2.70	-0.24	-0.03	-0.26	-0.01	1.015
REF4											
Ref4-P1-Oe	Podzol-Oe-2	-2.56	-2.35	-1.33	-1.08	-3.79	-0.44	-0.04	-0.42	0.04	1.107
Ref4-P2-Oe	Podzol-Oe-3	-2.49	-2.27	-1.24	-1.03	-3.71	-0.40	0.01	-0.40	0.01	1.121
Ref4-P3-Oe	Podzol-Oe-4	-2.25	-2.08	-1.13	-0.96	-3.39	-0.39	0.00	-0.39	-0.03	1.115
Ref4-P4-Oe	Podzol-Oe-5	-2.35	-2.18	-1.22	-1.02	-3.53	-0.43	-0.04	-0.41	-0.02	
Ref4-P5-Oe	Podzol-Oe-6	-2.37	-2.22	-1.16	-1.98	-3.72	-0.48	-0.01	-0.43	-0.02	1.132
Ref4-P1-Oa	Podzol-Oa-1	-1.93	-1.78	-0.96	-0.81	-2.93	-0.32	0.02	-0.33	-0.05	1.171
Ref4-P2-Oa	Podzol-Oa-2	-2.08	-1.88	-1.05	-0.84	-3.07	-0.32	0.00	-0.31	0.04	1.273
Ref4-P3-Oa	Podzol-Oa-3	-2.02	-1.88	-1.00	-0.83	-3.00	-0.32	0.02	-0.36	0.02	
Ref4-P4-Oa	Podzol-Oa-4	-2.16	-1.91	-1.09	-0.86	-3.23	-0.32	-0.01	-0.29	-0.02	1.178
Ref4-P5-Oa	Podzol-Oa-5	-2.01	-1.88	-1.00	-0.83	-3.03	-0.32	0.01	-0.37	-0.03	1.184
Ref4-P5-E	Podzol-E-2	-2.15	-1.90	-1.11	-0.85	-3.27	-0.31	-0.03	-0.29	-0.06	1.004
Ref4-P5-B	Podzol-B-1	-2.06	-1.88	-1.07	-0.87	-3.08	-0.35	-0.03	-0.33	-0.01	1.097

Table S3.3: Hg isotope data of soil samples from clear-cut sites.

Sample	δ^{202}Hg (‰)	δ^{201}Hg (‰)	δ^{200}Hg (‰)	δ^{199}Hg (‰)	δ^{204}Hg (‰)	Δ^{199}Hg (‰)	Δ^{200}Hg (‰)	Δ^{201}Hg (‰)	Δ^{204}Hg (‰)	Δ^{199}Hg/Δ^{201}Hg
CC3										
CC3-P2-He	-1.64	-1.63	-0.86	-0.84	-2.42	-0.43	-0.03	-0.40	0.02	1.08
CC3-P3-Oe	-2.21	-1.98	-1.12	-0.89	-3.22	-0.33	-0.01	-0.32	0.07	1.03
CC3-P4-Oe	-2.27	-2.14	-1.17	-1.00	-3.29	-0.43	-0.03	-0.43	0.11	0.98
CC3-P5-Oe	-2.04	-1.81	-1.02	-0.82	-3.01	-0.31	0.00	-0.28	0.03	1.08
CC3-P2-Ha	-1.68	-1.69	-0.93	-0.85	-2.53	-0.43	-0.08	-0.43	-0.03	1.00
CC3-P3-Oa	-1.76	-1.61	-0.95	-0.77	-2.53	-0.33	-0.06	-0.28	0.10	1.16
CC3-P4-Oa	-2.00	-1.85	-1.01	-0.84	-2.88	-0.34	-0.01	-0.34	0.10	0.99
CC3-P5-B	-1.76	-1.72	-0.91	-0.86	-2.59	-0.41	-0.03	-0.40	0.05	1.04
CC4										
CC4-P2-He	-2.48	-2.32	-1.26	-1.12	-3.64	-0.49	-0.02	-0.46	0.07	1.08
CC4-P3-He	-2.20	-2.04	-1.18	-0.95	-3.33	-0.39	-0.07	-0.38	-0.04	1.02
CC4-P4-He	-2.13	-1.94	-1.12	-0.92	-3.16	-0.38	-0.05	-0.34	0.02	1.12
CC4-P5-Oe	-2.21	-1.95	-1.15	-0.93	-3.30	-0.37	-0.04	-0.29	-0.01	1.29
CC4-P2-Ha	-1.91	-1.82	-1.02	-0.95	-2.85	-0.47	-0.07	-0.39	-0.01	1.19
CC4-P3-Ha	-1.75	-1.69	-0.91	-0.88	-2.58	-0.44	-0.03	-0.38	0.04	1.17
CC4-P4-Ha	-1.76	-1.76	-0.91	-0.89	-2.65	-0.44	-0.02	-0.44	-0.02	1.01
CC4-P5-Oa	-1.93	-1.78	-1.02	-0.80	-2.85	-0.31	-0.06	-0.33	0.03	0.95

Mixing model

To model the end-members of the different soil horizons we used the average and variance of the measured results. The results of the Hg isotope signatures, radiocarbon signatures, and Hg:C ratios are provided in Table S3.4. For soil horizons with only one measurement we used the standard deviation of the analytical precision to estimate the variance on the soil horizon. For the Hg isotope mixing a two-dimensional model combining MDF (δ^{202}Hg) and MIF (Δ^{199}) signatures was used as follows:

$$\delta^{202}\mathrm{Hg}_{\mathrm{mixed}} = f_{\mathrm{Oe/He}} \times \delta^{202}\mathrm{Hg}_{\mathrm{Oe/He}} + f_{\mathrm{Oa/Ha}} \times \delta^{202}\mathrm{Hg}_{\mathrm{Oa/Ha}} + f_{\mathrm{E+B}} \times \delta^{202}\mathrm{Hg}_{\mathrm{E+B}} \quad \text{(S3.1)}$$

$$\Delta^{199}\mathrm{Hg}_{\mathrm{mixed}} = f_{\mathrm{Oe/He}} \times \Delta^{199}\mathrm{Hg}_{\mathrm{Oe/He}} + f_{\mathrm{Oa/Ha}} \times \Delta^{199}\mathrm{Hg}_{\mathrm{Oa/Ha}} + f_{\mathrm{E+B}} \times \Delta^{199}\mathrm{Hg}_{\mathrm{E+B}} \quad \text{(S3.2)}$$

the radiocarbon signatures were calculated as follows:

$$\mathrm{F}^{14}\mathrm{C}_{\mathrm{mixed}} = f_{\mathrm{Oe/He}} \times \mathrm{F}^{14}\mathrm{C}_{\mathrm{Oe/He}} + f_{\mathrm{Oa/Ha}} \times \mathrm{F}^{14}\mathrm{C}_{\mathrm{Oa/Ha}} + f_{\mathrm{E+B}} \times \mathrm{F}^{14}\mathrm{C}_{\mathrm{E+B}} \quad \text{(S3.3)}$$

and the Hg/C ratios were calculated as follows:

$$\mathrm{Hg/C}_{\mathrm{mixed}} = f_{\mathrm{Oe/He}} \times \mathrm{Hg/C}_{\mathrm{Oe/He}} + f_{\mathrm{Oa/Ha}} \times \mathrm{Hg/C}_{\mathrm{Oa/Ha}} + f_{\mathrm{E+B}} \times \mathrm{Hg/C}_{\mathrm{E+B}} \quad \text{(S3.4)}$$

where $f_{\mathrm{Oe/He}}$, $f_{\mathrm{Oa/Ha}}$, and $f_{\mathrm{E+B}}$ correspond to the fraction of Hg or C from the Oe/He, Oa/Ha, and E+B horizon, respectively. The fractions of the different soil horizons were simulated using the linear distributed pseudorandom number generation function and the tracer signatures were simulated using the normal distributed pseudorandom number generation function of Matlab (R2012a, MathWorks). The results from the model simulations were compared to the measured values in the runoff and the average and standard deviation (σ) of model simulations in agreement with the measured values are reported.

Table S3.4: Compilation of Hg isotope signatures, radiocarbon signatures, and Hg:C ratios of different soil horizons and boreal forest catchment runoff. The average and standard deviation of the measured data were used to describe the source components in the mixing models.

Site	**δ^{202}Hg**			**δ^{199}Hg**			**F^{14}C**			**Hg:C**		
	n	average (‰)	σ (‰)	n	average (‰)	σ (‰)	n	average	σ	n	average (μg g^{-1})	σ (μg g^{-1})
reference site 1 - REF3												
Oe/He	5	-2.05	0.10	5	-0.34	0.03	3	1.12	0.01	5	0.37	0.10
Oa/Ha	4	-1.67	0.09	4	-0.43	0.02	3	0.95	0.06	4	0.60	0.10
E	1	-1.80		1	-0.24		1	1.02		1	0.52	
runoff	1	-1.99		1	-0.33		1	1.10		8	0.25	0.05
reference site 2 - REF4												
Oe	5	-2.41	0.12	5	-0.43	0.04	4	1.12	0.01	5	0.32	0.07
Oa	5	-2.04	0.08	5	-0.32	0.00	4	1.20	0.05	5	0.69	0.10
E+B	2	-2.10	0.06	2	-0.33	0.03	2	1.05	0.07	2	1.56	0.44
runoff	1	-2.29		1	-0.38		1	1.11		8	0.29	0.05
clear cut site 1 - CC3												
Oe/He	4	-2.04	0.28	4	-0.37	0.06				5	0.55	0.30
Oa/Ha	2	-1.81	0.17	3	-0.37	0.06				4	0.74	0.28
E+B	1	-1.76		1	-0.41					2	1.09	0.22
runoff	1	-2.05		1	-0.42					9	0.43	0.12
clear cut site 2 - CC4												
Oe/He	4	-2.25	0.15	4	-0.41	0.06				5	0.44	0.09
Oa/Ha	4	-1.84	0.09	4	-0.41	0.07				5	0.69	0.05
E+B	0			0						2	0.99	0.22
runoff	1	-2.01		1	-0.39					9	0.30	0.05

Table S3.5: Hg pool size (Hg tot pool) and annual outflow (Outflow) of boreal forest catchments. Data from Kronberg.[1]

Site		Hg tot pool average (g ha^{-1})	σ (g ha^{-1})	Outflow average (mg ha^{-1} a^{-1})
REF3	Oe/He	4.6	1.7	
	Oa/Ha	92.8	40.9	
	total	97.4		12.5
REF4	Oe	4.0	1.7	
	Oa	10.0	2.0	
	total	14.0		13.9
CC3	Oe/He	8.8	4.4	
	Oa/Ha	18.8	6.3	
	total	27.6		29.0
CC4	Oe/He	8.0	2.4	
	Oa/Ha	56.2	23.8	
	total	64.2		37.8

Table S3.6: Results of mixing models: Contributions of different soil horizons based on Hg isotopes, radiocarbon signature, and Hg:C ratio. Contribution of organic soil horizons to annual outflow (Outflow) and mobility of Hg as Hg in outflow relative to total soil pool.

Site	**Hg isotopes**		**radiocarbon**		**Hg:C ratio**		**Outflow**	**mobility**
	average f (%)	σ f (%)	average f (%)	σ f (%)	average f (%)	σ f (%)	average (mg ha^{-1} a^{-1})	average (% a^{-1})
REF3								
Oe/He	71	17	84	12	86	11	8.9	0.19
Oa/Ha	12	11	8	10	7	8	1.5	0.0017
E	16	14	8	8	7	8		
REF4								
Oe	58	18	64	28	91	10	8.1	0.20
Oa	20	15	16	17	6	7	2.7	0.027
E/B	22	16	20	19	3	6		
CC3								
Oe/He	55	25			66	26	15.8	0.18
Oa/Ha	25	21			21	22	7.3	0.039
B	20	16			13	13		
CC4								
Oe/He	48	22			78	25	18.3	0.23
Oa/Ha	52	9			8	9	19.5	0.035
E/B					14	20		

Table S3.7: Results of standards processed and measured together with the soil and water samples reported in this study and a parallel publication.[3] All measured values are in agreement with previously reported values (see references).

Standard	Name	form/matrix	n		δ^{202}Hg ‰	Δ^{199}Hg ‰	Δ^{200}Hg ‰	Δ^{201}Hg ‰	Δ^{204}Hg ‰	Reference
secondary standard	ETH-Fluka		26	average	-1.43	0.07	0.01	0.03	0.01	[4,5]
				2σ	0.12	0.05	0.05	0.07	0.11	
procedural standard	NIST SRM 2711	Montana soil	11	average	-0.12	-0.23	0.00	-0.18	0.01	[5,6]
				2σ	0.10	0.07	0.04	0.03	0.09	
procedural standard	Federsee-spike	Histosol[a]	2	average	-0.76	-0.01	0.00	-0.05	-0.03	
				2σ	0.09	0.08	0.04	0.12	0.04	

[a] = Histosol material has been characterized by Hoffmann et al.[7] and spiked to 2.9 μg g^{-1} with Hg(NO$_3$)$_2$-salt previously measured by Jiskra et al.[4]

References

[1] RM. Kronberg. *The Boreal Journey of Methyl Mercury- From Forest Harvest to Black Alder Swamps.* PhD thesis, 2014.

[2] R.S. Swift. *Organic matter characterization*, chapter 35, pages 1018–1020. Soil Sci. Soc. Am., Soil Sci. Soc. Am. Book Series: 5, Madison, WI, 1996.

[3] M. Jiskra, J. G. Wiederhold, U. Skyllberg, R.M. Kronberg, I. Hajdas, and R. Kretzschmar. Mercury isotopes reveal organic matter-driven reductive Hg loss from boreal forest soils. submitted.

[4] M. Jiskra, J. G. Wiederhold, B. Bourdon, and R. Kretzschmar. Solution speciation controls mercury isotope fractionation of Hg(II) sorption to goethite. *Environ. Sci. Technol.*, 46(12):6654–6662, 2012.

[5] R. S. Smith, J. G. Wiederhold, A. D. Jew, G. E. Brown Jr, B. Bourdon, and R. Kretzschmar. Small-scale studies of roasted ore waste reveal extreme ranges of stable mercury isotope signatures. *Geochim. Cosmochim. Acta*, 137(0):1–17, 2014.

[6] N. Estrade, J. Carignan, J. E. Sonke, and O. F. X. Donard. Measuring Hg isotopes in bio-geo-environmental reference materials. *Geostand. Geoanal. Res.*, 34(1):79–93, 2010.

[7] M. Hoffmann, C. Mikutta, and R. Kretzschmar. Bisulfide reaction with natural organic matter enhances arsenite sorption: Insights from X-ray absorption spectroscopy. *Environ. Sci. Technol.*, 46(21):11788–11797, 2012.

Supporting Information to Chapter 4

Materials and Methods

Stannous chloride ($SnCl_2 \times 2H_2O$), Analar Normapur, less than 0.05 ppm Hg, VWR; West Chester, USA), Hg(II)-nitrate ($Hg(NO_3)2 \times H_2O$, >97%, Fluka; Buchs SG, Switzerland), sodium chloride (NaCl, Analar Normapur, >99.5%, VWR), MOPS (3-Morpholinopropanesulfonic acid, $C_7H_{15}NO_4S$, >99%, Fluka), sodium sulfate (Na_2SO_4), >99%, Merck; Dietikon, Switzerland), hydrochloric acid (HCl 37%, Reag. ISO, Sigma-Aldrich; Steinheim, Germany), nitric acid (HNO_3>69%, Reag. ISO, Sigma-Aldrich), potassium bromide (KBr, >99.5%, Reag. ACS, Merck) and potassium bromate ($KBrO_3$, Reag. ISO, Merck) were used in this study. 0.2 μm PERFECT-FLOW Nylon Syringe filters were purchased from WICOM (Heppenheim, Germany).

0.2 M BrCl in 12M HCl was prepared according to Bloom et al.[1] Prior to solution preparation the reagent salts were baked in an oven at 220 ℃ for 48 h to remove potential traces of elemental Hg. BrCl was used as a stabilization agent in all samples and standards, and as a cleaning reagent in washing solutions and the acid bath. All vessels (Teflon centrifuge tubes, glass storage bottles) were kept for 24 h in an acid bath of ~6M HCl with 0.02 M BrCl as oxidizing and complexing agent. After removal from the acid bath the samples were rinsed three times with ultrapure water.

1% BrCl solution used as sample- and standard matrix was prepared by adding 1% v/v of the 0.2 M BrCl in 12M HCl solution to ultrapure water (>18 MΩ cm) resulting in 0.002 M BrCl in 0.12 M HCl. 2.5% $SnCl_2$ was used as reducing agent for the cold vapor (CV) introduction system and prepared by adding 2.5% w/v $SnCl_2$ to 1 M HCl. In order to remove traces of Hg, the solution was purged with argon for at least 30 minutes before using. The reducing agent was always freshly prepared and used within one week.

MOPS buffers have been extensively used in laboratory studies as inert pH buffers, however a recent study revealed that MOPS can have a significant influence on the sorption of Fe(II) to goethite in a concentration range also used in this study (2.5 mM).[2] Although we cannot exclude possible effects of MOPS in our study, we consider them to be negligible, based on the fact that the results of the MOPS buffered experimental series at pH 7 were identical to the unbuffered pH-series.

Hg isotope analysis

The continuous Hg^0 gas flow was generated with a HGX-200 cold vapor system (CETAC Technologies; Omaha, USA). All samples were measured at concentrations of 100 nM Hg (20 ppb) in 1% BrCl. Sample and bracketing standards were matched to have signal intensities not differing by more than 10%. Samples were introduced for a three minute stabilization period before data acquisition was started. Detector baseline was measured by electrostatic analyzer deflection (ESA deflection). Data were collected in 36 measurements of 5 s integration time each. The measurement was followed by a 5 min washout with 1% BrCl. After 5 min the ^{202}Hg signal had dropped below 15 mV, which represents less than 1% of the 100 nM signal intensity. Over the course of this project, the Tl introduction system was changed from an Aridus (CETAC Technologies) to an Apex (Elemental Scientific; Omaha, USA) desolvating nebulizer, resulting in a higher Tl signal stability. Hg isotope ratios were not affected by this modification. The Tl NIST-997 standard in a 0.1M HNO_3 matrix was used for mass bias correction in addition to standard bracketing with NIST-3133. Collectors of the Nu Plasma MC-ICP-MS were set for the masses 194, 196, 198, 199, 200, 201, 202, 203, 204, 206, and 208. Mass 194 detecting ^{194}Pt and masses 206 and 208 for ^{206}Pb and ^{208}Pb showed intensities which were always indistinguishable from the background signal, implying that interferences of Pb and Pt on the Hg signals could be neglected. For each measuring session, a gain calibration of the collectors was performed, signal intensities and peak shapes were tuned, followed by an in house standard measurement. Over the course of a measurement session, typically 3 in-house (ETH Fluka) standards were measured along with one UM-Almadèn standard.

Data analysis

The bulk mass balance and calculated isotopic bulk composition were assessed and minimum criteria were defined to ensure data quality.

For bulk mass balance all individual experiments were required to match within 10% to

$$\mathrm{m}_{\mathrm{diss}} + \mathrm{m}_{\mathrm{sorb}} = \mathrm{m}_{\mathrm{initial}} \tag{S4.1}$$

where the sum of dissolved Hg mass ($\mathrm{m}_{\mathrm{diss}}$) and sorbed Hg mass ($\mathrm{m}_{\mathrm{sorb}}$) recovered after equilibration must be equal to the initially added Hg ($\mathrm{m}_{\mathrm{initial}}$). Three data pairs did not fulfill this 10% criterion, but were within 20% and fulfilled the calculated bulk isotope composition criterion. These data were still included in this study, but are marked with asterisks in Table S4.4.

The isotopic bulk composition was calculated as follows

$$f_{\mathrm{sorb}} \times \delta^{202}\mathrm{Hg}_{\mathrm{sorb}} + f_{\mathrm{diss}} \times \delta^{202}\mathrm{Hg}_{\mathrm{diss}} = 0 \tag{S4.2}$$

where the sorbed fraction $\mathrm{f_{sorb}}$ ($\mathrm{m_{sorb}/(m_{sorb}+m_{diss})}$) and the dissolved fraction $\mathrm{f_{diss}}$ ($\mathrm{m_{diss}/(m_{sorb}+m_{diss})}$) were calculated from the concentration measurement. The uncertainty of the bulk isotope composition was calculated following the error propagation of the addition calculation:

$$\sigma^* = \sqrt{\sigma^2_{\mathrm{sorb}} + \sigma^2_{\mathrm{diss}}} = \sqrt{2 \times \sigma^2_{\mathrm{Std}}} \tag{S4.3}$$

where σ_{sorb} and σ_{diss} are equal to the external reproducibility of the standard measurements σ_{diss}. All experimental data pairs were within the 95% confidence interval of -0.133 to 0.133‰ in δ^{202}Hg (see Table S4.4).

Correction of the isotope composition of sorbed mercury.

The δ^{202}Hg value of the sorbed pool was corrected for the contribution of dissolved Hg which was left in the goethite residue after centrifugation. The volume of trapped solution ($\mathrm{V_{diss}}$) was determined gravimetrically. The total mass of Hg in the sample ($\mathrm{m_{tot}}$) was measured through concentration measurement after goethite dissolution. The concentration of the dissolved Hg ($\mathrm{C_{diss}}$) and its isotopic δ-value ($\delta^{202}\mathrm{Hg^{meas}_{diss}}$) were taken from the complementary filtered sample. For all samples the correction was smaller than the experimental precision.

$$\delta^{202}\mathrm{Hg^{corr}_{sorb}} = \frac{\delta^{202}\mathrm{Hg^{meas}_{sorb}} - (\mathrm{C_{diss}} \times \mathrm{V_{diss}}/\mathrm{m_{tot}})\delta^{202}\mathrm{Hg^{meas}_{diss}}}{\mathrm{m_{sorb}}/\mathrm{m_{tot}}} \tag{S4.4}$$

Calculation of Hg isotope enrichment factors

The enrichment factors ϵ^{202}Hg for a given experiment were defined as differences between the δ^{202}Hg value of the sorbed pool and the δ^{202}Hg value of the dissolved pool averaged over the number of individual batches (n) in an experimental series:

$$\epsilon^{202}\mathrm{Hg} = \frac{\sum_{\mathrm{i=1}}^{\mathrm{n}}(\delta^{202}\mathrm{Hg_{i(sorbed)}} - \delta^{202}\mathrm{Hg_{i(dissolved)}})}{\mathrm{n}} \tag{S4.5}$$

The true standard deviation of the enrichment factor was defined following the error propagation of the difference calculation as:

$$\sigma' = \frac{\sqrt{\sigma^2_{\mathrm{sorbed}} + \sigma^2_{\mathrm{dissolved}}}}{\sqrt{\mathrm{n}}} = \frac{\sqrt{2 \times \sigma^2_{\mathrm{Std}}}}{\sqrt{\mathrm{n}}} \tag{S4.6}$$

where σ_{sorbed} and $\sigma_{\mathrm{dissolved}}$ are equal to the external reproducibility of the standard measurements σ_{Std} and the increase in precision by the number of data pairs measured in one experimental series is accounted for by the denominator $\sqrt{\mathrm{n}}$. The $\mathrm{E}^{199}\mathrm{Hg}$ enrichment factor was calculated in analogous manner to $\epsilon^{202}\mathrm{Hg}$.

Statistical test

A two-sided z-test was performed to test whether there was a difference between the isotopic fractionation of two experimental series. The null hypothesis H_0 was defined as:

$$\mu' = \epsilon^{202}\mathrm{Hg}_{\mathrm{exp1}} - \epsilon^{202}\mathrm{Hg}_{\mathrm{exp2}} = 0 \tag{S4.7}$$

The test statistics were defined as:

$$z = \frac{\mu' - 0}{\sigma_{\mathrm{test}}} \sim \mathcal{N}(0,1) \tag{S4.8}$$

where σ_{test} was calculated from the standard deviations of the respective experimental series σ_{exp1} and σ_{exp2}:

$$\sigma_{\mathrm{test}} = \sqrt{{\sigma'_{\mathrm{exp1}}}^2 + {\sigma'_{\mathrm{exp2}}}^2} \tag{S4.9}$$

The individual tests (significance level $\alpha = 0.05$, two-sided) were performed using the method of Holm-Bonferroni[3] which accounts for multiple testing.

Table S4.1: Results of statistical tests comparing different experimental series as described in Table 4.1, where μ', σ_{test}, and the test statistic z are defined above, p is the p-value for the test statistic, and k the ranking according to the p-values used to calculate the adapted level of significance α/k according to Holm-Bonferroni.[3] As the null hypothesis H_0 of the test with the lowest p-value (MGR-72 series vs. MGR-Cl series was not rejected (p>α/k), all the null hypothesis H_0 were accepted.

series	μ'	σ_{test}	**z**	**p**	**k**	α**/k**	$\mathbf{H_0}$
MGR-72h vs. MGR-Cl	0.115	0.051	2.24	0.013	8	0.0031	accepted
pH-Cl vs. MGR-Cl	0.111	0.055	2.03	0.021	7	0.0036	accepted
MGR-72h vs. MGR-30d	0.103	0.051	2.01	0.022	6	0.0042	accepted
MGR-18h vs. MGR-30d	0.067	0.051	1.32	0.094	5	0.0050	accepted
MGR-72h vs. pH	0.049	0.045	1.09	0.138	4	0.0063	accepted
pH vs. pH-Cl	-0.045	0.049	-0.92	0.178	3	0.0083	accepted
MGR-72h vs. MGR-18h	0.035	0.047	0.74	0.229	2	0.0125	accepted
MGR-72h vs. MGR-sulfate	-0.017	0.051	-0.34	0.369	1	0.0250	accepted

Table S4.2: Results of statistical tests analyzing the significance of an enrichment in mass-independent fractionation ($E^{199}Hg$), where μ', σ_{test}, and the test statistic z are defined above, p is the p-value for the test statistic, and k the ranking according to the p-values used to calculate the adapted level of significance α/k according to Holm-Bonferroni.[3]

experimental series	μ'	σ_{test}	**z**	**p**	**k**	α/**k**	H_0
pH	0.028	0.011	2.47	0.0068	7	0.0036	accepted
MGR-720h	-0.026	0.015	-1.79	0.0370	6	0.0042	accepted
MGR-Cl	-0.026	0.015	-1.79	0.0370	2	0.0125	accepted
MGR-18h	-0.022	0.013	-1.71	0.0433	4	0.0063	accepted
MGR-72h	-0.018	0.013	-1.43	0.0763	3	0.0083	accepted
MGR-sulfate	0.015	0.015	1.02	0.1543	2	0.0125	accepted
pH-Cl	-0.001	0.015	-0.10	0.4619	1	0.0250	accepted

Comparison of model approaches

In order to obtain some first-order information concerning the reversibility of the adsorption reaction, we performed a statistical regression on the measured δ^{202}Hg values of the dissolved pool of all time series experiments (18 h, 72 h, and 720 h). In case of a reversible adsorption, where the sorbed pool is being equilibrated with the dissolved phase, one would expect a linear regression resulting from equilibrium isotope fractionation. In case of irreversible adsorption one would expect a logarithmic dependence of the δ^{202}Hg on the fraction sorbed caused by Rayleigh fractionation.[4] Figure S1 shows the regression of the linear model as solid line and the regression of the logarithmic model as dashed line. Both models show a good correlation with the experimental data for the calculated dissolved phase (closed symbols) as well as for the corresponding sorbed phase (open symbols) assuming a closed system. Based on these results, we were not able to exclude that the adsorption of Hg(II) to goethite was at least partly irreversible. However, it would require additional desorption experiments to further elucidate this issue.

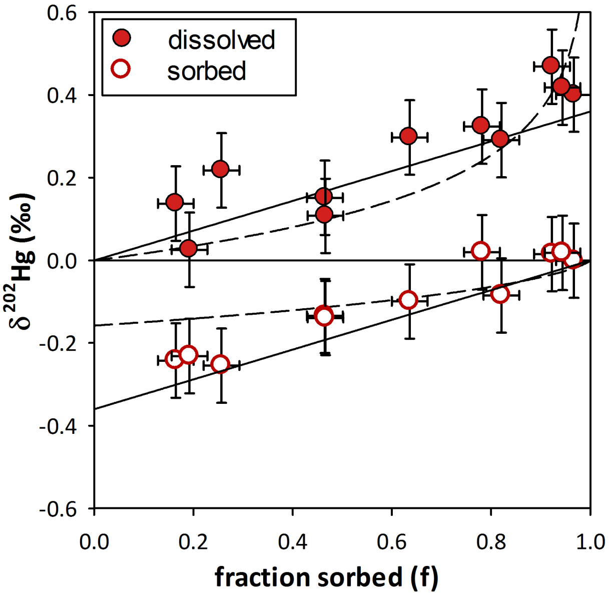

Figure S4.1: Hg isotope fractionation of all time series experiments (MGR-18h, MGR-72h and MGR-720h) of the dissolved pool are shown as closed symbols and the sorbed pool as open symbols. The solid line represents the linear regression and the dashed line represents the exponential Rayleigh model, both fitted for the dissolved phase.

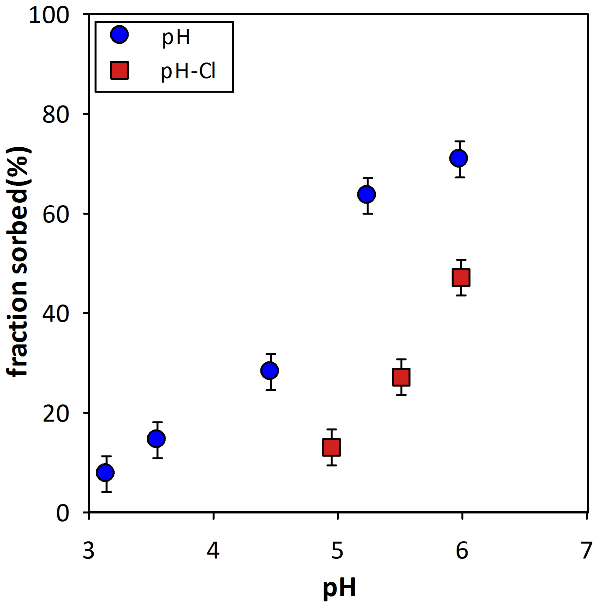

Figure S4.2: Fraction of Hg(II) sorbed to goethite as function of pH with a constant mercury-to-goethite ratio (MGR) of 0.030 μmol m^{-2}. The circles represent the pH series with no chloride (pH) and the squares represent the experiment in the presence of 0.5 mM Cl^{-} (pH-Cl series), where substantially less Hg was sorbing.

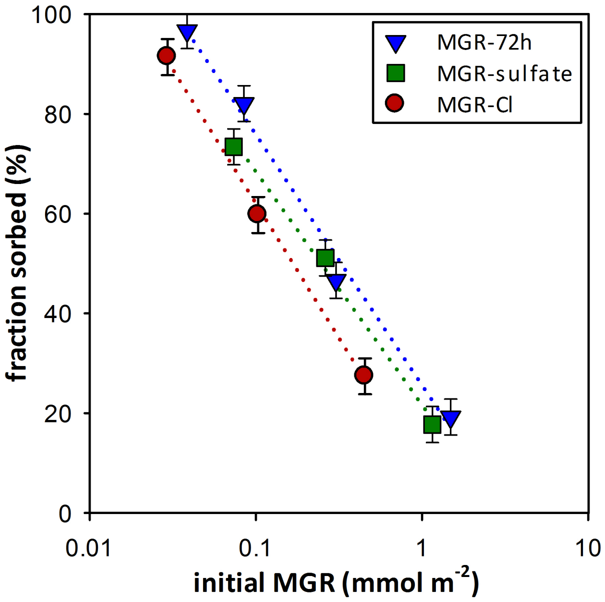

Figure S4.3: Fraction of Hg(II) sorbed to goethite as function of initial mercury-to-goethite-ratio (MGR) with different chloride and sulfate concentrations following Langmuir-type sorption. The fraction of Hg sorbed decreases from the experiment with no chloride and sulfate addition (triangles) to the 0.95 M sulfate series (squares) and the 0.5 mM chloride series (red circles). All experiments were performed at pH 7 (2.5 mM MOPS) with an equilibration time of 72 h.

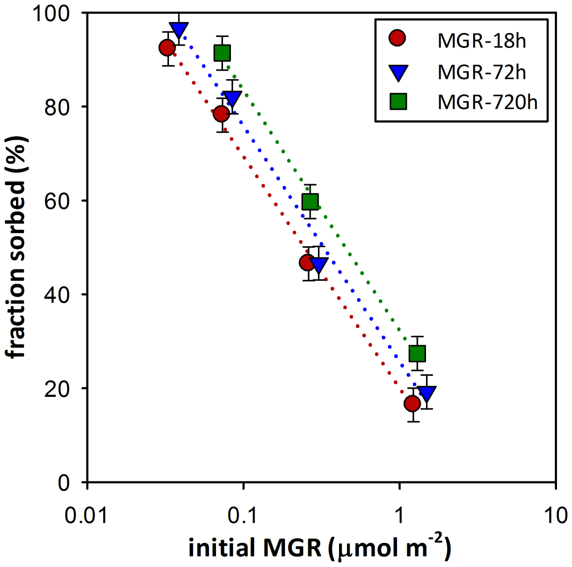

Figure S4.4: Fraction of Hg(II) sorbed to goethite as function of initial mercury-to-goethite-ratio (MGR) for different equilibration times following Langmuir-type sorption. The fraction of Hg sorbed increases from 18 h equilibration (circles) to 72 h (triangles) and 720 h (squares). All experiments were performed at pH 7 (2.5 mM MOPS).

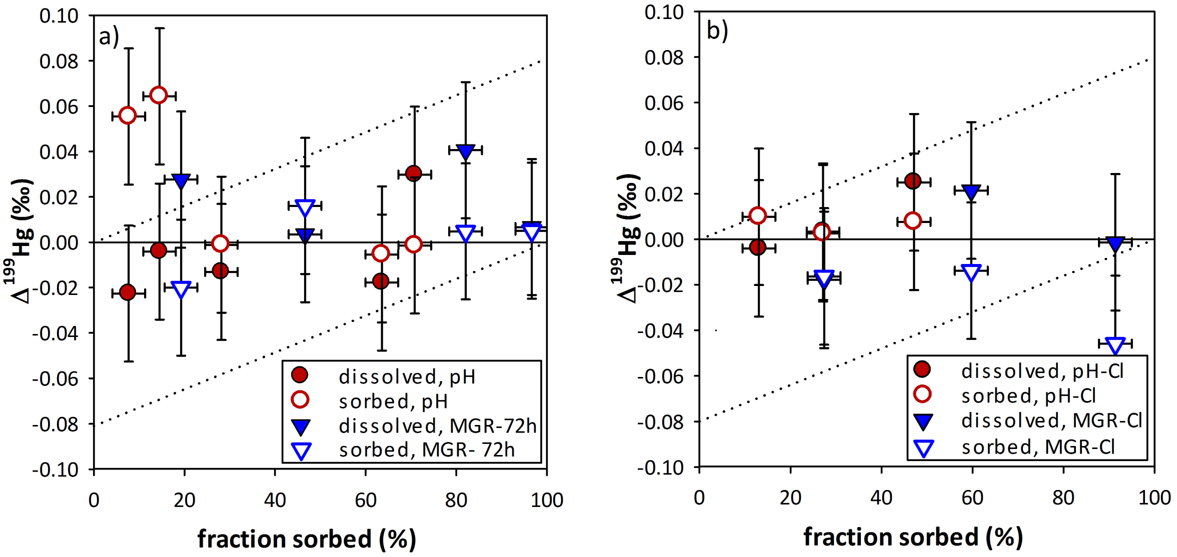

Figure S4.5: Mass independent Hg isotope fractionation during sorption of Hg(II) to goethite in the absence of chloride (a) and with 0.5 mM chloride (b). Δ^{199}Hg of sorbed (open symbols) and dissolved (closed symbols) pool as function of fraction sorbed. In the pH series (circles) the fraction of Hg sorbed was varied by pH (a: pH 3.1 - 6.0, b: pH 5 - 6) and in the MGR series by varying the Hg-to-goethite-ratio (a: 0.04 – 1.5 μmol m^{-2}, b: 0.03 - 0.45 μmol m^{-2}) at constant pH 7. The dotted lines represent the calculated MIF for nuclear volume fractionation for the cationic Hg species relative to the other solution species at pH 7 (a: Δ^{199}Hg = -0.081‰for $HgOH^+$, b: Δ^{199}Hg -0.080‰for $HgCl^+$).[5]

Table S4.3: Isotope measurements of Hg standard solutions relative to NIST 3133

	n		δ^{202}**Hg** ‰	δ^{199}**Hg** ‰	δ^{200}**Hg** ‰	δ^{201}**Hg** ‰	δ^{204}**Hg** ‰	Δ^{199}**Hg** ‰	Δ^{200}**Hg** ‰	Δ^{201}Hg ‰	Δ^{204}Hg ‰
UM-Almaden	4	mean	-0.55	-0.16	-0.27	-0.43	-0.82	-0.02	0.00	-0.01	0.00
		2σ	0.02	0.05	0.02	0.08	0.07	0.05	0.02	0.07	0.08
UM-Almaden published[6]		mean	-0.54	-0.14	-0.27	-0.44	-0.83	-0.01	0.00	-0.04	0.00
		2σ	0.08	0.06	0.04	0.07	0.11	0.02	0.02	0.04	0.01
ETH Fluka	16	mean	-1.38*	-0.27	-0.68	-1.00	-2.07	0.08	0.02	0.03	-0.02
		2σ	0.09	0.04	0.05	0.09	0.13	0.03	0.02	0.04	0.05
ETH Fluka published[5]	18	mean	-1.17*	-0.22	-0.57	-0.86	-1.76	0.07	0.02	0.02	-0.01
		2σ	0.15	0.04	0.08	0.11	0.22	0.02	0.02	0.03	0.03
Hg(II)-nitrate salt	4	mean	-0.69	-0.17	-0.34	-0.54	-1.02	0.01	0.01	-0.02	0.01
		2σ	0.09	0.03	0.02	0.04	0.15	0.03	0.03	0.03	0.02

* The reason for the small differences compared with the previously published Hg isotope data[5] of the ETH Fluka standard is not entirely clear. Both data sets are within analytical error of each other, but we think that the new isotope data reported in this study represent a more accurate estimate of the true isotopic composition. Aliquots of this standard have been distributed to different labs worldwide performing Hg isotope analyses to cross-calibrate its Hg isotope composition relative to NIST-3133.

Table S4.4a: **Compilation of experimental results:** Different experimental series sorted by pH or mercury-to-goethite-ratio (MGR): f: fraction, Γ: surface coverage, $\delta^{202}\mathrm{Hg}_{\mathrm{MB}}$: recalculated bulk isotope composition

pH	**MGR** μmol m^{-2}		(f) %	**Recovery** %	Γ μmol m^{-2}	$\delta^{202}\mathbf{Hg}_{\mathrm{MB}}$ ‰	δ^{202}**Hg** ‰	δ^{199}**Hg** ‰	δ^{200}**Hg** ‰	δ^{201}**Hg** ‰	δ^{204}**Hg** ‰	Δ^{199}**Hg** ‰	Δ^{200}**Hg** ‰	Δ^{201}Hg ‰	Δ^{204}Hg ‰
pH series, no chloride, 72h equilibration, MGR: 0.030 μmol m^{-2}															
5.2		dissolved	36.4	94.7		0.00	0.23	0.04	0.11	0.16	0.34	-0.02	-0.01	-0.01	-0.01
		sorbed	63.6		0.018		-0.14	-0.04	-0.07	-0.09	-0.19	-0.01	0.00	0.01	0.01
4.5		dissolved	71.9	98.8		0.02	0.11	0.01	0.04	0.07	0.13	-0.01	-0.02	-0.01	-0.03
		sorbed	28.1		0.009		-0.21	-0.05	-0.11	-0.13	-0.32	0.00	-0.01	0.03	-0.01
3.6		dissolved	85.5	97.2		0.03	0.10	0.02	0.04	0.08	0.12	0.00	-0.01	0.00	-0.03
		sorbed	14.5		0.004		-0.38	-0.03	-0.18	-0.29	-0.62	0.06	0.01	0.00	-0.06
6.0		dissolved	29.2	103.2		0.00	0.21	0.08	0.10	0.15	0.27	0.03	-0.01	-0.01	-0.03
		sorbed	70.8		0.022		-0.09	-0.02	-0.04	-0.09	-0.18	0.00	0.01	-0.02	-0.05
3.1		dissolved	92.3	102.6		-0.02	0.01	-0.02	0.01	-0.03	-0.03	-0.02	0.00	-0.03	-0.04
		sorbed	7.7		0.022		-0.37	-0.04	-0.18	-0.27	-0.57	0.06	0.01	0.01	-0.01
pH-Cl series, 0.5mM chloride, 72h equilibration, MGR: 0.030 μmol m^{-2}															
5.5		dissolved	72.9	108.8		-0.02	0.07	0.02	0.04	0.06	0.08	0.00	0.00	0.01	-0.02
		sorbed	27.1		0.009		-0.25	-0.06	-0.13	-0.20	-0.41	0.00	-0.01	-0.01	-0.04
6		dissolved	52.8	105.9		-0.03	0.13	0.06	0.07	0.09	0.15	0.03	0.00	0.00	-0.04
		sorbed	47.2		0.015		-0.21	-0.05	-0.11	-0.19	-0.37	0.01	-0.01	-0.03	-0.04
5		dissolved	87.0	104.7		0.01	0.05	0.01	0.02	0.03	0.03	0.00	-0.01	-0.01	-0.05
		sorbed	13.0		0.004		-0.26	-0.06	-0.14	-0.22	-0.43	0.01	0.00	-0.02	-0.03
MGR-72h series, 72h equilibration, no chloride, pH 7 (2.5 mM MOPS)															
	1.490	dissolved	80.8	100.9		-0.02	0.03	0.03	0.03	0.04	0.04	0.03	0.01	0.02	0.00
		sorbed	19.2		0.289		-0.23	-0.08	-0.12	-0.19	-0.35	-0.02	-0.01	-0.02	0.00
	0.303	dissolved	53.4	94.8		-0.01	0.11	0.03	0.05	0.08	0.13	0.00	-0.01	0.00	-0.03
		sorbed	46.6		0.134		-0.14	-0.02	-0.06	-0.10	-0.23	0.02	0.01	0.00	-0.02
	0.085	dissolved	17.9	99.8		-0.02	0.29	0.11	0.14	0.23	0.41	0.04	0.00	0.01	-0.03
		sorbed	82.1		0.070		-0.08	-0.02	-0.05	-0.06	-0.13	0.00	-0.01	0.01	0.00
	0.038	dissolved	3.3	92.1		0.01	0.40	0.11	0.20	0.29	0.51	0.01	0.00	-0.01	-0.08
		sorbed	96.7		0.034		0.00	0.00	0.00	0.01	-0.01	0.01	0.00	0.01	-0.01

All δ- and Δ- values are reported relative to the Hg isotope signature of the Hg(II)-nitrate salt.

The δ- and Δ- values of the sorbed pools are corrected for the contribution of dissolved Hg with remaining interstitial water in the centrifuged goethite residue.

Table S4.4b: **Compilation of experimental results:** Different experimental series sorted by pH or mercury-to-goethite-ratio (MGR): f: fraction, Γ: surface coverage, $\delta^{202}\mathrm{Hg}_{\mathrm{MB}}$: recalculated bulk isotope composition

pH	**MGR** μmol m^{-2}		(f) %	**Recovery** %	Γ μmol m^{-2}	$\delta^{202}\mathrm{Hg}_{\mathrm{MB}}$ ‰	δ^{202}Hg ‰	δ^{199}Hg ‰	δ^{200}Hg ‰	δ^{201}Hg ‰	δ^{204}Hg ‰	Δ^{199}Hg ‰	Δ^{200}Hg ‰	Δ^{201}Hg ‰	Δ^{204}Hg ‰
MGR-18h series, 18h equilibration, no chloride, pH 7 (2.5 mM MOPS)															
	1.225	dissolved	83.6	98.6		0.07	0.14	0.02	0.08	0.08	0.17	-0.02	0.01	-0.02	-0.03
		sorbed	16.4		0.196		-0.24	-0.10	-0.11	-0.24	-0.41	-0.05	0.01	-0.06	-0.05
	0.262	dissolved	53.5	91.5		0.02	0.15	0.06	0.07	0.15	0.20	0.01	-0.01	0.04	-0.02
		sorbed	46.5		0.110		-0.13	0.01	-0.05	-0.07	-0.18	0.03	0.02	0.03	0.02
	0.074	dissolved	21.8	87.9*		0.09	0.32	0.12	0.16	0.19	0.52	0.03	-0.01	-0.05	0.04
		sorbed	78.2		0.050		0.02	0.00	0.02	0.02	-0.02	-0.01	0.01	0.00	-0.05
	0.033	dissolved	7.7	82.1*		0.05	0.47	0.16	0.25	0.36	0.70	0.03	0.01	0.00	0.00
		sorbed	92.3		0.025		0.02	0.00	0.02	-0.01	0.03	-0.01	0.01	-0.02	0.01
MGR-720h series, 720h equilibration, no chloride, pH 7 (2.5 mM MOPS)															
	1.296	dissolved	74.4	91.4		0.10	0.22	0.03	0.10	0.15	0.30	-0.03	-0.01	-0.01	-0.02
		sorbed	25.6		0.302		-0.25	-0.10	-0.17	-0.24	-0.35	-0.05	-0.04	-0.05	0.03
	0.268	dissolved	36.4	92.4		0.05	0.30	0.03	0.11	0.17	0.44	-0.05	-0.05	-0.05	0.00
		sorbed	63.6		0.156		-0.10	-0.03	-0.06	-0.15	-0.20	-0.01	-0.01	-0.07	-0.05
	0.073	dissolved	5.6	90.5		0.04	0.42	0.17	0.27	0.29	0.55	0.05	0.06	-0.03	-0.07
		sorbed	94.4		0.062		0.02	0.06	0.02	0.05	-0.01	0.05	0.01	0.03	-0.04
MGR-Cl series, 0.5 mM chloride, 72h equilibration, pH 7 (2.5 mM MOPS)															
	0.454	dissolved	72.6	115.6*		0.03	0.12	0.02	0.04	0.11	0.16	-0.02	-0.03	0.02	-0.02
		sorbed	27.4		0.145		-0.22	-0.07	-0.14	-0.16	-0.31	-0.02	-0.03	0.00	0.01
	0.103	dissolved	40.3	108.9		-0.03	0.24	0.09	0.17	0.21	0.39	0.02	0.05	0.03	0.04
		sorbed	59.7		0.068		-0.22	-0.06	-0.10	-0.16	-0.36	-0.01	0.01	0.00	-0.04
	0.029	dissolved	8.6	103.3		-0.09	0.38	0.10	0.21	0.31	0.57	0.00	0.02	0.02	0.00
		sorbed	91.4		0.028		-0.13	-0.07	-0.09	-0.08	-0.24	-0.05	-0.03	0.02	-0.05
MGR-sulfate series, 0.95 M sulfate, 72h equilibration, no chloride, pH 7 (2.5 mM MOPS)															
	1.156	dissolved	82.3	105.2		0.00	0.05	0.00	0.02	0.02	0.05	-0.02	-0.01	-0.02	-0.03
		sorbed	17.7		0.217		-0.26	-0.05	-0.14	-0.21	-0.45	0.01	-0.01	-0.01	-0.06
	0.263	dissolved	48.9	104.7		-0.02	0.15	0.08	0.08	0.12	0.23	0.04	0.00	0.01	0.01
		sorbed	51.1		0.142		-0.19	-0.02	-0.07	-0.14	-0.31	0.02	0.02	0.00	-0.03
	0.073	dissolved	26.6	105.9		0.06	0.25	0.06	0.11	0.16	0.39	-0.01	-0.02	-0.03	0.01
		sorbed	73.4		0.058		-0.01	0.03	-0.01	-0.02	-0.14	0.02	-0.01	-0.02	-0.13

All δ- and Δ- values are reported relative to the Hg isotope signature of the Hg(II)-nitrate salt.

The δ- and Δ- values of the sorbed pools are corrected for the contribution of dissolved Hg with remaining interstitial water in the centrifuged goethite residue. *these batches were not fulfilling the mass balance criteria (90 - 110 % recovery)

Species calculation

Wiederhold et al.[5] calculated equilibrium isotope fractionation factors caused by nuclear volume fractionation (NVF) and mass dependent fractionation (MDF) of different Hg(II) species relative to elemental Hg vapor (calculated in gas phase). Table S4.5 reproduces the equilibrium isotopie enrichment factors (1000 ln $\beta^{202-198}$) of the relevant species in the experimental system at 298.15 K in the presence and absence of chloride. The relative contribution of the individual species was calculated by Visual MINTEQ.[7] The enrichment factor during species equilibration ($\epsilon^{202}\mathrm{Hg}_{\mathrm{SE}}$) was calculated from the difference of the equilibrium enrichment factor of the cationic species (1000 ln $\beta_{\mathrm{cat}}^{202-198}$) to the equilibrium enrichment factor of the neutral solution species $\sum_{\mathrm{i}}(f_{\mathrm{n_i}} \times 1000\ ln\ \beta_{\mathrm{cat}}^{202-198})$where $\mathrm{f}_{\mathrm{n_i}}$ is the abundance of the neutral species $\mathrm{n_i}$ relative to all neutral species.

$$\epsilon^{202}\mathrm{Hg}_{\mathrm{SE}} = 1000\ ln\beta_{\mathrm{cat}}^{202-198}\ - \sum\nolimits_{\mathrm{i}}(f_{\mathrm{n_i}} \times 1000\ ln\ \beta_{\mathrm{n_i}}^{202-198}) \qquad \text{(S4.10)}$$

Table S4.5: Calculated equilibrium isotopic enrichment factor for Hg species (‰)

1000 ln $\beta^{202-198}$4	**$Hg(OH)_2$**	**$Hg(OH)^+$**	**HgClOH**	**$HgCl_2$**	**$HgCl^+$**
NVF	1.00	1.41	1.11	1.25	1.49
MDF	1.19	0.42	1.06	0.84	0.39
Sum NVF + MDF	**2.19**	**1.82**	**2.17**	**2.09**	**1.88**
abundance (%)					
pH 7, no Cl^-	99.93	0.06			
pH 7, no Cl^-, 0.95 M SO_4^{2-}	99.99	0.0085			
pH 7, 0.5 mM Cl^-	36.95		49.63	13.37	0.006
ϵ^{202}Hg enrichment of cationic species relative to other species at pH 7 (‰)					
pH 7, no Cl^-		-0.37			
pH 7, 0.5 mM Cl^-					-0.28
E^{199}Hg enrichment of cationic species relative to other species at pH 7 (‰)					
pH 7, no Cl^-		-0.08			
pH 7, 0.5 mM Cl^-					-0.08

Derivation of equation 4.11 (main text) describing the isotopic enrichment during sorption.

The Hg-isotope enrichment during sorption of the cationic species ($\epsilon^{202}\mathrm{Hg}_{\mathrm{sorption}}$), consisting of the enrichment during outer-sphere complex formation ($\epsilon^{202}\mathrm{Hg}_{\mathrm{OS}}$) and during inner-sphere complex formation ($\epsilon^{202}\mathrm{Hg}_{\mathrm{IS}}$), can be described as:

$$\epsilon^{202}\mathrm{Hg}_{\mathrm{sorption}} = \delta^{202}\mathrm{Hg}_{\mathrm{sorbed}} - \delta^{202}\mathrm{Hg}_{\mathrm{cat}} \tag{S4.11}$$

The measured delta-value of the dissolved Hg pool ($\delta^{202}\mathrm{Hg}_{\mathrm{dissolved}}$) is a weighted sum of the isotope signature of the neutral ($\delta^{202}\mathrm{Hg}_{\mathrm{neut}}$) and the cationic ($\delta^{202}\mathrm{Hg}_{\mathrm{cat}}$) Hg-species, where $\mathrm{f}_{\mathrm{cat}}$ is the fraction of cationic species relative to all Hg species in solution.

$$\delta^{202}\mathrm{Hg}_{\mathrm{dissolved}} = \mathrm{f}_{\mathrm{cat}} \times \delta^{202}\mathrm{Hg}_{\mathrm{cat}} + (1 - \mathrm{f}_{\mathrm{cat}}) \times \delta^{202}\mathrm{Hg}_{\mathrm{neut}} \tag{S4.12}$$

Based on the assumption that 1000 ln $\beta^{202-198} \approx \epsilon^{202}\mathrm{Hg}$ and equations S4.10 and S4.12, $\delta^{202}\mathrm{Hg}_{\mathrm{cat}}$ can be expressed as:

$$\delta^{202}\mathrm{Hg}_{\mathrm{cat}} = \delta^{202}\mathrm{Hg}_{\mathrm{dissolved}} + (1 - \mathrm{f}_{\mathrm{cat}}) \times \epsilon^{202}\mathrm{Hg}_{\mathrm{SE}} \tag{S4.13}$$

The measured enrichment factor between the sorbed and the dissolved pool was defined in equation 4.4 in the main text as:

$$\epsilon^{202}\mathrm{Hg}_{\mathrm{sorbed-dissolved}} = \delta^{202}\mathrm{Hg}_{\mathrm{sorbed}} - \delta^{202}\mathrm{Hg}_{\mathrm{dissolved}} \tag{S4.14}$$

Expressing $\delta^{202}\mathrm{Hg}_{\mathrm{sorbed}}$ based on equation S4.11, this can be rewritten to:

$$\epsilon^{202}\mathrm{Hg}_{\mathrm{sorbed-dissolved}} = \epsilon^{202}\mathrm{Hg}_{\mathrm{sorption}} + \delta^{202}\mathrm{Hg}_{\mathrm{cat}} - \delta^{202}\mathrm{Hg}_{\mathrm{dissolved}} \tag{S4.15}$$

Expressing $\delta^{202}\mathrm{Hg}_{\mathrm{cat}}$ based on equation S4.13 the enrichment factor can be written as:

$$\epsilon^{202}\mathrm{Hg}_{\mathrm{sorbed-dissolved}} = \epsilon^{202}\mathrm{Hg}_{\mathrm{sorption}} + (1 - \mathrm{f}_{\mathrm{cat}}) \times \epsilon^{202}\mathrm{Hg}_{\mathrm{SE}} \tag{S4.16}$$

which is reported as equation 4.11 in the main text.

References

[1] N. S. Bloom, E. Preus, J. Katon, and M. Hiltner. Selective extractions to assess the biogeochemically relevant fractionation of inorganic mercury in sediments and soils. *Anal. Chim. Acta*, 479(2):233–248, 2003.

[2] A. Buchholz, C. Laskov, and S. B. Haderlein. Effects of zwitterionic buffers on sorption of ferrous iron at goethite and its oxidation by CCl_4. *Environ. Sci. Technol.*, 45(8):3355–60, 2011.

[3] S. Holm. A simple sequentially rejective multiple test procedure. *Scand. J. Stat.*, 6(2):65–70, 1979.

[4] J. Hoefs. *Stable Isotope Geochemistry.* Springer-Verlag, Berlin Heidelberg, Germany, 6 edition, 2009.

[5] J. G. Wiederhold, C. J. Cramer, K. Daniel, I. Infante, B. Bourdon, and R. Kretzschmar. Equilibrium mercury isotope fractionation between dissolved Hg(II) species and thiol-bound Hg. *Environ. Sci. Technol.*, 44(11):4191–4197, 2010.

[6] J. Blum and B. Bergquist. Reporting of variations in the natural isotopic composition of mercury. *Anal. Bioanal. Chem.*, 388(2):353–359, 2007.

[7] J.P. Gustafsson. Visual minteq 3.0, 2011.

Supporting Information to Chapter 5

Materials and reagents

Resins

The physicochemical properties of both resins are summarized in Table S5.1. Carboxyl- and thiol-resins were washed with 1 M HCl for one day, rinsed ten times with ultrapure water, and then equilibrated in ultrapure water acidified to pH 4 with 1 M HNO_3 until solution pH remained stable over time (pH 4 ± 0.1). $AgNO_3$ tests showed no detectable concentrations of dissolved Cl^-. Before weighing, resin beads were placed on a tissue paper and rinsed frequently with ultrapure water to keep them wet.

Table S5.1: Physicochemical properties of thiol-resin and carboxyl-resin

functional group (ionic form)	total exchange capacity (eq L^{-1})	moisture content (%)	mean particle size (μm)	operating pH	pK_a
Thiol (H^+)	$\geq 1.3^a$ (SH form)	$48.9 \pm 1.9\%^b$	450 - 700^a	1 - 13^a	2.7^c
Carboxyl (Na^+)	0.5^a (Na^+ form)	$55.7 \pm 2.2\%^b$	300 - 1,180^a	5 - 14^a	5^a

[a] values provided by the supplier
[b] standard deviation
[c] determined by pH titration

Enriched stable Hg isotope tracers

Table S5.2: Isotope abundance and molar masses of enriched Hg isotope tracers and natural abundance (NA)-Hg

mass	198-Hg^a (%)	200-Hg^a (%)	NA-Hg^b (%)
196	0.60	0.02	0.15
198	91.75	0.13	9.97
199	1.00	0.99	16.87
200	0.40	96.41	23.10
201	5.90	1.46	13.18
202	0.20	0.91	29.86
204	0.15	0.10	6.87
M (g mol^{-1})	198.21	200.06	200.51

[a] values provided by the supplier
[b] values provided by IUPAC[1]

Kinetic models - differential equations

1 pool model

corresponding to model **1** in Figure 2 of the main manuscript.

$$\frac{\mathrm{dN_{aq}^{202}}}{\mathrm{dt}} = -\mathrm{k^{ads}} \times \mathrm{N_{aq}^{202}} + \mathrm{k^{des}} \times \mathrm{N_{S1}^{202}} \tag{S5.1}$$

$$\frac{\mathrm{dN_{S1}^{202}}}{\mathrm{dt}} = -\mathrm{k^{des}} \times \mathrm{N_{S1}^{202}} + \mathrm{k^{ads}} \times \mathrm{N_{aq}^{202}} \tag{S5.2}$$

$$\frac{\mathrm{dN_{aq}^{198}}}{\mathrm{dt}} = -\mathrm{k^{ads}} \times \mathrm{N_{aq}^{198}} + \mathrm{k^{des}} \times \mathrm{N_{S1}^{198}} \tag{S5.3}$$

$$\frac{\mathrm{dN_{S1}^{198}}}{\mathrm{dt}} = -\mathrm{k^{des}} \times \mathrm{N_{S1}^{198}} + \mathrm{k^{ads}} \times \mathrm{N_{aq}^{198}} \tag{S5.4}$$

2 pool model

corresponding to model **2** in Figure 2 of the main manuscript.

$$\frac{\mathrm{dN_{aq}^{202}}}{\mathrm{dt}} = -\mathrm{k^{ads1}} \times \mathrm{N_{aq}^{202}} - \mathrm{k^{ads2}} \times \mathrm{N_{aq}^{202}} + \mathrm{k^{des1}} \times \mathrm{N_{S1}^{202}} + \mathrm{k^{des2}} \times \mathrm{N_{S2}^{202}} \tag{S5.5}$$

$$\frac{\mathrm{dN_{S1}^{202}}}{\mathrm{dt}} = -\mathrm{k^{des1}} \times \mathrm{N_{S1}^{202}} + \mathrm{k^{ads1}} \times \mathrm{N_{aq}^{202}} \tag{S5.6}$$

$$\frac{\mathrm{dN_{S2}^{202}}}{\mathrm{dt}} = -\mathrm{k^{des2}} \times \mathrm{N_{S2}^{202}} + \mathrm{k^{ads2}} \times \mathrm{N_{aq}^{202}} \tag{S5.7}$$

$$\frac{\mathrm{dN_{aq}^{198}}}{\mathrm{dt}} = -\mathrm{k^{ads1}} \times \mathrm{N_{aq}^{198}} - \mathrm{k^{ads2}} \times \mathrm{N_{aq}^{198}} + \mathrm{k^{des1}} \times \mathrm{N_{S1}^{198}} + \mathrm{k^{des2}} \times \mathrm{N_{S2}^{198}} \tag{S5.8}$$

$$\frac{\mathrm{dN_{S1}^{198}}}{\mathrm{dt}} = -\mathrm{k^{des1}} \times \mathrm{N_{S1}^{198}} + \mathrm{k^{ads1}} \times \mathrm{N_{aq}^{198}} \tag{S5.9}$$

$$\frac{\mathrm{dN_{S2}^{198}}}{\mathrm{dt}} = -\mathrm{k^{des2}} \times \mathrm{N_{S2}^{198}} + \mathrm{k^{ads2}} \times \mathrm{N_{aq}^{198}} \tag{S5.10}$$

2 pool model - with dissolved organic ligands

corresponding to model **3** in Figure 2 of the main manuscript.

$$\frac{\mathrm{dN_{L1}^{202}}}{\mathrm{dt}} = -\mathrm{k^{ads1}} \times \mathrm{N_{L1}^{202}} + \mathrm{k^{des1}} \times \mathrm{N_{S1}^{202}} \tag{S5.11}$$

$$\frac{\mathrm{dN_{L2}^{202}}}{\mathrm{dt}} = -\mathrm{k^{ads2}} \times \mathrm{N_{L2}^{202}} + \mathrm{k^{des2}} \times \mathrm{N_{S1}^{202}} \tag{S5.12}$$

$$\frac{\mathrm{dN_{S1}^{202}}}{\mathrm{dt}} = -\mathrm{k^{des1}} \times \mathrm{N_{S1}^{202}} + \mathrm{k^{ads1}} \times \mathrm{N_{L1}^{202}} - \mathrm{k^{des2}} \times \mathrm{N_{S1}^{202}} + \mathrm{k^{ads2}} \times \mathrm{N_{L2}^{202}} \tag{S5.13}$$

$$\frac{\mathrm{dN_{L1}^{198}}}{\mathrm{dt}} = -\mathrm{k^{ads1}} \times \mathrm{N_{L1}^{198}} + \mathrm{k^{des1}} \times \mathrm{N_{S1}^{198}} \tag{S5.14}$$

$$\frac{\mathrm{dN_{L2}^{198}}}{\mathrm{dt}} = -\mathrm{k^{ads2}} \times \mathrm{N_{L2}^{198}} + \mathrm{k^{des2}} \times \mathrm{N_{S1}^{198}} \tag{S5.15}$$

$$\frac{\mathrm{dN_{S1}^{198}}}{\mathrm{dt}} = -\mathrm{k^{des1}} \times \mathrm{N_{S1}^{198}} + \mathrm{k^{ads1}} \times \mathrm{N_{L1}^{198}} - \mathrm{k^{des2}} \times \mathrm{N_{S1}^{198}} + \mathrm{k^{ads2}} \times \mathrm{N_{L2}^{198}} \tag{S5.16}$$

Initial conditions

Table S5.3: Initial conditions for isotope exchange models: Concentrations (nmol $\mathrm{L^{-1}}$) of NA-Hg added in the preconditioning phase (NA-$\mathrm{Hg_{precond}}$), in removed solution after 96h (NA-$\mathrm{Hg_{removed}}$), and 198-Hg tracer added for the isotope exchange phase.

series	NA-$\mathrm{Hg_{precond.}}$ (nmol $\mathrm{L^{-1}}$)	NA-$\mathrm{Hg_{removed}}$ (nmol $\mathrm{L^{-1}}$)	198-$\mathrm{Hg_{tracer}}$ (nmol $\mathrm{L^{-1}}$)
$\mathrm{Hg(II)_{aq}}$ − C-resin	9’971	41	94[a]
$\mathrm{Hg(II)_{aq}}$ − T-resin	103’191	29	943[a]
Hg(II)-EDTA − C-resin	10’617	1’780	1’747
Hg(II)-cysteine − C-resin	8’621	507	482
Hg(II)-NOM − C-resin	12’218	1’880	1’555
Hg(II)-NOM − T-resin	105’193	3’063	2’541
$\mathrm{Hg(II)_{aq}}$ − goethite	807	99	103
$\mathrm{Hg(II)Cl_{aq}}$ − goethite	943	580	624

[a] ≈1% of NA-Hg in the system

The initial conditions for the one pool equilibrium model (model **1a**, Figure 2 main manuscript) were calculated as follows:

$$\mathrm{N}_{\mathrm{aq}}^{202}(0) = \text{198-Hg}_{\mathrm{tracer}} \times ^{202}\mathrm{ab}_{198-\mathrm{Hg}} \times \mathrm{V} \tag{S5.17}$$

$$\mathrm{N}_{\mathrm{S1}}^{202}(0) = (\text{NA-Hg}_{\mathrm{precond}} - \text{NA-Hg}_{\mathrm{removed}}) \times \mathrm{V} \times ^{202}\mathrm{ab}_{\mathrm{NA-Hg}} \tag{S5.18}$$

$$\mathrm{N}_{\mathrm{aq}}^{198}(0) = \text{198-Hg}_{\mathrm{tracer}} \times ^{198}\mathrm{ab}_{198-\mathrm{Hg}} \times \mathrm{V} \tag{S5.19}$$

$$\mathrm{N}_{\mathrm{S1}}^{198}(0) = (\text{NA-Hg}_{\mathrm{precond}} - \text{NA-Hg}_{\mathrm{removed}}) \times \mathrm{V} \times ^{198}\mathrm{ab}_{\mathrm{NA-Hg}} \tag{S5.20}$$

where $\text{198-Hg}_{\mathrm{tracer}}$, $\text{NA-Hg}_{\mathrm{precond}}$ and $\text{NA-Hg}_{\mathrm{removed}}$ correspond to the experimental concentrations given in Table S5.3, $^{202}\mathrm{ab}_{198-\mathrm{Hg}}$ and $^{198}\mathrm{ab}_{198-\mathrm{Hg}}$ correspond to the relative abundance of ^{202}Hg and ^{198}Hg in the enriched 198-Hg tracer, $^{202}\mathrm{ab}_{\mathrm{NA-Hg}}$ and $^{198}\mathrm{ab}_{\mathrm{NA-Hg}}$ correspond to the relative abundance of ^{202}Hg and ^{198}Hg in the natural abundance NA-Hg (Table S5.2) and V to the experimental volume of 9.5×10^{-3} L.

The initial conditions of the dissolved Hg(II) for the two pool model (model **2**, Figure 2 main manuscript) were calculated as described in equations S5.17 and S5.19. The initial conditions of the different solid-bound Hg(II) pools were calculated from the sorbed NA-Hg concentration after the preconditioning phase similar to the one-pool model (equations S5.18 and S5.20). The initial total sorbed concentrations were divided into the two sorbed pools (S1 and S2) as follows:

$$\mathrm{N}_{\mathrm{S1}}^{202}(0) = (\text{NA-Hg}_{\mathrm{precond.}} - \text{NA-Hg}_{\mathrm{removed}}) \times \mathrm{V} \times ^{202}\mathrm{ab}_{\text{NA-Hg}} \times (1 - f_{\mathrm{S-NE}}) \times f1 \tag{S5.21}$$

$$\mathrm{N}_{\mathrm{S2}}^{202}(0) = (\text{NA-Hg}_{\mathrm{precond.}} - \text{NA-Hg}_{\mathrm{removed}}) \times \mathrm{V} \times ^{202}\mathrm{ab}_{\text{NA-Hg}} \times (1 - f_{\mathrm{S-NE}}) \times (1 - f1) \tag{S5.22}$$

$$\mathrm{N}_{\mathrm{S1}}^{198}(0) = (\text{NA-Hg}_{\mathrm{precond.}} - \text{NA-Hg}_{\mathrm{removed}}) \times \mathrm{V} \times ^{198}\mathrm{ab}_{\text{NA-Hg}} \times (1 - f_{\mathrm{S-NE}}) \times f1 \tag{S5.23}$$

$$\mathrm{N}_{\mathrm{S2}}^{198}(0) = (\text{NA-Hg}_{\mathrm{precond.}} - \text{NA-Hg}_{\mathrm{removed}}) \times \mathrm{V} \times ^{198}\mathrm{ab}_{\text{NA-Hg}} \times (1 - f_{\mathrm{S-NE}}) \times (1 - f1) \tag{S5.24}$$

where f1 corresponds to the initial pool size of the fast exchanging solid-bound Hg(II) relative to the total exchanging Hg(II). The pool of non-exchangeable NA-Hg(II) ($f_{\mathrm{S-NE}}$) relative to the total sorbed pool after the preequilibration phase was subtracted from the initial sorbed NA-Hg(II). The parameters $f_{\mathrm{S-NE}}$ and $f1$ were derived from the Monte Carlo simulations.

The initial conditions af the dissolved Hg(II) for the two pool model in presence of dissolved organic ligands (model **3**, Figure 2 main manuscript) were calculated as follows:

$$\mathrm{N}^{202}_{\mathrm{L1}}(0) = 198\text{-}\mathrm{Hg}_{\mathrm{tracer}} \times^{202} \mathrm{ab}_{198\text{-}\mathrm{Hg}} \times \mathrm{V} \times (1 - f_{\mathrm{L-NE}}) \times f1 \tag{S5.25}$$

$$\mathrm{N}^{202}_{\mathrm{L2}}(0) = 198\text{-}\mathrm{Hg}_{\mathrm{tracer}} \times^{202} \mathrm{ab}_{198\text{-}\mathrm{Hg}} \times \mathrm{V} \times (1 - f_{\mathrm{L-NE}}) \times (1 - f1) \tag{S5.26}$$

$$\mathrm{N}^{202}_{\mathrm{S1}}(0) = (\mathrm{NA\text{-}Hg}_{\mathrm{precond.}} - \mathrm{NA\text{-}Hg}_{\mathrm{removed}}) \times \mathrm{V} \times^{202} \mathrm{ab}_{\mathrm{NA\text{-}Hg}} \times (1 - f_{\mathrm{S-NE}}) \tag{S5.27}$$

$$\mathrm{N}^{198}_{\mathrm{L1}}(0) = 198\text{-}\mathrm{Hg}_{\mathrm{tracer}} \times^{198} \mathrm{ab}_{198\text{-}\mathrm{Hg}} \times \mathrm{V} \times (1 - f_{\mathrm{L-NE}}) \times f1 \tag{S5.28}$$

$$\mathrm{N}^{198}_{\mathrm{L2}}(0) = 198\text{-}\mathrm{Hg}_{\mathrm{tracer}} \times^{198} \mathrm{ab}_{198\text{-}\mathrm{Hg}} \times \mathrm{V} \times (1 - f_{\mathrm{L-NE}}) \times (1 - f1) \tag{S5.29}$$

$$\mathrm{N}^{198}_{\mathrm{S1}}(0) = (\mathrm{NA\text{-}Hg}_{\mathrm{precond.}} - \mathrm{NA\text{-}Hg}_{\mathrm{removed}}) \times \mathrm{V} \times^{198} \mathrm{ab}_{\mathrm{NA\text{-}Hg}} \times (1 - f_{\mathrm{S-NE}}) \tag{S5.30}$$

where $f_{\mathrm{L-NE}}$ corresponds to the pool size of non-exchangeable ligand-bound 198-Hg(II) relative to the total pool of dissolved Hg(II), $f1$ corresponds to the initial pool size of the fast exchanging dissolved-organic-ligand-bound Hg(II) relative to the total exchanging Hg(II) in solution and $f_{\mathrm{S-NE}}$ corresponds to the non-exchangeable pool derived from the isotope exchange experiments in absence of dissolved organic ligands. For carboxyl-resin $f_{\mathrm{S-NE}}$=0 and for thiol-resin $f_{\mathrm{S-NE}}$=0.57.

For experimental series modeled with a non-exchangeable pool of dissolved-organic-ligand-bound Hg(II) ($f_{\mathrm{L-NE}}$>0) R and $\mathrm{Hg_{tot}}$ were calculated as follows:

$$\mathrm{R}_{\mathrm{aq}}(\mathrm{t}) = \frac{\mathrm{N}^{202}_{\mathrm{L1}}(\mathrm{t}) + \mathrm{N}^{202}_{\mathrm{L2}}(\mathrm{t}) + f_{\mathrm{L-NE}} \times 198\text{-}\mathrm{Hg}_{\mathrm{tracer}} \times^{202} \mathrm{ab}_{198\text{-}\mathrm{Hg}} \times \mathrm{V}}{\mathrm{N}^{198}_{\mathrm{L1}}(\mathrm{t}) + \mathrm{N}^{198}_{\mathrm{L2}}(\mathrm{t}) + f_{\mathrm{L-NE}} \times 198\text{-}\mathrm{Hg}_{\mathrm{tracer}} \times^{198} \mathrm{ab}_{198\text{-}\mathrm{Hg}} \times \mathrm{V}} \tag{S5.31}$$

$$\mathrm{Hg}^{\mathrm{aq}}_{\mathrm{tot}}(\mathrm{t}) = \frac{\frac{\mathrm{N}^{202}_{\mathrm{L1}}(\mathrm{t})}{^{202}\mathrm{ab}_{\mathrm{NA\text{-}Hg}}} + \frac{\mathrm{N}^{202}_{\mathrm{L2}}(\mathrm{t})}{^{202}\mathrm{ab}_{\mathrm{NA\text{-}Hg}}} + \frac{\mathrm{N}^{198}_{\mathrm{L1}}(\mathrm{t})}{^{198}\mathrm{ab}_{198\text{-}\mathrm{Hg}}} + \frac{\mathrm{N}^{198}_{\mathrm{L2}}(\mathrm{t})}{^{198}\mathrm{ab}_{198\text{-}\mathrm{Hg}}}}{\mathrm{V}} + f_{\mathrm{L-NE}} \times 198\text{-}\mathrm{Hg}_{\mathrm{tracer}} \tag{S5.32}$$

Alternative approach to calculate pool size of non-exchangeable Hg

Solid-bound non-exchangeable Hg

Alternatively to the determination of the pool sizes of non-exchangeable Hg using the Monte Carlo simulation approach, as described in this study, we would like to highlight that a mass balance approach not requiring model simulations can be used. This approach requires the experimental initial conditions (Table S3), the isotope abundances (Table S2), and the isotope ratio in solution at steady state (plateau) ($R^{\infty}_{\mathrm{diss}}$), which can also be determined graphically without kinetic models. The isotope ratio of the system (R_{system}) can be described by:

$$R_{\mathrm{system}} = f_{\mathrm{ex}} \times R^{\infty}_{\mathrm{diss}} + f_{\mathrm{NE}} \times R_{\mathrm{S-NE}} \tag{S5.33}$$

where f_{ex} corresponds to the exchangeable and f_{NE} to the non-exchangeable fraction relative to the total Hg. The isotope ratio of the non-exchangeable pool ($R_{\mathrm{S-NE}}$) corresponds to the isotope ratio after the preconditioning phase, in this case to ^{202}Hg/^{198}Hg of NA-Hg. After rearrangement of equation S5.33, the fraction of non-exchangeable solid-bound Hg ($f_{\mathrm{S-NE}}$) relative to the total sorbed Hg can be calculated as follows:

$$f_{S-NE} \;=\; \frac{1 - \frac{R^{\infty}_{diss}}{R_{\mathrm{system}}}}{f_{sorb}\left(\frac{R_{\mathrm{S-NE}}}{R_{\mathrm{system}}} - \frac{R^{\infty}_{diss}}{R_{\mathrm{system}}}\right)} \tag{S5.34}$$

where f_{sorb} corresponds to the sorbed fraction relative to total Hg and $R_{\mathrm{diss}}{}^{\infty}$ to the isotope ratio in solution at steady state (plateau value). The mass balance approach provided similar results to the Monte Carlo approach used in this study, e.g., for the Hg(II)$_{\mathrm{aq}}$ - T-resin experiment a non-exchangeable pool (f_{NE}) of 62 % was determined, compared to 57 % from the Monte Carlo approach.

Ligand-bound non-exchangeable Hg

In case the non-exchangeable pool is in the dissolved phase the fraction of non-exchangeable ligand-bound Hg ($f_{\mathrm{L-NE}}$), relative to the total dissolved Hg was expressed as follows:

$$f_{\mathrm{L-NE}} \;=\; \frac{\left(\frac{f_{\mathrm{diss}}}{f_{\mathrm{sorb}}} + 1\right)\frac{R^{\infty}_{\mathrm{diss}}}{R_{\mathrm{system}}} - \left(\frac{1}{f_{\mathrm{sorb}}}\right)}{\frac{R_{\mathrm{L-NE}}}{R_{\mathrm{system}}} - \frac{1}{f_{\mathrm{sorb}}}\left(1 + f_{\mathrm{diss}}\frac{R^{\infty}_{\mathrm{diss}}}{R_{\mathrm{system}}}\right)} \tag{S5.35}$$

where f_{diss} and f_{sorb} correspond to the dissolved and sorbed fraction relative to total Hg, respectively. $R^{\infty}_{\mathrm{diss}}$ corresponds to the isotope ratio in solution at steady state (plateau value). The isotope ratio of the non-exchangeable ligand-bound pool ($R_{\mathrm{L-NE}}$) corresponds to the isotope ratio of the enriched Hg isotope tracer added in the isotope exchange phase, in this case to ^{202}Hg/^{198}Hg of 198-Hg.

Diffusion into non-exchangeable pool

To test the assumption, whether the pool of non-exchangeable Hg remains constant over the isotope exchange phase, we added a diffusive flux to the two pool model (model 2 in main manuscript). Since we were lacking the concentration gradient in the solid phases of the experiment we simplified the modes by assuming a constant diffusive flux (D):

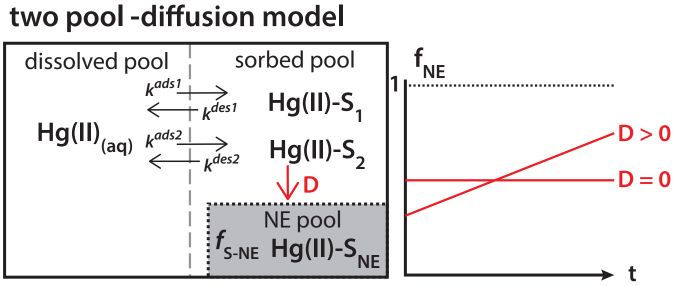

Figure S5.1: Adaptation of two pool model (model 2 in main manuscript) including a diffusive flux of solid-bound Hg (Hg(II)-S$_2$) to the non-exchangeable pool (NE pool). In absence of a diffusive flux (D=0) the non-exchangeable pool is constant over the isotope exchange phase and in case of a diffusive flux (D<0) the pool of non-exchangeable Hg increases over the isotope exchange phase.

$$\frac{\mathrm{dN_{aq}^{202}}}{\mathrm{dt}} = -\mathrm{k^{ads1}} \times \mathrm{N_{aq}^{202}} - \mathrm{k^{ads2}} \times \mathrm{N_{aq}^{202}} + \mathrm{k^{des1}} \times \mathrm{N_{S1}^{202}} + \mathrm{k^{des2}} \times \mathrm{N_{S2}^{202}} \tag{S5.36}$$

$$\frac{\mathrm{dN_{S1}^{202}}}{\mathrm{dt}} = -\mathrm{k^{des1}} \times \mathrm{N_{S1}^{202}} + \mathrm{k^{ads1}} \times \mathrm{N_{aq}^{202}} \tag{S5.37}$$

$$\frac{\mathrm{dN_{S2}^{202}}}{\mathrm{dt}} = -\mathrm{k^{des2}} \times \mathrm{N_{S2}^{202}} + \mathrm{k^{ads2}} \times \mathrm{N_{aq}^{202}} - \mathrm{D} \tag{S5.38}$$

$$\frac{\mathrm{dN_{aq}^{198}}}{\mathrm{dt}} = -\mathrm{k^{ads1}} \times \mathrm{N_{aq}^{198}} - \mathrm{k^{ads2}} \times \mathrm{N_{aq}^{198}} + \mathrm{k^{des1}} \times \mathrm{N_{S1}^{198}} + \mathrm{k^{des2}} \times \mathrm{N_{S2}^{198}} \tag{S5.39}$$

$$\frac{\mathrm{dN_{S1}^{198}}}{\mathrm{dt}} = -\mathrm{k^{des1}} \times \mathrm{N_{S1}^{198}} + \mathrm{k^{ads1}} \times \mathrm{N_{aq}^{198}} \tag{S5.40}$$

$$\frac{\mathrm{dN_{S2}^{198}}}{\mathrm{dt}} = -\mathrm{k^{des2}} \times \mathrm{N_{S2}^{198}} + \mathrm{k^{ads2}} \times \mathrm{N_{aq}^{198}} - \mathrm{D} \tag{S5.41}$$

We modeled the experimental data of the Hg(II)$_{aq}$ - thiol resin experiment and the two experimental series with goethite as solid phase. The addition of a diffusive flux from the slow exchanging pool (Hg(II)-S_2) presumably consisting of inner-sphere bound Hg resulted in a better representation of the data for the Hg(II)$_{aq}$ - thiol-resin experiment (Figure S5.2 and Table S5.4). The addition of a diffusive flux to the goethite experiment did not result in a better model representation of the data.

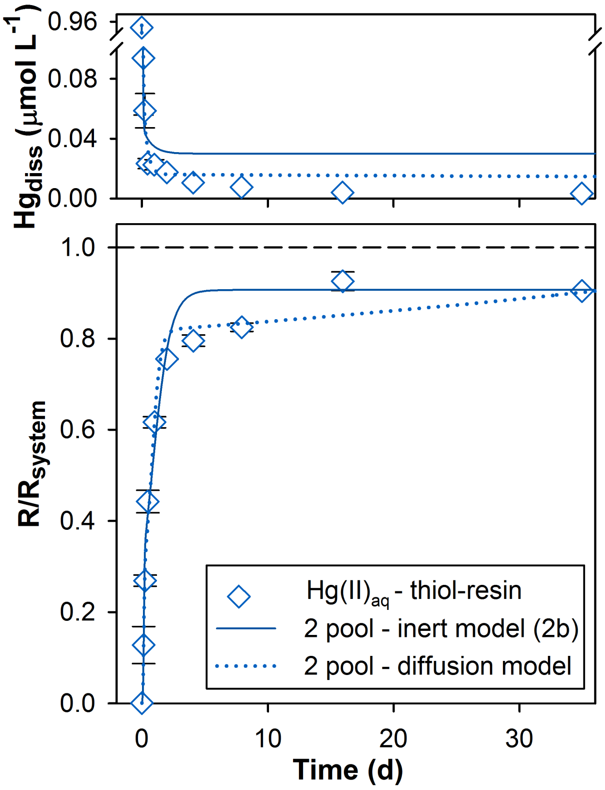

Figure S5.2: Comparison of model fits of different isotope exchange models (corresponding to Figure 2 in main mauscript) for the isotope exchange between Hg(II)$_{aq}$ and thiol-resin-bound Hg(II).

Table S5.4: Comparison of model parameters for Hg(II)$_{aq}$ - thiol-resin experiment: Adsorption and desorption rate coefficients (k^{ads1}, k^{ads2}, k^{des1} and k^{des2}), initial size of fast exchangeable pool relative to total exchangeable pool ($f1$), pool size of non-exchangeable Hg (f_{NE}), time to reach equilibrium (t_{eq}), and coefficient of determination for the isotope ratio fit (R^2 (R)) and the concentration fit (R^2 ($Hg_{dissolved}$)).

model	k^{ads1} (h^{-1})	k^{ads2} (h^{-1})	k^{des1} (h^{-1})	k^{des2} (h^{-1})	D (nmol h^{-1})	f1 (%)	f_{NE} (%)	R^2(R)	R^2(Hg_{diss})
2b	1.9×10^{-1}	1.0	6.9×10^{-2}	6.0×10^{-4}	0.0	0.5	57	0.984	0.990
2b-D	1.4×10^{-1}	1.0	1.5×10^{-1}	5.4×10^{-4}	6.0×10^{-3}	1.3	74	0.992	0.999

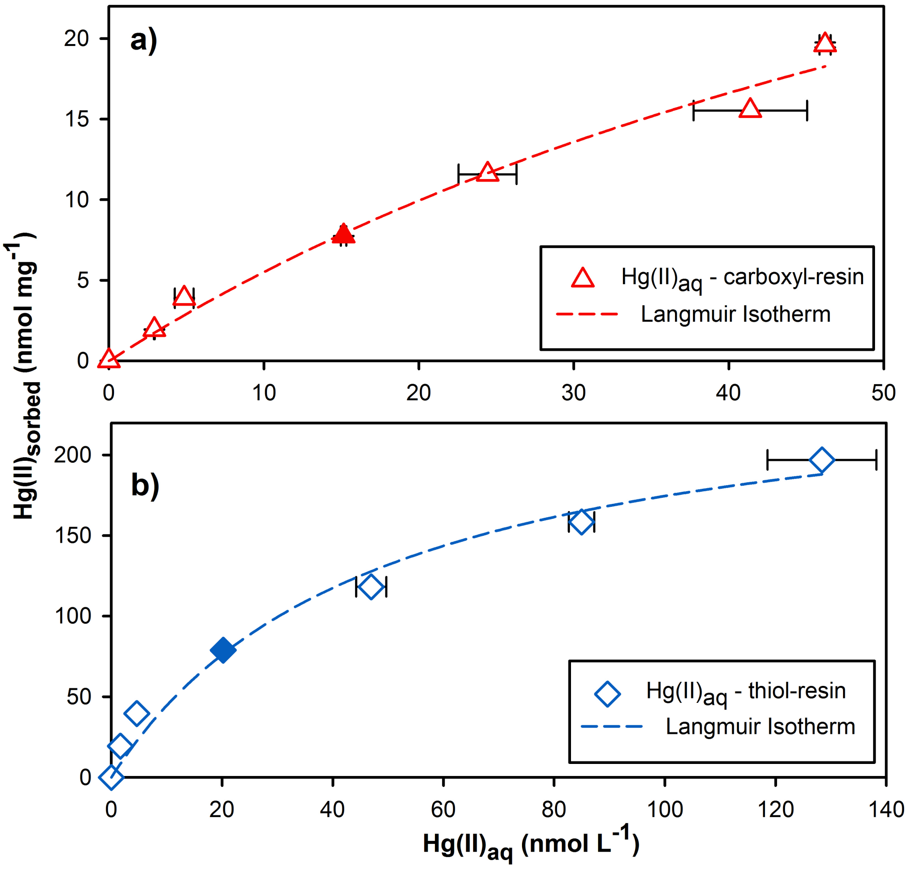

Figure S5.3: Sorption isotherms of Hg(II) adsorption to carboxyl-resin (**a**) and thiol-resin (**b**) after 96 h equilibration time. The symbols represent the measured data, with the closed symbols corresponding to the experimental conditions used during the isotope exchange experiments. Langmuir sorption isotherms are shown as dashed lines. Error bars represent the range of duplicate samples.

Table S5.5: Fitting parameters of Langmuir isotherms[a] for Hg(II) sorption to carboxyl- and thiol-resin (Figure S3).

	L (L nmol^{-1})	capacity Q_{max} (nmol mg^{-1})	R^2
carboxyl-resin	0.012 (±0.006)	50.5 (±17)	0.98
thiol-resin[b]	0.021 (±0.006)	258 (±30)	0.98

[a] $Q = Q_{\max} \frac{LC}{1+LC}$, where Q corresponds to the Hg loading on the resin (nmol mg^{-1}), C to the dissolved Hg concentration (nmol L^{-1}), L to the affinity of Hg for the resin (L nmol^{-1}), and $Q_{\max}$ to the adsorption capacity of the resin (nmol mg^{-1}).

[b] consider with care as equilibrium was not reached after 96h adsorption time (see main manuscript).

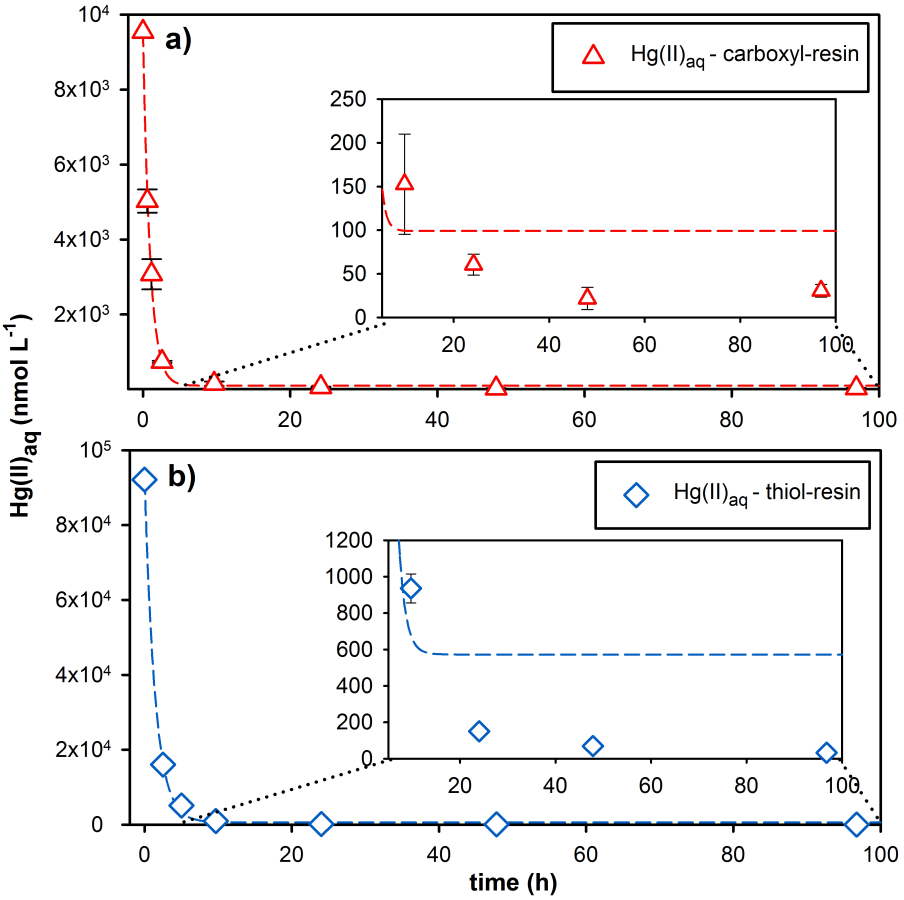

Figure S5.4: Initial adsorption kinetics of Hg(II) adsorption to carboxyl-resin (**a**) and thiol-resin (**b**) during 96 h preconditioning time. The lines indicate the model fits for the 1 pool exchange models (Figure 5.2a, concentration optimization). Error bars represent the range of duplicate samples.

Table S5.6: Hg(II) adsorption and desorption kinetics during the preconditioning phase on carboxyl- and thiol-resin (Figure S5.4).

	k^{ads} (h^{-1})	k^{des} (h^{-1})	R^2
carboxyl-resin	1.04	0.011	0.998
thiol-resin	0.695	0.0043	0.9993

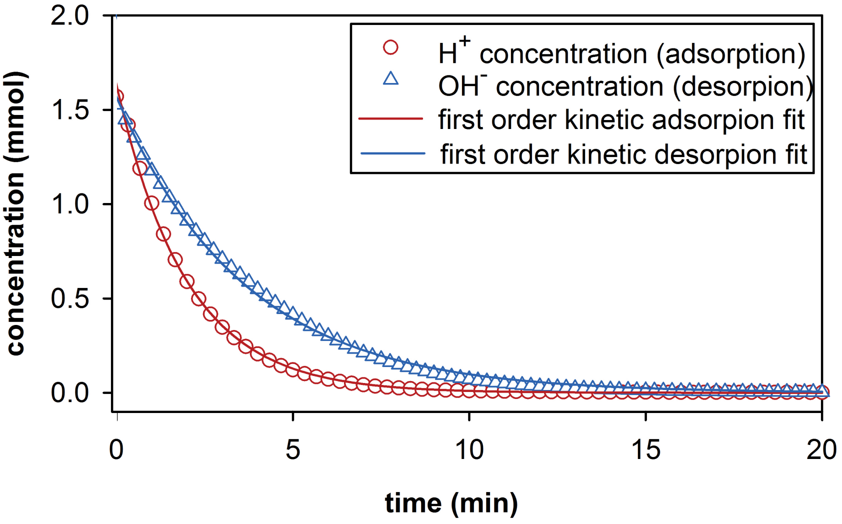

Figure S5.5: Adsorption kinetics of protons (red circles) as H^+ concentration and desorption kinetics of protons (blue triangles) as OH^- concentration on carboxyl-resin. (The response time of the electrode in a control experiment was considerably faster than with carboxyl-resin).

Table S5.7: Proton adsorption and desorption kinetics on carboxyl-resin (Figure S5.5).

	rate (h^{-1})	R^2
adsorption	30.5 (±0.1)	0.999
desorption	0.28 (±0.001)	0.998

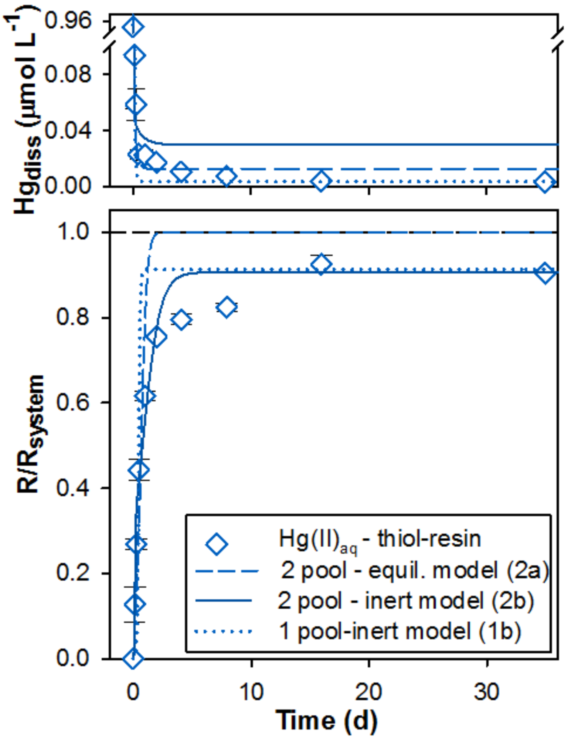

Figure S5.6: Comparison of model fits of different isotope exchange models (Figure 5.2) for the isotope exchange between $Hg(II)_{aq}$ and thiol-resin-bound Hg(II).

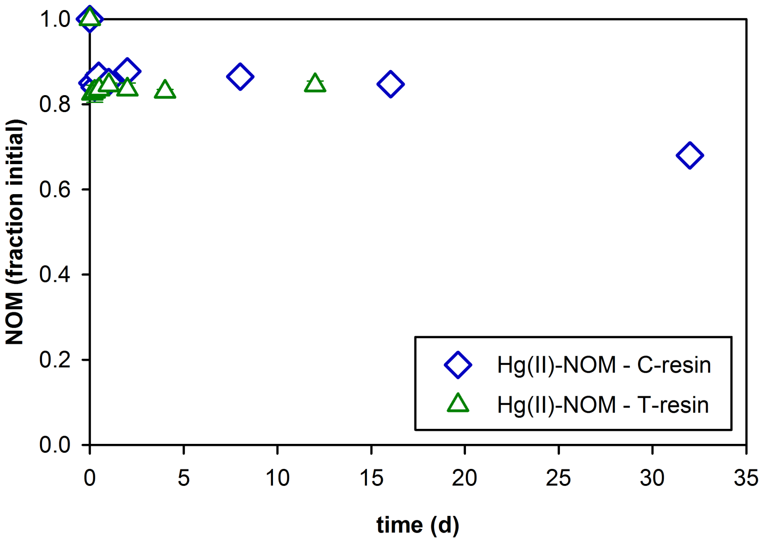

Figure S5.7: Concentration of dissolved Suwannee River natural organic matter (NOM) in percent of the initial standard (measured by UV absorbance at 245 nm). Error bars represent the range of duplicate samples.

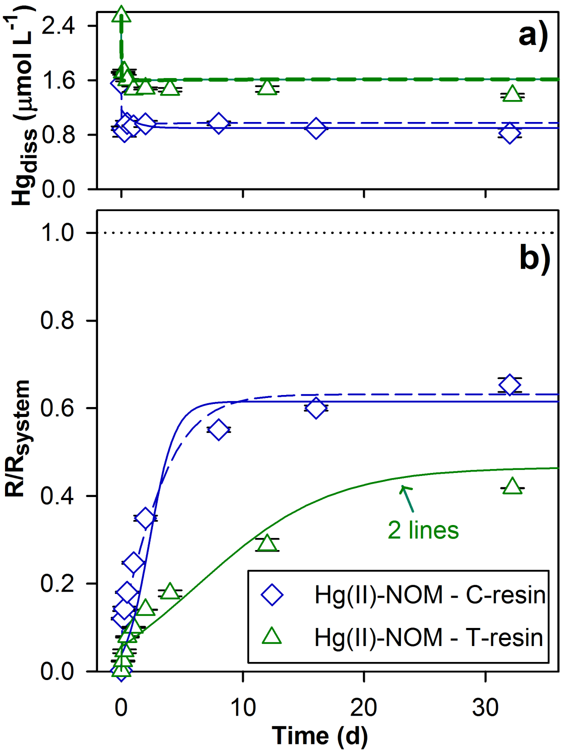

Figure S5.8: Comparison of modeled concentration and isotope ratio kinetics for Hg-NOM exchange with carboxyl- and thiol-resin with dashed line considering initial Hg concentrations and solid line considering recovered Hg concentrations.

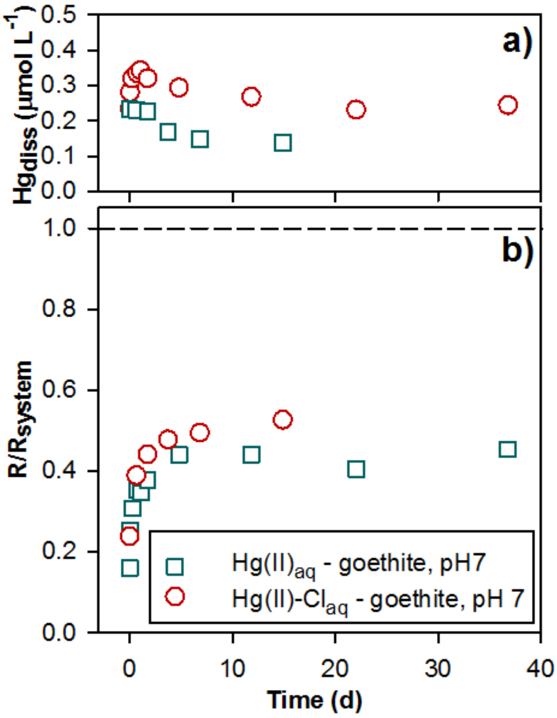

Figure S5.9: Preliminary isotope exchange experiments between dissolved Hg(II)$_{\text{aq}}$ and Hg(II) sorbed to goethite in absence of chloride (squares) and with 0.5 mM chloride (triangles) at pH 7 (with 2.5 mM MOPS buffer). The preconditioning time was 72 h.

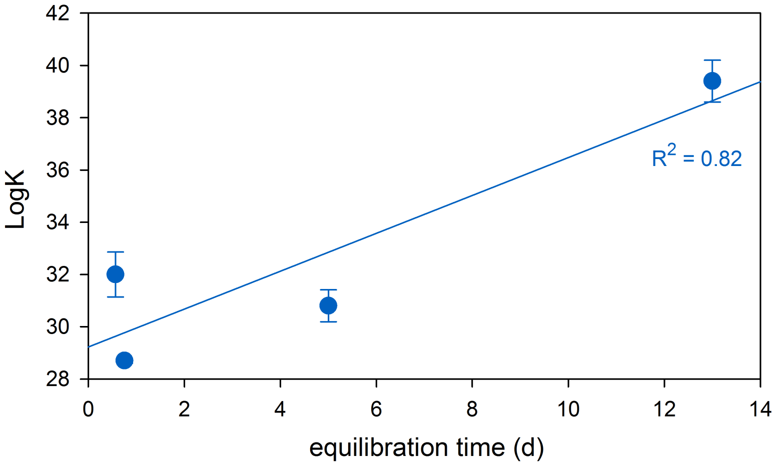

Figure S5.10: Correlation between equilibration time used in previous experiments and reported stability constants from the literature for bidentate Hg-thiol complexes in NOM ($Hg^{2+} + 2L^{-} = HgL_2$).[2–5] In addition to the equilibration time, these experimental studies to determine stability constants differed in type of NOM, methods, and pKa of the thiol-group which could also contribute to the wide range in LogK values observed.

References

[1] J. K. Bohlke, J. R. De Laeter, P. De Bievre, H. Hidaka, H. S. Peiser, K. J. R. Rosman, and P. D. P. Taylor. Isotopic compositions of the elements, 2001. *J. Phys. Chem. Ref. Data*, 34(1):57–67, 2005.

[2] W. Dong, Y. Bian, L. Liang, and B. Gu. Binding constants of mercury and dissolved organic matter determined by a modified ion exchange technique. *Environ. Sci. Technol.*, 45(8):3576–3583, 2011.

[3] M. Haitzer, G. R. Aiken, and J. N. Ryan. Binding of mercury(II) to aquatic humic substances: Influence of pH and source of humic substances. *Environ. Sci. Technol.*, 37(11):2436–2441, 2003.

[4] F. J. Black, K. W. Bruland, and A. R. Flegal. Competing ligand exchange-solid phase extraction method for the determination of the complexation of dissolved inorganic mercury(II) in natural waters. *Anal. Chim. Acta*, 598(2):318–333, 2007.

[5] A. R. Khwaja, P. R. Bloom, and P. L. Brezonik. Binding constants of divalent mercury (Hg^{2+}) in soil humic acids and soil organic matter. *Environ. Sci. Technol.*, 40(3):844–849, 2006.

Dank

Ein grosses Dankeschön möchte ich an meine Betreuer Ruben Kretzschmar, Jan Wiederhold und Bernard Bourdon für ihre Unterstützung während meiner Doktorarbeit aussprechen. Die guten Diskussionen und vielen Ratschläge haben sehr zum erfolgreichen Gelingen dieser Doktorarbeit beigetragen. Bei Ruben möchte ich mich speziell für die super Arbeitsbedingungen und seine Unterstützung, neue Ideen in die Tat umzusetzen, bedanken. Auch wenn sie zum Teil beim ersten Anlauf schief gingen, wie bei der Ultrafiltration, war das Vertrauen in den eingeschlagenen Weg stets spürbar. Einen riesigen Dank geht an Jan, seine Begeisterung für Quecksilberisotope und der beinahe unendliche Optimismus waren ansteckend und haben mich stets motiviert. Die Bereitschaft sich mit Robin und mir in den Journalclubs durch die Quecksilberisotopenliteratur durchzuarbeiten, das Lexikonwissen, das schneller aktualisiert war als das Web of Science, die Geduld mit uns an der Maschine zu sitzen um all die Probleme zu beheben und die Beharrlichkeit, mit der unzählige "r" aus "derrived" in meinen Manuskripten gestrichen wurden, verdienen eine spezielle Anerkennung. I would like to thank Bernard very much for his support, input and the great discussions. I think they added a very important fundamental aspect to my thesis. Merci beaucoup! I would also like to thank Jeroen Sonke for accepting the co-examination of my thesis.

Ein grosser Dank geht an Damian Saile, der seine Masterarbeit im Rahmen meiner Dorktorarbeit machte. Seine riesige Motivation, die schnelle Auffassungsgabe sich in ein komplexes Thema einzuarbeiten und die beinahe grenzenlose Bereitschaft die Pläne umzusetzen haben zu einer super Arbeit geführt, die ich nun auch in dieser Doktorarbeit aufführen darf. Die BM's, bei denen wir über Quecksilber und die Welt diskutiert haben, werden mir in guter Erinnerung bleiben.

A huge Merci goes to Robin Smith, it was great to have a buddy like her and not to be the only mad hatter wanting to bang his head on the wall when the background problem didn't go away. I would like to thank her for her help and the wonderful Pumkinpies in the last years.

I would like to thank Ulf Skyllberg, Erik Björn and Rose-Marie Kronberg for the great collaboration and for hosting me during my visits in Umeå. The enthusiasm and knowledge of Ulf about the mercury cycling in boreal environments was a great help for the outcome of this work and an important inspiration to me. I would like to thank Erik for sharing his experience on enriched stable Hg isotope tracers and for helping me with the isotope exchange experiments. I am grateful to Rose for her help with collecting the samples and for her willingness to take some of the mosquito bites. I really hope that some day you will take me to Granö! Tack så mycket!

I would also like to thank the Hg isotope devotees, fractionation factor seekers, chocolate cake appreciators and Hg isotope diffusionists; the honorable members of the Hg isotope journal club: Jan, Robin and Michi Köberich for the great discussions we had throughout the last years.

I would like to thank Daniel Obrist for his interest in my work, his helpful comments and the inspiring discussions we had during his sabbatical in Zürich. Sehr dankbar bin ich auch Kurt Barmettler für seine Hilfe im Bodenchemielabor und dass er mir all meine Extrawünsche immer erfüllt hat, inklusive eines Papiertuchhalters, damit ich meine Hände nicht mehr an den Hosen abtrocknen musste. Ich möchte mich bei Donat Niederer, Urs Menet und Andreas Süsli für ihre grossratige Hilfe bei der Konstruktion von dem Ofen und den Filtrationssystemen bedanken. Auch Daniel Schnarwiler möchte ich für seine kompetente Beratung und die perfekte Ausführung der Glasarbeiten danken, ohne die der Ofen nicht so gut funktioniert hätte.

Vielen Dank auch an Christa Bodmer, Alexandra Metzger und Alex Brunner für ihre Hilfe bei der Probenaufbereitung und Konzentrationsmessungen der Bodenproben. I would like to thank Irka Hajdas for measuring the radiocarbon ages and introducing me into radiocarbon dating. Ein grosser Dank geht an Colin Maden und Felix Oberli für ihre kompetente und hilfsbereite Unterstützung bei den MC-ISPMS Mesungen. Zudem möchte ich mich auch bei Maria Schönbächler und Derek Vance bedanken, die mich in ihren neuen Gruppen aufgenommen haben.

Ich möchte mich bei allen Mitgliedern der Isotopengeochemie und Bodenchemie Gruppen bedanken für die gute Zeit, die wir zusammen verbracht haben und ihre Hilfe bedanken. Die unzähligen engagierten Diskussionen während Kaffee- und Mittagspausen oder beim Feierabendbier. Die schönen Ski- und Wanderwochenenden waren immer eine Bereicherung.

Merci beaucoup à Jan Jiskra et Anthi Liati pour avoir traduit le résumé en français.

Ein riesiger Dank geht an meine Eltern Marianne und Jan Jiskra, ohne ihre grossartige Unterstützung in den letzten 30 Jahren wäre meine Ausbildung, die in dieser Doktorarbeit mündete, nicht möglich gewesen wäre. Ein grosses Merci geht natürlich auch an meine beiden Geschwister Meli und Kusi.

Der letzte und grösste Dank geht an Marita für ihre grossartige Unterstützung und Hilfe während der letzten Jahre. Ihre ehrliche Meinung zu meiner Arbeit und zu meiner Einstellung gegenüber der Arbeit haben mich immer weiter und manchmal auch wieder auf den Boden gebracht. Für das grosse Verständnis für die vielen Quecksilberisotope in meinem Kopf, vorallem in den letzten Monaten bin ich sehr dankbar. *ευχαριστω* Μ*αριτακιμου*!

Curriculum Vitae

Martin Jiskra
Born on June 17th, 1984 in Richterswil, Switzerland
Citizen of Herisau AR, Switzerland

1999 – 2003	**Baccalaureate**, German Gymnasium, Biel-Bienne, Switzerland
2004 – 2008	**Bachelor of Science ETH in Environmental Sciences** ETH Zurich, Switzerland
2004 – 2008	**Master of Science ETH in Environmental Sciences** ETH Zurich, Switzerland Major in Biogeochemistry and Pollutant Dynamics, Minor in Analytical Chemistry,
2010 – 2014	**Doctoral Student and Teaching Assistant** Institute of Biogeochemistry and Pollutant Dynamics (IBP), at the Department of Environmental Sciences, ETH Zurich, Switzerland and Institute of Geochemistry and Petrology (IGP), at the Department of Earth Sciences, ETH Zurich, Switzerland